The Formation of the Concertina Pattern: Experiments, Analysis, and Numerical Simulations

Dissertation

zur Erlangung des Doktorgrades (Dr. rer. nat.)
der Mathematisch-Naturwissenschaftlichen Fakultät der
Rheinischen Friedrich-Wilhelms-Universität Bonn

vorgelegt von
Jutta Steiner
aus
München

Bonn, Dezember 2010

Angefertigt mit Genehmigung der Mathematisch-Naturwissenschaftlichen Fakultät der Rheinischen Friedrich-Wilhelms-Universität Bonn am Institut für Angewandte Mathematik

Diese Dissertation ist auf dem Hochschulschriftenserver der ULB Bonn unter `http://hss.ulb.uni-bonn.de/diss_online` elektronisch publiziert

1. Gutachter Prof. Dr. Felix Otto
2. Gutachter Prof. Dr. Stefan Müller

Tag der Promotion: 12. Mai 2011
Erscheinungsjahr: 2011

Abstract

The concertina pattern is a ubiquitous pattern observed in ferromagnetic thin-film elements. It occurs during the switching process due to the reversal of an applied homogeneous magnetic field. The pattern-forming quantity is the magnetization, which we think of as a unit-length vector field. The pattern consists of stripe-like quadrangular and triangular regions – called *domains* – with a uniform, in-plane magnetization that is, in particular, constant in the direction of the film thickness. The domains are separated by sharp transition layers in which the magnetization quickly turns – called *walls*.

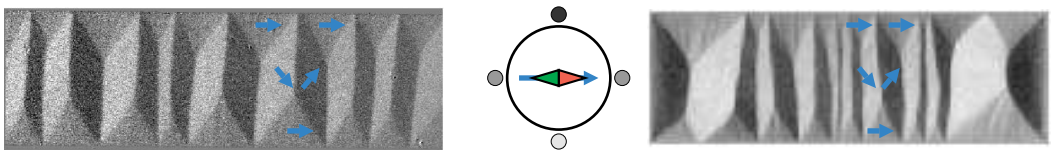

Figure 0.1.: Concertina in a very elongated (length 2 mm) sample of width 50 μm and thickness 50 nm (left) and in a sample of width 35 μm, thickness 40 nm and length 110 μm (right). The left image shows only the center of the stripe which is less than 10 percent of the whole sample. As indicated by the blue arrows, the gray-scales encode the transversal component of the magnetization in the domains. By courtesy of R. Schäfer.

The term *concertina* was introduced by van den Berg in [vdBV82] for this bellow-like structure which is shown in Figure 0.1. In that reference, he discusses its formation in thin rectangular-shaped ferromagnetic elements. He provides an explanation of the domain pattern in a fairly thick (350 nm), not too elongated Permalloy sample (width 15 μm and length 50 μm). He argues that the stripe-like pattern grows into the sample from the tips due to boundary effects as the strength of an external homogeneous magnetic saturation field – parallel to the long edge – is reduced.

We claim that in very elongated (length 2mm) thin (thickness 10 to 150 nm) ferromagnetic samples (width 10 to 100 μm) the concertina does *not* grow from the tips into the sample. For these extreme aspect ratios experiments rather suggest that a bifurcation is at the origin of the concertina pattern, see Figure 0.2: As the strength of an applied homogeneous magnetic field is reduced and finally reversed, the uniform magnetization becomes unstable and buckles. As the strength of the

destabilizing field increases, the oscillatory buckling of the magnetization grows into the concertina pattern – simultaneously all over the sample. Cantero and Otto performed a linear stability analysis on the basis of the micromagnetic energy functional, see [CÁO06a] and [CÁO06b]. They identified a thin-film regime in which the most unstable perturbation, the so called unstable mode, has the form of an oscillatory buckling. They find that the period of that instability is determined by the width and the thickness of the sample together with the exchange length, a material parameter. In [CÁOS07] a reduced energy functional was deduced as the scaling limit of the micromagnetic energy in the oscillatory buckling regime. Numerical simulations of the reduced energy functional showed that the unstable mode grows into a concertina pattern. The bifurcation is slightly subcritical but exhibits a turning point. This means that the bifurcating branch of stationary points is unstable but becomes stable after the turning point (both under perturbations of the same period). A comparison of the period of the unstable mode with the experimentally measured period yields a good agreement over a wide range of widths and thicknesses. However, there is a clear tendency that the experimental period is always larger by a factor up to approximately two. In the experiments, one additionally observes that the concertina pattern exhibits several coarsening events as the strength of the destabilizing external field increases: Folds collapse, increasing the average period of the pattern until it finally disappears. In order to understand these observations, it is necessary to study the stability w.r.t. perturbations whose period is a multiple of the period of the unstable mode or of the concertina, respectively.

The genesis of the concertina pattern is a prototypic example of a hysteretic process. The aim of this work is an extensive understanding of the experimental observations in the formation process of the concertina pattern on the basis of the reduced energy functional. In particular, we explain the deviation of the experimental period from the period of the unstable mode and investigate the coarsening of the concertina. This is achieved by an application of a mixture of rigorous analysis, numerical simulations and heuristic arguments.

- The application of a heuristic sharp interface model, namely domain theory, shows that the optimal period of the concertina is an increasing function of the (destabilizing) external field. This is rigorously confirmed on the level of the reduced energy functional based on the construction of appropriate Ansatz functions and new nonlinear interpolation estimates providing Ansatz-free lower bounds. Domain theory is (partially) justified by a compactness result for minimizers of the reduced energy functional.

- Domain theory suggests that the concertina becomes unstable under long wave-length modulations as the destabilizing external field increases. The instability is analyzed and confirmed by a Bloch wave analysis of the Hessian of the reduced energy functional in combination with numerical simulations of the reduced energy functional. Simulations show that the instability finally leads to the coarsening of the concertina pattern.

- A (generalized) bifurcation analysis shows that the deviation of the period of the unstable mode from the experimental observations is due to a non-linear modulation instability. This instability is in turn related to the so called Eckhaus instability.
- Domain theory and numerical simulations are applied to investigate the effect of a uniaxial transversal and longitudinal anisotropy, respectively. This confirms the experimental observation that a transversal anisotropy has a stabilizing effect while in case of a longitudinal anisotropy the concertina cannot be observed at all.
- Based on a linearization of the reduced energy functional, the ripple-like structure, which occurs in polycrystalline material, is investigated. In the experiments, one observes that the ripple continuously grows into the concertina pattern. The analysis shows that both the ripple and the concertina are driven by the same physical mechanisms. Numerical simulations confirm this result and reproduce the transition from the ripple to the concertina.

In Chapter 1, we review the previously known results and extensively present and physically interpret our new insights. For proofs, explanations of the methods applied, and further investigations, we refer to the subsequent chapters.

The experiments that we discuss and present were carried out at the IfW Dresden by J. McCord, R. Schäfer, and H. Wieczoreck.

Danksagung

An erster Stelle möchte ich mich herzlich bei Herrn Prof. Dr. Felix Otto für die Betreuung dieser Arbeit und seine intensive Förderung und fortwährende Unterstützung bedanken.

Herrn Prof. Dr. Stefan Müller danke ich für die Übernahme des Zweitgutachtens. Frau Prof. Dr. Ursula Hamenstädt, Herrn Prof. Dr. Herbert Koch und Herrn Prof. Dr. Karl Maier danke ich für ihr Mitwirken in der Promotionskommission.

Herrn Dr. Jeffrey McCord, Herrn Dr. Rudolf Schäfer und Herrn Dr. Holm Wieczoreck vom IfW in Dresden danke ich für die fruchtbare Zusammenarbeit. Den Mitgliedern der dortigen Arbeitsgruppe danke ich für ihre Gastfreundschaft.

Herrn Prof. Dr. Alexander Mielke gilt mein Dank für seine Hinweise zur Eckhaus-Instabilität. Herrn Martin Zimmermann danke ich für die technische Hilfe.

Mit Sicherheit wäre ohne meine Kollegen und Kommilitonen die Entstehung dieser Arbeit nicht denkbar gewesen: Ihnen danke ich herzlich für die intensiven Diskussionen, die Hilfe beim Beseitigen von IT-Problemen jeder Art, die aufbauenden Worte und die gemeinsamen Erholungspausen.

Besonderer Dank gilt meiner Familie und meinen Freunden für ihre Unterstützung und vor allem Artur für seine liebevollen Aufmunterungen und seine Geduld.

Diese Arbeit wurde unterstützt durch den SFB 611 und die Bonn International Graduate School in Mathematics.

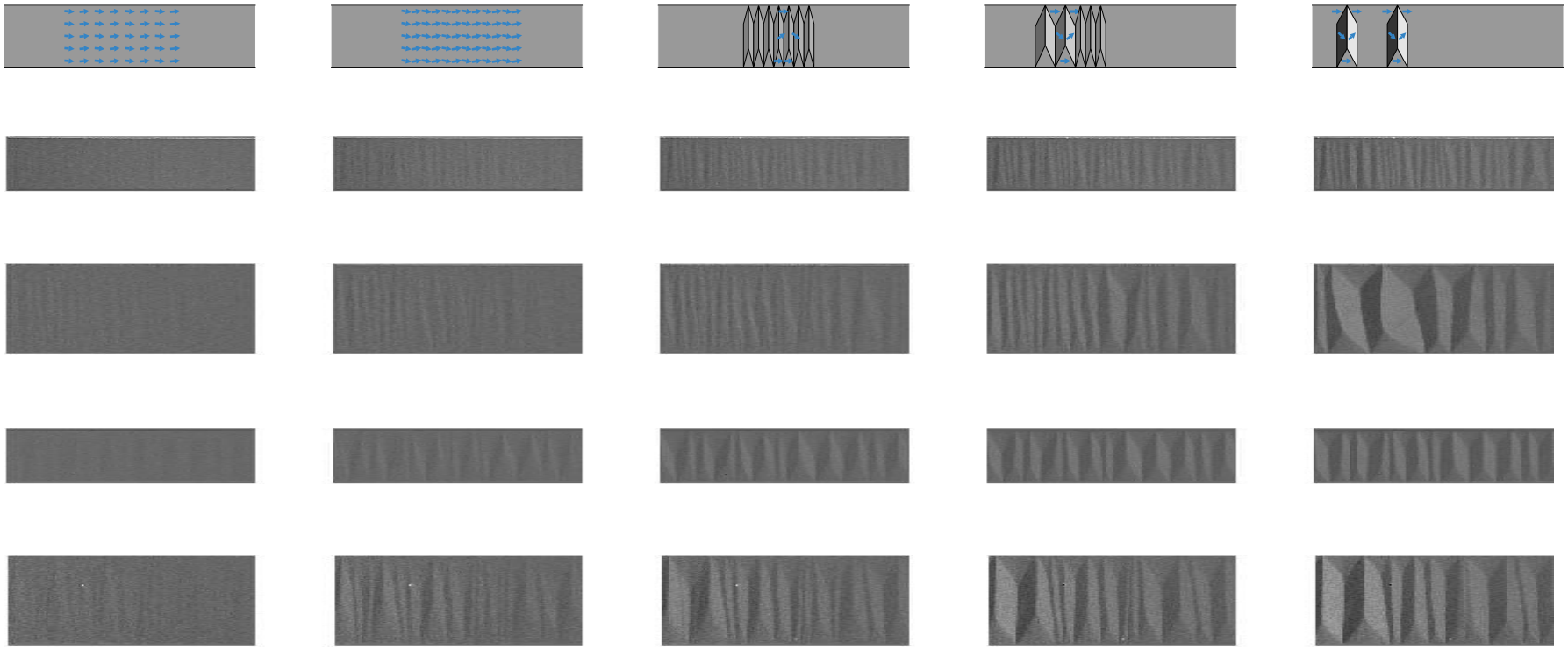

Figure 0.2.: Formation of the concertina pattern in the experiment: The pictures show a section near the center of four different elongated thin film elements for different values of the external field. The two upper series show samples of 30 nm thickness of low anisotropy. The two lower series show samples of 30 nm thickness of higher transversal anisotropy. The width is 30 µm and 50 µm, respectively. The magnetization was saturated by a homogeneous external magnetic field applied in direction of the long axis. The strength of that field was decreased and it was eventually reversed. At some critical field, the uniform magnetization buckles into the concertina pattern. This domain-wall pattern coarsens several times before it finally disappears (no picture).

Contents

1

Introduction

In this chapter, we start with an introduction of the underlying physical model. Afterwards, we review the linear stability analysis in [CÁO06a] and give a motivation for the reduced model which was derived in [CÁOS07] in the relevant parameter regime (identified in the linear stability analysis). We proceed with a discussion of van den Berg's explanation of the concertina.

Motivated by the experiments and numerical simulations of the reduced model, a heuristic sharp interface model – *domain theory* – is discussed which is based on a piece-wise constant approximation of the magnetization on a mesoscopic scale. This provides a first understanding of the coarsening of the concertina which is then further investigated on the basis of the reduced model. Finally, we discuss two very different effects of anisotropy which were neglected in the analysis before: We first address the effect of a polycrystalline anisotropy which is relevant in Permalloy material; it turns out that the oscillatory ripple structure, which is triggered by the polycrystallinity of Permalloy material, is intimately related to the concertina. Afterwards, we address the effect of a uniaxial anisotropy on the formation of the concertina.

Details on the experimental setup and the samples are discussed in Section 1.12 at the end of the introduction. Details on the numerical simulations, shortly addressed in Section 1.11, are postponed to Chapter 4. In particular, Section 4.10 contains the specific choices of the parameters in the simulations.

1.1. The micromagnetic energy

Since the applied magnetic field in the experiment varies on a very slow time scale, the magnetization always relaxes to equilibrium. Therefore we assume that the observed configurations are local minima of some free energy. The well-accepted model that we apply is given by the micromagnetic (free) energy, see below. This model was first introduced by Landau and Lifshitz in [LL35].

Let us denote by $\Omega \subset \mathbb{R}^3$ the space which is occupied by a ferromagnetic sample and by $m\colon \Omega \to \mathbb{S}^2$ the magnetization of the sample. The micromagnetic energy

$E(m)$ is given by

$$\begin{aligned} E(m) = \quad & d^2 \int_\Omega |\nabla m|^2 \, \mathrm{d}x && \text{Exchange energy} \\ & + \int_{\mathbb{R}^3} |H_{\text{stray}}|^2 \, \mathrm{d}x && \text{Stray-field energy} \\ & - Q \int_\Omega (m \cdot e)^2 \, \mathrm{d}x && \text{Anisotropy energy} \\ & - 2 \int_\Omega H_{\text{ext}} \cdot m \, \mathrm{d}x && \text{Zeeman energy.} \end{aligned} \tag{1.1}$$

The micromagnetic energy in the form of (1.1) is partially non-dimensionalized, i.e., except for lengths. Therefore the magnetization is described by a vector field of unit-length that vanishes identically outside of the sample:

$$|m|^2 = 1 \quad \text{in} \quad \Omega \quad \text{and} \quad m = 0 \quad \text{in} \quad \mathbb{R}^3 - \Omega. \tag{1.2}$$

Let us briefly introduce and discuss the different energy contributions:

Exchange energy. The first contribution is the so called exchange energy which is of quantum-mechanical origin. (The gradient acts component wise, i.e., $|\nabla m|^2 = \sum_{i=1}^3 \sum_{j=1}^3 (\partial_i m_j)^2$.) It obviously favors a uniform magnetization. The material parameter d is called the exchange length and measures the relative strength between exchange and stray-field energy. This length is typically of the order of some nm.

Stray-field energy. The second contribution is the stray-field energy. Due to the static Maxwell equations, the magnetization m generates a stray-field $H_{\text{stray}}\colon \mathbb{R}^3 \to \mathbb{R}^3$ which satisfies

$$\nabla \times H_{\text{stray}}(m) = 0 \quad \text{and} \quad \nabla \cdot (H_{\text{stray}}(m) + m) = 0 \quad \text{in} \quad \mathbb{R}^3, \tag{1.3}$$

where $B = H_{\text{stray}} + m$ is the magnetic induction. Hence, the stray-field is the field which is generated by the divergence of the magnetization. Since the magnetization is discontinuous at the boundary $\partial\Omega$ of the sample, cf. (1.2), the second equation has to be understood in the sense:

$$\nabla \cdot H_{\text{stray}} = \begin{cases} 0 & \text{in } \mathbb{R}^3 - \Omega \\ -\nabla \cdot m & \text{in } \Omega \end{cases} \quad \text{and} \quad [H_{\text{stray}} \cdot \nu] = m \cdot \nu \quad \text{on} \quad \partial\Omega, \tag{1.4}$$

where ν is the outward pointing normal of $\partial\Omega$ and $[H_{\text{stray}} \cdot \nu]$ denotes the jump $H_{\text{stray}} \cdot \nu$ experiences across the surface $\partial\Omega$. We therefore distinguish two different types of sources of the stray-field – in analogy to electrostatics, we speak of charges – namely

$$\begin{aligned} &\text{magnetic volume charges} && -\nabla \cdot m \quad \text{in} \quad \Omega \quad \text{and} \\ &\text{magnetic surface charges} && m \cdot \nu \quad \text{on} \quad \partial\Omega. \end{aligned}$$

There are several equivalent formulations for (1.4). Due to (1.3), it can be represented as $H_{\text{stray}} = -\nabla u$, where the potential $u : \mathbb{R}^3 \to \mathbb{R}$ is given as the solution to

$$-\Delta u = \begin{cases} 0 & \text{in } \mathbb{R}^3 - \Omega \\ -\nabla \cdot m & \text{in } \Omega \end{cases} \quad \text{and} \quad [\nabla u \cdot \nu] = -m \cdot \nu \text{ on } \partial\Omega.$$

Another formulation is given by

$$\int_{\mathbb{R}^3} |H_{\text{stray}}(m)|^2 = \int_{\mathbb{R}^3} \left| |\nabla|^{-1} \nabla \cdot m \right|^2 \mathrm{d}x,$$

where $|\nabla|^{-1}$ is defined in Fourier space via the multiplier $|k|^{-1}$.

Anisotropy energy. The third contribution is the anisotropy energy which models the dependence (of the energy) on the direction of the magnetization relative to the so called *easy axis* $e = (e_1, e_2, e_3)$ of a *uniaxial* material. The relevant anisotropy in our samples is either a longitudinal anisotropy, i.e., $e = (1, 0, 0)$, or a transversal anisotropy, i.e., $e = (0, 1, 0)$, see Section 1.12. The material parameter $Q > 0$ is called the quality factor. It measures the relative strength between anisotropy and stray-field energy. A uniaxial anisotropy originates for example in crystalline or so-called induced anisotropy, see [CG08, Chapter 7, Chapter 10]. Later on we will also consider polycrystalline anisotropy which plays an important role in Permalloy material. This can be modeled with the help of a (random) position-dependent easy axis $e(x)$.

Zeeman energy. The last contribution is called Zeeman energy. It models the interaction and favors the alignment of the magnetization with an applied external magnetic field $H_{\text{ext}} : \mathbb{R}^3 \to \mathbb{R}^3$.

We note that we usually do not explicitly denote the dependence of the energy on the extrinsic or intrinsic parameters, i.e., external field H_{ext}, dimensions of the sample Ω, and the material parameters d and Q.

1.2. Linear stability analysis

We are interested in magnetization patterns in very elongated thin-film elements of width ℓ (in x_2-direction) and thickness $t \ll \ell$ (in x_3-direction) which form under the reversal of a homogeneous external magnetic field. This field is aligned with the long axis (the x_1-axis) of the sample. Hence it is of the form $H_{\text{ext}} = (-h_{\text{ext}}, 0, 0)$, see Figure 1.1. (The minus is introduced so that the critical field in case of vanishing uniaxial anisotropy is positive which simplifies the notations, see below.)

Experimental observations of the samples, that have a length about 2mm at least 20 times larger than the width ℓ, suggest that the pattern away from the sample edges in x_1-direction is not influenced by boundary effects at the sample's tips (we later

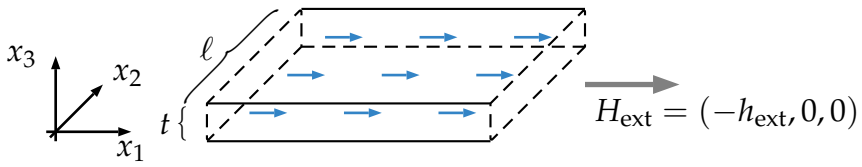

Figure 1.1.: The idealized geometry of the sample. The homogeneous external saturation field H_{ext} is parallel to the long axis of the sample.

come back to this point in Section 1.4). The pattern was recorded at three different locations, equidistant to the small edges of the cross section, where qualitatively the same pattern at the same values of the external field was observed. We therefore assume from now on that the sample is infinite in x_1-direction, i.e., $\Omega = \mathbb{R} \times (0, \ell) \times (0, t)$, or periodic, i.e., $\Omega = [0, L) \times (0, \ell) \times (0, t)$ with period L sufficiently large. As a consequence of the idealized geometry the uniform magnetization $m^* = (1, 0, 0)$ is a stationary point of the energy functional for all values h_{ext} of the external field $H_{\text{ext}} = (-h_{\text{ext}}, 0, 0)$.

Let us neglect anisotropy – it can and will be included later on in Section 1.10. Observe that $\pm m^*$ is the global minimizer of the energy (1.1) for $h_{\text{ext}} \lesseqgtr 0$. Experiments suggest that as the strength of the field is reduced starting from saturation (i.e., for large negative value of h_{ext}) and finally reversed, a bifurcation at some critical value $h^*_{\text{ext}} > 0$ of the external field $(-h_{\text{ext}}, 0, 0)$ is at the origin of the concertina pattern. The investigation of the concertina starts with a linear stability analysis of the uniform magnetization in the following section.

1.2.1. Hessian and unstable modes

In Theorem 1 in [CÁO06a, p.357], a linear stability analysis of the saturated state $m^* = (1, 0, 0)$ was performed. Due to the unit length constraint (1.2), infinitesimal variations of m^* are of the form $\delta m = (0, \delta m_2, \delta m_3)$. The uniform magnetization only generates Zeeman energy. Therefore, the Hessian of the energy in m^* is given by the exchange energy and the stray-field energy of the infinitesimal variation, augmented by the linearization of the Zeeman energy:

$$\text{Hess}E(m^*)(\delta m, \delta m) = \int_\Omega |\nabla \delta m|^2 \,\mathrm{d}x + \int_{\mathbb{R}^3} |H_{\text{stray}}(\delta m)|^2 \,\mathrm{d}x - h_{\text{ext}} \int_\Omega (\delta m_2^2 + \delta m_3^2) \,\mathrm{d}x. \tag{1.5}$$

In the following, we discuss potentially unstable modes δm on the basis of (1.5). One particular result will be the identification of the relevant parameter regime – for the occurrence of the concertina pattern – as a function of the thickness t, the width ℓ and the value of the exchange length d.

We continue to neglect uniaxial anisotropy (i.e., we set $Q = 0$) at that point, since on the level of this infinitesimal discussion, a longitudinal or transversal anisotropy

just leads to a shift of the critical field $h^*_{\text{ext}} \rightsquigarrow h^*_{\text{ext}} \pm Q$, see Section 1.10. However, since the shift entails that the sign of the critical field can change, we note in that if we speak about *reducing* the strength of the (stabilizing) external field, we usually mean that the critical field is approached from saturation ($h_{\text{ext}} = -\infty$) if not stated differently. Similarly, we say that the external field is *increased* after the critical field is passed. In this sense, the critical field is interpreted as the *zero point* on the scale of the external field, cf. Figure 1.2.

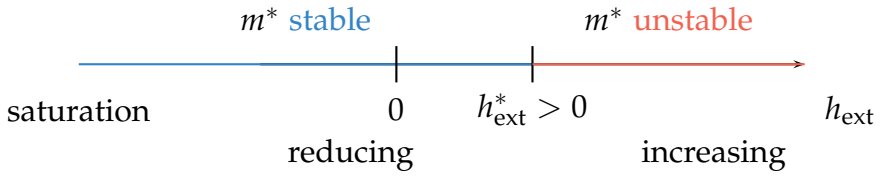

Figure 1.2.: The scale of the external field h_{ext}.

Regime I. The first unstable mode discussed in [CÁO06a] is a coherent, in-plane rotation, i.e., $\delta m = (0, 1, 0)$, cf. Figure 1.3. On the basis of (1.5), let us argue at which field this mode becomes unstable by determining the infinitesimal release of energy in terms of scaling. A coherent rotation releases Zeeman energy per length in x_1-direction of the infinitesimal amount $h_{\text{ext}}\ell t$. A coherent rotation generates surface charges. Over distances ℓ much larger than t, the surface charges act like two oppositely charged wires at distance ℓ of line density t – also in the following if not mentioned otherwise always infinitesimally and per length in x_1-direction. This generates an infinitesimal stray-field of the order $t^2(\ln \ell t^{-1})$. Therefore, this mode becomes unstable at a field h_{ext} of the order $t\ell^{-1}(\ln \ell t^{-1})$ for t much smaller than ℓ – in short hand notation $h_{\text{ext}} \sim t\ell^{-1}(\ln \ell t^{-1})$ for $t \ll \ell$. [1].

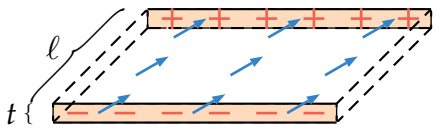

Figure 1.3.: Coherent rotation and generated surface charges.

Regime II. The second unstable mode we consider is buckling, cf. Figure 1.4. The magnetization avoids the lateral surface charges by just laterally buckling in the middle of the cross section, i.e.,

$$\delta m = (0, \sin(\pi \tfrac{x_2}{\ell}), 0).$$

[1] By $f \ll g$ we mean that there exists a universal constant $C > 1$ such that $Cf < g$. Moreover, $\lesssim$ and $\gtrsim$ stand for $\leq$ and $\geq$ up to a generic constant and by $\sim$ we mean both $\lesssim$ and $\gtrsim$.

However, since $\nabla \cdot \delta m = \pi \ell^{-1} \cos(\pi \frac{x_2}{\ell})$, the surface charges of the coherent rotation turn into volume charges. At distances much larger than t from the cross section, these volume charges act like surface charges of amplitude $\ell^{-1} t$ which generate a stray-field energy $\sim t^2$. This is slightly smaller (by a logarithm) than the infinitesimal stray-field energy case of the previous mode of coherent rotation. Moreover, since $|\nabla \delta m|^2 = \pi^2 \ell^{-2} \cos(\pi \frac{x_2}{\ell})^2$, the buckling mode generates exchange energy $\sim d^2 \ell^{-1} t$, where we recall that d denotes the exchange length as introduced in (1.1). Since the release of Zeeman energy scales as $\sim h_{\text{ext}} \ell t$ as above, this mode becomes unstable at $h_{\text{ext}} \sim d^2 \ell^{-2}$ in the regime $t \lesssim d^2 \ell^{-1}$ and at $h_{\text{ext}} \sim t \ell d^{-2}$ in the regime $t \gtrsim d^2 l^{-1}$. The second mode beats the first mode for $d^2 \ell^{-1} (\ln^{-1} \ell d^{-1}) \lesssim t$ in the sense that it becomes unstable earlier, i.e., at a smaller field h_{ext}.

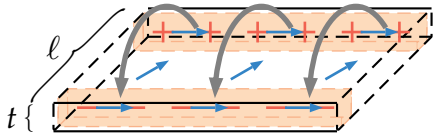

Figure 1.4.: Buckling mode and its generated volume charges (shaded region) and stray-field (gray arrows).

Regime III. The third unstable mode we discuss is oscillatory buckling, cf. Figure 1.5. This mode reduces the stray-field energy through a modulation of the lateral buckling in x_1-direction, i.e.,

$$\delta m = (0, \sin(\pi \tfrac{x_2}{\ell}) \sin(2\pi \tfrac{x_1}{w}), 0)$$

with a wave length w with $t \ll w \ll \ell$. Since $w \gg t$, the volume charges generated by this mode act like surface charges of amplitude $\ell^{-1} t$ over distances much larger than t from the cross section. However, these surface charges change sign over a distance $w \ll \ell$, so that the generated stray-field only extends over a distance w away from the cross section. Hence this mode generates a stray-field energy $\sim \ell^{-1} t^2 w$, which is substantially less than the stray-filed energy of the two prior modes for $w \ll \ell$. Due to $w \ll \ell$, the exchange energy is now dominated by the oscillation in x_1-direction, which leads to an infinitesimal exchange energy $\sim d^2 \ell w^{-2} t$. Hence the w, which leads to the minimal infinitesimal combined stray-field and exchange energy of $d^{2/3} \ell^{-1/3} t^{5/3}$, is given by $w^* \sim d^{2/3} \ell^{2/3} t^{-1/3}$. This is consistent with $t \ll w \ll \ell$ provided $d^2 \ell^{-1} \lesssim t \lesssim (d\ell)^{1/2}$. The oscillatory buckling mode becomes unstable at $h_{\text{ext}} \sim d^{2/3} \ell^{-4/3} t^{2/3}$ and, therefore, beats the first and second mode provided $d^2 \ell^{-1} \lesssim t$.

Regime IV. The fourth unstable mode we consider is curling. This mode avoids charges altogether by an x_3-dependent magnetization whose flow lines have a cork-skew shape, i.e.,

$$\delta m = (0, \sin(\pi \tfrac{x_2}{\ell}) \cos(\pi \tfrac{x_3}{t}), \ell^{-1} t \cos(\pi \tfrac{x_2}{\ell}) \sin(\pi \tfrac{x_3}{t})).$$

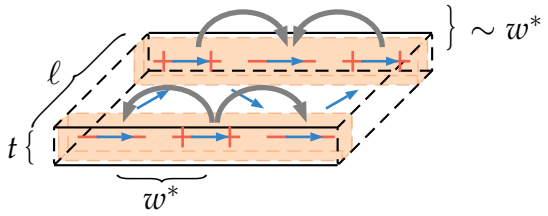

Figure 1.5.: Oscillatory buckling mode and its generated volume charges (shaded region) and stray-field (gray arrows).

The exchange energy is now dominated by the gradient in x_3-direction which scales as $d^2\ell t^{-1}$. Hence the curling mode becomes unstable at $h_{\text{ext}} \sim d^2 t^{-2}$. It beats the other modes provided $(d\ell)^{1/2} \lesssim t$.

The infinitesimal perturbations discussed above only provide upper bounds for the critical field h^*_{ext}. Matching lower bounds in terms of scaling were proofed in [CÁO06a] by Ansatz-free lower bounds for the Hessian using interpolation estimates. The analysis in [CÁO06a] thus shows that there are exactly four regimes for the instability, see 1.6.

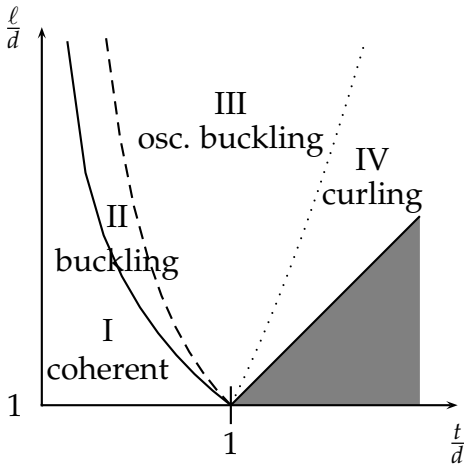

Figure 1.6.: Phase diagram of the four regimes of instability.

1.3. Period of the unstable mode: Experiment vs. theory

Clearly, the regime of interest to us is the Regime III. Based on a Γ-convergence result for the Rayleigh quotient of the Hessian, it was shown that the unstable mode in Regime III is indeed of the form

$$\delta m = (0, \sin(\pi \tfrac{x_2}{\ell}) \sin(2\pi \tfrac{x_1}{w}), 0), \tag{1.6}$$

see Theorem 1 in [CÁO06b, p. 389]. Moreover, the asymptotic behavior – including the factor – of w^* was determined, namely

$$w^* \approx (32\pi)^{1/3} d^{2/3} \ell^{2/3} t^{-1/3}. \tag{1.7}$$

Here, $\approx$ means asymptotically equal. So far, we have learned that in Regime III at field strengths $h^*_{\text{ext}} \sim d^{2/3}\ell^{2/3}t^{-4/3}$ there is a bifurcation in direction of the oscillatory buckling mode (1.6) with period given by (1.7). We claim, cf. Section 1.6, that the concertina pattern grows out of this unstable mode. If so, we expect that the experimentally observed period w^*_{exp} should be close to the period w^* of the unstable mode. Defining and determining w^*_{exp} is delicate, see Figure 0.2: As h_{ext} increases, there is a continuous transition from the magnetization ripple – for details see Subsection 1.9 – to the concertina pattern, which is far from exactly periodic, and which coarsens subsequently, see Section 1.8. As w^*_{exp} we take the average period as soon as the concertina pattern is discernible to the eye. Let us note that counting by hand and automatic determination via Fourier analysis coincide. Figure 1.7 shows the result of this comparison for a broad range of sample dimensions ℓ and t and therefore a fairly broad range of periods w^*: The ratio of the widest compared to the smallest sample is 5 and the ratio of the thickest compared to the thinnest is 15. The smallest period w^* is expected for a thick film of small width, the largest period for a thin film of large width, differing by a factor close to six – neglecting the prediction for the defect samples. The ratio $\frac{w^*_{\text{exp}}}{w^*}$ is approximately two. We basically see this as a confirmation of our hypothesis that the concertina grows out of the unstable mode and inherits its period. Notice that the deviation has a clear trend: w^*_{exp} is larger than w^*. We give an explanation for this systematic deviation in Section 1.8.

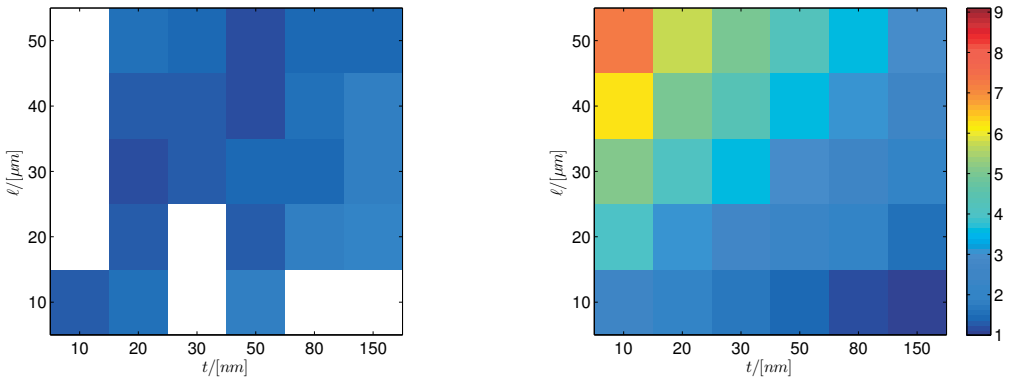

Figure 1.7.: The theoretical period of the unstable mode is in good correspondence to the measurements: The left image shows the ratio of the average experimentally observed period (observed in low anisotropic Permalloy) and the period of the unstable mode. The white patches correspond to defect samples. The right image displays the ratio of the period w^* and the smallest expected period at all, i.e., w^* for the values $\ell = 50\,\mu\text{m}$, $t = 150$ nm. Both images share the same color map.

1.4. Van den Berg's vs. our explanation

Let us turn to van den Berg's explanation in [vdBV82]. The combination of van den Berg's explanation of the concertina with the insights from [BS89, DKM$^+$01]

leads to the following updated version of the explanation in [vdBV82, Sections A & B]: In sufficiently large thin-film elements and for sufficiently low external fields, [BS89] postulate that the *mesoscopic* two-dimensional magnetization pattern, i.e., in-plane $m_3 = 0$ and independent of the thickness direction $m = m(x_1, x_2)$, with sharp charge-free walls and that is tangential to the lateral edges of the sample, arranges itself in such a way that the corresponding continuous magnetic charge density $\sigma = -(\partial_1 m_1 + \partial_2 m_2)$ generates a stray-field H_{stray} that expels the external field H_{ext} from inside of the sample – like in electrostatics.

In [DKMO05], see [DKM$^+$01] for an efficient account, it is shown that in the regime of sufficiently large thin-film elements – i.e., $t \ll \ell$ and $\ell t \gg d^2 \log \frac{\ell}{t}$ and comparable lateral dimensions $\sim \ell$ – this principle extends to moderately large fields $\sim \frac{t}{\ell}$: In this case the stray-field H_{stray} in general can no longer expel the external field H_{ext} everywhere in the sample, since the total charge density $\sigma = -(\partial_1 m_1 + \partial_2 m_2)$ is limited by $m_1^2 + m_2^2 = 1$. The charge density σ is uniquely determined by a *convex* variational problem only involving the stray-field energy and the Zeeman term. At least some aspects of the mesoscopic two-dimensional magnetization pattern (m_1, m_2) can be recovered from σ: The characteristics of (m_1, m_2), i.e., the curves along which (m_1, m_2) is normal (called "trajectories" in [vdBV82]), have curvature given by σ. However, due to the even charge-free discontinuity curves of the mesoscopic magnetization (m_1, m_2), this seemingly rigid condition does not suffice to determine (m_1, m_2) – even if it is easy to construct a solution via the maximal solution of a modified eikonal equation [DKM$^+$01, p.2987]. On the other hand, in the region where the external field has penetrated, (m_1, m_2) is unique [DKM$^+$01, p.2987] and has no discontinuities [vdBV82, p.883].

Van den Berg explains the experimental observations as follows: For sufficiently large external fields $H_{\text{ext}} \gg \frac{t}{\ell}$ [2], the sum of the external field and the generated stray-field $H_{\text{ext}} + H_{\text{stray}}$ does not vanish in the sample, besides in the vicinity of the two distant edges; as a consequence walls only occur in the two flux closure pattern at the distant edges. As the external field is reduced, the penetrated region shrinks as the walls invade the sample. Each of the two flux closure patterns has a "doublet" which is a point on one of the long edges where two wall segments intersect. The doublets were created at the very beginning of the experiment, as the 180° wall of the Landau state touched the edge and broke up due to the application of a strong external field parallel to the long edge. The inner (most distant to the short edges) ones of the doublet walls fade out in the middle of bar. As the field decreases, each of these two walls grows – necessarily in direction of the characteristic – till it hits the opposite edge. There it must generate a "triplet" (a point on the edge where three walls meet); the middle wall must coincide with the previous one originating in the doublet. Again, the inner of the three walls grows towards the original, opposite edge. From there on, the process repeats till the built-up concertina structure is linked in the middle of the bar. For very elongated samples, the linking is expected at a field

[2] This is the strength of the applied field that can be compensated in a thin film element of lateral dimensions $\sim \ell$ and thickness t.

strength of order $H_{\text{ext}} \sim t\ell L^{-2} \ln t\ell^{-1}$ and thus differs from the field at the beginning of the growth process by a factor $\ell^2 L^{-2} \ll 1$ (up to a logarithm)[3]. We note that, mathematically speaking, van den Berg appeals to continuity via the external field to overcome the non-uniqueness of the magnetization (m_1, m_2) mentioned above.

Our explanation for the genesis of the concertina pattern is very different from the one of van den Berg. Instead of an outgrowth of the closure domains, we explain the concertina as an outgrowth of an unstable mode best captured in very elongated thin film elements. Indeed, our experiments were performed on thin film elements of thicknesses t in the range of 10 nm to 150 nm, widths ℓ in the range of 10 µm to 100 µm, but lengths in the range of 2mm. As mentioned, we recorded the pattern at different sections and observed qualitatively the same pattern at the same values of the external field.

Not surprisingly, our theoretical predictions are quite different from those in [vdBV82] – already in terms of scaling. Van den Berg's explanation contains two different scales of the external field ($H_{\text{ext}} \sim \frac{t}{\ell}$ for the beginning of the building process and $H_{\text{ext}} \sim t\ell L^{-2} \ln t\ell^{-1}$ for the completion when the external field can be totally expelled from the sample) whereas in our case $H_{\text{ext}} \sim d^{2/3}\ell^{-4/3}t^{2/3}$, see Regime III in Subsection 1.2.1, which is in accordance with the simultaneous formation along the sample independent of the specific position. Whereas in [vdBV82] the appropriate scale for the concertina width w is given by ℓ, in particular independent on the thickness t, it is given by and $d^{2/3}\ell^{2/3}t^{-1/3}$ in our case, in accordance with our experimental observations illustrated in Figure 1.8.

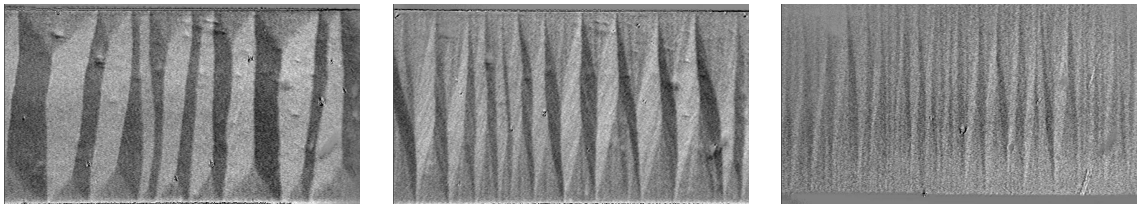

Figure 1.8.: Concertina in Permalloy samples of width $\ell = 100\,\mu\text{m}$ and thickness $t = 30$ nm (left), $t = 80$ nm (center), and $t = 300$ nm (right). The average period of the pattern is a decreasing function of the thickness of the sample.

[3]Notice that the potential u corresponding to a stray-field that compensates the uniform external field in the sample $(-L/2, L/2) \times (0, \ell) \times (0, t)$ is expected to be of the form $u \approx h_{\text{ext}} x_1 (\ln LR^{-1})(\ln^{-1} L\ell^{-1})$ at distance $\ell \ll R = (x_2^2 + x_3^2)^{1/2} \ll L$ for $\ell - L/2 \ll x_1 \ll L/2 - \ell$. This can be used to estimate the total flux through a test cylinder of radius R and thickness $\Delta x_1 \gg R$ which is equal to the net charge density. This entails $x_1 h_{\text{ext}} \ln^{-1} L\ell^{-1} \sim t \int_0^\ell \sigma \, \mathrm{d}x_2$. Provided there are no boundary charges at the lateral edges of the sample we find that $\int_0^{L/2} x_1 h_{\text{ext}} \ln^{-1} L\ell^{-1} \, \mathrm{d}x_1 \sim t \int_0^{L/2} \int_0^\ell \sigma \, \mathrm{d}x_2 \, \mathrm{d}x_1 \sim t \int_0^\ell m_1(x_1 = 0, x_2) \, \mathrm{d}x_2 \leq t\ell$. This indicates that a field of strength $h_{\text{ext}} \lesssim -t\ell L^{-2} \ln t\ell^{-1}$ can be expelled from within the sample.

1.5. A reduced energy functional

In order to understand the type of bifurcation, it is useful to pass to a reduced model adapted to Regime III. This reduced model was rigorously deduced based on the notion of Γ-convergence in Theorem 3 in [CÁOS07, p.233]. Let us give a short heuristic motivation for the reduced model by identifying higher order terms:

	m, $\lvert m\rvert^2 = 1$	$\lvert\nabla m\rvert^2$	$\int_{\mathbb{R}^3} \lvert\lvert\nabla\rvert^{-1}\nabla\cdot m\rvert^2 \,\mathrm{d}x$
thin-film $t \ll w$	$m_3 \equiv 0$	$\lvert\nabla' m\rvert^2$	$\frac{t^2}{2}\int_{\mathbb{R}^2} \lvert\lvert\nabla\rvert^{-1/2}\nabla'\cdot m'\rvert^2 \,\mathrm{d}x'$
scale sep. $w \ll \ell$		$\lvert\partial_1 m'\rvert^2$	$\frac{t^2}{2}\int_{\mathbb{R}^2} \lvert\lvert\partial_1\rvert^{-1/2}\nabla'\cdot m'\rvert^2 \,\mathrm{d}x'$
low-angle approx.	$m_1 \approx 1 - \frac{m_2^2}{2}$	$\lvert\partial_1 m_2\rvert^2$	$\frac{t^2}{2}\int_{\mathbb{R}^2} \lvert\lvert\partial_1\rvert^{-1/2}(-\partial_1\frac{m_2^2}{2} + \partial_2 m_2)\rvert^2 \,\mathrm{d}x'$

Table 1.1.: Successive identification of leading order terms due to scale-separation and low-angle approximation.

In view of the form of the unstable mode, the dependence on the thickness variable and the out-of-plane component can be neglected, i.e., $m = m(x_1, x_2)$ and $m = m'$, respectively, where $m' = (m_1, m_2)$ denotes the first two components of m (likewise we write for example $x' = (x_1, x_2)$ and $\nabla' = (\partial_1, \partial_2)^T$). Since the unstable mode varies faster in x_1-direction than in x_2-direction, $|\partial_2 m'|^2$ can be neglected with respect to $|\partial_1 m'|^2$ in the exchange energy density. Moreover, we can approximate the stray-field potential of an in-plane, thickness-invariant magnetization in a thin-film, i.e., $\Omega' \times (0, t)$, by the potential due to the charge density $-t\nabla'\cdot m'$ on the plate Ω':

$$-\Delta u = 0 \text{ in } \mathbb{R}^3 - (\Omega' \times \{0\}) \quad \text{and} \quad [\partial_3 u] = -t\,\nabla'\cdot m' \text{ on } \partial\Omega' \times \{0\}. \tag{1.8}$$

Based on (1.8), it is a straight-forward calculation in Fourier space – by a transform w.r.t. x_1 and x_2 – to show that

$$\int_{\mathbb{R}^3} |\nabla u|^2 \,\mathrm{d}x = \tfrac{t^2}{2}\int_{\mathbb{R}^2} \lvert\lvert\nabla'\rvert^{-1/2}\nabla'\cdot m'\rvert^2 \,\mathrm{d}x'. \tag{1.9}$$

Since the oscillation in the sign of the charge density is on smaller length scales in x_1-direction than in x_2-direction, the non-locality w.r.t. x_2 can be neglected:

$$\tfrac{t^2}{2}\int_{\mathbb{R}^2} \lvert\lvert\nabla'\rvert^{-1/2}\nabla'\cdot m'\rvert^2 \,\mathrm{d}x' \approx \tfrac{t^2}{2}\int_{\mathbb{R}^2} \lvert\lvert\partial_1\rvert^{-1/2}\nabla'\cdot m'\rvert^2 \,\mathrm{d}x'.$$

Finally, since we are interested in small deviations from $m^* = (1, 0, 0)$, the Taylor expansion $m_1 = \sqrt{1 - m_2^2} \approx 1 - \frac{m_2^2}{2}$ entails that we may neglect $|\nabla m_1|^2$ with respect to $|\nabla m_2|^2$ in the exchange energy density. We also use $m_1 \approx 1 - \frac{m_2^2}{2}$ in the the stray-field and in the Zeeman contribution. Up to an additive constant, we are therefore

left with the *reduced energy functional* $E_0(m_2)$ given by

$$E(m) \approx E_0(m_2) = d^2 t \int_{\Omega'} (\partial_1 m_2)^2 \,\mathrm{d}x_1 \,\mathrm{d}x_2 + \tfrac{t^2}{2} \int_{\Omega'} \big||\partial_1|^{-1/2}(-\partial_1 \tfrac{m_2^2}{2} + \partial_2 m_2)\big|^2 \,\mathrm{d}x_1 \,\mathrm{d}x_2 - h_{\mathrm{ext}}\, t \int_{\Omega'} m_2^2 \,\mathrm{d}x_1 \,\mathrm{d}x_2, \quad (1.10)$$

where $\Omega' = [0, L) \times (0, \ell)$ is periodic w.r.t. x_1 of some large period L. The stray-field energy is only finite if m_2 vanishes at the lateral edges, i.e., $m_2(x_1, x_2) = 0$ for $x_2 \in \{0, \ell\}$ – as is true for the unstable mode.

We note that the only non-quadratic term in the energy comes from the charge distribution $\sigma = -\partial_1 \frac{m_2^2}{2} + \partial_2 m_2$. This is used to derive the scaling of the amplitude of the magnetization: It should be such that both terms in the charge distribution balance. In view of the unstable mode, the typical x_1-scale of the variations of m_2 is given by $w^* \sim d^{2/3}\ell^{2/3}t^{-1/3}$, whereas the typical x_2-scale of variations of m_2 is given by the sample width ℓ. This entails that the terms $\partial_1 \frac{m_2^2}{2}$ and $\partial_2 m_2$ balance provided the amplitude of m_2 scales as $d^{2/3}\ell^{-1/3}t^{-1/3}$ which suggests the following non-dimensionalization of length and reduced units for the stray-field and the magnetization:

$$\begin{aligned} &x_1 = d^{2/3}\ell^{2/3}t^{-1/3}\widehat{x}_1, \quad x_2 = \ell \widehat{x}_2, \quad x_3 = t\widehat{x}_3, \\ &m_2 = d^{2/3}\ell^{-1/3}t^{-1/3}\widehat{m}_2. \end{aligned} \quad (1.11)$$

For the rescaling of the external field and the energy itself according to

$$h_{\mathrm{ext}} = d^{2/3}\ell^{-4/3}t^{2/3}\widehat{h}_{\mathrm{ext}}, \quad (1.12)$$

$$E_0 = d^{8/3}\ell^{-1/3}t^{2/3}\widehat{E}_0, \quad (1.13)$$

we obtain the reduced *rescaled* energy functional

$$\widehat{E}_0(\widehat{m}_2) = \int_{\widehat{\Omega}'} (\widehat{\partial}_1 \widehat{m}_2)^2 \,\mathrm{d}\widehat{x}_1 \,\mathrm{d}\widehat{x}_2 + \int_{\widehat{\Omega}'} \big||\widehat{\partial}_1|^{-1/2}\widehat{\sigma}\big|^2 \,\mathrm{d}\widehat{x}_1 \,\mathrm{d}\widehat{x}_2 - \widehat{h}_{\mathrm{ext}} \int_{\widehat{\Omega}'} \widehat{m}_2^2 \,\mathrm{d}\widehat{x}_1 \,\mathrm{d}\widehat{x}_2, \quad (1.14)$$

where $\widehat{\sigma} = -\widehat{\partial}_1 \frac{\widehat{m}_2^2}{2} + \widehat{\partial}_2 \widehat{m}_2$, under the constraints

$$\begin{aligned} &\widehat{m}_2 = 0 \quad \text{for} \quad \widehat{x}_2 \in \{0, 1\}, \\ &\widehat{m}_2(\widehat{x}_1, \widehat{x}_2) = \widehat{m}_2(\widehat{x}_1 + \widehat{L}, \widehat{x}_2). \end{aligned} \quad (1.15)$$

Note that the stray-field energy can be rewritten as the Dirichlet energy of some potential $\widehat{u}$ which satisfies

$$-(\widehat{\partial}_1^2 + \widehat{\partial}_3^2)\widehat{u} = 0 \quad \text{for } \widehat{x}_3 \neq 0 \quad \text{and} \quad [\partial_3 \widehat{u}] = \widehat{\sigma} \quad \text{for } \widehat{x}_3 = 0,$$

so that

$$\int_{\widehat{\Omega}'} \big||\widehat{\partial}_1|^{-1/2}\widehat{\sigma}\big|^2 \,\mathrm{d}\widehat{x}_1 \,\mathrm{d}\widehat{x}_2 = \int_{\widehat{\Omega}' \times \mathbb{R}} (\widehat{\partial}_1 \widehat{u})^2 + (\widehat{\partial}_3 \widehat{u})^2 \,\mathrm{d}\widehat{x}_1 \,\mathrm{d}\widehat{x}_2 \,\mathrm{d}\widehat{x}_3. \quad (1.16)$$

Notice that due to periodicity, admissible magnetizations additionally suffice

$$\int_0^{\widehat{L}} \widehat{m}_2 \, \mathrm{d}\widehat{x}_1 = 0,$$

i.e., $\int_0^{\widehat{L}} \widehat{\sigma} \, \mathrm{d}\widehat{x}_1 = 0$. Let us not that the Hessian of the reduced energy in $\widehat{m}_2 = 0$ can be explicitly diagonalized with eigenvalues

$$\lambda(\widehat{k}_1, \widehat{k}_2) = 2(\widehat{k}_1)^2 - \frac{\pi(\widehat{k}_2)^2}{|\widehat{k}_1|} - 2\widehat{h}_{\mathrm{ext}},$$

and two-dimensional eigenspaces

$$V_{k_1,k_2} = \mathrm{span}\{\cos(\widehat{k}_1\widehat{x}_1)\sin(\widehat{k}_2\widehat{x}_2), \sin(\widehat{k}_1\widehat{x}_1)\sin(\widehat{k}_2\widehat{x}_2)\},$$

where $\widehat{k}_1 \in \frac{2\pi}{L}\mathbb{N}$ and $\widehat{k}_2 \in \pi\mathbb{N}$ due to the boundary condition (1.15).

Let us compare the full three-dimensional micromagnetic energy (1.1) with our reduced model: The reduced *rescaled* formulation shows that the reduced energy functional contains just *one* non-dimensional parameter, namely the reduced external field $\widehat{h}_{\mathrm{ext}}$ – instead of *four* parameters – exchange length, sample dimensions and h_{ext} – for the full model. Moreover, the *vector* field $m = (m_1, m_2, m_3)$, function of *three* variables (x_1, x_2, x_3), has been replaced by the *scalar* function $\widehat{m}_2$, function of *two* variables $(\widehat{x}_1, \widehat{x}_2)$. Finally, the computation of the stray-field is a *two*-dimensional computation – in $(\widehat{x}_1, \widehat{x}_3)$ only with $\widehat{x}_2$ as a parameter – instead of a *three*-dimensional one. All this simplifies both the theoretical treatment and the numerical simulation. For clarity, we will mostly discuss our results in the rescaled variables (1.14) – and only occasionally return to the original variables, mostly for comparison with the experiment and if we take into account anisotropy.

The reduced rescaled energy was identified as the Γ-limit w.r.t. the L^2-topology of the properly rescaled micromagnetic energy close to the uniform magnetization m^* in the neighborhood of the critical field h^*_{ext} in [CÁOS07]. It is a two-fold limit in the parameters

$$\varepsilon = d^{4/3}\ell^{-2/3}t^{-2/3} \quad \text{and} \quad \delta = d^{-2/3}\ell^{-2/3}t^{4/3}, \tag{1.17}$$

which characterize Regime III, more precisely $\varepsilon, \delta \ll 1$ is equivalent to $d^2\ell^{-1} \ll t \ll (d\ell)^{1/2}$. Table 1.2 shows the values of (1.17) for specific sample dimensions.

1.6. Bifurcation analysis

On the level of the reduced model (1.14), the type of bifurcation was determined in [CÁOS07]. Let us present the main steps and the result of the analysis: As mentioned before, the Hessian of the reduced model in $\widehat{m}_2 \equiv 0$ can be explicitly diagonalized and the first unstable mode is given by $\widehat{m}_2^* = \sin(\pi\widehat{x}_2)\sin(2\pi\frac{x_1}{\widehat{w}^*})$, where $\widehat{w}^* = (32\pi)^{1/3}$. The reduced critical field is given by

$$\widehat{h}^*_{\mathrm{ext}} = 3\left(\tfrac{\pi}{2}\right)^{4/3}. \tag{1.18}$$

t \ ℓ	10 µm	100 µm
10 nm	$\varepsilon = 0.0040$ $\delta = 0.016$	$\varepsilon = 0.00085$ $\delta = 0.0034$
150 nm	$\varepsilon = 0.00065$ $\delta = 0.59$	$\varepsilon = 0.00015$ $\delta = 0.13$

Table 1.2.: Parameters ε and δ for characteristic sample sizes where the exchange length is given by $d = 5$ nm. Regime III is related to samples of small thickness t and large width ℓ.

We note that this is consistent with the Γ-limit of the Hessian in Regime III, see [CÁO06b]. In order to determine the type of bifurcation, one has to investigate the energy functional $\widehat{E}_0$ close to the one-dimensional subspace $\{A\widehat{m}_2^*\}_{A\in\mathbb{R}}$ generated by the unstable mode $\widehat{m}_2^* = \sin(\pi x_2)\sin(2\pi\frac{x_1}{\widehat{w}^*})$. Because of the invariance of both $\widehat{E}_0$ and the unstable mode $\{A\widehat{m}_2^*\}_{A\in\mathbb{R}}$ under the transform $\widehat{m}_2 \rightsquigarrow -\widehat{m}_2$ and $\widehat{x}_2 \rightsquigarrow 1-\widehat{x}_2$, all odd terms in A in the expansion of $\widehat{E}_0(A\widehat{m}_2^*)$ vanish. The first non-vanishing term in the expansion of $\widehat{E}_0$ at the critical field $\widehat{h}_{\text{ext}}^*$ is at least quartic. Hence it is not sufficient to consider $\widehat{E}_0$ just along the linear space $\{A\widehat{m}_2^*\}_{A\in\mathbb{R}}$ but it has to be analyzed along a curve $\{A\widehat{m}_2^* + A^2\widehat{m}_2^{**}\}_{A\in\mathbb{R}}$ in configuration space, where the curvature direction $\widehat{m}_2^{**}$, which affects the quartic term in the expansion, has to be determined such that $\widehat{E}_0$ is minimal. This minimization problem (of the coefficient of the quartic term) is quadratic in $\widehat{m}_2^{**}$ and can thus be explicitly solved. One obtains

$$\widehat{m}_2^{**} = -\tfrac{1}{10}(\tfrac{2}{\pi})^{1/3}\sin(2\pi x_2)\sin(4\pi\tfrac{x_1}{\widehat{w}^*}),$$

which leads to a negative coefficient of the quartic term in the expansion of $\widehat{E}_0$:

$$\widehat{E}_0(A\widehat{m}_2^* + A^2\widehat{m}_2^{**}) \approx (\widehat{h}_{\text{ext}} - \widehat{h}_{\text{ext}}^*)\left(\tfrac{\pi}{2}\right)^{1/3} A^2 - \tfrac{\pi}{640}A^4. \tag{1.19}$$

The negative quartic coefficient implies that the bifurcation is *subcritical*, also called of *first order*. Subcriticality means that close to $\widehat{m}_2 \equiv 0$, there are only *unstable* stationary points for $\widehat{h}_{\text{ext}}$ slightly below $\widehat{h}_{\text{ext}}^*$, and *no* stationary points close to $\widehat{m}_2 \equiv 0$ for $\widehat{h}_{\text{ext}}$ slightly above $\widehat{h}_{\text{ext}}^*$, cf. Figure 1.9.

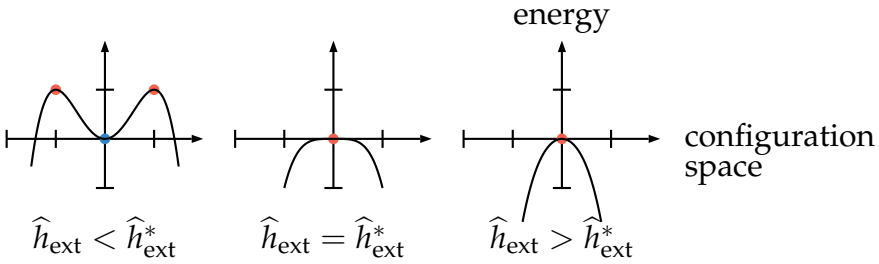

Figure 1.9.: Energy landscape close to the bifurcation. The loss of stability at the critical field leads to a subcritical bifurcation.

At first sight, it is surprising that the stray-field energy contribution to $\widehat{E}$, which gives rise to the only quartic term in $\widehat{m}_2$, and clearly is non-negative, may nevertheless allow for a negative coefficient in front of the quartic term in the expansion (1.19). This comes from the fact that the two terms in the charge density $-\widehat{\partial}_1 \frac{\widehat{m}_2^2}{2} + \widehat{\partial}_2 \widehat{m}_2$ interact, giving rise to a cubic term in $\widehat{m}_2$, which indeed allows for cancellations. The way how this operates is better understood in physical space: The term $\widehat{m}_2^{**}$ in $A\widehat{m}_2^* + A^2\widehat{m}_2^{**}$, i.e., the curvature direction in configuration space, leads to a tilt in the charge distribution, see Figure 1.10. This tilt brings opposite charges closer together, thereby reducing the stray-field energy (while increasing the exchange energy to a lesser amount).

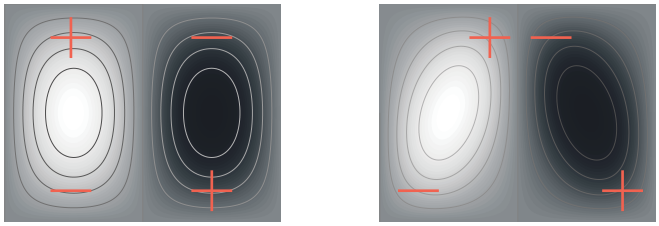

Figure 1.10.: Unstable mode $\{A\widehat{m}_2^*\}$ and additional curvature correction $\{A\widehat{m}_2^* + A^2\widehat{m}_2^{**}\}$ with its generated charges. The gray scales indicate the $\widehat{m}_2$-component.

Since the bifurcation is subcritical, it is not obvious whether minimizers of the reduced energy functional can be related to the unstable mode. In particular, this finding sheds doubt on the hypothesis that the concertina pattern inherits the period of the unstable mode. It is even not obvious whether minimizers of the reduced energy functional exist at all. However, it was shown that the reduced model is coercive for all values of the external field $\widehat{h}_{\text{ext}}$, see Theorem 4 in [CÁOS07, p.236]. This in particular implies that there always exists a global minimizer of the reduced energy, in particular for fields larger than the critical field. But it is not immediately clear how and whether it is related to the unstable mode.

It is natural to resort to numerical simulations. A short introduction is given in Section 1.11; for details on the discretization scheme and the algorithms, see Chapter 4. To confirm the conjecture that the unstable mode in Regime III is indeed related to the concertina pattern, we use a numerical path-following in order to compute the bifurcation branch. Figure 1.11 displays the outcome of the numerical simulations.

As expected due to the coercivity of the energy functional, we find a turning point as we follow the bifurcation branch. The turning point is located at a field which is just slightly – about one percent – smaller than the critical field. After the turning point the branch is stable, at least under perturbations of the same period.

As the field increases beyond the turning point, the unstable mode grows into a domain pattern of concertina type with its clear scale separation between the wall

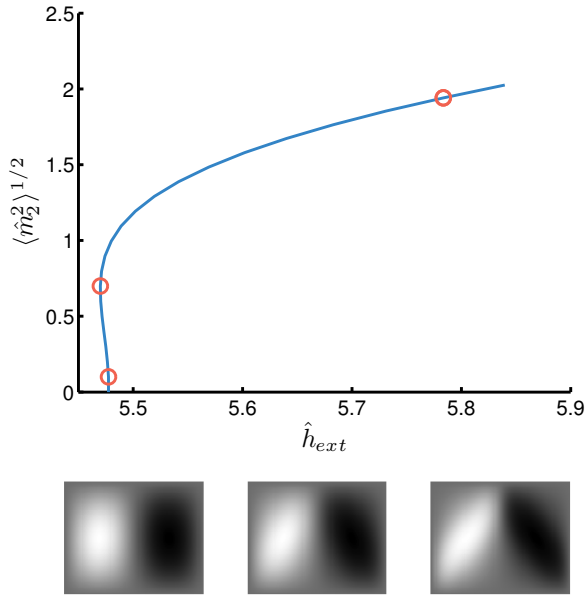

Figure 1.11.: Numerical simulations: The $\widehat{w}^*$-periodic branch close to the bifurcation (top) and the computed pattern at the indicated fields (bottom). The gray scales encode the $\widehat{m}_2$-component (light gray corresponds to negative, dark gray to positive $\widehat{m}_2$) but are in this case *not* comparable – the scale is exhausted so that the structure of the configuration is resolved.

width and the domain size, cf. Figure 1.12. We thus find a continuous transformation from the unstable mode to the concertina pattern – confirming our hypothesis.

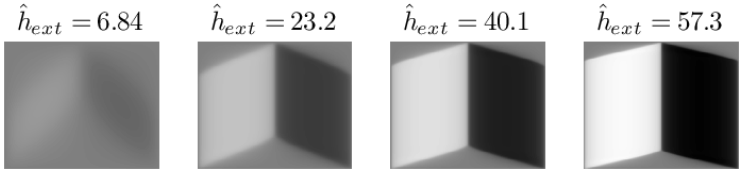

Figure 1.12.: Numerical simulations: The $\widehat{w}^*$-periodic concertina pattern exhibits a clear scale separation (domain width $\gg$ wall width) for large external fields. The gray scales encode the $\widehat{m}_2$ component and are comparable.

The numerical simulations lead to the conjecture that in a perfectly homogeneous sample without anisotropy the magnetization exhibits a first order phase transition from the uniformly magnetized state to the concertina state of period w^* at the critical field. Clearly, this does not explain the deviation of the average wavelength in the experimental measurements from the period of the unstable mode.

1.7. Domain theory

In the numerical simulations we observe for large external fields a clear scale separation: The width of the domains, where the magnetization is almost constant, is much larger than the width of the walls, in which the magnetization quickly turns, cf. Figure 1.12. This suggests the application of a sharp interface model, namely domain theory, which is introduced in detail in Chapter 2. It is used in Section 1.8 and 1.10 in order to get a better understanding of the concertina, in particular its period.

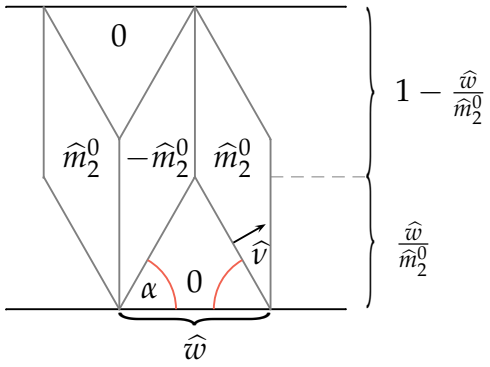

Figure 1.13.: Domain theory: Sketch of the piecewise constant Ansatz function. Its angles are fixed by (1.20).

On a mesoscopic scale, the computed magnetization is close to a piecewise constant magnetization of amplitude $\widehat{m}_2^0$, i.e., $\widehat{m}_2 = \pm\widehat{m}_2^0$ in the quadrangular domains and $\widehat{m}_2 = 0$ in the triangular domains as indicated in Figure 1.13. We observe that the angles in the pattern are determined by the amplitude; approximately we have that $\sin\alpha = 2\widehat{m}_2^0$. This is related to the fact that the reduced stray-field energy is strongly penalized for large fields. In fact, the piecewise constant magnetization with angles given by $\sin\alpha = 2\widehat{m}_2^0$ is a distributional solution of

$$-\widehat{\partial}_1 \tfrac{\widehat{m}_2^2}{2} + \widehat{\partial}_2 \widehat{m}_2 = 0. \tag{1.20}$$

The energy which discriminates between these solutions will be given by the total wall energy, which is an appropriate line energy density $\widehat{e}$ integrated over the interfaces, augmented by Zeeman energy:

$$\widehat{E}_{\text{domain}}(\widehat{m}_2) \;=\; \int_{\text{jump set}} \widehat{e}\Big(\tfrac{[\widehat{m}_2]}{2}\Big)\, \mathrm{d}\mathcal{H}^0\, \mathrm{d}\widehat{x}_2 - \widehat{h}_{ext} \int \widehat{m}_2^2\, \mathrm{d}\widehat{x}_1\, \mathrm{d}\widehat{x}_2,$$

where $\mathcal{H}^0$ denotes the zero-dimensional Hausdorff measure. The optimal transition layers are low angle Néel walls for which the specific line energy is a function of the jump $[\widehat{m}_2]$ of the magnetization and of the length of the logarithmic tails of the Néel wall, which scales as the period $\widehat{w}$:

$$\widehat{e}\Big(\tfrac{[\widehat{m}_2]}{2}\Big) \;=\; \widehat{e}(\widehat{m}_2^0) \approx \tfrac{\pi}{8}(\widehat{m}_2^0)^4 \ln^{-1}\widehat{w}(\widehat{m}_2^0)^2.$$

For details, we refer to Chapter 2 where we will see that within the class of admissible magnetizations, the domain theoretic energy per period becomes a function of only three parameters, namely the transversal component $\widehat{m}_2^0$, the period $\widehat{w}$ and the external field $\widehat{h}_{\text{ext}}$:

$$\widehat{E}_{\text{domain}}(\widehat{m}_2^0, \widehat{w}) = 2\left(1 - \frac{\widehat{w}}{\widehat{m}_2^0}\right)\widehat{e}(\widehat{m}_2^0) + 4\,\frac{\widehat{w}}{\widehat{m}_2^0}\,\widehat{e}\left(\frac{\widehat{m}_2^0}{2}\right) - \widehat{h}_{ext}(\widehat{m}_2^0)^2\left(\widehat{w} - \frac{\widehat{w}^2}{\widehat{m}_2^0}\right).$$

Of course, domain theory is only applicable (and thus a good approximation for the reduced model) for $1 \ll \widehat{h}_{\text{ext}}$, in which case there is a clear scale separation between walls and domains. Figure 1.15 shows that the optimal amplitude on the level of domain theory and the amplitude extracted from the numerical computations are in good agreement for large external fields $1 \ll \widehat{h}_{\text{ext}}$.

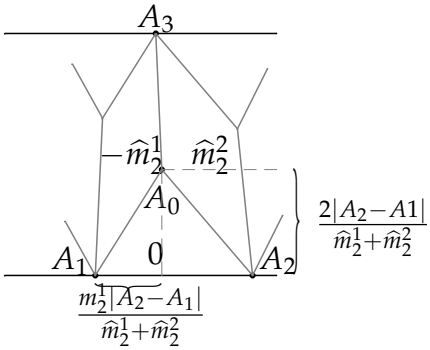

Figure 1.14.: Domain theory: Sketch of a generalized tilted Ansatz function.

The experimentally observed concertina is of course not of uniform period and equal amplitude as our domain theoretic Ansatz above. As shown in Figure 1.14, there are also oblique piecewise constant weak solutions of (2.1). Nevertheless, this class of Ansatz functions is very rigid, for details see Section 2.3.

Domain theory is (partially) justified as a consequence of Theorem 3.3 in Chapter 3 published in [OS10]. This Theorem states that minimizers of the reduced energy functional are close to weak solutions of the Burgers equation (1.20).

1.8. Coarsening of the concertina pattern

1.8.1. Domain theory: The optimal period of the concertina pattern

Experiments show an increase in the average concertina period w as the external field h_{ext} is further increased after the critical field is passed and the pattern has formed. The general tendency that w is an increasing function of h_{ext} can be understood on the basis of domain theory in the reduced variables $\widehat{m}_2^0$, $\widehat{w}$ and $\widehat{h}_{\text{ext}}$. By optimizing the energy per *unit length* with respect to the period $\widehat{w}$ and the amplitude $\widehat{m}_2^0$ of the transversal component for given external field $\widehat{h}_{\text{ext}}$, we obtain the following scaling of the optimal period $\widehat{w}_a$ of the pattern:

$$\widehat{w}_a(\widehat{h}_{\text{ext}}) \sim \widehat{h}_{\text{ext}} \ln \widehat{h}_{\text{ext}} \quad \text{for} \quad \widehat{h}_{\text{ext}} \gg 1,$$

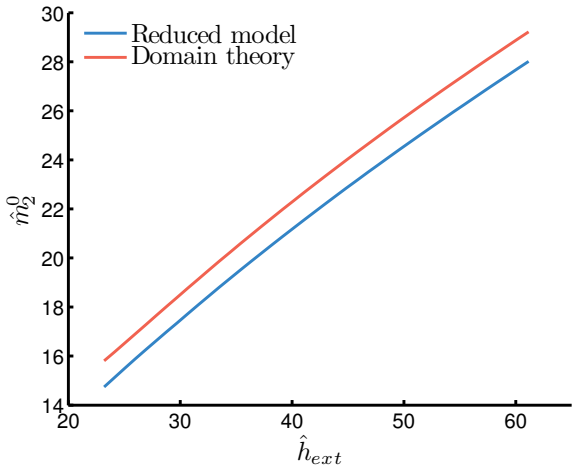

Figure 1.15.: Domain theory and numerical simulations: The optimal amplitude on the level of domain theory (red) and the computed amplitude based on the reduced model (blue). For the reduced model we display the amplitude, i.e., the maximal value which is attained in the quadrangular domain.

see c) in Subsection 2.2. In particular, the optimal period increases with increasing field. Domain theory also yields the same scaling behavior for the optimal inclination of the magnetization

$$\widehat{m_{2a}}(\widehat{h}_{\text{ext}}) \sim \widehat{h}_{\text{ext}} \ln \widehat{h}_{\text{ext}} \quad \text{for} \quad \widehat{h}_{\text{ext}} \gg 1,$$

see b) in Subsection 2.2. Both scalings are confirmed on the basis of the reduced model using a concertina Ansatz for the upper bounds and new interpolation estimates for the lower bounds in Theorem 3.1 in Chapter 3, also published in [OS10]. Numerical simulations of the reduced energy functional moreover show that the optimal period increases with increasing field also for small external fields, see Figure 1.16. The optimal period was computed by minimizing the energy per unit length both w.r.t. the magnetization and the period for varying external field, for details see Subsection 4.8.

1.8.2. Coarsening: A modulation instability

Although the analysis predicts that the optimal period increases as the field increases, see above, it does not explain why and in which way a concertina pattern of period $\widehat{w}$ becomes *unstable* as $\widehat{h}_{\text{ext}}$ increases. We will see that both the increasing period for large fields and the deviation of the initial period from the one of the unstable mode are due to an instability under long-wave length modulations of the pattern. The mechanism behind the instability is the following: Given $\widehat{h}_{\text{ext}}$ and a period $\widehat{w}$, an optimization in the transversal component $\widehat{m}_2$ yields that the optimal energy *per period* $\widehat{E}_{\text{opt}}(\widehat{h}_{\text{ext}}, \widehat{w})$ is a *concave* function in $\widehat{w}$ – provided $\widehat{h}_{\text{ext}}(\widehat{w})$

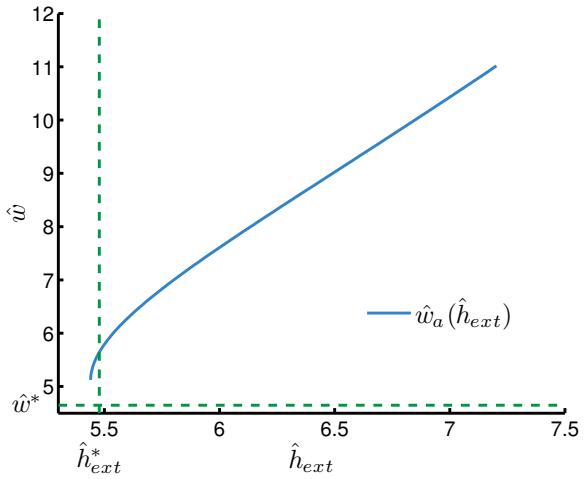

Figure 1.16.: Numerical simulations: The optimal period of the concertina pattern as a function of the external field computed on the basis of the reduced model.

is sufficiently large. Concavity suggests – as depicted in Figure 1.17 – that the concertina pattern of a uniform period $\widehat{w}$ becomes unstable under modulations of the period, i.e., perturbations which increase the period to $\widehat{w} + \varepsilon$ and the corresponding optimal transversal component in some folds, and decrease the period to $\widehat{w} - \varepsilon$ and the corresponding optimal transversal component in other folds. However, in view of the non-locality of the stray-field energy, it is not clear whether this simplified picture, i.e., that the energy of the modulation amounts to the modulation of the energy, applies. As discussed in Subsection 1.8.3, a modulation of the period on a very long length scale overcomes this objection. Thus the concavity of the minimal energy implies an instability under long wave-length modulations of the pattern.

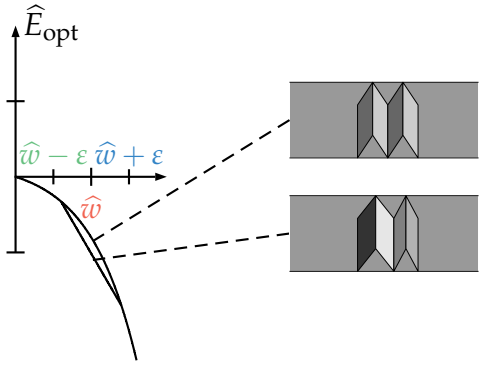

Figure 1.17.: Concavity of the minimal energy per period implies an instability under wave-length modulation.

In order to derive the concavity of the minimal energy, we apply domain theory for large external fields, for details see d) in Subsection 2.2, and an extended bifurcation

analysis close to the critical field, for details see Chapter 6. Furthermore, we will see that both asymptotics match the results of the numerical simulation of our reduced model.

The modulation instability of the concertina pattern is closely related to the Eckhaus instability which was discovered in the context of non-linear instabilities in convective systems leading to a change in wave length of the observed periodic pattern, for a review see [Eck92]. A higher degeneracy of the bifurcation in case of the reduced energy functional leads to an asymmetric Eckhaus unstable region. More precisely we will see that periodic minimizers of period $\widehat{w}^* + \delta\widehat{w}$ are Eckhaus unstable for $\delta\widehat{w} < \delta\widehat{w}^*$ for some $\delta\widehat{w}^* > 0$. In case of the generic Eckhaus bifurcation, a state is unstable if $|\delta\widehat{w}|$ is above a certain threshold.

We note that the same concavity criterion was shown to imply sideband instability for spatially periodic solutions to some hyperbolic/parabolic equation on an infinitely extended strip in [BM96, Mie07]. Using a localization argument for the stray-field energy – similar to (5.31) in Section 5.2 – it was shown in [Sei08] that the concavity implies modulation instability of periodic minimizers to the one-dimensional version of (1.14), which describes a configuration of low-angle Néel walls. This is related to the transition of the ripple structure to the so called blocked state observed during field reversal in extended thin films of polycrystalline Permalloy, cf. Section 1.9.

1.8.3. Bloch wave theory: Instability with increasing field

As indicated above, for $\widehat{h}_{\text{ext}} \gg 1$, not only the optimal period but also the coarsening can be explained on the basis of domain theory which relies on the optimal energy *per period* $\min_{\widehat{m}_2^0} \widehat{E}_{\text{domain}}(\widehat{m}_2^0, \widehat{h}_{\text{ext}}, \widehat{w})$. More precisely we find that for periods much smaller then the optimal period, i.e., $\widehat{w} \ll \widehat{w}_a(\widehat{h}_{\text{ext}}) \sim \widehat{h}_{\text{ext}} \ln \widehat{h}_{\text{ext}}$, and for $1 \ll \widehat{h}_{\text{ext}} \ln \widehat{h}_{\text{ext}}$:

$$\min_{\widehat{m}_2^0} \widehat{E}_{\text{domain}}(\widehat{m}_2^0, \widehat{w}) \;\sim\; -\widehat{h}_{\text{ext}}^2 \widehat{w}^2 \ln(\widehat{h}_{\text{ext}} \widehat{w}^2),$$

see d) in Section 2.2. The optimal energy per period is thus indeed *concave* in the period $\widehat{w}$ (if $\widehat{w}$ is much smaller than the optimal period), implying the instability under long wave-length modulations. Although domain theory suggests such a type of perturbation, domain theory itself is too rigid to allow for such a type of perturbation of the concertina pattern even in the class of generalized Ansatz functions as depicted in Figure 1.14, for details see Section 2.3.

It is rather on the level of the reduced model that it can be seen that the concavity translates into an instability (despite the potentially long-range interactions coming from the stray-field). Indeed, a Bloch wave analysis, cf. [RS78, Maroo], of the reduced model shows that the concavity is in a one-to-one correspondence with a long wavelength modulation of the pattern: One can show that there are eigenfunctions of the

Hessian of the form

$$\delta\widehat{m}_2 \;=\; \mathrm{e}^{-i\widehat{x}_1\xi}\,\delta\widehat{m}_2^{\xi}, \quad \text{where} \quad \xi = \tfrac{2\pi}{N\widehat{w}} \quad \text{and} \quad N \in \mathbb{N},$$

with $\delta\widehat{m}_2^{\xi}$ $\widehat{w}$-periodic with respect to $\widehat{x}_1$, i.e.,

$$\operatorname{Hess}\widehat{E}(\widehat{m}_2)(\mathrm{e}^{-i\widehat{x}_1\xi}\delta\widehat{m}_2^{\xi}) = \lambda^{\xi}\mathrm{e}^{-i\widehat{x}_1\xi}\,\delta\widehat{m}_2^{\xi}. \tag{1.21}$$

Here, $N\widehat{w}$ is the wave length of the modulation. An asymptotic expansion of (1.21) for $\xi = \frac{2\pi}{N\widehat{w}} \ll 1$ shows that the (first) eigenvalue λ^{ξ} can be related to the second derivative of the minimal energy per period $\widehat{E}_{\mathrm{opt}} = \min_{\widehat{m}_2}\widehat{E}$, for details see Chapter 5. More precisely, we find that the eigenvalue has the following expansion:

$$\lambda^{\xi} \approx \frac{\mathrm{d}^2}{\mathrm{d}\widehat{w}^2}\widehat{E}_{\mathrm{opt}}(\widehat{h}_{\mathrm{ext}},\widehat{w})\;\xi^2 \quad \text{for} \quad \xi \ll 1.$$

This shows that the concavity of $\widehat{E}_{\mathrm{opt}}(\widehat{h}_{\mathrm{ext}},\widehat{w})$ with respect to $\widehat{w}$ implies that the concertina pattern of a given period $\widehat{w}$ becomes unstable as the field increases. Domain theory predicts that the marginally stable $\widehat{w}_s$, i.e., $\widehat{w}_s$ such that $\frac{\mathrm{d}^2}{\mathrm{d}\widehat{w}^2}\widehat{E}_{\mathrm{opt}}(\widehat{h}_{\mathrm{ext}},\widehat{w}_s) = 0$, scales as $\widehat{w}_s \sim \widehat{h}_{\mathrm{ext}}\ln\widehat{h}_{\mathrm{ext}}$. Figure 1.18 shows the optimal and marginally stable period computed on the basis of the reduced energy functional.

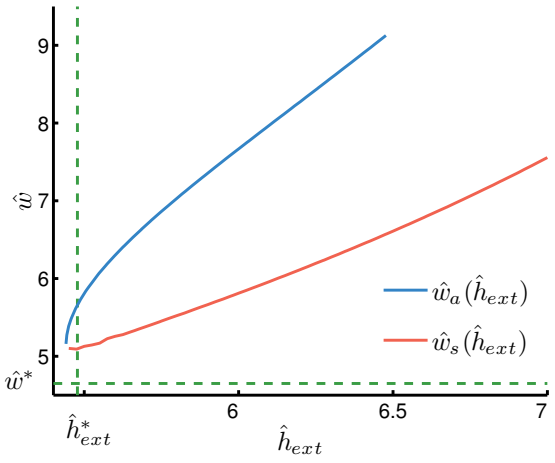

Figure 1.18.: Numerical simulations: The optimal and marginal stable period of the concertina pattern as a function of the external field – both computed on the basis of the reduced model (1.14). In the region below the red curve, the minimal energy per period is concave and thus a concertina of that period is unstable under modulation of the period. The dashed dark-green lines indicate the period of the unstable mode and the critical field, respectively.

Figure 1.19 shows that the prediction of the optimal and marginal stable period on the basis of domain theory match the numerical simulations on the basis of the reduced model for $\widehat{h}_{\mathrm{ext}} \gg 1$.

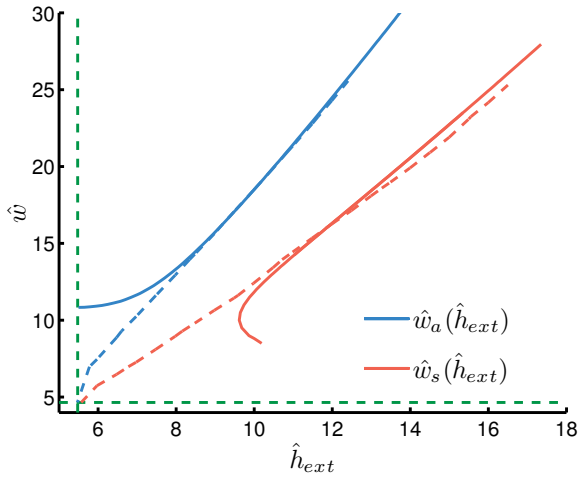

Figure 1.19.: Numerical simulations and domain theory: The optimal and marginal stable period computed on the basis of the reduced model (1.14) (dashed) match the predictions on the basis of domain theory in the regime $\widehat{h}_{\text{ext}} \gg 1$. The dashed dark-green lines indicate the period of the unstable mode and the critical field, respectively.

1.8.4. Bifurcation analysis: Instability for small fields

The numerical computations, cf. Figure 1.18, show that the minimal energy per period is concave not only for large external field as predicted by domain theory. In fact, we extract from our numerical data that $\frac{\mathrm{d}^2}{\mathrm{d}\widehat{w}^2}\widehat{E}_{\text{opt}}(\widehat{h}_{\text{ext}}, \widehat{w} = \widehat{w}^*)$ is negative also for small external fields up to the turning point, cf. Figure 1.18. This is consistent with the numerical computation of the eigenvalue λ^ξ based on the asymptotic expansion of equation (1.21). Hence, the Bloch wave analysis implies that the $\widehat{w}^*$-periodic concertina pattern is unstable under long wave length modulations. This qualitatively explains the trend in the experimental observation (see Section 1.3) of the concertina period w^*_{exp}.

The concavity of the minimal energy can be confirmed with the help of an asymptotic bifurcation analysis close to the critical field. To see this, we extend our Ansatz from Section 1.6 and take into account small deviations of the wave number $\widehat{k}_1 = \widehat{k}_1^* + \widehat{\delta k_1}$, for details see Section 6.2. As we have seen in (1.19) in Section 1.6, the quartic coefficient in the energy expansion is (relatively to the second order coefficient and the scale of the external field) small. Due to that almost degeneracy, it is necessary to take into account the cubic order for the perturbation of $\widehat{m}_2 = 0$, i.e., we use the extended Ansatz

$$\widehat{m}_2 \approx A\widehat{m}_2^* + A^2\widehat{m}_2^{**} + A^3\widehat{m}_2^{***}.$$

Optimizing both in $\widehat{m}_2^{**}$ and $\widehat{m}_2^{***}$ leads to an expansion of the energy density of the

form

$$\frac{\widehat{k}_1}{2\pi}\widehat{E}(A\widehat{m}_2^* + A^2\widehat{m}_2^{**} + A^3\widehat{m}_2^{***}) \approx \ \frac{1}{4}(\widehat{h}_{\text{ext}}^*(\widehat{k}_1) - \widehat{h}_{\text{ext}})A^2 - c_4(\widehat{k}_1)A^4 + c_6(\widehat{k}_1)A^6,$$

where $c_4(\widehat{k}_1^*) = \frac{\pi}{640}\frac{\widehat{k}_1^*}{2\pi}$, see (6.13). Under the assumption that the quartic coefficient $c_4(\widehat{k}_1^*)$ is small, the energy density to leading order can be approximated by

$$\begin{aligned}\frac{\widehat{k}_1}{2\pi}\widehat{E}(A\widehat{m}_2^* + A^2\widehat{m}_2^{**} + A^3\widehat{m}_2^{***}) \approx \frac{1}{4}\big(\frac{\mathrm{d}^2}{\mathrm{d}k_1^2}\widehat{h}_{\text{ext}}^*(\widehat{k}_1)_{|k_1=k_1^*}\frac{\widehat{\delta k_1}^2}{2} + \widehat{\delta h_{\text{ext}}}\big)A^2 \\ - (c_4(\widehat{k}_1^*) + \frac{\mathrm{d}}{\mathrm{d}\widehat{k}_1}c_4(\widehat{k}_1)_{|\widehat{k}_1=\widehat{k}_1^*}\widehat{\delta k_1})A^4 + c_6(\widehat{k}_1^*)A^6. \quad (1.22)\end{aligned}$$

First notice that it turns out that $c_6(\widehat{k}_1^*)$ is positive, confirming the numerically observed turning point of the $\widehat{w}^*$-periodic branch. Moreover, the asymptotic expansion displays the afore mentioned asymmetric behavior in $\widehat{\delta k_1}$; the energy decreases for $\widehat{\delta k_1} < 0$. Based on the expansion (1.22), one can characterize the optimal wave number/period and the marginally Eckhaus stable wave number/period. We note that the concavity of the minimal energy per period is equivalent to the concavity of the energy density as a function of the wave number $\widehat{k}_1$. More precisely we have that

$$\frac{\mathrm{d}^2}{\mathrm{d}\widehat{w}^2}\widehat{E}(\widehat{w}) \ = \ \frac{\widehat{k}_1^3}{(2\pi)^2}\frac{\mathrm{d}^2}{\mathrm{d}\widehat{k}_1^2}\Big(\widehat{k}_1\widehat{E}\big(\frac{2\pi}{\widehat{k}_1}\big)\Big).$$

The result is displayed in Figure 1.20. We read off that the $\widehat{w}^*$-periodic concertina pattern is indeed unstable at the critical field. A comparison between Figure 1.18 and Figure 1.20 shows that our asymptotic expansion does not match the optimal and marginal stable period computed on the basis of the reduced model very well (notice the scale of the external field). This deviation is related to our assumption that the quartic coefficient is negligible. In fact, Figure 1.21 shows that the asymptotics match the reduced model if we add a quartic contribution $\frac{\widehat{Q}}{4}\int m_2^4$ to the reduced energy for which the value of the parameter $\widehat{Q}$ is chosen in the way that the coefficient $c_4(\widehat{k}_1^*)$ in (1.22) is (almost) canceled ($\widehat{Q} \approx 0.03$). In Section 1.10 we will see that such an additional quartic contribution has a physical meaning related to a uniaxial anisotropy. It turns out that the parameter $\widehat{Q}$ is an appropriate rescaling of the quality factor Q, close to the bifurcation.

1.8.5. Wave-length modulation in the experiments

In the experiments, the wave length of the modulation is restricted not only by the finiteness of the sample but even more strongly by the inhomogeneities and defects of the material, in particular those at the long edges of the boundaries. This is related to the fact that walls usually occur at the same pinning sites when the experiment is rerun. The existence of pinning sites hence leads to a smaller effective modulation wave length which is just a small multiple of the wave length of the pattern. In fact, it is observed that as a consequence of the collapse of a fold only the width of the neighboring folds is adjusted. In particular, pinning sites have a stabilizing effect and prevent coarsening.

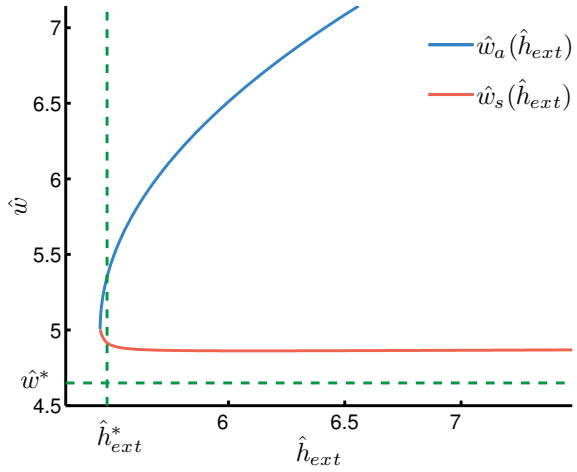

Figure 1.20.: Bifurcation analysis: The optimal and marginal stable period as a function of the external field computed on the basis on the extended bifurcation analysis. We read off that states of period $\widehat{w}^* + 0.212$ are Eckhaus unstable for all values of the external field. The dashed dark-green lines indicate the period of the unstable mode and the critical field, respectively.

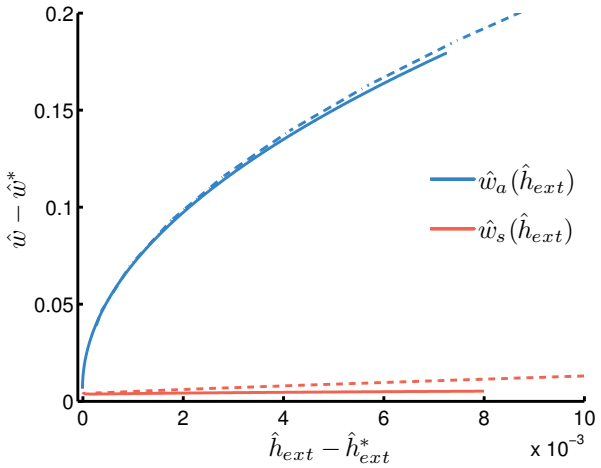

Figure 1.21.: Numerical simulations and bifurcation analysis: The prediction on the basis of the reduced model (1.14) (dashed) matches the prediction on the basis of the extended bifurcation analysis for a near-degenerate value of $\widehat{Q} = 0.0295$ close to $\widehat{Q}^* \approx 0.03$, cf. Section 1.10. The dashed dark-green lines indicate the period of the unstable mode and the critical field, respectively.

1.8.6. Numerical bifurcation analysis: Type of secondary instability and downhill path in energy-landscape

With the help of a bifurcation detection algorithm, we are able to compute at which field the pattern becomes unstable under $N\widehat{w}^*$-periodic perturbations while we follow the primary branch. For details of the numerical schemes applied, see Section 4.4 and Section 4.5. Figure 1.22 shows how the secondary critical field decreases as N increases. As expected (cf. Subsection 1.8.4 and Figure 1.18),the first instability approaches the turning point as N increases – it is reached for finite N.

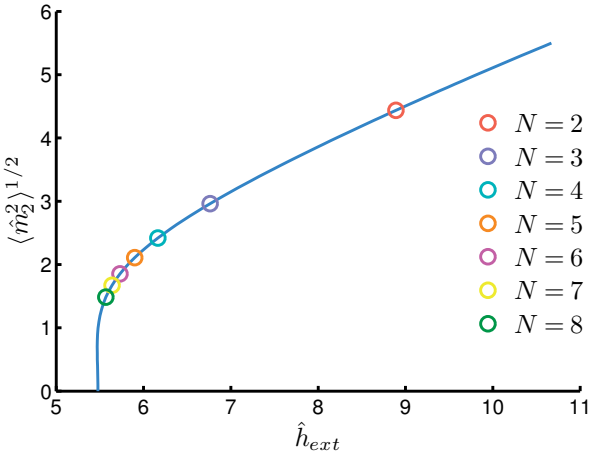

Figure 1.22.: Numerical simulations: The appearance of the secondary instability under $N\widehat{w}^*$-periodic perturbations as a function of N. The critical field for $N = 8$ is given by 5.602.

In the following, we want to study in which *way* the concertina pattern becomes unstable. We first present the outcome of the computation of the secondary bifurcation branches. We note hat due to the symmetries of the pattern, the bifurcations are not simple in the sense that more than one branch bifurcates. The symmetries of the $N\widehat{w}$-periodic concertina pattern can be identified as linear representations of the dihedral group D_{2N}, where N denotes the number of folds. The secondary bifurcation branches are computed with the help of a numerical branch switching algorithm which is adapted to the problem of multiple bifurcations. Generically, there are two distinct types of branches: Branches along which rotational symmetry is broken and reflectional symmetry is conserved and branches along which rotational symmetry is conserved and reflectional symmetry is broken. In case of the first type of branches, a fold collapses as two neighboring faces disappear, cf. Figure 1.24. In case of the second type of branches, the number of folds decreases as one face disappears and the two adjacent faces merge, cf. Figure 1.25. During the coarsening process, the width of the remaining folds is adjusted in both cases. In correspondence to the experimental observations, the actual coarsening process is rather local in the sense that *neighboring* folds or faces collapse or merge, respectively.

Due to the choice of an artificial and finite computational domain one might doubt the relevance of the numerical simulations. However, as mentioned before, the wavelength of the modulation in the experiments is effectively reduced by the defects and inhomogeneities in the samples.

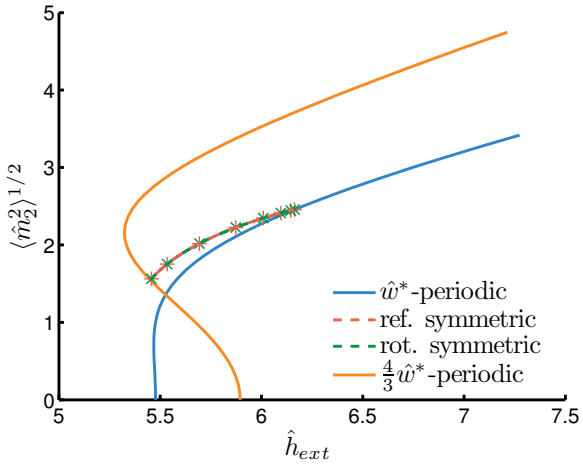

Figure 1.23.: Numerical simulations: Bifurcation diagram for $4\widehat{w}^*$ perturbations: The bifurcation branches that connect the $\widehat{w}^*$-periodic (blue) and the $\frac{4}{3}\widehat{w}^*$-periodic branch (orange). The magnetization patterns at the indicated fields are shown in Figure 1.24 and Figure 1.25. The bifurcation points of the secondary branches coincide. In between, the branches slightly differ.

1.8.7. Domain theory: Instability for decreasing field

Let us consider a concertina after several coarsening events. The experiments show that the concertina period decreases as the strength of the destabilizing field decreases, cf. Figure 1.29. This also has a simple explanation on the level of domain theory, for details see e) in Subsection 2.2. As the decreasing external field $\widehat{h}_{\text{ext}}$ drops below its optimal scaling for a given period $\widehat{w}$, that is, for $\widehat{w} \gg \widehat{h}_{\text{ext}} \ln \widehat{h}_{\text{ext}}$, the optimal concertina pattern degenerates in the sense that the triangular closure domains invade the whole sample cross section. We expect that at this stage the concertina refines its period towards the optimal period. The numerical backward cycle in Figure 1.26, in which we start at the multiply coarsened state and then after minimization repeatedly decrease the external field by a fixed increment, reveals that the coarsened pattern is stable up to the first turning point at which it degenerates. Depending on the initial level of coarsening, the period is then either refined or we reach the uniformly magnetized state after the minimization.

Let us introduce the maximal period $\widehat{w}_m$ at the field $\widehat{h}_{\text{ext}}$ as the period for which the corresponding $\widehat{w}_m(\widehat{h}_{\text{ext}})$-periodic pattern degenerates. Figure 1.27 shows that the prediction of domain theory matches the result of the simulation of the reduced model.

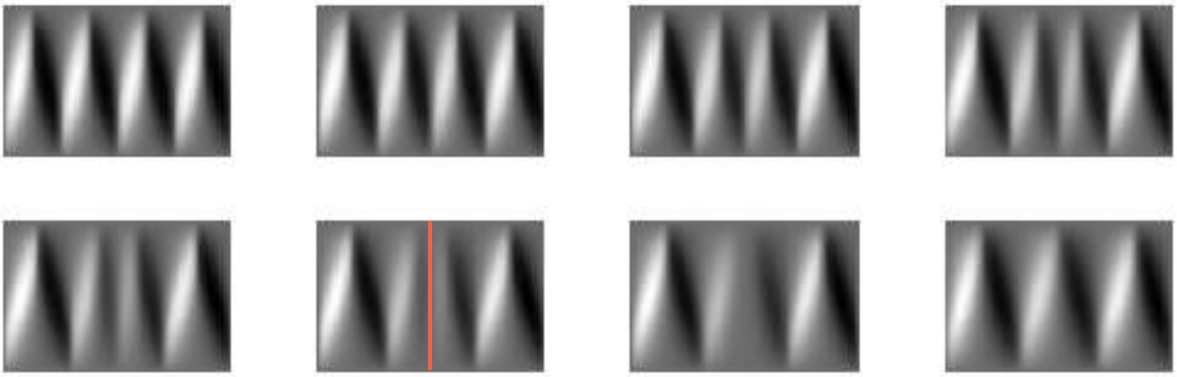

Figure 1.24.: Numerical simulations: Reflectional symmetric magnetization pattern on the unstable bifurcation branch connecting the $\widehat{w}^*$-periodic and the $\frac{4}{3}\widehat{w}^*$-periodic branch. The central fold collapses. The pattern is invariant under odd reflection at the center line $\widehat{m}_2(\widehat{x}_1, \widehat{x}_2) \rightsquigarrow -\widehat{m}_2(2\widehat{w} - \widehat{x}_1, \widehat{x}_2)$.

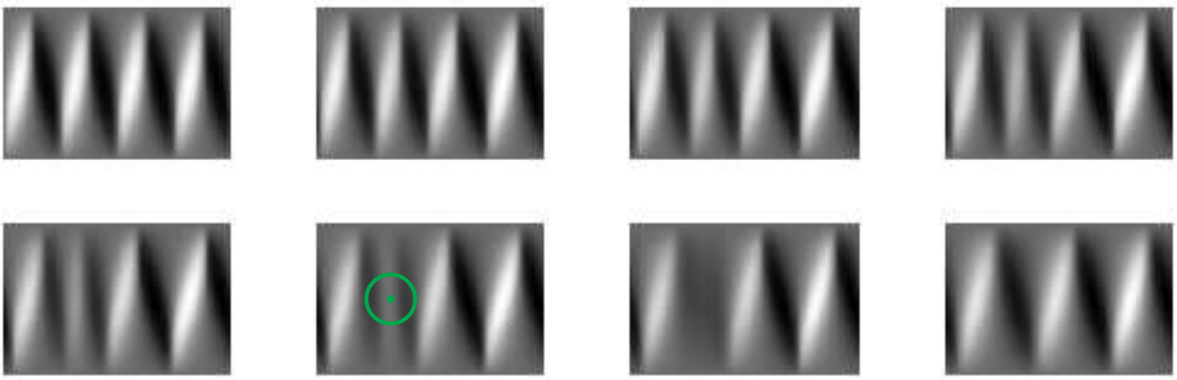

Figure 1.25.: Numerical simulations: Rotational symmetric magnetization pattern on the unstable bifurcation branch connecting the $\widehat{w}^*$-periodic and the $\frac{4}{3}\widehat{w}^*$-periodic branch. A white face disappears and two adjacent black faces merge. The pattern is invariant under rotation around the midpoint of the white face $\widehat{m}_2(\widehat{x}_1, \widehat{x}_2) \rightsquigarrow \widehat{m}_2(\frac{3}{2}\widehat{w} - \widehat{x}_1, 1 - \widehat{x}_2)$.

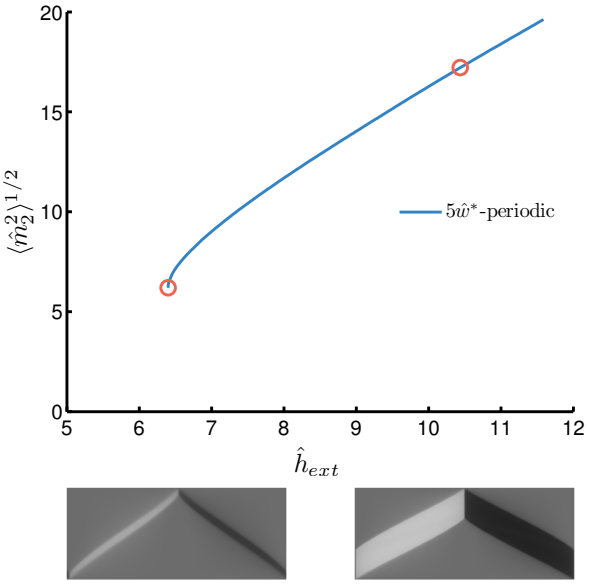

Figure 1.26.: Numerical simulations: The coarsened concertina pattern computed on the basis of the reduced model (1.14) up to the turning point. The numerical simulations confirm the prediction based on domain theory, namely that the pattern degenerates at the turning point of the branch.

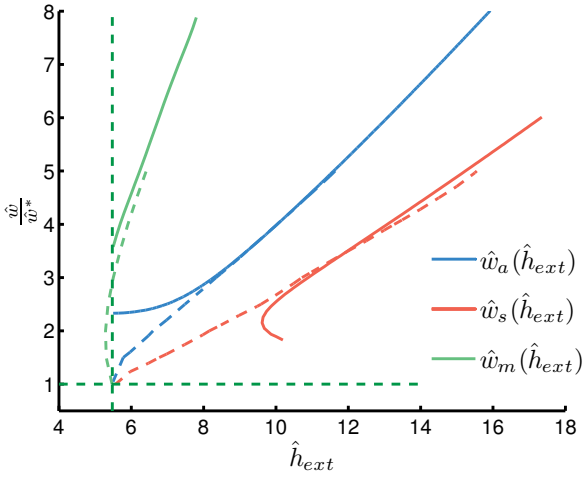

Figure 1.27.: Numerical simulations: The marginal stable $\widehat{w}_s$, optimal $\widehat{w}_a$ and maximal period $\widehat{w}_m$ of the concertina pattern as a function of the external field $\widehat{h}_{\text{ext}}$. The field $\widehat{h}_{\text{ext}}(\widehat{w}_s)$ is the field at which the $\widehat{w}_s$-periodic branch exhibits its turning point or degenerates, respectively. The dashed lines display the results of the numerical simulation of the reduced energy, the solid lines display the results of the minimization of the domain theoretic energy. The dashed dark-green lines indicate the period of the unstable mode and the critical field, respectively.

1.8.8. Conclusion: Hysteresis and Scattering of Data

Summing up, domain theory in conjunction with a Bloch wave argument indicates, that the concertina pattern of period $\widehat{w}$ is present or stable at a given field $\widehat{h}_{\text{ext}}$ if and only if $\widehat{w} \sim \widehat{h}_{\text{ext}} \ln \widehat{h}_{\text{ext}}$. This is confirmed by the numerical simulations. In particular we expect that the height of the triangular domains ($\sim \frac{\widehat{w}}{\widehat{m}_2^0}$) is close to constant as the external field increases. If the period deviates by a (large) factor from that expression, it becomes unstable. On the other hand, this analysis also suggest that there is a range of $\widehat{w} \sim \widehat{h}_{\text{ext}} \ln \widehat{h}_{\text{ext}}$ for which the concertina pattern is stable. This may explain some of the scatter in the experimental data and the pattern's hysteresis, see Figure 1.28.

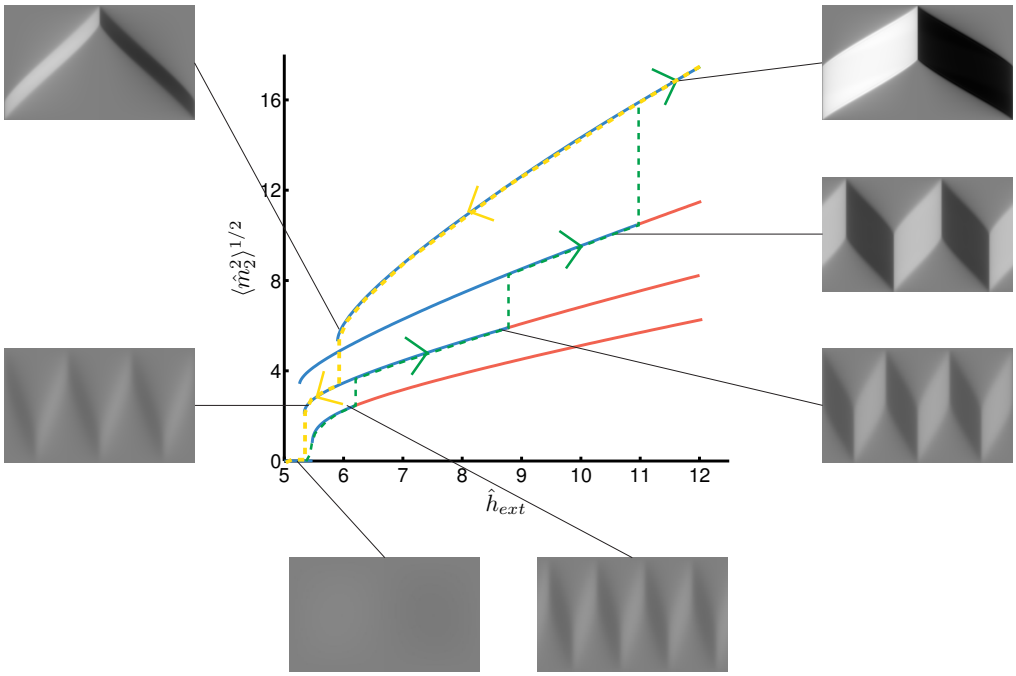

Figure 1.28.: Numerical simulations: The hysteresis loop obtained from the incremental minimization (iteration of $\widehat{h}_{\text{ext}} \rightsquigarrow \widehat{h}_{\text{ext}} + \delta\widehat{h}_{\text{ext}}$ and successive minimization on the $4\widehat{w}^*$-periodic domain) of the reduced energy including a small symmetry-breaking white-noise perturbation of the external field. As the external field increases, we follow the green path: The concertina pattern coarsens if the period is much smaller than the stable period. As the field decreases, we follow the yellow path: Starting from a multiply coarsened state, the pattern degenerates as we reach the turning point of the branch. The pattern refines towards the optimal period until it finally disappears. Red and blue parts indicate instability and stability under $4\widehat{w}^*$-periodic perturbations.

Figure 1.29.: Experiment: The hysteresis cycles of a Permalloy sample of 30 nm thickness and 50 μm width. First row: increasing destabilizing field from left to right. Bottom row: decreasing destabilizing field from right to left. The configurations of the same column are observed at the same value of the external field.

1.9. Polycrystalline anisotropy

The experiments usually do not show a clear-cut critical field with a first order transition, cf. Figure 1.30. This can be due to lack of experimental resolution or due to the presence of the ripple-like structure that smoothes out the transition. The ripple is the typical oscillation of the magnetization on a small scale and of small amplitude in an *extended* thin-film. This oscillation is perpendicular to the mean magnetization of the sample. The ripple is triggered by an effective random field on a small scale which originates in the heterogeneity of the material. We will focus on the effect of the polycrystallinity of Permalloy, which is the random orientation of grains possessing a uniaxial (crystal) anisotropy. In the literature other sources of the random field are discussed, for example local mechanical stresses due to magnetostriction.

As we will see in detail in Chapter 7, the ripple itself and the transition to the concertina can be understood based on an extension of the reduced model; the linear ripple theory developed in [Hof68, Har68] can be incorporated into our theory of the concertina. This explains the smoothing-out of the first order phase transition encountered in Section 1.6.

We learn from the analysis that, as the strength h_{ext} of the external field increases from moderate negative values towards the critical field the average wave length of the ripple continuously increases from the values characteristic for an extended film to the wave length of the unstable mode that is at the origin of the concertina pattern with its low-angle symmetric Néel walls. This suggests that the reduced model also provides the appropriate framework to analyze the nonlinear corrections to the linear ripple theory and thus captures the transition from the ripple to the so called blocked state – consisting of an array of Néel walls – in an extended film, see [Fel61].

In Section 7.2 we also contrast the effect of thermal fluctuations to the effect of quenched disorder – due to for example polycrystalline anisotropy. The first one leads to a random torque in the Landau-Lifshitz-Gilbert equation that is white noise in space *and* time whereas the latter one only leads to a white-noise in space. Based on an analysis of the stationary Gibbs measure we will see that the space-time white-noise causes a divergence of the expected average amplitude of the magnetization and an excitation in the small wave numbers, cf. [BG05]. This divergence is related to phase transitions in the Heisenberg spin model. In thin films, the dominant wavelength excited by a spatially random field is determined by both exchange and stray-field energy and can be seen to be much larger than the atomistic length scale, i.e., the exchange length d, and the grain size.

In Subsection 7.1.2, we address the numerical simulation of the spatially random field. Figure 1.30 compares the numerical simulations of the reduced energy functional including the random anisotropy with the experimental observations in a polycrystalline Permalloy sample.

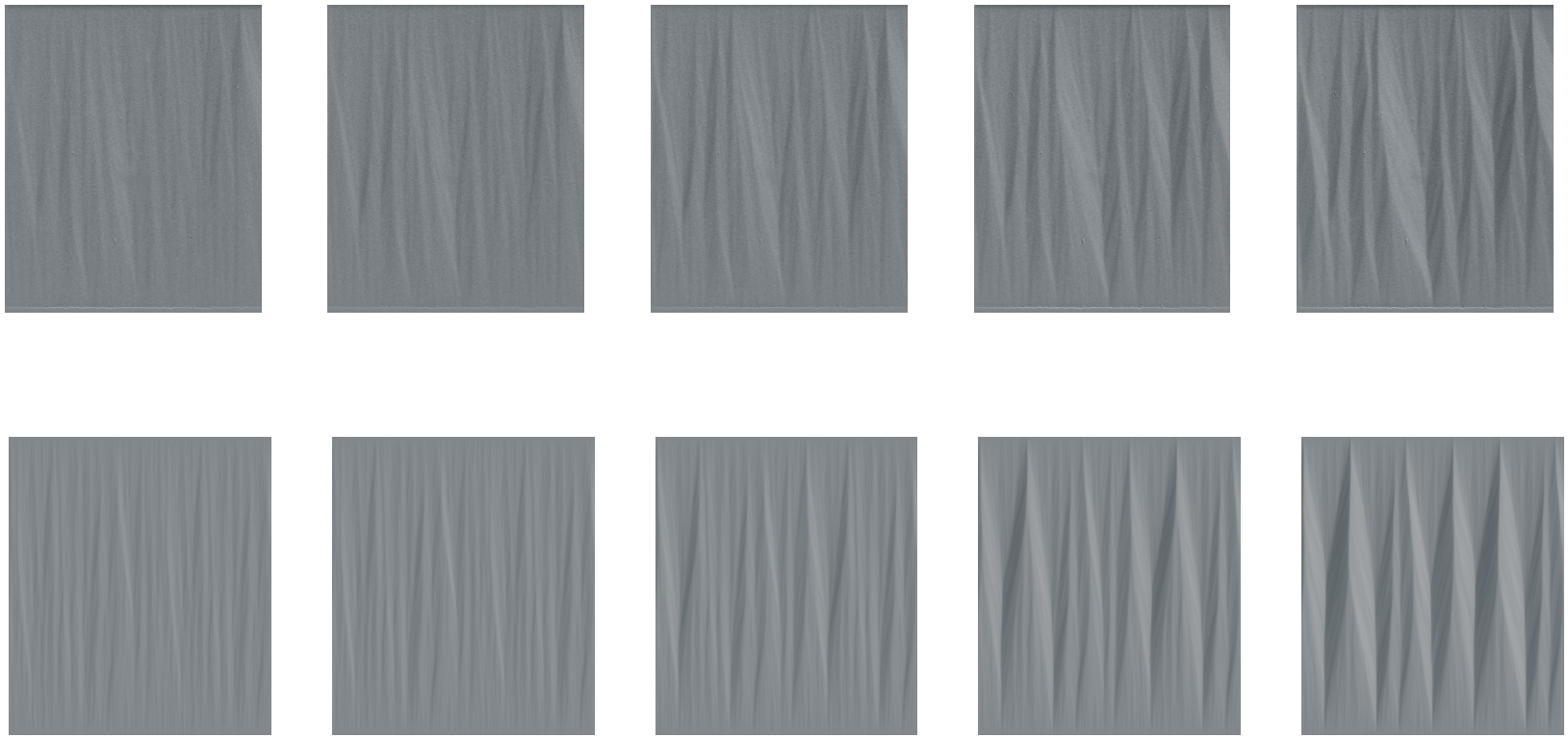

Figure 1.30.: Experiment and numerical simulations: The coarsening of the concertina pattern in a Permalloy sample (top row) of 30 nm thickness and 70 µm width compared to the numerical simulations (bottom row). A ripple-like structure grows into the concertina pattern. Within the numerical simulations we iteratively increment the external field and minimize the energy, see Section 4.7. The computational domain is of period $6\widehat{w}^*$. The numerical images are scaled according to (1.11). The images hence display approximately 1.8 times the unit cell; the numerical images therefore appear to be more uniform than the experimental concertina. Details on the numerical simulation of the random anisotropy are discussed in Subsection 7.1.2.

1.10. Uniaxial anisotropy

Due to its experimental relevance, we now address the effect of a uniaxial anisotropy that is constant throughout the sample, on the formation and evolution of the concertina pattern. We focus on two cases: The easy axis coincides with the x_2-axis – transversal anisotropy, i.e., $e = (0,1,0)$ in (1.1) – or the easy axis coincides with the x_1-axis – longitudinal anisotropy, i.e., $e = (1,0,0)$ in (1.1). Clearly, such type of anisotropy has no effect on the stationarity of $m^* = (1,0,0)$. On the level of the reduced model both cases are represented up to an additive constant by the additional quadratic term

$$-Q\,t\int_{\Omega'} m_2^2\,\mathrm{d}x_1\,\mathrm{d}x_2, \tag{1.23}$$

with a *signed* quality factor Q. Transversal anisotropy corresponds to $Q > 0$, longitudinal anisotropy corresponds to $Q < 0$.

As will become clear below when considering the effects of anisotropy, it is appropriate to expand the Zeeman term to quartic order, i.e.,

$$-h_{\mathrm{ext}}\,t\int_{\Omega'}(m_2^2 + \tfrac{1}{4}m_2^4)\,\mathrm{d}x_1\,\mathrm{d}x_2.$$

The following Gedankenexperiment is helpful in understanding the sequel: In extended thin films, i.e., infinite width $\ell = \infty$, there is no incentive for a spatially varying magnetization so that we may consider a constant magnetization m_2. The only energy contributions are due to the external field and the anisotropy so that the energy per volume is thus given by $-Qm_2^2 - h_{\mathrm{ext}}(m_2^2 + \frac{1}{4}m_2^4)$. In this context, the critical field is given by $h_{\mathrm{ext}}^* = -Q$. For longitudinal anisotropy, the bifurcation is subcritical, whereas for transversal anisotropy, the bifurcation is supercritical and yields

$$m_2 = \pm(2(1 + Q^{-1}h_{\mathrm{ext}}))^{1/2}. \tag{1.24}$$

Hence for *finite* ℓ, there are two competing mechanisms which lead to a bifurcation and a selection of an amplitude for m_2: uniaxial anisotropy and stray-field energy.

As we will see in the sequel, there are essentially three different effects of anisotropy: a *linear* one, a *weakly nonlinear* one, and a *strongly nonlinear* one. We list and characterize these effects below. However, the order at which these effects arise with increasing anisotropy does not agree with their ordering with increasing nonlinearity, cf. Figure 1.31: The linear effect becomes pronounced for $|Q| \gg d^{2/3}\ell^{-4/3}t^{2/3}$, the strongly nonlinear one for $|Q| \gg \ell^{-1}t$, and the weakly nonlinear one only for $|Q| \gg d^{-2/3}\ell^{-2/3}t^{4/3}$. Note that we have that $d^{-2/3}\ell^{4/3}t^{-2/3} \ll \ell^{-1}t \ll d^{-2/3}\ell^{-2/3}t^{4/3}$ provided $d^2\ell^{-1} \ll t$, which is the lower bound on the film thickness which characterizes Regime III.

We mainly focus on the case of transversal anisotropy $Q > 0$. In case of longitudinal anisotropy $Q < 0$ we give an explanation for the experimental fact that the

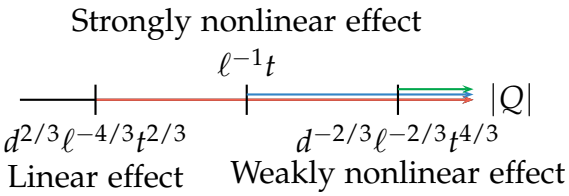

Figure 1.31.: The order of the different effects of anisotropy.

concertina cannot be observed at all. The forthcoming discussion is based on the *unrescaled* version of the reduced model, (1.10) augmented by (1.23).

Linear effect for weak anisotropy $|Q| \gg d^{2/3}\ell^{-4/3}t^{2/3}$. An obvious effect of anisotropy is a shift of the critical field h^*_{ext} by the amount $-Q$; we call it the *linear effect* of anisotropy since it arises on the level of the linearization at $m_2 \equiv 0$. In view of the scaling of the critical field h^*_{ext} at $Q = 0$, i.e., (1.12), we infer that the critical field behaves as

$$h^*_{\mathrm{ext}} \approx -Q \quad \text{for} \quad |Q| \gg d^{2/3}\ell^{-4/3}t^{2/3}. \tag{1.25}$$

We note that a transversal anisotropy decreases the distance between the two critical fields $\pm h_{\mathrm{ext}}$ of $\pm m^*$; in particular, the the sign of the critical field changes provided $Q \sim d^{-2/3}\ell^{4/3}t^{-2/3}$ and thus the order between the two critical fields switches. Likewise, for longitudinal anisotropy the distance decreases. Although a clear-cut critical field cannot be observed in the experiments – due to the polycrystalline structure which triggers the ripple and since the value of the effective external field at the observed sample section is not available – the linear effect has been qualitatively confirmed: For Permalloy samples of high transversal anisotropy we observed that the oscillatory instability occurs before the external field is reversed. For wide films the relative strength of anisotropy increases, see (1.25), and the oscillation is observed even earlier in the experiments. For low-anisotropic Permalloy the oscillation is first observed close to zero external field.

Weakly nonlinear effect for strong anisotropy $|Q| \gg t(w^*)^{-1} \sim d^{-2/3}\ell^{-2/3}t^{4/3}$. For sufficiently strong anisotropy Q the quartic term coming from the stray-field energy no longer dominates the quartic term coming from the Zeeman energy near the bifurcation. We call this effect the *weakly nonlinear effect* of anisotropy, since it can be analyzed on the level of an expansion near $m_2 \equiv 0$ and $h_{\mathrm{ext}} = h^*_{\mathrm{ext}}$, cf. (1.19). We additionally have to take into account the quartic Zeeman term $-\frac{h_{\mathrm{ext}}}{4}tA^4\int (m_2^*)^4\,\mathrm{d}x_1\,\mathrm{d}x_2$. The shift of the critical field suggests the following rescaling for the external field

$$\widehat{h}_{\mathrm{ext}} = d^{-2/3}\ell^{4/3}t^{-2/3}(h_{\mathrm{ext}} + Q).$$

Note that for $|Q| \gg d^{-2/3}\ell^{-2/3}t^{4/3} \gg d^{-2/3}\ell^{4/3}t^{-2/3}$ the critical field is of order $h^*_{\mathrm{ext}} \approx -Q$. Therefore we set

$$\widehat{Q} = -\tfrac{1}{4}d^{2/3}\ell^{2/3}t^{-4/3}h_{\mathrm{ext}}.$$

We obtain – with the same rescaling of energy, length and magnetization as in (1.11) and (1.13) – the reduced energy functional augmented by $+\widehat{Q}\int_{\widehat{\Omega}'}\widehat{m}_2^4\,\mathrm{d}\widehat{x}_1\,\mathrm{d}\widehat{x}_2$. Therefore the reduced energy close to the bifurcation takes the form of

$$\widehat{E}(A\widehat{m}_2^* + A^2\widehat{m}_2^{**}) \approx -(\tfrac{\pi}{2})^{1/3}(\widehat{h}_{\mathrm{ext}} - \widehat{h}_{\mathrm{ext}}^*)\,A^2 + (\tfrac{9}{64}\widehat{Q} - \tfrac{\pi}{640})A^4,$$

cf. (1.19). For $|Q| \gg d^{-2/3}\ell^{-2/3}t^{4/3} \gg d^{-2/3}\ell^{4/3}t^{-2/3}$, the critical field is of order $h_{\mathrm{ext}}^* \approx -Q$, so that the reduced quality factor scales as $\widehat{Q} \approx \frac{1}{4}d^{2/3}\ell^{2/3}t^{-4/3}\,Q$. From the latter we read off that in the regime $Q \gg t(w^*)^{-1} \sim d^{-2/3}\ell^{-2/3}t^{4/3}$ the quartic coefficient becomes positive and therefore the bifurcation becomes supercritical, cf. Figure 1.32. Essentially it is a perturbation of the constant-magnetization bifurcation in infinitely extended films mentioned above. In particular, the selected amplitude in this case scales as $m_2 \sim A \sim (1 + h_{\mathrm{ext}}Q^{-1})^{1/2}$.

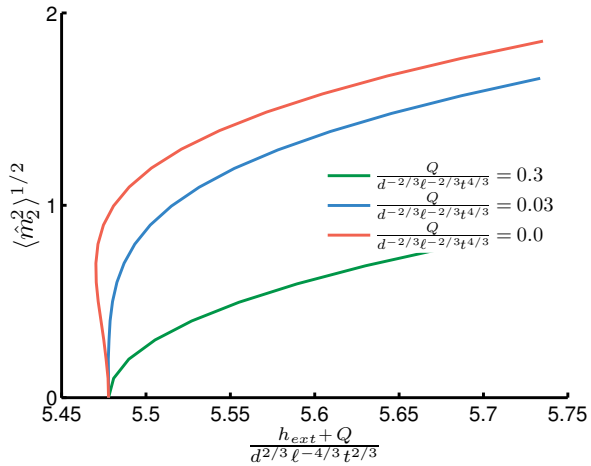

Figure 1.32.: Numerical simulations: Transition from sub- to supercritical bifurcation as strength of transversal anisotropy increases. For $\widehat{Q} = 0.03 \approx \widehat{Q}^*$ the bifurcation degenerates.

On the other hand, for large longitudinal anisotropy, i.e., $-Q \gg d^{-2/3}\ell^{-2/3}t^{4/3}$, we expect that there is no turning point on the bifurcating branch so that it remains unstable to the effect that no concertina pattern forms in the first place. The numerical simulations in Figure 1.33 show a second turning point which coincides with the break-up of the concertina pattern. For very large longitudinal anisotropy the first turning point is destroyed.

This observation can be confirmed on the level of domain theory within the original scaling, cf. (1.11), where we include anisotropy and the quartic term in the Zeeman energy:

$$\begin{aligned} E_{\mathrm{domain}}(m_2^0, w) \;=\; & 2\left(\ell - \tfrac{w}{m_2^0}\right)e(m_2^0) + 4\,\tfrac{w}{m_2^0}\,e\left(\tfrac{m_2^0}{2}\right) \\ & - (h_{\mathrm{ext}} + Q)(m_2^0)^2 t\left(w\ell - \tfrac{w^2}{m_2^0}\right) - h_{\mathrm{ext}}\tfrac{1}{4}(m_2^0)^4 t\left(w\ell - \tfrac{w^2}{m_2^0}\right). \end{aligned} \tag{1.26}$$

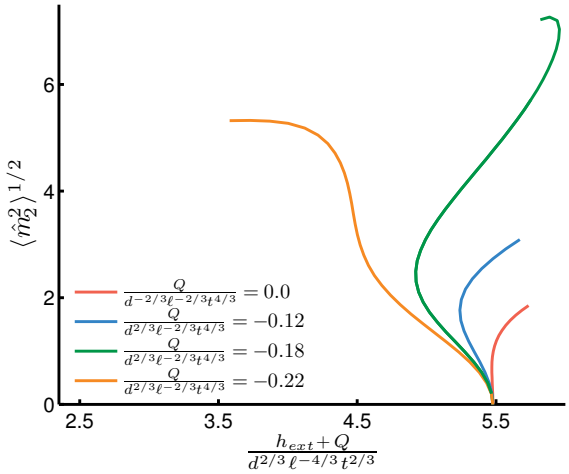

Figure 1.33.: Numerical simulations: Loss of the turning point as strength of longitudinal anisotropy increases

We note that the line-energy density $e(m_2^0)$ scales as $\frac{\pi}{8}t^2(m_2^0)^4$ up to a logarithm. Hence, the stray-field energy cannot compensate the destabilizing quartic Zeeman contribution provided $h_{\text{ext}}\, t\, w \gg t^2$ (up to a logarithm). Since $h_{\text{ext}}^* \sim -Q$ and $w \sim d^{2/3}\ell^{2/3}t^{-1/3}$ close to the bifurcation there are no (local) minimizers of the energy.

Typical values for our Permalloy samples of strong uniaxial anisotropy range from $\widehat{Q} = \frac{|Q|}{4d^{-2/3}\ell^{-2/3}t^{4/3}} \approx 2.1 \times 10^{-4}$ to 0.023 depending on the sample's width and thickness ($Q = 5 \times 10^{-4}$, $t = 10$ nm to 150 nm, $\ell = 10\,\mu$m to $50\,\mu$m, see Chapter 1.12). Typical values for CoFeB range from $\widehat{Q} = 7.8 \times \times 10^{-4}$ to 0.011 ($Q \approx 1.5 \times 10^{-3}$, $t = 30$ nm-100 nm, $\ell = 10\,\mu$m-$50\,\mu$m, see Chapter 1.12). The uniaxial anisotropy is thus too small to cause the weakly non-linear effect. Although local minimizers of the energy though might exist in case of longitudinal anisotropy, still the energy augmented by the quartic Zeeman energy is not coercive as soon as the external field is reversed.

Strongly nonlinear effects for moderate anisotropy $|Q| \gg \ell^{-1}t$. In that case we find two different scenarios, which are investigated in detail in Section 2.5 on the level of domain theory augmented by the quartic Zeeman energy, i.e., (1.26).

- Scenario I: If the amplitude and shape of the concertina pattern would not be affected by anisotropy, like in an infinitely extended film, its optimal amplitude would scale as

$$m_2 \sim \ell t^{-1}(h_{\text{ext}} - h_{\text{ext}}^*) \overset{(1.25)}{\approx} \ell t^{-1}(h_{\text{ext}} + Q) = \ell t^{-1} Q(1 + Q^{-1}h_{\text{ext}}), \qquad (1.27)$$

  up to a logarithm, as we have seen in Section 1.8.1.

- Scenario II: If the amplitude of the concertina pattern would be dominated by transversal anisotropy, it would behave as

$$m_2 \overset{(1.24)}{\sim} (1 + Q^{-1}h_{\text{ext}})^{1/2} \quad \text{for} \quad 0 < (1 + Q^{-1}h_{\text{ext}}) \ll 1, \tag{1.28}$$

as we have seen at the beginning of this Section in (1.24). Hence, we expect that for $Q \gg \ell^{-1}t$ the amplitude of the concertina pattern is limited by stray-field effects as long as $0 < 1 + Q^{-1}h_{\text{ext}} \ll (Q^{-1}\ell^{-1}t)^2$ and by anisotropy effects once $(Q^{-1}\ell^{-1}t)^2 \ll 1 + Q^{-1}h_{\text{ext}} \ll 1$. Loosely speaking, the effect of anisotropy kicks in for a large amplitude and is most prominent close to field strength where the concertina pattern vanishes. We call this the *strongly nonlinear effect* of anisotropy. Also this provides a reason to expand the Zeeman term to higher order.

We note that the optimal period in Scenario II is determined by the lower order wall energy. A minimization of the energy per length yields the following scaling behavior of the optimal period (up to a logarithm)

$$w_a \sim (\ell t)^{1/2} Q^{-1/2} (1 + Q^{-1}h_{\text{ext}})^{1/4},$$

cf. Section 2.5 b). As we know from Section 1.8, the experimentally more relevant quantity is the marginally stable period, i.e., the largest period – as a function of the external field – for which the minimal energy is convex. At the cross-over we expect that the marginal stable period is of the order $\sim tQ^{-1}$, cf. Figure 2.6. In fact, due to $(Q^{-1}\ell^{-1}t)^2 \sim 1 + Q^{-1}h_{\text{ext}}$ at the cross-over, we have that $\ell^2 t^{-1} Q(1 + Q^{-1}h_{\text{ext}}) \sim (t\ell)^{1/2} Q^{-1/2}(1 + Q^{-1}h_{\text{ext}})^{1/4}$ entails that the period is of the order $w \sim tQ^{-1}$. We will see that for a period of that order, the minimal energy in scenario II turns out to be convex, see c) in Section 2.5. Hence we expect that the coarsening stops once $(Q^{-1}\ell^{-1}t)^2 \ll 1 + Q^{-1}h_{\text{ext}} \ll 1$. Still the transversal component of the magnetization increases as $m_2 \sim (1 + Q^{-1}h_{\text{ext}})^{1/2}$ so that the size and height of the closure domains decrease. As h_{ext} approaches zero, the energy 1.26 looses coercivity, so that the low-angle approximation is not valid anymore since the amplitude m_2^0 diverges. At this stage the pattern is suspected to collapse so that the magnetization in the end switches completely.

Let us mention another observation supporting the conjecture that anisotropy effects are most prominent close to the field strength where the concertina collapses: For $Q \gg \ell^{-1}t$, the ground state for vanishing external field $h_{\text{ext}} = 0$ is no longer given by the uniform magnetization $m = (\pm 1, 0, 0)$, but a Landau or concertina-type pattern, see Figure 1.35, has lower energy. The period w of the two latter patterns is determined by a balance of the wall energy and the anisotropy energy in the closure domains and scales as $w \sim Q^{-1/2}\ell^{1/2}t^{1/2}$ up to a logarithm. Hence we expect that in this regime, the concertina does not switch to $m = (-1, 0, 0)$, but evolves to the pattern in Figure 1.35. In fact, that type of evolution of the concertina pattern can be observed in the CoFeB samples which possess a relatively strong transversal anisotropy, cf. Figure 1.37.

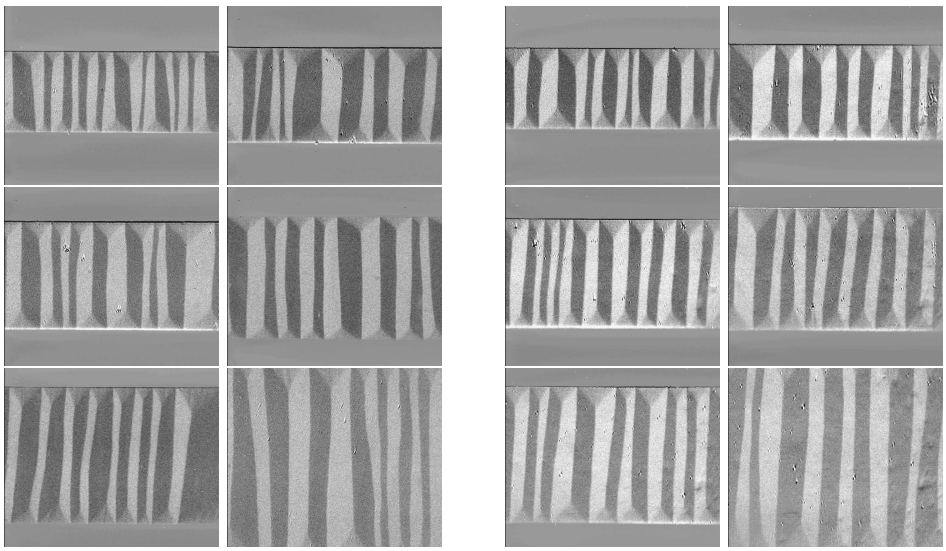

Figure 1.34.: Experiment: Permalloy samples of width 60 µm to 150 µm of high anisotropy and the end of the coarsening process. The 6 samples on the right are of thickness 30 nm, the 6 samples on the right are of thickness 50 nm. The period of the pattern appears to be independent of the width of the samples.

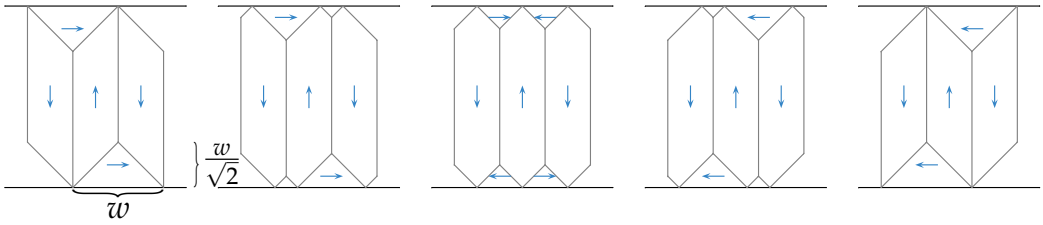

Figure 1.35.: Continuous transition from the concertina pattern via the Landau state to the reverse concertina.

1.11. Discretization and numerical simulations

The numerical simulations are based on a finite difference discretization of the reduced rescaled energy functional (1.14). The transversal component $\widehat{m}_2$ is approximated on a uniform Cartesian grid. The discretization of the exchange, anisotropy and Zeeman energy is straight-forward. In case of the non-linear charge density $\widehat{\sigma} = -\widehat{\partial}_1 \frac{\widehat{m}_2^2}{2} + \widehat{\partial}_2 \widehat{m}_2$, our choice of a finite difference stencil is motivated by the inheritance of the shear-invariance of $\widehat{\sigma}$, see 4.1. The stray-field energy can efficiently be computed using Fast Fourier Transform with respect to $\widehat{x}_1$. For a detailed introduction of the discretization scheme, see [Steo6, Subsection 3.2]. Note that the computation of the energy and related quantities such as the gradient or the Hessian can be parallelized – the non-locality is only with respect to one dimension – for which we decompose the computational domain into horizontal slices, i.e., with respect to $\widehat{x}_2$.

We apply numerical simulations to compute minimizers and stationary points. The naive approach, using steepest descent algorithms for the computation of minimizers ,is slow and even fails close to bifurcations points. The iterative path-following techniques that we apply in order to compute an approximation to a branch of stationary points are adapted to such situations, cf. [Geo01].

A bifurcation point can be detected with the help of an appropriate indicator function. However, both the bifurcation detection and the branch-switching technique which are described in [Geo01] are applicable for simple bifurcations points only. As described in detail in Chapter 4, we extend these methods to cope with multiple bifurcation points. The extension relies on the fact that multiple bifurcations, which occur due to symmetries of the primary solution, generically can be reduced to simple bifurcation points, cf. [GS02].

1.12. Experimental setup and samples

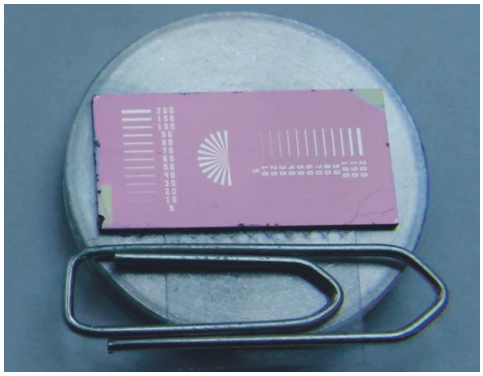

Figure 1.36.: Photograph of a complete specimen. The numbers on the substrate next to the stripes denote the width (in μm). By courtesy of H. Wieczoreck.

Figure 1.36 displays one of the samples which were investigated at the IfW Dresden by J. McCord, R. Schäfer, and H. Wieczoreck. The samples were manufactured in cooperation with R. Mattheis at IPHT Jena. In the experiments we investigated magnetic films of nano-crystalline Permalloy, $Ni_{81}Fe_{19}$, and amorphous $Co_{60}Fe_{20}B_{20}$ of various thicknesses and varying induced magnetic anisotropy values. The films were deposited by magnetron sputtering under ultra high vacuum conditions. In order to control the grain growth of the polycrystalline films a Ta (Tantalum) seed (5 nm) layer was used for the $Ni_{81}Fe_{19}$ deposition. In all cases, a magnetic in-plane saturation field was applied during film deposition to control the induced anisotropy strength and direction. By varying the magnetic field history, films with different effective induced anisotropy values were obtained.

- In a first set of samples the uniaxial anisotropy was induced by a deposition in the presence of a homogeneous, static magnetic field. This results in a

maximum and also well-aligned induced magnetic anisotropy. A series of Permalloy and CoFeB samples was obtained by this method.

- In a second set of Permalloy samples the induced anisotropy was strongly reduced. In order to ensure this, the films were deposited in a magnetic field with alternating orthogonal alignment. The field direction was changed approximately after every 5 nm of film growth. The superposition of orthogonally aligned magnetic anisotropy axis results in a strongly *reduced* induced anisotropy.

The material parameters, relevant for the comparison of the experimental observations to theoretical predictions, are the following:

- Exchange length d: Permalloy 5 nm, CoFeB 3 nm.
- For both materials the saturation polarization is $J_s \approx 1$ T and the stray-field energy density is given by $K_d \approx 4 \times 10^5$ J/m^3.
- The uniaxial anisotropy coefficient is $K_u^{\text{Permalloy}} \approx 200$ J/m^3 for the high anisotropic Permalloy and $K_u^{\text{CoFeB}} \approx 600$ J/m^3 for CoFeB, respectively. For the low anisotropic Permalloy films we obtain $K_u^{\text{Permalloy}} \approx 50$ J/m^3.
- Quality factor $Q = K_u/K_d$: High anisotropy Permalloy $Q \approx 0.5 \times 10^{-3}$ and CoFeB $Q \approx 1.5 \times 10^{-3}$.
- The average size of the individual grains of Permalloy is $\ell_{\text{grain}} \approx 12$ to 15 nm. It is assumed that up to a film thickness of about 30 nm the grains display a column-like shape.
- The film thicknesses range from 10 to 150 nm, the investigated film widths from 10 to 100 µm.

After film deposition, elongated stripes of various widths and a length of 2000 µm were patterned by photolithography and subsequent ion beam etching. The stripes are aligned parallel and orthogonal to the induced anisotropy axis, see Figure 1.36.

The observation of domains and magnetization processes was carried out in a digitally-enhanced Kerr microscope, see [HS98]. The longitudinal Kerr effect was applied with its magneto-optical sensitivity axis transverse to the long edge of the stripe. The dominant wavelength of the patterns was computed by Fast Fourier transform. The result of the computation is in agreement with the average wavelength determined by counting the folds as soon as the concertina becomes discernible to the eye as the magnetic field is decreased starting from saturation. The typical strength of the magnetic fields which were applied for saturation is of the order of some mT.

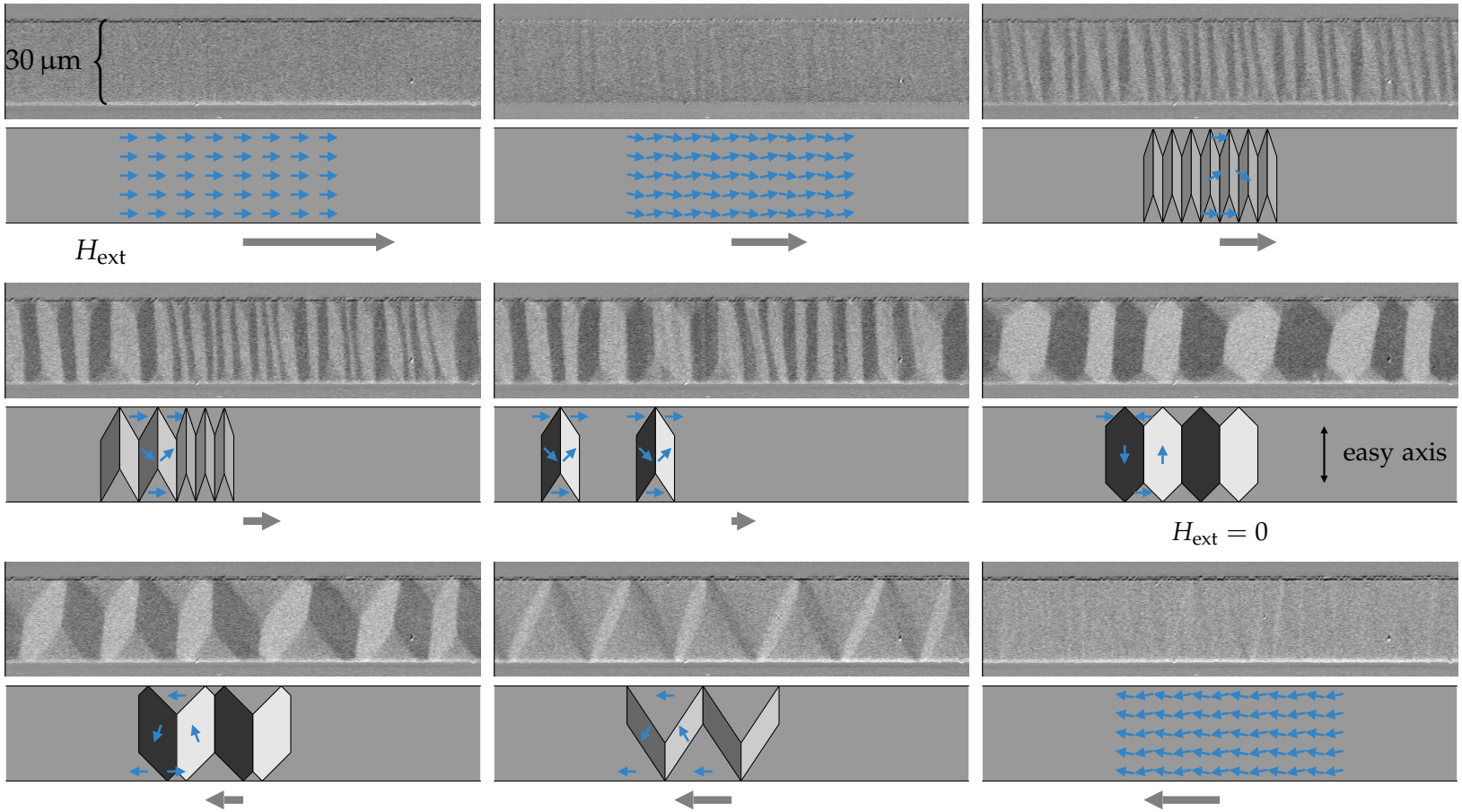

Figure 1.37.: Experiment: Hysteresis of a CoFeB sample of 60 nm thickness and 30 µm width. After several coarsening events we observe a transition to a Landau state at zero external field which turns into a concertina that degenerates and refines, and finally disappears.

2

Domain theory

In the numerical simulations of the reduced energy functional, we observe for large external field $\widehat{h}_{\text{ext}} \gg 1$ that the minimizers are approximately piecewise constant on a mesoscopic scale, see Section 1.7 in the introductory chapter and Figure 1.12 therein. In this chapter, we make use of the scale-separation and heuristically derive a sharp-interface model, namely domain theory, as a limit of the reduced energy for $\widehat{h}_{\text{ext}} \gg 1$. This model is partially justified in the subsequent Chapter 3, see Theorem 3.3 therein, which states that minimal energy configurations of the reduced model (1.14) are close to weak solution of the Burgers equation.

2.1. Derivation of the energy

Motivated by the numerical simulations and as mentioned in the introduction, we assume that admissible magnetizations within domain theory are given by weak solutions to the Burgers equation

$$-\widehat{\partial}_1\Big(\tfrac{\widehat{m}_2^2}{2}\Big) + \widehat{\partial}_2\widehat{m}_2 = 0. \tag{2.1}$$

In view of the boundary conditions, i.e., $\widehat{m}_2 = 0$ for $\widehat{x}_2 \in \{0,1\}$, the method of characteristics shows that non-trivial weak solutions of (2.1) cannot be continuous. Typically, they will have line discontinuities, i.e., a one-dimensional jump set $\widehat{J}$, cf. Figure 2.1. The energy which discriminates between these solutions is given by an appropriate line-energy density $\widehat{e}$ integrated over the jump set $\widehat{J}$, augmented by Zeeman energy. In its rescaled version, the energy is given by:

$$\widehat{E}_{\text{domain}}(\widehat{m}_2) \;=\; \int_{\widehat{J}} \widehat{e}\Big(\tfrac{[\widehat{m}_2]}{2}\Big)\,\mathrm{d}\mathcal{H}^0\,\mathrm{d}\widehat{x}_2 - \widehat{h}_{\text{ext}}\int \widehat{m}_2^2\,\mathrm{d}\widehat{x}_1\,\mathrm{d}\widehat{x}_2,$$

where $\mathcal{H}^0$ denotes the zero-dimensional Hausdorff measure. Not surprisingly, the specific line – or wall – energy $\widehat{e}$ is a function of the jump $[\widehat{m}_2]$ of $\widehat{m}_2$ across $\widehat{J}$. In case of the vertical walls, it can be derived by restricting (1.14) to one-dimensional configurations with prescribed boundary data $\pm\widehat{m}_2^0$, minimizing

$$\widehat{E}_{\text{Néel}}(\widehat{m}_2) \;=\; \int(\widehat{\partial}_1\widehat{m}_2)^2\,\mathrm{d}\widehat{x}_1 + \tfrac{1}{8}\int ||\widehat{\partial}_1|^{1/2}\widehat{m}_2^2|^2\,\mathrm{d}\widehat{x}_1. \tag{2.2}$$

The optimal transition layers are low-angle Néel walls whose line-energy density is given by

$$\widehat{e}\Big(\tfrac{[\widehat{m}_2]}{2}\Big) \;=\; \widehat{e}(\widehat{m}_2^0) \;=\; \tfrac{\pi}{8}(\widehat{m}_2^0)^4 \ln^{-1} \tfrac{\widehat{w}_{\text{tail}}}{\widehat{w}_{\text{core}}}, \tag{2.3}$$

where $\widehat{w}_{\text{tail}}$ and $\widehat{w}_{\text{core}}$ are the two characteristic length scales of the Néel wall, namely the tail and core width, see [Melo3] and [DKMO05, Section 6]. For the scaling of these two parameters in case of the concertina pattern, see below. Due to the shear invariance of the reduced energy functional (1.14), i.e.,

$$\widehat{x}_1 = s\widehat{x}_2 + \tilde{x}_1, \quad \widehat{x}_2 = \tilde{x}_2, \quad \widehat{m}_2 = \tilde{m}_2 - s \quad \text{for some} \quad s \in \mathbb{R}, \tag{2.4}$$

a diagonal wall of jump size $[\widehat{m}_2] = \pm\widehat{m}_2^0$ can be transformed into a vertical wall of equal jump size (with the choice of $s = \pm\frac{\widehat{m}_2^0}{2}$). This shows that the specific line-energy density is in fact a function of the jump size.

We want to use an Ansatz which mimics the concertina pattern with its quadrangular and triangular domains and which is determined by just two parameters, namely the period $\widehat{w}$ and the inclination $\widehat{m}_2 = \pm\widehat{m}_2^0$ in the quadrangular domains ($\widehat{m}_2 = 0$ in the triangular domains), cf. Figure 2.1.

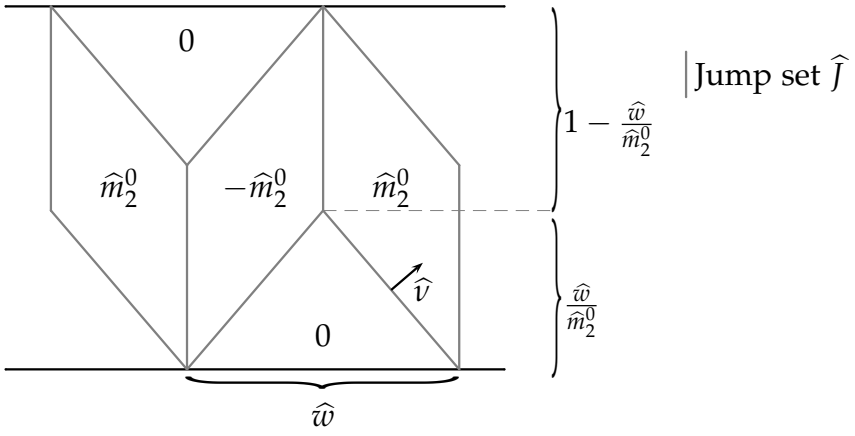

Figure 2.1.: Sketch of the Ansatz function.

Indeed, the angles in the pattern are fixed by the constraint that $\widehat{m}_2$ is a weak solution to Burgers' equation: If $\widehat{\nu}$ denotes the normal to the diagonal jump set, indicated in Figure 2.1, then the jump of the normal component of the magnetization has to vanish:

$$0 \;=\; [\widehat{\nu} \cdot (-\tfrac{1}{2}\widehat{m}_2^2, \widehat{m}_2)] \;=\; \widehat{\nu} \cdot (-\tfrac{1}{2}(\widehat{m}_2^0)^2, \widehat{m}_2^0).$$

This condition fixes the angles in the pattern. We note that it is always necessary to impose $m_2^0 > \widehat{w}$ to avoid a degenerated pattern – for $m_2^0 = \widehat{w}$ the triangular domains invade the whole cross-section.

We claim that with our Ansatz, the energy per length in $\widehat{x}_1$ becomes a function of only two parameters, namely $\widehat{m}_2^0$ and $\widehat{w}$. To see that, we first turn to the two

parameters $\widehat{w}_{\text{tail}}$ and $\widehat{w}_{\text{core}}$ in (2.3). The tails of the Néel wall spread as much as possible; in case of the concertina pattern, they are only limited by the neighboring walls – thus $\widehat{w}_{\text{tail}} \sim \frac{\widehat{w}}{4}$. A more careful inspection of (2.2) shows that the core width decreases with increasing jump size, more precisely $\widehat{w}_{\text{core}} \sim \frac{1}{(\widehat{m}_2^0)^2}$, see [Ste06]. Hence (2.3) turns into

$$\widehat{e}(\widehat{m}_2^0) \;=\; \tfrac{\pi}{8}(\widehat{m}_2^0)^4 \ln^{-1} c_0 \tfrac{\widehat{w}}{4}(\widehat{m}_2^0)^2. \tag{2.5}$$

In [Ste06], the constant c_0 was determined by fitting the numerically computed minimal energy (on the basis of (2.2)) as a function of its boundary conditions to (2.5).

Notice that one period of the pattern in Figure 2.1 contains

- two vertical walls of height $1 - \frac{\widehat{w}}{\widehat{m}_2^0}$ and of jump size $2\,\widehat{m}_2^0$, leading to an energy contribution of $2\,(1 - \frac{\widehat{w}}{\widehat{m}_2^0})\,\widehat{e}(\widehat{m}_2^0)$,
- four diagonal walls of projected height $\frac{\widehat{w}}{\widehat{m}_2^0}$ and of jump size $\widehat{m}_2^0$, leading to an energy contribution of $4\,\frac{\widehat{w}}{\widehat{m}_2^0}\,e(\frac{\widehat{m}_2^0}{2})$,
- two quadrangular domains of total area $\widehat{w} - \frac{\widehat{w}^2}{\widehat{m}_2^0}$, leading to a Zeeman energy of $-\widehat{h}_{\text{ext}}(\widehat{m}_2^0)^2\,(\widehat{w} - \frac{\widehat{w}^2}{\widehat{m}_2^0})$.

Hence, the total energy per period is given by:

$$\widehat{E}_{\text{domain}}(\widehat{m}_2^0, \widehat{w}) \;= 2\left(1 - \tfrac{\widehat{w}}{\widehat{m}_2^0}\right)\widehat{e}(\widehat{m}_2^0) + 4\,\tfrac{\widehat{w}}{\widehat{m}_2^0}\,\widehat{e}\left(\tfrac{\widehat{m}_2^0}{2}\right) - \widehat{h}_{\text{ext}}(\widehat{m}_2^0)^2\left(\widehat{w} - \tfrac{\widehat{w}^2}{\widehat{m}_2^0}\right), \tag{2.6}$$

under the constraint $\widehat{m}_2^0 \geq \widehat{w}$. Figure 1.15 shows that domain theory provides a good approximation of the reduced energy (1.14) for $\widehat{h}_{\text{ext}} \gg 1$.

2.2. Minimality and stability of domain theory for large fields

Based on (2.6), we now derive certain properties of minimizing configurations whose physical interpretation was discussed in Section 1.8. The following statements a)-d) address the scaling behavior of the minimal energy per length, the optimal inclination of the magnetization, the optimal period of the pattern, and the minimal energy for periods much smaller than the optimal period. The last item e) states that that there is a smallest field for which a concertina of prescribed period exists. We note that the coarsening of the concertina is related to statement d) while the refining of the pattern is related to statement e).

For large external field $\widehat{h}_{\text{ext}} \gg 1$ we have:

a) The minimal energy per *length* in $\widehat{x}_1$-direction scales as

$$\min_{\{(\widehat{m}_2^0,\widehat{w})\,|\,\widehat{m}_2^0\geq\widehat{w}\}} \frac{1}{\widehat{w}}\widehat{E}_{\text{domain}}(\widehat{m}_2^0,\widehat{w}) \sim -\widehat{h}_{\text{ext}}^3 \ln^2 \widehat{h}_{\text{ext}}.$$

b) The optimal inclination of the magnetization scales as

$$\widehat{m}_{2_a}^0(\widehat{h}_{\text{ext}}) \sim \widehat{h}_{\text{ext}} \ln \widehat{h}_{\text{ext}}.$$

c) The optimal period scales as

$$\widehat{w}_a(\widehat{h}_{\text{ext}}) \sim \widehat{h}_{\text{ext}} \ln \widehat{h}_{\text{ext}}.$$

d) For $\widehat{m}_2^0 \gg \widehat{w}$, the minimal energy per *period* scales as

$$\min_{\{(\widehat{m}_2^0)\,|\,\widehat{m}_2^0\gg\widehat{w}\}} \widehat{E}_{\text{domain}}(\widehat{m}_2^0,\widehat{w}) \sim -\widehat{h}_{\text{ext}}^2\widehat{w}^2 \ln(w^2 h_{\text{ext}}).$$

e) For fixed $\widehat{w}$ there exist no non-trivial minimizers $\widehat{m}_2^0 \geq \widehat{w}$ provided $\widehat{h}_{\text{ext}} \lesssim \widehat{w}\ln^{-1}\widehat{w}$.

Argument for the scaling behavior of a)-e). Observe that due to the constraint $\widehat{w} \leq \widehat{m}_2^0$ we have that

$$\tfrac{1}{\widehat{w}}\widehat{E}_{\text{domain}}(\widehat{m}_2^0,\widehat{w}) \gtrsim \tfrac{1}{4}\tfrac{\pi}{8}(\widehat{m}_2^0)^3 \ln^{-1}(m_2^0)^3 - \widehat{h}_{\text{ext}}(\widehat{m}_2^0)^2 + \widehat{h}_{\text{ext}}\widehat{w}^2.$$

Hence we obtain for $\widehat{w} \gg \widehat{h}_{\text{ext}} \ln \widehat{h}_{\text{ext}}$ and $\widehat{m}_2^0 \gg \widehat{h}_{\text{ext}} \ln \widehat{h}_{\text{ext}}$ the expression

$$\min_{(\widehat{w},\widehat{m}_2^0)} \tfrac{1}{\widehat{w}}\widehat{E}_{\text{domain}}(\widehat{m}_2^0,\widehat{w}) \gtrsim \widehat{h}_{\text{ext}}^3 \ln^2 \widehat{h}_{\text{ext}} \geq 0.$$

In order to prove a)-c), consider the following change of variables

$$\begin{aligned} \widehat{w} &= \widehat{h}_{\text{ext}}(\ln \widehat{h}_{\text{ext}})\,\widetilde{w}, \\ \widehat{m}_2^0 &= \widehat{h}_{\text{ext}}(\ln \widehat{h}_{\text{ext}})\,\widetilde{m}_2^0, \\ \widehat{E}_{\text{domain}} &= \widehat{h}_{\text{ext}}^4(\ln^3 \widehat{h}_{\text{ext}})\,\widetilde{E}_{\text{domain}}, \text{ and } \widehat{e} = \widehat{h}_{\text{ext}}^4(\ln^3 \widehat{h}_{\text{ext}})\,\widetilde{e}. \end{aligned} \tag{2.7}$$

For $\widetilde{m}_2^0$, $\widetilde{w} \sim 1$ and $\widehat{h}_{\text{ext}} \gg 1$, we have that $\ln \widehat{w}(\widehat{m}_2^0)^2 \approx 3\ln \widehat{h}_{\text{ext}}$ so that by (2.5)

$$\tfrac{1}{\widetilde{w}}\,\widetilde{e}(\widetilde{m}_2^0) \approx \tfrac{1}{\widetilde{w}}\tfrac{\pi}{24}(\widetilde{m}_2^0)^4,$$

and

$$\tfrac{1}{\widetilde{w}}\widetilde{E}_{\text{domain}}(\widetilde{m}_2^0,\widetilde{w}) = 2\left(1-\tfrac{\widetilde{w}}{\widetilde{m}_2^0}\right)\tfrac{1}{\widetilde{w}}\widetilde{e}(\widetilde{m}_2^0) + 4\,\tfrac{\widetilde{w}}{\widetilde{m}_2^0}\tfrac{1}{\widetilde{w}}\,\widetilde{e}\left(\tfrac{\widetilde{m}_2^0}{2}\right) - (\widetilde{m}_2^0)^2\left(1-\tfrac{\widetilde{w}}{\widetilde{m}_2^0}\right).$$

Hence, in the regime $\widehat{h}_{\text{ext}} \gg 1$ this change of variables leads to the parameter-free variational problem

$$\tfrac{1}{\widetilde{w}}\widetilde{E}_{\text{domain}}(\widetilde{m}_2^0,\widetilde{w}) \approx \tfrac{\pi}{24}\left(2\,\tfrac{(\widetilde{m}_2^0)^4}{\widetilde{w}} - \tfrac{7}{4}(\widetilde{m}_2^0)^3\right) - \left((\widetilde{m}_2^0)^2 - \widetilde{w}\,\widetilde{m}_2^0\right). \tag{2.8}$$

Due to the constraint $\widetilde{w} \leq \widetilde{m}_2^0$, we have

$$\tfrac{1}{\widetilde{w}}\widetilde{E}_{\text{domain}}(\widetilde{m}_2^0, \widetilde{w}) \gtrapprox \tfrac{\pi}{24}\tfrac{1}{4}(\widetilde{m}_2^0)^3 - (\widetilde{m}_2^0)^2 + \widetilde{w}^2, \tag{2.9}$$

so that that the energy is coercive. In particular

$$\liminf_{|(\widetilde{m}_2^0, \widetilde{w})| \to \infty} \tfrac{1}{\widetilde{w}}\widetilde{E}_{\text{domain}}(\widetilde{m}_2^0, \widetilde{w}) = +\infty.$$

On the other hand, $\frac{1}{\widetilde{w}}\widetilde{E}_{\text{domain}}$ assumes negative values for $0 < \widetilde{w} \ll \widetilde{m}_2^0 \lesssim 1$. Therefore we have $\min \frac{1}{\widetilde{w}}\widetilde{E}_{\text{domain}} \sim -1$. Finally we note that from (2.9) we have

$$\liminf_{\widetilde{m}_2^0 \to 0} \tfrac{1}{\widetilde{w}}\widetilde{E}_{\text{domain}}(\widetilde{m}_2^0, \widetilde{w}) \geq 0 \quad \text{uniformly in} \quad \widetilde{w}^2,$$

and from

$$\tfrac{1}{\widetilde{w}}\widetilde{E}_{\text{domain}}(\widetilde{m}_2^0, \widetilde{w}) \gtrapprox \tfrac{\pi}{24}\tfrac{1}{4}\tfrac{(\widetilde{m}_2^0)^4}{\widetilde{w}} - (\widetilde{m}_2^0)^2$$

we gather

$$\liminf_{\widetilde{w} \to 0} \tfrac{1}{\widetilde{w}}\widetilde{E}_{\text{domain}}(\widetilde{m}_2^0, \widetilde{w}) \geq 0 \quad \text{for fixed} \quad (\widetilde{m}_2^0)^4 > 0.$$

Therefore, $\min \frac{1}{\widetilde{w}}\widetilde{E}_{\text{domain}}$ is assumed for $\widetilde{m}_2^0 \sim 1$ and $\widetilde{w} \sim 1$.

Let us address d). For $\widehat{m}_2^0 \gg \widehat{w}$ we have that

$$\widehat{E}_{\text{domain}}(\widehat{m}_2^0, \widehat{w}) \approx 2\widehat{e}(\widehat{m}_2^0) - \widehat{h}_{\text{ext}}(\widehat{m}_2^0)^2\widehat{w}.$$

The rescaling

$$\begin{aligned} \widehat{m}_2^0 &= (\widehat{w}\,\widehat{h}_{\text{ext}} \ln(w^2 h_{\text{ext}}))^{1/2}\widetilde{m}_2^0, \\ \widehat{E}_{\text{domain}} &= \widehat{h}_{\text{ext}}^2\widehat{w}^2 \ln(w^2 h_{\text{ext}})\widetilde{E}_{\text{domain}}, \end{aligned}$$

leads to a parameter-free minimization problem

$$\widetilde{E}_{\text{domain}}(\widetilde{m}_2^0) = 2\widetilde{e}(\widetilde{m}_2^0) - (\widetilde{m}_2^0)^2$$

in $\widetilde{m}_2^0$. Obviously $\widetilde{E}_{\text{domain}}$ is coercive and assumes negative values for $\widetilde{m}_2^0 \sim 1$. Moreover we have that $\lim_{\widetilde{m}_2^0 \to 0} \widetilde{E}_{\text{domain}} \geq 0$. Hence in the regime $\widehat{m}_2^0 \gg \widehat{w}$ the minimal energy is achieved for

$$\widehat{m}_2^0 \sim (\widehat{w}\,\widehat{h}_{\text{ext}} \ln(w^2 h_{\text{ext}}))^{1/2},$$

in which case

$$\min_{\widehat{m}_2^0 \gg \widehat{w}} \widehat{E}_{\text{domain}}(\widehat{m}_2^0, \widehat{w}) \sim -\widehat{h}_{\text{ext}}^2\widehat{w}^2 \ln(w^2 h_{\text{ext}}).$$

Finally, e) can best be seen using the rescaling

$$\begin{aligned} \widehat{h}_{\text{ext}} &= \widehat{w} \ln^{-1} \widehat{w}\,\widetilde{h}_{\text{ext}}, \\ \widehat{m}_2^0 &= \widehat{w}\,\widetilde{m}_2^0, \\ \widehat{E}_{\text{domain}} &= \widehat{w}^4 \ln^{-1} \widehat{w}\widetilde{E}_{\text{domain}}. \end{aligned}$$

which leads to the minimization problem

$$\widetilde{E}_{\text{domain}}(\widetilde{m}_2^0) \approx \tfrac{\pi}{24}\big(2\,(\widetilde{m}_2^0)^4 - \tfrac{7}{4}(\widetilde{m}_2^0)^3\big) - h_{\text{ext}}\big((\widetilde{m}_2^0)^2 - \widetilde{m}_2^0\big),$$

under the constraint $\widetilde{m}_2^0 \geq 1$. For $h_{\text{ext}} \geq 0$ there exists exactly one positive (local) minimizer of the energy. The amplitude of the minimizer decreases as $\widetilde{h}_{\text{ext}}$ decreases from large positive values. An explicit minimization shows that at $\widetilde{h}_{\text{ext}} = \frac{11}{96}\pi$ the minimal amplitude $\widetilde{m}_2^0$ drops below one.

2.3. Extensions of domain theory

The concertina in the experiments is far from being uniform and one occasionally displays certain sub-structures. We therefore now discuss several possible generalizations of the uniform concertina Ansatz within domain theory. In particular we try to include modulations.

2.3.1. Tilted Ansatz

In the prior section we have seen that the minimal energy per period is concave for periods much smaller than the optimal period, i.e., $\widehat{w} \ll \widehat{h}_{\text{ext}} \ln \widehat{h}_{\text{ext}}$. We now show that, although domain theory predicts a modulation instability, it is too rigid to allow for such perturbations. Note that for any weak solution of the Burgers equation we have conservation of the following quantity

$$I = \int_0^1 \widehat{m}_2^2 \,\mathrm{d}\widehat{x}_2, \quad \text{more precisely} \quad \tfrac{\mathrm{d}}{\mathrm{d}x_1} I(x_1) = 0. \tag{2.10}$$

This can easily be seen by integrating the Burgers equation w.r.t. $\widehat{x}_2$ and using the zero boundary conditions at $\widehat{x}_2 \in \{0, 1\}$.

We want to extend the set of uniform piecewise constant Ansatz functions to piecewise constant Ansatz functions with possibly different values of $\widehat{m}_2^1$ and $\widehat{m}_2^2$ in the quadrangular domains of different width as depicted in Figure 2.2.
A particular consequence of (2.1) is that if we choose specific values $\widehat{m}_2^1$ and $\widehat{m}_2^2$ and the width of the fold $A_2 - A_1$, then all the angles and the two triple points A_0 and A_3 are fixed. Therefore we can either choose the amplitude or the width of the adjacent facet for the continuation of the pattern due to the conservation of I.

2.3.2. Rigidity of domain theory

In this part we will see that a concertina of period $\widehat{w} - \varepsilon$ with its optimal amplitude cannot be connected within the class of generalized Ansatz functions to a concertina of period $\widehat{w} + \varepsilon$ with its optimal amplitude, cf. Figure 2.3. Thus domain theory is too rigid to take into account modulations.

Let $\widehat{w} - \varepsilon$ be the period of the spatially uniform state on the left side and $\widehat{w} + \varepsilon$ on the right side in Figure 2.3. According to statement d) in Section 2.2 the minimal

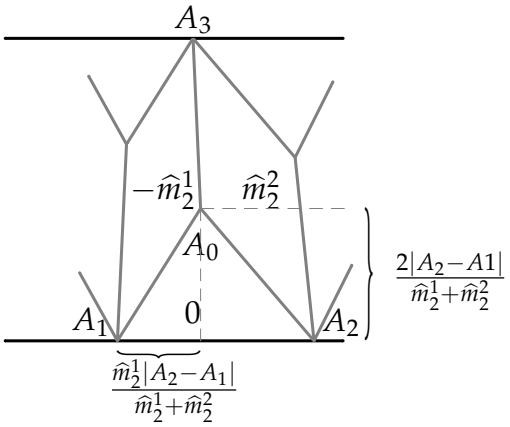

Figure 2.2.: Domain Theory: Generalized Ansatz function. Observe that $\widehat{m}_2^2 > \widehat{m}_2^1$ leads to a tilt of the vertical wall towards the quadrangular domain with $\widehat{m}_2 = \widehat{m}_2^1$. The slope of the diagonal walls is inversely proportional to the amplitude of the neighboring quadrangular domain.

energy per period (and therefore the Zeeman energy per period) scales up to a logarithm as $-\widehat{h}_{\text{ext}}(\widehat{w}-\varepsilon)^2$ and $-\widehat{h}_{\text{ext}}(\widehat{w}+\varepsilon)^2$, respectively. The Zeeman energy density thus scales as $-h_{\text{ext}}I = -h_{\text{ext}}\int \widehat{m}_2^2\,\mathrm{d}\widehat{x}_2 = -\widehat{h}_{\text{ext}}(w-\varepsilon)$ and $-h_{\text{ext}}I = -\widehat{h}_{\text{ext}}(\widehat{w}+\varepsilon)$, respectively. This is in contradiction to the fact that I has to be conserved along $\widehat{x}_1$.

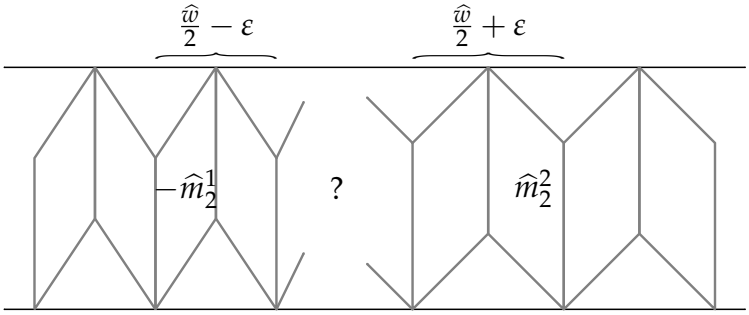

Figure 2.3.: A modulation is not compatible with domain theory.

2.3.3. Refining

Based on domain theory, we can also study the backward hysteresis: After several coarsening steps and before the concertina disappears, we decrease the strength of the external field. As a consequence, the transversal component decreases. The periodic concertina pattern degenerates as $\widehat{m}_2^0$ approaches $\widehat{w}$. Due to statement e) at the beginning of Section 2.2 this happens at a field $\widehat{h}_{\text{ext}} \sim \widehat{w}\ln^{-1}\widehat{w}$.

Kite-like perturbation. In the experiments, one sometimes observes the formation of a certain substructure before the concertina degenerates. In the following, we try to include such type of configurations in the class of admissible Ansatz functions of domain theory, cf. Figure 2.5.

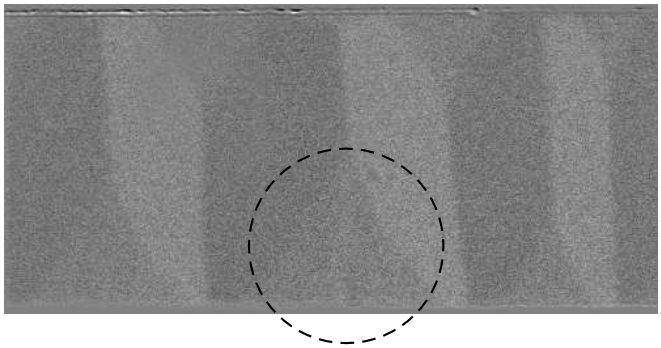

Figure 2.4.: Experiments: Kite-like substructure of the concertina which arises in the coarsened concertina as the external field is reduced (CoFeB sample of thickness 30 nm and width 30 µm).

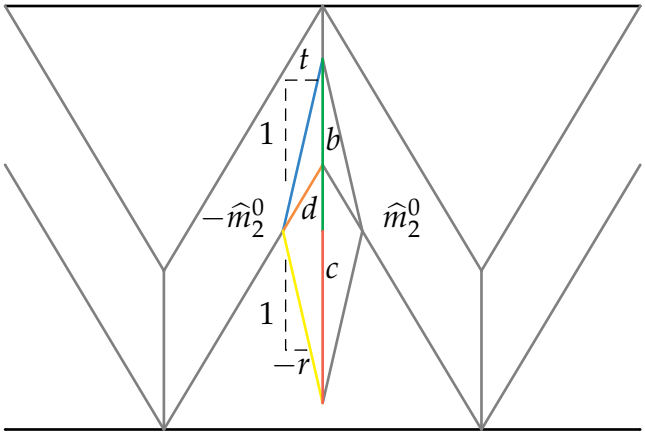

Figure 2.5.: Domain Theory: Kite-like perturbation. The slope of the diagonal wall indicated by the dashed triangle.

The substructure has the form of a kite with values $\pm\widehat{m}_2^1$ in its two triangular facets. For the stability analysis, we only have to determine the loss and gain in wall energy since the Zeeman energy is invariant due to the conservation of I, see (2.10). Let $a = b + c$ be the length of the vertical wall of the kite. Then all angles are fixed by the jump condition if we prescribe the value of $\widehat{m}_2 = \pm\widehat{m}_2^1$ in the two facets. We set

$$s = \tfrac{1}{2}\widehat{m}_2^0, \qquad r = \tfrac{1}{2}\widehat{m}_2^1, \qquad t = \tfrac{1}{2}(\widehat{m}_2^0 - \widehat{m}_2^1).$$

Let b be the length of the upper green component and c the length of the lower red component of a, and d be the length of the $\widehat{x}_2$-projection of the orange diagonal wall. A straight-forward calculation shows that $b = a\frac{r}{s}$, $c = a\frac{t}{s}$ and $d = a\frac{rt}{s^2}$.

Due to the shear invariance of the energy, the wall energy of a diagonal wall is given by the energy of the symmetric wall of equal jump size multiplied by the length of the $\widehat{x}_2$-projection of the diagonal wall, cf. (2.4). The kite perturbation introduces

- a vertical wall of length $a = b + c$ and jump size $2\widehat{m}_2^1$, leading to a contribution $a\widehat{e}(\widehat{m}_2^1)$,
- two times the blue wall of (projected) length b and jump size $\widehat{m}_1^0 - \widehat{m}_2^1$, leading to a contribution $2b\,\widehat{e}(\frac{\widehat{m}_2^0 - \widehat{m}_2^1}{2})$,
- two times the yellow wall of (projected) length c and jump size $\widehat{m}_2^1$, leading to a contribution $2c\,\widehat{e}(\frac{\widehat{m}_2^1}{2})$.
- The vertical wall decreases by the length of the green part $b - d$ leading to a contribution $-(b-d)\,\widehat{e}(\widehat{m}_2^0)$.
- The diagonal wall decreases by the (projected) length of the orange part d leading to a contribution $-2d\widehat{e}(\frac{\widehat{m}_2^0}{2})$.

Summing up, we obtain that the loss and gain in wall energy is given by

$$\begin{aligned}\Delta\widehat{E}_{\text{wall}} &= a\widehat{e}(\widehat{m}_2^1) + 2b\,\widehat{e}(\tfrac{\widehat{m}_2^0 - \widehat{m}_2^1}{2}) + 2c\,\widehat{e}(\tfrac{\widehat{m}_2^1}{2}) - (b-d)\widehat{e}(\widehat{m}_2^0) - 2d\widehat{e}(\tfrac{\widehat{m}_2^0}{2}) \\ &= a\widehat{e}(\widehat{m}_2^1) + 2a\tfrac{r}{s}\,\widehat{e}(\tfrac{\widehat{m}_2^0 - \widehat{m}_2^1}{2}) + 2a\tfrac{t}{s}\,\widehat{e}(\tfrac{\widehat{m}_2^1}{2}) - a\tfrac{r^2}{s^2}\widehat{e}(\widehat{m}_2^0) - 2a\tfrac{rt}{s^2}\widehat{e}(\tfrac{\widehat{m}_2^0}{2}).\end{aligned}$$

Hence up to a logarithm we obtain to leading order

$$\begin{aligned}\Delta\widehat{E}_{\text{wall}} &= a\pi(2r^4 + \tfrac{r}{8s}t^4 + \tfrac{t}{8s}r^4 - 2\tfrac{r^2}{s^2}s^4 - \tfrac{rt}{8s^2}s^4) \\ &= a\pi r^2(\tfrac{13r^2}{8} + \tfrac{3rs}{4} - \tfrac{19s^2}{8}) \\ &\leq 0,\end{aligned}$$

since $r \leq s$. Note that this estimate is strict, i.e., $\Delta\widehat{E}_{\text{wall}} < 0$ for $r < s$ and $\Delta\widehat{E}_{\text{wall}} = 0$ for $r = s$. A kite-like perturbation thus always decreases the energy. Since $\Delta\widehat{E}_{\text{wall}}$ is linear in a the perturbation should be such that the kite hits the boundary $\widehat{x}_2 = 0$.

An instability of that type of the coarsened concertina pattern as $\widehat{h}_{\text{ext}}$ decreases could not be observed in the numerical simulations. Up to the turning point, at which the quadrangular folds (almost) degenerate, the concertina pattern is stable. This seems contradictory in the first place but the finite width of the walls is related to energy barriers which domain theory does not take into account. However, if we numerically follow the branch beyond the turning point, a kite-like structure develops. This structure grows into a concertina of one-third the period of the original pattern. Although this transition is observed on the unstable part of the branch, it can be suspected that such states are stabilized in the experiments due to inhomogeneities and defects.

2.4. Charged walls

In the previous sections it was shown that the class of Ansatz functions within domain theory is quite rigid. Another extension of domain theory might be related to the fact that the diagonal walls are not charge-free on a mesoscopic scale. However, this question is beyond the scope of our work and will be addressed in the future.

2.5. Minimality and stability for moderate uniaxial anisotropy

In this section, we study the effect of a moderate uniaxial anisotropy $Q \gg \ell^{-1}t$ within the framework of domain theory. We restrict the analysis to the most interesting case of transversal anisotropy $Q > 0$. Due to the shift of the critical field, it is necessary to include the next order term in the Zeeman energy if we take into account a non-zero anisotropy. The analysis hence relies on the *unrescaled* domain theoretic energy, namely

$$E_{\text{domain}}(m_2^0, w) = 2\big(\ell - \tfrac{w}{m_2^0}\big)e(m_2^0) + 4\,\tfrac{w}{m_2^0}\,e\left(\tfrac{m_2^0}{2}\right) \\ - (h_{\text{ext}} + Q)(m_2^0)^2 tw\big(\ell - \tfrac{w}{m_2^0}\big) - h_{\text{ext}}(m_2^0)^4 tw\big(\ell - \tfrac{w}{m_2^0}\big).$$

In order to simplify the following discussions we neglect the logarithm in the energy density of the Néel wall, i.e., we consider $e(m_2^0) = \frac{\pi}{8}t^2(m_2^0)^4$. As discussed in the introduction, for moderate uniaxial anisotropy the critical field is given by $h_{\text{ext}} \approx -Q$. Since the energy looses coercivity for $h_{\text{ext}} > 0$ – and hence m_2^0 tends to infinity so that the low-angle approximation is not valid anymore and the pattern is suspected to collapse – we assume in the following that h_{ext} varies between $-Q$ and 0.

We will see in this section that for small external fields, i.e., $0 < 1 + Q^{-1}h_{\text{ext}} \ll (Q^{-1}\ell^{-1}t)^2$, the optimal inclination of the concertina is dominated by the competition between stray-field and Zeeman energy. For large fields $0 < (Q^{-1}\ell^{-1}t)^2 \ll 1 + Q^{-1}h_{\text{ext}} \ll 1$ it is dominated by the competition between the bulk energies, i.e., anisotropy and Zeeman energy. Nevertheless, the optimal period is determined by the competition between stray-field and bulk energy in both cases, though the related contribution is of lower order for large fields. We will see that for large fields the minimal energy per period becomes convex. It is not surprising that we verify the statement above on the basis of an appropriate rescaling, see below:

Scenario I: Regime of dominant stray-field energy.
Let $Q \gg \ell^{-1}t$. For $0 \le 1 + Q^{-1}h_{\text{ext}} \ll (Q^{-1}\ell^{-1}t)^2$
a) the optimal inclination of the magnetization scales as

$$m_{2_a}^0 \sim \ell t^{-1} Q(1 + Q^{-1}h_{\text{ext}}),$$

b) the optimal period scales as

$$w_a \sim \ell^2 t^{-1} Q(1 + Q^{-1}h_{\text{ext}}),$$

c) for $w \ll w_a \sim \ell^2 t^{-1} Q(1 + Q^{-1}h_{\text{ext}})$ the minimal energy per *period* is concave.

Note that these are just the rescaled statements with h_{ext} shifted to $h_{\text{ext}} + Q$ from the beginning of Section 2.2. Hence, besides the shift of the field, minimizers in the regime $0 \le 1 + Q^{-1}h_{\text{ext}} \ll (Q^{-1}\ell^{-1}t)^2$ are of the same form as in the case of zero anisotropy, cf. Section 2.2.

Statements a) and b) can be seen using the rescaling

$$\begin{aligned} m_2^0 &= \ell t^{-1} Q(1+Q^{-1}h_{\text{ext}})\,\widetilde{m}_2^0,\\ w &= \ell^2 t^{-1} Q(1+Q^{-1}h_{\text{ext}})\,\widetilde{w},\\ E_{\text{domain}} &= Q^4(1+Q^{-1}h_{\text{ext}})^4 \ell^5 t^{-2}\,\widetilde{E}_{\text{domain}}. \end{aligned}$$

In fact, the rescaled energy per length is given by

$$\tfrac{1}{\widetilde{w}}\widetilde{E}_{\text{domain}} = \tfrac{\pi}{8}\big(2\,\tfrac{(\widetilde{m}_2^0)^4}{\widetilde{w}} - \tfrac{7}{4}(\widetilde{m}_2^0)^3\big) - \big((\widetilde{m}_2^0)^2 - \widetilde{w}\,\widetilde{m}_2^0\big) + \varepsilon(\widetilde{m}_2^0)^2\big((\widetilde{m}_2^0)^2 - \widetilde{w}\,\widetilde{m}_2^0\big),$$

where in this case $\varepsilon = -Q^{-1}h_{\text{ext}}(Q^{-1}h_{\text{ext}}+1)(Q\ell t^{-1})^2$. Notice that in the regime considered, we have that $-Q \le h_{\text{ext}} \lesssim -Q + \ell^{-2}t^2Q^{-1}$, so that $0 < \varepsilon \ll 1$.

In order to see a) and b), observe that the fourth order (in $\widetilde{m}_2^0$) bulk contribution amounts to a lower order (positive) perturbation of the rescaled energy functional so that the arguments from the beginning of Section 2.2 carry over. Statement c) can best be seen on the level of the rescaling

$$m_2^0 = (wt^{-1}Q(1+Q^{-1}h_{\text{ext}}))^{1/2}\widetilde{m}_2^0.$$

We note that again the quartic bulk contribution is of higher order.

Scenario II: Regime of dominant bulk energy.
Let $Q \gg \ell t^{-1}$. In the regime $0 < (Q^{-1}\ell^{-1}t)^2 \ll 1 + Q^{-1}h_{\text{ext}} \ll 1$ we have that
a) the optimal inclination of the magnetization scales as

$$m_{2_a}^0 \sim (1+Q^{-1}h_{\text{ext}})^{1/2},$$

b) the optimal period scales as

$$w_a \sim (\ell t)^{1/2}Q^{-1/2}(1+Q^{-1}h_{\text{ext}})^{1/4},$$

c) for $tQ^{-1} \ll w \le w_a \sim (\ell t)^{1/2}Q^{-1/2}(1+Q^{-1}h_{\text{ext}})^{1/4}$ the minimal energy per period is convex.

Consider the rescaling

$$\begin{aligned} m_2^0 &= (1+Q^{-1}h_{\text{ext}})^{1/2}(-Q^{-1}h_{\text{ext}})^{-1/2}\,\widetilde{m}_2^0,\\ w &= (\ell t)^{1/2}Q^{-1/2}(1+Q^{-1}h_{\text{ext}})^{1/4}(-Q^{-1}h_{\text{ext}})^{-3/4}\,\widetilde{w},\\ E_{\text{domain}} &= (1+Q^{-1}h_{\text{ext}})^{9/4}(-Q^{-1}h_{\text{ext}})^{-7/4}(\ell t)^{3/2}Q^{1/2}\,\widetilde{E}_{\text{domain}}. \end{aligned}$$

Hence the rescaled energy per period is given by

$$\begin{aligned} \tfrac{1}{\widetilde{w}}\widetilde{E}_{\text{domain}}(\widetilde{m}_2^0,\widetilde{w},\varepsilon) = \tfrac{\pi}{8}\big(2\tfrac{\varepsilon}{\widetilde{w}}\,(\widetilde{m}_2^0)^4 - \tfrac{7}{4}\varepsilon^2(\widetilde{m}_2^0)^3\big)\\ - \big((\widetilde{m}_2^0)^2 - \varepsilon\widetilde{w}\,\widetilde{m}_2^0\big) + (\widetilde{m}_2^0)^2\big((\widetilde{m}_2^0)^2 - \varepsilon\widetilde{w}\,\widetilde{m}_2^0\big), \end{aligned} \quad (2.11)$$

where

$$\varepsilon = (Q\ell t^{-1})^{-1/2}(1+Q^{-1}h_{\text{ext}})^{-1/4}(-Q^{-1}h_{\text{ext}})^{-1/4}.$$

Observe that $1+Q^{-1}h_{\text{ext}} \ll 1$ entails that $-Q \leq h_{\text{ext}} \leq -\frac{1}{C}$ for some $C>1$. Hence in the regime $0 < (Q^{-1}\ell^{-1}t)^2 \ll 1+Q^{-1}h_{\text{ext}} \ll 1$ we have that $\varepsilon \ll 1$. For the same reason $\widetilde{w} \sim 1$ implies $w \sim (\ell t)^{1/2}Q^{-1/2}(1+Q^{-1}h_{\text{ext}})^{1/4}$. Notice that the constraint $w \leq m_2^0$ turns into $\varepsilon\widetilde{w} \leq \widetilde{m}_2^0$. Obviously, for $\widetilde{m}_2^0 \geq 1$ or $\varepsilon\widetilde{w} = \widetilde{m}_2^0$

$$\tfrac{1}{\widetilde{w}}\widetilde{E}_{\text{domain}}(\widetilde{m}_2^0, \widetilde{w}, \varepsilon) \geq 0.$$

For $\widetilde{m}_2^0 \leq 1$ we find by neglecting the positive wall energy

$$\begin{aligned}\tfrac{1}{\widetilde{w}}\widetilde{E}_{\text{domain}}(\widetilde{m}_2^0, \widetilde{w}, \varepsilon) &\geq -(\widetilde{m}_2^0)^2 + (\widetilde{m}_2^0)^4 + \varepsilon\widetilde{w}\,\widetilde{m}_2^0(1-(\widetilde{m}_2^0)^2)\\ &\geq -(\widetilde{m}_2^0)^2 + (\widetilde{m}_2^0)^4.\end{aligned}$$

On the other hand, the energy assumes negative values ~ -1 for $1 \sim \widetilde{m}_2^0$ and $\widetilde{w} \sim 1$. For fixed $\widetilde{m}_2^0 \leq 1$ we can minimize the energy w.r.t. $\widetilde{w}$ and obtain

$$\widetilde{w}_a(\widetilde{m}_2^0) = \frac{(\widetilde{m}_2^0)^4}{\widetilde{m}_2^0 - (\widetilde{m}_2^0)^3}.$$

Let us assume that the optimal amplitude can – up to higher order terms – be expanded in the following way:

$$\widetilde{m}_2^0(\widetilde{w}, \varepsilon) = \operatorname*{argmin}_{\{\widetilde{m}_2^0 | \widetilde{m}_2^0 \geq \varepsilon\widetilde{w}\}} \widetilde{E}_{\text{domain}}(\widetilde{m}_2^0, \widetilde{w}, \varepsilon) \approx \widetilde{m}_2^0(\widetilde{w}, 0) + \varepsilon\partial_\varepsilon\widetilde{m}_2^0(\widetilde{w}, 0). \tag{2.12}$$

Obviously we have due to (2.11) that

$$\widetilde{m}_2^0(\widetilde{w}, 0) = 2^{-1/2}.$$

Moreover we obtain that

$$\partial_\varepsilon\widetilde{m}_2^0(\widetilde{w}, 0) = -\tfrac{\pi}{4\widetilde{w}}2^{-3/2} + \tfrac{\widetilde{w}}{8}.$$

Let us plug (2.12) into (2.11), then

$$\begin{aligned}\frac{1}{\widetilde{w}}\widetilde{E}_{\text{domain}}(\widetilde{m}_2^0(\widetilde{w}, \varepsilon), \widetilde{w}, \varepsilon) &\approx \frac{1}{\widetilde{w}}\widetilde{E}_{\text{domain}}(\widetilde{m}_2^0(\widetilde{w}, 0), \widetilde{w}, 0)\\ &\quad + \Big(\partial_{\widetilde{m}_2^0}(\tfrac{1}{\widetilde{w}}\widetilde{E}_{\text{domain}})(\widetilde{m}_2^0(\widetilde{w}, 0), \widetilde{w}, 0)\partial_\varepsilon\widetilde{m}_2^0(\widetilde{w}, 0)\\ &\quad + \partial_\varepsilon(\tfrac{1}{\widetilde{w}}\widetilde{E}_{\text{domain}})(\widetilde{m}_2^0(\widetilde{w}, 0), \widetilde{w}, 0)\Big)\varepsilon\\ &= -\tfrac{1}{4} + \left(\tfrac{\pi}{16\widetilde{w}} + \tfrac{\widetilde{w}}{2^{3/2}}\right)\varepsilon,\end{aligned} \tag{2.13}$$

where we used that $\partial_{\widetilde{m}_2^0}(\frac{1}{\widetilde{w}}\widetilde{E}_{\text{domain}})(\widetilde{m}_2^0(\widetilde{w}, 0)\widetilde{w}, 0) = 0$. We read off that the optimal period is given by $\widetilde{w}_a = \pi^{1/2}2^{-5/4}$ (up to higher order terms). This is consistent with

the constraint $\varepsilon\widetilde{w} \leq \widetilde{m}_2^0$. Summing up, this establishes a) and b). Let us now address c): From (2.13) we derive that the minimal energy per period scales as

$$\widetilde{E}_{\text{domain}}(\widetilde{m}_2^0(\widetilde{w},\varepsilon)\widetilde{w},\varepsilon) \approx -\tfrac{\widetilde{w}}{4} + \left(\tfrac{\pi}{16} + \tfrac{\widetilde{w}^2}{2^{3/2}}\right)\varepsilon.$$

This is to order zero (in ε) linear in $\widetilde{w}$ and to first order convex in the period $\widetilde{w}$. We note that on the level of the rescaled variables $tQ^{-1} \ll w \leq w_a \sim (\ell t)^{1/2}Q^{-1/2}(1 + Q^{-1}h_{\text{ext}})^{1/4}$ turns into $\varepsilon \ll \widetilde{w} \leq 1$ which entails that the quadratic (in ε) contribution in the latter expansion is indeed of higher order.

Formation and coarsening of the concertina in a film of moderate uniaxial transversal anisotropy. In the previous section we derived the scaling behavior of the optimal and marginal stable period and the optimal amplitude of the transversal component. Figure 2.6 provides an interpretation of the results: As the external field increases from the critical field, domain theory is applicable once the amplitude of the magnetization is of the order $d^{2/3}\ell^{-1/2}t^{-1/3}$, so that $\widehat{m}_2^0 \sim 1$, $\widehat{h}_{\text{ext}} \sim 1$. At that point, we enter Scenario I: As the field increases the optimal inclination increases. Domain theory predicts a modulation instability due to the concavity of the minimal energy per period, once the period is much smaller than the optimal period. The concertina coarsens, so its period increases towards the optimal period. As the field increases further we enter Scenario II. The period of the concertina at that point is of the order tQ^{-1}. Since the minimal energy per period for periods much smaller than the optimal period is convex, the coarsening stops. Only the inclination grows.

Consistency. In the following part, the consistency of the predictions derived above with the underlying assumptions for the applicability of domain theory is checked. On the one hand, there is the assumption of scale separation between the x_1 and x_2 variable, i.e., $w \ll \ell$, and the low-angle approximation for $m_2^0 \ll 1$ which both stem from the reduced model. On the other hand, domain theory itself is a good approximation of the reduced energy and applicable provided $h_{\text{ext}} + Q \gg d^{2/3}\ell^{-4/3}t^{2/3}$. At the cross-over between Scenario I and II we expect that the period of the concertina pattern is of the order $w \sim tQ^{-1}$ and that the transversal component is of the order $m_2 \sim t(\ell Q)^{-1}$. In the regime of moderate anisotropy $Q \gg \ell^{-1}t$, this is consistent with the assumptions of the reduced model, i.e., the low-angle approximation and the scale separation, since $tQ^{-1} \ll \ell$ and $t(\ell Q)^{-1} \ll 1$. Note that m_2 tends towards one in Scenario II which displays the limitation of the model as h_{ext} tends towards 0. Observe that for strong anisotropy $Q \gg d^{-2/3}\ell^{-2/3}t^{4/3}$, Scenario I disappears and we expect no coarsening at all. In fact, in that case the distance between the two characterizing fields $-Q + d^{2/3}t^{2/3}\ell^{-2/3}$ and $-Q + t^2\ell^{-2}Q^{-1}$ shrinks to zero. This is consistent with the bifurcation analysis close to the critical field which predicts stability of w^*-periodic states for strong transversal anisotropy, see Figure 6.3.

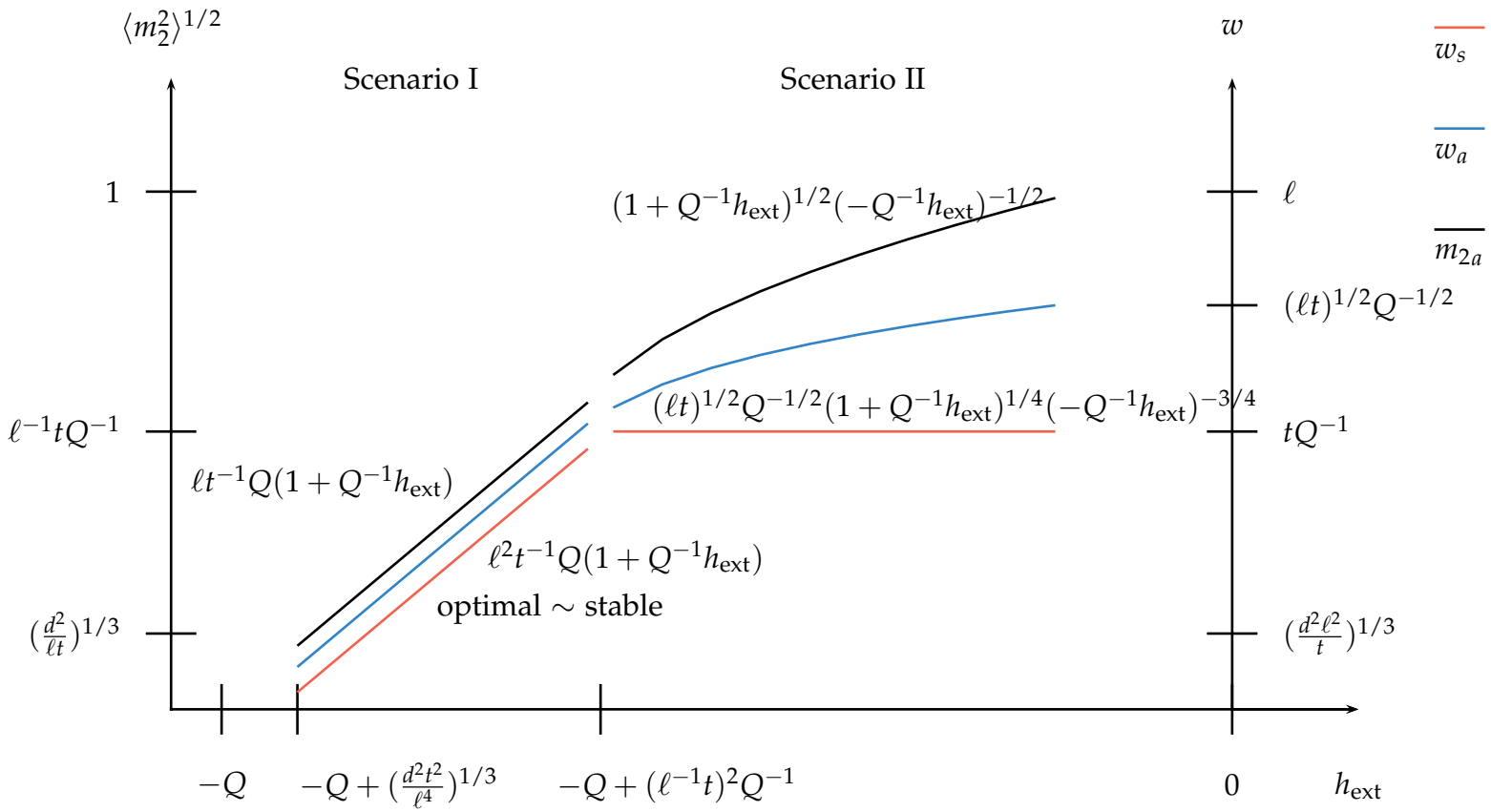

Figure 2.6.: Scaling behavior of the optimal and marginal stable period and the amplitude of the transversal component in the regime $t\ell^{-1} \ll Q \ll d^{-2/3}\ell^{-2/3}t^{4/3}$.

3

Analysis of the reduced energy for large external field

In Chapter 2, we argue one the level of domain theory that for $\widehat{h}_{\text{ext}} \gg 1$

a) the minimal energy per length in $\widehat{x}_1$-direction scales as $-\widehat{h}_{\text{ext}}^3 \ln^2 \widehat{h}_{\text{ext}}$,

b) the optimal inclination of the magnetization scales as $\widehat{m}_2^0 \sim \widehat{h}_{\text{ext}} \ln \widehat{h}_{\text{ext}}$, and

c) the optimal period scales as $\widehat{w}_{opt} \sim \widehat{h}_{\text{ext}} \ln \widehat{h}_{\text{ext}}$.

These results were first published in [OS10]. We point out that c) is the explanation why a larger period is preferred for a stronger external field, as observed in the experiments and the numerical simulations.

Until now there is no rigorous derivation of domain theory. In the following, we rigorously prove the above predictions by domain theory starting from the reduced energy $\widehat{E}_0$ and show in addition that global minimizers are close to weak solutions of Burgers' equation. Theorem 3.1 below addresses: a) the scaling behavior of the minimal energy and b) the scaling behavior of the average inclination of minimizing magnetizations. Estimate c1), which amounts to a control of a fractional derivative of $\widehat{m}_2$ in direction $\widehat{x}_1$ in the L^2-norm by the L^2-norm of $\widehat{m}_2$, shows that – on average – there cannot be substantial oscillations of $\widehat{m}_2$ in $\widehat{x}_1$ on length scales $\ll \widehat{h}_{\text{ext}} \ln \widehat{h}_{\text{ext}}$. In this sense, it confirms the heuristically produced scaling of the optimal period as a lower bound. On the other hand, estimate c2), which controls averages of $\widehat{m}_2$ in $\widehat{x}_1$ in the L^1-norm by $\widehat{m}_2$ itself in the L^2-norm, shows that – on average – there has to be substantial cancellations on length scales $\gg \widehat{h}_{\text{ext}} \ln \widehat{h}_{\text{ext}}$. In this sense, c2) confirms the predicted scaling as an upper bound. All statements include the logarithm.

3.1. Main results

Theorem 3.1. *Let $\widehat{h}_{\text{ext}} \gg 1$ and $\widehat{L} \geq \widehat{h}_{\text{ext}} \ln h_{\text{ext}}$. Then for $\widehat{E}_0$ as in (1.14) and $\widehat{m}_2$ as in (1.15):*

a) The minimal energy per length scales as

$$\min_{\widehat{m}_2} \widehat{L}^{-1} \widehat{E}_0 \sim -\widehat{h}_{\text{ext}}^3 \ln^2 \widehat{h}_{\text{ext}}.$$

b) Let $\widehat{m}_2$ *with* $\widehat{L}^{-1}\widehat{E}_0(\widehat{m}_2) \sim \min_{\widehat{m}_2} \widehat{L}^{-1}\widehat{E}_0$*, then*

$$\widehat{A}^2 := \widehat{L}^{-1} \int_0^{\widehat{L}} \int_0^1 \widehat{m}_2^2 \,\mathrm{d}\widehat{x}_2 \,\mathrm{d}\widehat{x}_1 \sim \widehat{h}_{\mathrm{ext}}^2 \ln^2 \widehat{h}_{\mathrm{ext}}.$$

c1) For and any shift $\widehat{w} > 0$ *in* $\widehat{x}_1$*-direction we have*

$$\widehat{L}^{-1} \int_0^{\widehat{L}} \int_0^1 (\widehat{m}_2(\widehat{x}_1 + \widehat{w}, \widehat{x}_2) - \widehat{m}_2(\widehat{x}_1, \widehat{x}_2))^2 \,\mathrm{d}\widehat{x}_2 \,\mathrm{d}\widehat{x}_1 \lesssim \left(\frac{\widehat{w}}{\widehat{h}_{\mathrm{ext}} \ln \widehat{h}_{\mathrm{ext}}}\right)^{\alpha} \widehat{A}^2,$$

for $\alpha \in [0, \frac{2}{5})$*.*

c2) Let $(\widehat{m}_2)_{\widehat{w}}$ *denote the mean of* $\widehat{m}_2$ *in* $\widehat{x}_1$*-direction over intervals of size* $\widehat{w}$*, i.e., for any* $\widehat{L}$*-periodic* $f(\widehat{x}_1, \widehat{x}_2)$*, i.e.,* $f_{\widehat{w}}(\widehat{x}_1, \widehat{x}_2) := \widehat{w}^{-1} \int_{-\frac{\widehat{w}}{2}}^{\frac{\widehat{w}}{2}} f(\widehat{x}_1 + \widehat{x}_1', \widehat{x}_2) \,\mathrm{d}\widehat{x}_1'$*. Then for any* $\widehat{w} > 0$ *we have*

$$\widehat{L}^{-1} \int_0^{\widehat{L}} \int_0^1 |(\widehat{m}_2)_{\widehat{w}}(\widehat{x}_1, \widehat{x}_2)| \,\mathrm{d}\widehat{x}_2 \,\mathrm{d}\widehat{x}_1 \lesssim \left(\frac{\widehat{h}_{\mathrm{ext}} \ln \widehat{h}_{\mathrm{ext}}}{\widehat{w}}\right)^{1/2} A.$$

Remark 3.2. *Instead of a separate definition for the asymptotic relations* $\sim, \lesssim$ *and so forth, we explain their meaning in the context of Theorem 3.1:*

There exist universal constants $1 \leq C, C_a, C_{b_1}, C_{b_2} < +\infty$ *such that for all* $\widehat{h}_{\mathrm{ext}} \geq C$ *and all* $\widehat{L} \geq \widehat{h}_{\mathrm{ext}} \ln \widehat{h}_{\mathrm{ext}}$*:*

a) The minimal energy per length can be bounded by

$$-C_a \widehat{h}_{\mathrm{ext}}^3 \ln^2 \widehat{h}_{\mathrm{ext}} \leq \min_{\widehat{m}_2} \widehat{L}^{-1}\widehat{E}_0 \leq -\frac{1}{C_a} \widehat{h}_{\mathrm{ext}}^3 \ln^2 \widehat{h}_{\mathrm{ext}}.$$

b) Let $\widehat{m}_2$ *with* $\widehat{L}^{-1}\widehat{E}_0(\widehat{m}_2) \leq \frac{1}{C_{b1}} \min_{\widehat{m}_2} \widehat{L}^{-1}\widehat{E}_0$*. Then we have*

$$\frac{1}{C_{b_1}} \widehat{h}_{\mathrm{ext}}^2 \ln^2 \widehat{h}_{\mathrm{ext}} \leq \widehat{A}^2 := \widehat{L}^{-1} \int_0^{\widehat{L}} \int_0^1 \widehat{m}_2^2 \,\mathrm{d}\widehat{x}_2 \,\mathrm{d}\widehat{x}_1 \leq C_{b_2} \widehat{h}_{\mathrm{ext}}^2 \ln^2 \widehat{h}_{\mathrm{ext}}.$$

c1) For any $\alpha \in [0, \frac{2}{5})$ *there exists* $C_\alpha > 0$ *such that for any* $\widehat{w} > 0$

$$\widehat{L}^{-1} \int_0^{\widehat{L}} \int_0^1 (\widehat{m}_2(\widehat{x}_1 + \widehat{w}, \widehat{x}_2) - \widehat{m}_2(\widehat{x}_1, \widehat{x}_2))^2 \,\mathrm{d}\widehat{x}_2 \,\mathrm{d}\widehat{x}_1 \leq C_\alpha \left(\frac{\widehat{w}}{\widehat{h}_{\mathrm{ext}} \ln \widehat{h}_{\mathrm{ext}}}\right)^{\alpha} \widehat{A}^2.$$

c2) There exists $C_{c2} > 0$ *such that for any* $\widehat{w} > 0$

$$\widehat{L}^{-1} \int_0^{\widehat{L}} \int_0^1 |(\widehat{m}_2)_{\widehat{w}}(\widehat{x}_1, \widehat{x}_2)| \,\mathrm{d}\widehat{x}_2 \,\mathrm{d}\widehat{x}_1 \leq C_{c2} \left(\frac{\widehat{h}_{\mathrm{ext}} \ln \widehat{h}_{\mathrm{ext}}}{\widehat{w}}\right)^{1/2} \widehat{A}.$$

The upper bound on the minimal energy for large external fields $\widehat{h}_{\mathrm{ext}}$ in a) is proven on the basis of the Ansätze from domain theory, where the discontinuities are replaced by the optimal 1-d transitions layers (low-angle Néel walls). The proof of

the lower bound and b) and c1) is based on a non-linear interpolation estimate, cf. Lemma 3.15. As opposed to the result in [CÁOS07, Theorem 4], the new interpolation estimate provides also $\widehat{L}$-independent coercivity of the reduced energy $\widehat{E}_0$. The proof of c2) is based on standard convolution estimates combined with the coercivity of the energy, treated in Lemma 3.17, which is derived from Lemma 3.15.

In Theorem 3.3 we use again Lemma 3.15 to prove that global minimizers are close to weak solutions of Burgers' equation for $\widehat{h}_{\text{ext}} \gg 1$.

Theorem 3.3. *Let $\widehat{h}_{\text{ext}} \gg 1$ and $\widehat{L} \sim \widehat{h}_{\text{ext}} \ln \widehat{h}_{\text{ext}}$. Then for $\widehat{E}_0$ and any $\widehat{m}_2$ as in* (1.15) *with $\widehat{L}^{-1}\widehat{E}_0(\widehat{m}_2) \sim -\widehat{h}_{\text{ext}}^3 \ln^2 \widehat{h}_{\text{ext}}$ there exists $\widehat{m}_2^*$ with*

$$-\widehat{\partial}_1 \tfrac{1}{2}(\widehat{m}_2^*)^2 + \widehat{\partial}_2 \widehat{m}_2^* = 0$$

distributionally and

$$\widehat{L}^{-1} \int_0^{\widehat{L}} \int_0^1 (\widehat{m}_2 - \widehat{m}_2^*)^2 \, \mathrm{d}\widehat{x}_2 \, \mathrm{d}\widehat{x}_1 \ll \widehat{L}^{-1} \int_0^{\widehat{L}} \int_0^1 \widehat{m}_2^2 \, \mathrm{d}\widehat{x}_2 \, \mathrm{d}\widehat{x}_1.$$

Although the lower and the upper bound on the energy in Theorem 3.1 agree in terms of scaling with the simple Ansatz from domain theory (see above), it cannot be excluded that additional substructures in the concertina Ansatz, such as branched structures sometimes observed in the experiments, further reduce the energy.

To our knowledge, Theorem 3.3 is the first example of a rigorous connection between minimizers of the 3-d micromagnetic energy functional and solutions to a (linearized) eikonal equation – Burgers' equation – via the Γ-convergence in [CÁOS07, Theorem 3] and Theorem 3.3 in this paper.

Rescaling. In view of Theorem 3.1, it is convenient to rescale length, magnetization and energy according to

$$\begin{aligned}
\widehat{x}_1 &= \widehat{h}_{\text{ext}} \, (\ln \widehat{h}_{\text{ext}}) \, \widetilde{x}_1, \\
\widehat{x}_2 &= \widetilde{x}_2, \\
\widehat{m}_2 &= \widehat{h}_{\text{ext}} \, (\ln \widehat{h}_{\text{ext}}) \, \widetilde{m}_2, \\
\widehat{L}^{-1}\widehat{E}_0 &= \widehat{h}_{\text{ext}}^3 \, (\ln^2 \widehat{h}_{\text{ext}}) \, \widetilde{L}^{-1}\widetilde{E}_0.
\end{aligned}$$

In these new variables we obtain

$$\begin{aligned}
\widetilde{L}^{-1}\widetilde{E}_0(\widetilde{m}_2) \, = & \, \widehat{h}_{\text{ext}}^{-3} \, (\ln^{-2} \widehat{h}_{\text{ext}}) \, \widetilde{L}^{-1} \int_0^{\widetilde{L}} \int_0^1 (\widetilde{\partial}_1 \widetilde{m}_2)^2 \, \mathrm{d}\widetilde{x}_2 \, \mathrm{d}\widetilde{x}_1 \\
& + (\ln \widehat{h}_{\text{ext}}) \, \tfrac{1}{2} \widetilde{L}^{-1} \int_0^{\widetilde{L}} \int_0^1 ||\widetilde{\partial}_1|^{-1/2} (-\widetilde{\partial}_1 (\tfrac{1}{2} \widetilde{m}_2^2) + \partial_2 \widetilde{m}_2)|^2 \, \mathrm{d}\widetilde{x}_2 \, \mathrm{d}\widetilde{x}_1 \\
& - \widetilde{L}^{-1} \int_0^{\widetilde{L}} \int_0^1 \widetilde{m}_2^2 \, \mathrm{d}\widetilde{x}_2 \, \mathrm{d}\widetilde{x}_1.
\end{aligned}$$

It is convenient to introduce

$$\varepsilon := \widehat{h}_{\text{ext}}^{-3} \ln^{-2} \widehat{h}_{\text{ext}},$$

such that for $\widehat{h}_{\text{ext}} \gg 1$

$$\ln \tfrac{1}{\varepsilon} = 3 \ln \widehat{h}_{\text{ext}} + 2 \ln \ln \widehat{h}_{\text{ext}} \approx 3 \ln \widehat{h}_{\text{ext}}.$$

Hence, to leading order

$$\begin{aligned} \widetilde{E}_0(\widetilde{m}_2) =& \varepsilon \int_0^{\widetilde{L}} \int_0^1 (\widetilde{\partial}_1 \widetilde{m}_2)^2 \, \mathrm{d}\widetilde{x}_2 \, \mathrm{d}\widetilde{x}_1 \\ &+ (\ln \tfrac{1}{\varepsilon}) \, \tfrac{1}{6} \int_0^{\widetilde{L}} \int_0^1 ||\widetilde{\partial}_1|^{-1/2} (-\widetilde{\partial}_1 (\tfrac{1}{2} \widetilde{m}_2^2) + \partial_2 \widetilde{m}_2)|^2 \, \mathrm{d}\widetilde{x}_2 \, \mathrm{d}\widetilde{x}_1 \\ &- \int_0^{\widetilde{L}} \int_0^1 \widetilde{m}_2^2 \, \mathrm{d}\widetilde{x}_2 \, \mathrm{d}\widetilde{x}_1. \end{aligned}$$

With this rescaling, Theorem 3.1 assumes the form:

Theorem 3.4. *Let $0 < \varepsilon \ll 1$ and $\widetilde{L} \geq 1$.*
a) Then

$$\min_{\widetilde{m}_2} \widetilde{L}^{-1} \widetilde{E}_0 \sim -1.$$

b) Let $\widetilde{m}_2$ with $\widetilde{L}^{-1} \widetilde{E}_0(\widetilde{m}_2) \sim -1$. Then we have

$$\widetilde{L}^{-1} \int_0^{\widetilde{L}} \int_0^1 \widetilde{m}_2^2 \, \mathrm{d}\widetilde{x}_2 \, \mathrm{d}\widetilde{x}_1 \sim 1,$$

c1) and for any $\widetilde{w} > 0$

$$\widetilde{L}^{-1} \int_0^{\widetilde{L}} \int_0^1 (\widetilde{m}_2(\widetilde{x}_1 + \widetilde{w}, \widetilde{x}_2) - \widetilde{m}_2(\widetilde{x}_1, \widetilde{x}_2))^2 \, \mathrm{d}\widetilde{x}_2 \, \mathrm{d}\widetilde{x}_1 \lesssim \widetilde{w}^{\alpha} \quad \text{for} \quad \alpha \in [0, \tfrac{2}{5}),$$

c2) and

$$\widetilde{L}^{-1} \int_0^{\widetilde{L}} \int_0^1 |(\widetilde{m}_2)_{\widetilde{w}}(\widetilde{x}_1, \widetilde{x}_2)| \, \mathrm{d}\widetilde{x}_2 \, \mathrm{d}\widetilde{x}_1 \lesssim \widetilde{w}^{-1/2},$$

where $(\widetilde{m}_2)_{\widetilde{w}}$ is defined as in Theorem 3.1.

With the rescaling above, Theorem 3.3 assumes the form:

Theorem 3.5. *Let $0 < \varepsilon \ll 1$ and $\widetilde{L} \sim 1$. Then for any $\widetilde{m}_2$ with $\widetilde{L}^{-1} \widetilde{E}_0(\widetilde{m}_2) \sim -1$ there exists $\widetilde{m}_2^*$ with*

$$-\widetilde{\partial}_1 \tfrac{1}{2} (\widetilde{m}_2^*)^2 + \widetilde{\partial}_2 \widetilde{m}_2^* = 0$$

distributionally and

$$\widetilde{L}^{-1} \int_0^{\widetilde{L}} \int_0^1 (\widetilde{m}_2 - \widetilde{m}_2^*)^2 \, \mathrm{d}\widetilde{x}_2 \, \mathrm{d}\widetilde{x}_1 \ll 1.$$

3.2. Proofs

For notational convenience, we drop the tilde $\tilde{\cdot}$. In the following we will write u instead of m_2, x instead of x_1, t instead of x_2, and E instead of E_0.

3.2.1. Upper bound

Proposition 3.6. *For any $0 < \varepsilon \ll 1$ and any $L \geq 1$*

$$\min_u L^{-1} E \lesssim -1. \tag{3.1}$$

Proof of Proposition 3.6. Let us explain the main features of our construction.

Symmetry. Our Ansatz will have the following symmetry properties, cf. Fig. 3.1:

- It will be periodic in x with period $w \sim 1$, i.e.,

  $$u(x + w, t) = u(x, t).$$

  The parameter $w \sim 1$ will be chosen later such that L is an integer multiple of w. (By $w \sim 1$ we mean that $w \in (\frac{1}{C}, C]$ for some universal constant $1 < C < \infty$.)

- It will be odd w.r.t. reflection at $x = 0$ (one of the vertical walls), i.e.,

  $$u(-x, t) = -u(x, t).$$

- It will be even w.r.t. rotation in $(\frac{w}{4}, \frac{1}{2})$ (the center of mass of one of the quadrangular domains), i.e.,

  $$u(\tfrac{w}{4} + x, \tfrac{1}{2} + t) = u(\tfrac{w}{4} - x, \tfrac{1}{2} - t).$$

Hence, u will be determined by its values

$$u(x, t) \text{ on the fundamental domain } (x, t) \in (0, \tfrac{w}{2}) \times (0, \tfrac{1}{2}).$$

Mesoscopic pattern. On a mesoscopic level, our u will be of the form

$$u_{meso}(x, t) = \begin{cases} 0 & \text{for } t \leq \frac{x}{s}, \\ -2\,s & \text{for } t \geq \frac{x}{s}, \end{cases}$$

where the parameter $s \sim 1$ will be chosen later. Notice that $s > \frac{w}{2}$ is necessary to avoid a degenerated pattern. In favor of a clear presentation we only show the construction for the case $s \geq w$ in detail. This will be enough to obtain the desired upper bound on the minimal energy. We will comment on the differences for the case $\frac{w}{2} < s < w$ at the end of the proof.

The mesoscopic Ansatz u_{meso} satisfies

$$-\partial_x(\tfrac{1}{2}u_{meso}^2) + \partial_t u_{meso} \;=\; 0$$

distributionally. Notice that u_{meso} has the following discontinuity lines within $(0, \frac{w}{2}) \times (0, \frac{1}{2})$:

- a jump between $2s$ and $-2s$ across $x = 0$ for $0 \le t \le \frac{1}{2}$,
- a jump between $-2s$ and $2s$ across $x = \frac{w}{2}$ for $t \ge \frac{w}{2s}$,
- a jump between $-2s$ and 0 across $t = \frac{x}{s}$ for $0 \le x \le \frac{w}{2}$.

The first two discontinuity lines carry a weight of $\frac{1}{2}$, since they also belong to the neighboring cell, cf. Section 2.

Néel walls. We must choose appropriate transition layers, i.e., walls, in order to construct a microscopic u starting from u_{meso}. The construction will additionally depend on two parameters α and β, with $\varepsilon \ll \alpha \ll \beta \ll w$, which will be chosen later in function of ε. In fact, we distinguish 3 regions, cf. Fig. 3.1:

- Bulk: Here we set $u = u_{meso}$.
- Walls: Here we use a one-dimensional construction. Within the fundamental domain $(0, \frac{w}{2}) \times (0, \frac{1}{2})$ the wall region is given by

  $$\begin{aligned}&\{(x,t)\,|\,0 \le x \le \beta,\ \tfrac{2\beta}{s} \le t \le \tfrac{1}{2}\}\\ \cup&\{(x,t)\,|\,\tfrac{w}{2} - \beta \le x \le \tfrac{w}{2},\ \tfrac{w}{2s} \le t \le \tfrac{1}{2}\}\\ \cup&\{(x,t)\,|\,st - \beta \le x \le st + \beta,\ \tfrac{2\beta}{s} \le t \le \tfrac{w}{2s} - \tfrac{\beta}{s}\}.\end{aligned}$$

  Notice that $\beta \le \frac{w}{4}$ is necessary.
- Corners: Here, we interpolate the x-dependent boundary data linearly in t. Within the fundamental domain $(0, \frac{w}{2}) \times (0, \frac{1}{2})$ the corner region is described by

  $$\big((0, 3\beta) \times (0, \tfrac{2\beta}{s})\big) \cup \big((\tfrac{w}{2} - 2\beta, \tfrac{w}{2}) \times (\tfrac{w}{2s} - \tfrac{\beta}{s}, \tfrac{w}{2s})\big).$$

  Notice that $3\beta \le \frac{w}{2}$ is necessary.

The function u will be constructed to be continuous across the regions. These regions contribute differently to the three parts of the energy:

- Exchange energy: This local energy contribution behaves in an additive way; only the walls and the corners contribute.

- Magnetostatic energy: Only walls and corners contribute to the charge density σ, i.e., the support of the charge density is a subset of the wall and corner region. Since the magnetostatic energy is non-local in the charge density σ, it behaves in a non-additive way. However, if $\sigma = \sigma_1 + \sigma_2 + \sigma_3$ is a decomposition, we have an upper bound by the triangle inequality

$$\int \left||\partial_x|^{-1/2}\sigma\right|^2 \mathrm{d}x \leq 3\int \left||\partial_x|^{-1/2}\sigma_1\right|^2 \mathrm{d}x + 3\int \left||\partial_x|^{-1/2}\sigma_2\right|^2 \mathrm{d}x + 3\int \left||\partial_x|^{-1/2}\sigma_3\right|^2 \mathrm{d}x, \quad (3.2)$$

  where we have to ascertain $\int_{-\frac{w}{2}}^{\frac{w}{2}} \sigma_1 \,\mathrm{d}x = \int_{-\frac{w}{2}}^{\frac{w}{2}} \sigma_2 \,\mathrm{d}x = \int_{-\frac{w}{2}}^{\frac{w}{2}} \sigma_3 \,\mathrm{d}x = 0$, so that the r.h.s. is finite. Since modulo w-periodicity in x, there are at most 3 walls or corners at a given t-value, (3.2) suffices.

- Zeeman energy: Here, we seek a *lower* bound for $\int\int u^2 \,\mathrm{d}t\,\mathrm{d}x$. The main contribution will come from the bulk.

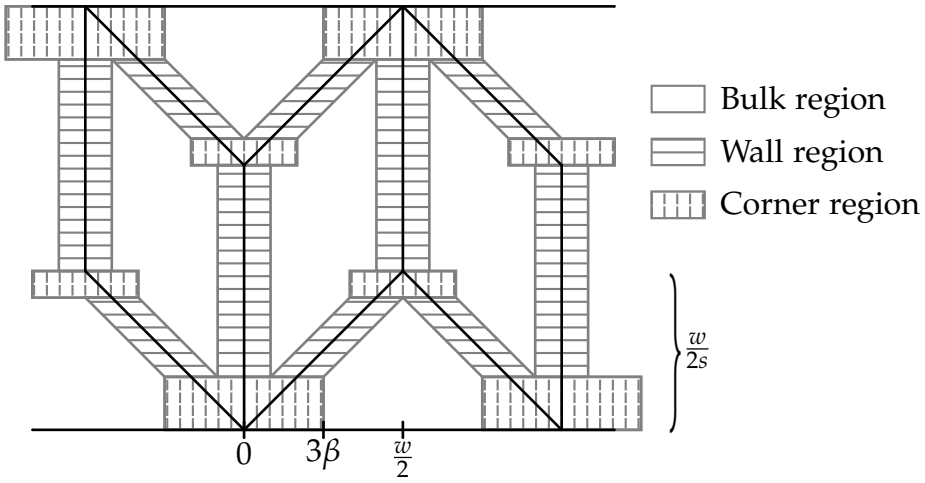

Figure 3.1.: The Ansatz u.

Vertical Néel walls. In this section, we construct the vertical Néel walls. Without loss of generality, we focus on the construction in the region

$$\left\{(x,t)\,\middle|\, -\beta \leq x \leq \beta,\ \tfrac{2\beta}{s} \leq t \leq \tfrac{1}{2}\right\}. \quad (3.3)$$

We consider the exchange and magnetostatic energy $E_{\mathrm{ex+ma}}$. Within (3.3), u coincides with an odd function v of the form

$$u = -2\,s\,v(x), \quad v(\pm\beta) = \pm 1,$$

which we think of as being w-periodic and $v(x+\frac{w}{2}) = -v(x)$. In terms of v, we have the estimate

$$\begin{aligned}
&E_{\text{ex+ma}} \\
&= (\tfrac{1}{2} - \tfrac{2\beta}{s}) \left(4\, s^2\, \varepsilon \int_{-\frac{w}{2}}^{\frac{w}{2}} (\partial_x v)^2 \,\mathrm{d}x + \tfrac{8}{3}\, s^4\, (\ln \tfrac{1}{\varepsilon}) \int_{-\frac{w}{2}}^{\frac{w}{2}} \left| |\partial_x|^{-1/2} \partial_x (-\tfrac{1}{2} v^2) \right|^2 \mathrm{d}x \right) \\
&\lesssim s^2\, \varepsilon \int_{-\frac{w}{2}}^{\frac{w}{2}} (\partial_x v)^2 \,\mathrm{d}x + s^4\, (\ln \tfrac{1}{\varepsilon}) \int_{-\frac{w}{2}}^{\frac{w}{2}} \left| |\partial_x|^{1/2}\, v^2 \right|^2 \mathrm{d}x \\
&\lesssim s^2\, \varepsilon \int_{-\frac{w}{2}}^{\frac{w}{2}} \tfrac{1}{v^2} (\partial_x v^2)^2 \,\mathrm{d}x + s^4\, (\ln \tfrac{1}{\varepsilon}) \int_{-\frac{w}{2}}^{\frac{w}{2}} \left| |\partial_x|^{1/2}\, v^2 \right|^2 \mathrm{d}x.
\end{aligned}$$

It is convenient to think in terms of $\varrho = v^2$ which satisfies

$$\begin{aligned}
&\varrho = 1 \text{ for } \beta \le |x| \le \tfrac{w}{2} - \beta, \\
&\varrho = 0 \text{ for } x = 0, \\
&\varrho \text{ is } \tfrac{w}{2}\text{-periodic},
\end{aligned}$$

so that

$$E_{\text{ex+ma}} \lesssim s^2\, \varepsilon \int_{-\frac{w}{4}}^{\frac{w}{4}} \frac{1}{\varrho} (\partial_x \varrho)^2 \,\mathrm{d}x + s^4\, \ln \frac{1}{\varepsilon} \int_{-\frac{w}{4}}^{\frac{w}{4}} \left| |\partial_x|^{1/2} \varrho \right|^2 \mathrm{d}x.$$

We make the Néel-wall Ansatz, cf. [Melo3] and [DKMO05, Section 6],

$$\varrho(x) = \begin{cases} \frac{\ln \frac{\alpha^2 + x^2}{\alpha^2}}{\ln \frac{\alpha^2 + \beta^2}{\alpha^2}} & \text{for } |x| \le \beta, \\ 1 & \text{for } \beta \le |x| \le \frac{w}{4}, \end{cases} \tag{3.4}$$

where ε and α with $\varepsilon \ll \alpha \ll \beta \ll w$ will be chosen later. We first turn to the magnetostatic part and use the trace characterization of the homogeneous $H^{1/2}$-norm, i.e.,

$$\begin{aligned}
\int_{-\frac{w}{4}}^{\frac{w}{4}} \left| |\partial_x|^{1/2} \varrho \right|^2 \mathrm{d}x = \inf\{ &\int_{-\frac{w}{4}}^{\frac{w}{4}} \int_0^\infty (\partial_x \bar{\varrho})^2 + (\partial_z \bar{\varrho})^2 \,\mathrm{d}z \,\mathrm{d}x \,| \\
&\bar{\varrho}(x,z) \text{ is } \tfrac{w}{2}\text{-periodic in } x \text{ and } \bar{\varrho}(x,0) = \varrho(x) \},
\end{aligned} \tag{3.5}$$

which yields by extending ϱ in a radially symmetric way in the (x,z)-plane:

$$\begin{aligned}
&\int_{-\frac{w}{4}}^{\frac{w}{4}} \left| |\partial_x|^{1/2} \varrho \right|^2 \mathrm{d}x \\
&\quad \lesssim \frac{1}{\ln^2 \frac{\alpha^2+\beta^2}{\alpha^2}} \iint\limits_{x^2+z^2 \le \beta^2} \left(\partial_x \left(\ln \tfrac{\alpha^2+x^2+z^2}{\alpha^2} \right) \right)^2 + \left(\partial_z \left(\ln \tfrac{\alpha^2+x^2+z^2}{\alpha^2} \right) \right)^2 \mathrm{d}x \,\mathrm{d}z \\
&\quad \overset{\alpha \ll \beta}{\lesssim} \frac{1}{\ln^2 \frac{\beta}{\alpha}} \int_0^\beta (\partial_r (\ln \tfrac{\alpha^2+r^2}{\alpha^2}))^2 r \,\mathrm{d}r \\
&\quad \sim \frac{1}{\ln \frac{\beta}{\alpha}}.
\end{aligned}$$

We now turn to the exchange energy. Since

$$\tfrac{1}{\varrho}\left(\tfrac{\mathrm{d}\varrho}{\mathrm{d}x}\right)^2 \;=\; \frac{1}{\ln\frac{\alpha^2+\beta^2}{\alpha^2}}\begin{cases}\frac{1}{\ln\frac{\alpha^2+x^2}{\alpha^2}}\,\frac{4x^2}{(\alpha^2+x^2)^2} & \text{for } |x|<\beta,\\ 0 & \text{for } \beta<|x|<\frac{w}{4},\end{cases}$$

we have

$$\int_{-\frac{w}{4}}^{\frac{w}{4}} \tfrac{1}{\varrho}\left(\tfrac{\mathrm{d}\varrho}{\mathrm{d}x}\right)^2 \mathrm{d}x \overset{\alpha\ll\beta}{\lesssim} \frac{1}{\ln\frac{\beta}{\alpha}}\int_{-\beta}^{\beta}\frac{1}{\ln\frac{\alpha^2+x^2}{\alpha^2}}\frac{x^2}{(\alpha^2+x^2)^2}\,\mathrm{d}x \;\sim\; \frac{1}{\alpha\,\ln\frac{\beta}{\alpha}}. \tag{3.6}$$

Hence we obtain

$$E_{\text{ex+ma}} \lesssim s^2\,\varepsilon\frac{1}{\alpha\,\ln\frac{\beta}{\alpha}} + s^4\left(\ln\tfrac{1}{\varepsilon}\right)\frac{1}{\ln\frac{\beta}{\alpha}} \;\approx\; s^4\left(\ln\tfrac{1}{\varepsilon}\right)\frac{1}{\ln\frac{\beta}{\alpha}}, \tag{3.7}$$

where the last asymptotic identity follows from $\varepsilon \ll \alpha \ll w \sim 1$ and $s \sim 1$.

Diagonal Néel walls. We now address the construction in the region

$$\{(x,t)|s\,t-\beta\le\; x\le\; s\,t+\beta,\; \tfrac{2\beta}{s}\le\; t\le\; \tfrac{w}{2s}-\tfrac{\beta}{s}\}.$$

Since exchange and magnetostatic energy $E_{\text{ex+ma}}$ are invariant under the shear transform

$$x \;=\; s\,t+\tilde{x},\quad t \;=\; \tilde{t},\quad u \;=\; \tilde{u}-s, \tag{3.8}$$

we can reduce this construction to a construction of a vertical Néel wall in

$$\{(\tilde{x},\tilde{t})|\;-\beta\;\le\;\tilde{x}\;\le\;\beta,\;\tfrac{2\beta}{s}\;\le\;\tilde{t}\;\le\;\tfrac{w}{2s}-\tfrac{\beta}{s}\}.$$

The only difference to the vertical Néel wall before is that the construction connects $-s$ to s instead of $-2s$ to $2s$. Hence we obtain as there

$$E_{\text{ex+ma}} \;\lesssim\; s^4\left(\ln\tfrac{1}{\varepsilon}\right)\frac{1}{\ln\frac{\beta}{\alpha}}. \tag{3.9}$$

Corners. Without loss of generality we consider the corner $(-3\,\beta,3\,\beta)\times(0,\frac{2\beta}{s})$. In view of (3.4) (for $\varrho \;=\; v^2$) and (3.8), we have to interpolate

$$u(x,0) \;=\; 0$$

and

$$u(x,\tfrac{2\beta}{s}) \;=\; \begin{cases} s\,(v(x+2\,\beta)+1) & \text{for } -3\,\beta\;\le\; x\;\le\; -\beta,\\ -2\,s\,v(x) & \text{for } \;-\beta\;\le\; x\;\le\; \beta,\\ s\,(v(x-2\,\beta)-1) & \text{for } \;\;\beta\;\le\; x\;\le\; 3\,\beta\end{cases} \tag{3.10}$$

in t, where

$$v(x) \;=\; \operatorname{sign} x\, \varrho(x)^{1/2}.$$

We opt for a linear interpolation, i.e.,

$$u(x,t) \;=\; \tfrac{s\,t}{2\beta} u(x, \tfrac{2\beta}{s}).$$

We first turn to the exchange energy $E_{\rm ex}$. Because of the linear interpolation, we infer from (3.6)

$$E_{\rm ex} \lesssim \frac{\beta}{s} \frac{\varepsilon\, s^2}{\alpha \ln \frac{\beta}{\alpha}}.$$

We now address the magnetostatic energy $E_{\rm ma}$. Notice

$$\begin{aligned} \sigma(x,t) \;&=\; (-\partial_x(\tfrac{1}{2}u^2) + \partial_t u)(x,t) \\ &=\; -(\tfrac{s\,t}{2\beta})^2 \partial_x(\tfrac{1}{2}u^2)(x, \tfrac{2\beta}{s}) + \tfrac{s}{2\beta}\, u(x, \tfrac{2\beta}{s}). \end{aligned} \tag{3.11}$$

Because of the symmetry property

$$u(-x, \tfrac{2\beta}{s}) \;=\; -u(x, \tfrac{2\beta}{s}),$$

we have in particular for all $t \in (0, \frac{2\beta}{s})$

$$\int_{-\frac{w}{2}}^{\frac{w}{2}} \sigma(x,t)\,\mathrm{d}x \;=\; 0. \tag{3.12}$$

Since $\operatorname{supp} \sigma(\cdot,t) \subset [-3\beta, 3\beta]$, we claim that

$$\int_{-\frac{w}{2}}^{\frac{w}{2}} \left|(|\partial_x|^{-1/2}\sigma)(\cdot,t)\right|^2 \mathrm{d}x \;\lesssim\; \beta \int_{-\frac{w}{2}}^{\frac{w}{2}} \sigma(x,t)^2\,\mathrm{d}x. \tag{3.13}$$

Let us give the argument for (3.13). By duality, this is equivalent to

$$\int_{-\frac{w}{2}}^{\frac{w}{2}} \zeta(x)\sigma(x,t)\,\mathrm{d}x \;\lesssim\; \left(\beta \int_{-3\beta}^{3\beta} \sigma(x,t)^2\,\mathrm{d}x \int_{-\frac{w}{2}}^{\frac{w}{2}} \left||\partial_x|^{1/2}\zeta(x)\right|^2 \mathrm{d}x\right)^{1/2},$$

for all w-periodic functions $\zeta(x)$. By the trace characterization of the homogeneous $H^{1/2}$-norm (3.5), this estimate is equivalent to

$$\int_{-\frac{w}{2}}^{\frac{w}{2}} \zeta(x,0)\sigma(x,t)\,\mathrm{d}x \;\lesssim\; \left(\beta \int_{-3\beta}^{3\beta} \sigma(x,t)^2\,\mathrm{d}x \int_{-\frac{w}{2}}^{\frac{w}{2}} \int_0^\infty (\partial_x\zeta)^2 + (\partial_z\zeta)^2\,\mathrm{d}x\,\mathrm{d}z\right)^{1/2}$$

for all functions $\zeta(x,z)$ which are w-periodic in x. Because of (3.12) and $\operatorname{supp} \sigma(\cdot,t) \subset [-3\beta, 3\beta]$, this estimate in turn follows from

$$\int_{-3\beta}^{3\beta} (\zeta(x,0) - \tfrac{1}{6\beta} \int_{-3\beta}^{3\beta} \zeta(\tilde{x},0)\,\mathrm{d}\tilde{x})^2\,\mathrm{d}x \;\lesssim\; \beta \int_{-\frac{w}{2}}^{\frac{w}{2}} \int_0^\infty (\partial_x\zeta)^2 + (\partial_z\zeta)^2\,\mathrm{d}x\,\mathrm{d}z,$$

for all functions $\zeta(x,z)$. which because of $\beta \ll w$ follows from a standard trace estimate. This establishes (3.13).

Inserting (3.11) into (3.13) yields

$$\begin{aligned}
&\int_{-\frac{w}{2}}^{\frac{w}{2}} \left|(|\partial_x|^{-1/2}\sigma)(\cdot,t)\right|^2 \mathrm{d}x \\
&\overset{\frac{st}{2\beta}\le 1}{\lesssim} \beta\left(\int_{-3\beta}^{3\beta}(\partial_x(u^2)(x,\tfrac{2\beta}{s}))^2\,\mathrm{d}x + (\tfrac{s}{\beta})^2\int_{-3\beta}^{3\beta}(u(x,\tfrac{2\beta}{s}))^2\,\mathrm{d}x\right) \\
&\lesssim \beta \sup_{x\in(-3\beta,3\beta)}\{u^2(x,\tfrac{2\beta}{s})\}\int_{-3\beta}^{3\beta}(\partial_x u(x,\tfrac{2\beta}{s}))^2\,\mathrm{d}x + \tfrac{s^2}{\beta}\sup_{x\in(-3\beta,3\beta)}\{u^2(x,\tfrac{2\beta}{s})\} \\
&\overset{(3.10),(3.6)}{\lesssim} \beta\left(\frac{s^4}{\alpha\ln\frac{\beta}{\alpha}} + \frac{s^4}{\beta}\right) \\
&\overset{\alpha\ll\beta}{\lesssim} \frac{\frac{\beta}{\alpha}}{\ln\frac{\beta}{\alpha}}s^4.
\end{aligned}$$

Therefore

$$E_{\mathrm{ma}} = \tfrac{1}{6}(\ln\tfrac{1}{\varepsilon})\int_0^{\frac{2\beta}{s}}\int_{-\frac{w}{2}}^{\frac{w}{2}}\left||\partial_x|^{-1/2}\sigma\right|^2\mathrm{d}x\,\mathrm{d}t \lesssim \frac{\beta^2 s^3}{\alpha}\frac{\ln\frac{1}{\varepsilon}}{\ln\frac{\beta}{\alpha}}.$$

Hence, we obtain for the sum $E_{\mathrm{ex+ma}}$ of exchange and magnetostatic energies

$$E_{\mathrm{ex+ma}} \lesssim \frac{\beta\,\varepsilon\,s}{\alpha\ln\frac{\beta}{\alpha}} + \frac{\beta^2 s^3}{\alpha}\frac{\ln\frac{1}{\varepsilon}}{\ln\frac{\beta}{\alpha}} = \frac{\beta\,s}{\alpha\ln\frac{\beta}{\alpha}}(\varepsilon + \beta\,s^2\ln\tfrac{1}{\varepsilon}),$$

so that because of $\varepsilon \ll \beta \ll w \sim 1$ and $s \sim 1$, this estimate asymptotically turns into

$$E_{\mathrm{ex+ma}} \lesssim \frac{\beta^2 s^3}{\alpha}\frac{\ln\frac{1}{\varepsilon}}{\ln\frac{\beta}{\alpha}}. \tag{3.14}$$

Optimizing in the parameters. We first consider the exchange and magnetostatic energy $E_{\mathrm{ex+ma}}$ in $(-\frac{w}{2},\frac{w}{2})\times(0,1)$. Collecting (3.7), (3.9) and (3.14) we obtain

$$E_{\mathrm{ex+ma}} \lesssim s^4\frac{\ln\frac{1}{\varepsilon}}{\ln\frac{\beta}{\alpha}} + \frac{\beta^2 s^3}{\alpha}\frac{\ln\frac{1}{\varepsilon}}{\ln\frac{\beta}{\alpha}}.$$

Choosing for instance

$$\alpha = \varepsilon^{2/3}, \quad \beta = \varepsilon^{1/2},$$

which is compatible with $\varepsilon \ll \alpha \ll \beta \ll w \sim 1$, the estimate asymptotically turns into

$$E_{\mathrm{ex+ma}} \lesssim s^4 + \varepsilon^{1/3}s^3 \overset{\varepsilon\ll 1}{\lesssim} s^4.$$

Since $\beta \ll w$, we have for the Zeeman contribution that

$$\int_0^1 \int_{-\frac{w}{2}}^{\frac{w}{2}} u^2 \,\mathrm{d}x\,\mathrm{d}t \approx \int_0^1 \int_{-\frac{w}{2}}^{\frac{w}{2}} u_{meso}^2 \,\mathrm{d}x\,\mathrm{d}t \;=\; (2\,s)^2\, w\,(1-\tfrac{w}{2\,s}).$$

Choosing $s \;=\; w$, we obtain for the total energy

$$E \;\leq\; C_1\, w^4 - \tfrac{1}{2} C_2\, w^3.$$

Hence we obtain for the total energy per length x

$$e(w) \;\leq\; C_1\, w^3 - \tfrac{1}{2} C_2\, w^2.$$

Obviously, there is a $w' \;\leq\; 1$ s.t. for all $w \in (\frac{w'}{2}, w']$

$$e(w) \;\lesssim\; -1. \tag{3.15}$$

Hence we can always choose w such that L is an integer multiple of w and (3.15) holds. The corresponding Ansatz function provides the upper bound on the energy.

The case $w > s > \frac{w}{2}$. Notice that the three discontinuity lines of the mesoscopic pattern have a common triple point at $(\frac{1}{2}, \frac{w}{2s})$ in the fundamental domain, cf. Fig. 3.1. If we allowed for $w \;>\; s \;>\; \frac{w}{2}$ this triple point would be at $(0, 1-\frac{w}{2s})$ in the fundamental domain. The construction of the microscopic pattern with smooth transition layers can be carried out in the same way as in the case $s \;\geq\; w$. For the upper bound on the magnetostatic energy, we have to take into account (at most) 4 walls or corners at a given t-value modulo w-periodicity. □

3.2.2. Lower bound

Remark 3.7. *We introduce the notation for the average of an L-periodic function $\zeta(x,t)$ in x*

$$\langle \zeta \rangle \;:=\; L^{-1} \int_0^L \zeta \,\mathrm{d}x,$$

and the average both in x and t

$$\langle\!\langle \zeta \rangle\!\rangle \;:=\; L^{-1} \int_0^1 \int_0^L \zeta \,\mathrm{d}x\,\mathrm{d}t.$$

We further define the translation of a function ζ by $\Delta \in \mathbb{R}$ in the x_1-variable:

$$\zeta^{\Delta}(x_1, x_2) := \zeta(x_1 + \Delta, x_2).$$

Proposition 3.8. *Let $0 < \varepsilon \ll 1$ and $L > 0$. Then*

$$\min_u L^{-1} E \;\gtrsim\; -1.$$

The main ingredient for the lower bound is a new estimate on smooth solutions u of the inhomogeneous, inviscid Burgers equation, i.e.,

$$\partial_t u - \partial_x(\tfrac{1}{2}u^2) \;=\; \sigma. \tag{3.16}$$

This type of estimate was introduced in [Otto9, Section 2.6]; it relies on a generalization of Oleinik's E-principle [Ole63]. That principle states that for smooth solutions of the homogeneous inviscid Burgers equation, i.e.,

$$\partial_t u - \partial_x(\tfrac{1}{2}u^2) \;=\; 0, \tag{3.17}$$

a one-sided Lipschitz bound improves over time in the sense that for any $\tau > 0$

$$\partial_x u(t=0,\cdot) \geq -\tau^{-1} \quad \Rightarrow \quad \partial_x u(t,\cdot) \;\geq\; -(\tau+t)^{-1}. \tag{3.18}$$

In fact, the main insight of [Otto9] is that in addition, the L^2-distance to the set of functions ζ with a one-sided Lipschitz bound improves over time. To make this more precise, we need

Definition 3.9. *Let $u(x)$ be L-periodic in x. Define*

$$\begin{aligned}\mathcal{D}^-(u,\tau) \;&:=\; \inf\{\,\langle(\zeta-u)^2\rangle \mid \zeta \text{ smooth and L-periodic}, \tau\partial_x\zeta \geq -1\,\},\\ \mathcal{D}^+(u,\tau) \;&:=\; \inf\{\,\langle(\zeta-u)^2\rangle \mid \zeta \text{ smooth and L-periodic}, \tau\partial_x\zeta \;\leq\; 1\,\}.\end{aligned}$$

If $u(x,t)$ is L-periodic in x we use the abbreviation

$$\mathcal{D}^\pm(t,\tau) \;:=\; \mathcal{D}^\pm(u(\cdot,t),\tau).$$

For $\mathcal{D}^\pm$ we denote the average w.r.t. t by

$$\langle\mathcal{D}^\pm\rangle(\tau) \;:=\; \int_0^1 \mathcal{D}^\pm(t,\tau)\,\mathrm{d}t.$$

It was shown in [Otto9] that if u satisfies the homogeneous Burgers equation (3.17), $\mathcal{D}^-$ satisfies the *linear* homogeneous differential inequality

$$\partial_t\mathcal{D}^- + \partial_\tau\mathcal{D}^- + \tau^{-1}\,\mathcal{D}^- \;\leq\; 0. \tag{3.19}$$

Obviously, (3.19) contains (3.18), which follows from $\partial_t\mathcal{D}^- + \partial_\tau\mathcal{D}^- \;\leq\; 0$. The new and crucial feature is the $\tau^{-1}\mathcal{D}^-$- term in (3.19).

It was also shown in [Otto9] that (3.19) survives for the inhomogeneous Burgers equation (3.16) in the form

$$\partial_t\mathcal{D}^- + \partial_\tau\mathcal{D}^- + \tau^{-1}\,\mathcal{D}^- \;\leq\; 2\,\langle\big||\partial_x|^{-1/2}\sigma\big|^2\rangle^{1/2}\,\langle\big||\partial_x|^{1/2}u\big|^2\rangle^{1/2}. \tag{3.20}$$

However, (3.20) is not of use to us since we do not control $\langle\big||\partial_x|^{1/2}u\big|^2\rangle$ independently of ε. The idea is to replace u on the r.h.s. of (3.20) by the optimal ζ in the definition of $\mathcal{D}^-(u,\tau)$, since a ζ with a one-sided Lipschitz bound has (up to a logarithm) half of a derivative in L^2. This is the content of the next two lemmas.

Lemma 3.10. *Let $\zeta(x,t)$ be smooth, L-periodic in x and satisfy*

$$\tau\partial_x\zeta \;\geq\; -1$$

for some $\tau > 0$. Then for $0 < r \leq R$

$$\begin{aligned}\langle\big||\partial_x|^{1/2}\zeta\big|^2\rangle &\lesssim r\,\tfrac{1}{2}\,\langle(\partial_x\zeta)^2\rangle + (\ln\tfrac{R}{r})\,\tau^{-1}\,\langle|\zeta|\rangle + R^{-1}\,\tfrac{1}{2}\,\langle\zeta^2\rangle\\ &\leq r\,\tfrac{1}{2}\,\langle(\partial_x\zeta)^2\rangle + (\ln\tfrac{R}{r})\,\tau^{-1}\,\langle|\zeta|^2\rangle^{1/2} + R^{-1}\,\tfrac{1}{2}\,\langle\zeta^2\rangle. \qquad (3.21)\end{aligned}$$

This interpolation inequality in turn relies on

Lemma 3.11. *Let $\zeta(x,t)$ be smooth, L-periodic in x and satisfy*

$$\tau\,\partial_x\zeta \;\geq\; -1$$

for some $\tau > 0$. Then

$$\sup_{\Delta>0}\tfrac{1}{\Delta}\langle|\zeta^\Delta-\zeta|^2\rangle \;\lesssim\; \tau^{-1}\,\langle|\zeta|\rangle. \qquad (3.22)$$

Let us comment on both lemmas: The estimate $\sup_{\Delta>0}\frac{1}{\Delta}\langle|\zeta^\Delta-\zeta|^2\rangle \lesssim \sup|\partial_x\zeta|\,\langle|\zeta|\rangle$ is obvious. The insight of (3.22) is that the two-sided control $\sup|\partial_x\zeta|$ can be replaced by the one-sided control.

We now turn to Lemma 3.10: Although $\langle\big||\partial_x|^{1/2}\zeta\big|^2\rangle$ and $\sup_{\Delta>0}\frac{1}{\Delta}\langle|\zeta^\Delta-\zeta|^2\rangle$ have the same scaling, the estimate

$$\langle\big||\partial_x|^{1/2}\zeta\big|^2\rangle \;\lesssim\; \sup_{\Delta>0}\tfrac{1}{\Delta}\langle|\zeta^\Delta-\zeta|^2\rangle$$

fails. However, if very short wave lengths ($\leq r$) and very long wave lengths ($\geq R$) are treated separately, one obtains the logarithmic estimate (3.21).

Mimicking the proof of (3.20), using Lemma 3.10, we will derive

Lemma 3.12. *For any smooth L-periodic $u(x,t)$ and $0 < \varepsilon \leq 1$*

$$\begin{aligned}&\partial_t\tfrac{1}{2}(\mathcal{D}^- - \langle u^2\rangle) + \partial_\tau\tfrac{1}{2}\mathcal{D}^- + \tau^{-1}\tfrac{1}{2}\mathcal{D}^-\\ &\quad\lesssim \langle\big||\partial_x|^{-1/2}\sigma\big|^2\rangle^{1/2}\,[\,\varepsilon^{1/2}\,\langle(\partial_x u)^2\rangle^{1/2}\,\langle u^2\rangle^{1/2} + (\ln\tfrac{1}{\varepsilon})\,\tau^{-1}\,\langle u^2\rangle^{1/2}\,]^{1/2}. \qquad (3.23)\end{aligned}$$

Note that the second factor on the r.h.s of (3.23) is related to the r.h.s. of (3.21) by optimizing in $r \leq R$ while keeping $\varepsilon = \frac{r}{R}$ fixed.

We use Lemma 3.12 to derive the following interpolation inequality:

Corollary 3.13. *For any smooth L-periodic $u(x,t)$ with $u(\cdot,0) = u(\cdot,1) = 0$ and $0 < \varepsilon \leq 1$ it holds*

$$\begin{aligned}\int_0^1\langle u^2\rangle\,\mathrm{d}t \;\lesssim\; &\Big((\ln\tfrac{1}{\varepsilon})\int_0^1\langle\big||\partial_x|^{-1/2}\sigma\big|^2\rangle\,\mathrm{d}t\Big)^{2/3}\\ &+\Big(\int_0^1\langle\big||\partial_x|^{-1/2}\sigma\big|^2\rangle\,\mathrm{d}t\Big)^{2/3}\,\Big(\varepsilon\int_0^1\langle(\partial_x u)^2\rangle\,\mathrm{d}t\Big)^{1/3}. \qquad (3.24)\end{aligned}$$

We also use Lemma 3.12 to derive a regularity estimate:

Corollary 3.14. *For any smooth L-periodic $u(x,t)$ with $u(\cdot,0) = u(\cdot,1) = 0$ and $0 < \varepsilon \leq 1$ it holds*

$$\begin{aligned}\sup_{\tau>0} \tau^{-1/2} \int_0^1 \mathcal{D}^+ \,\mathrm{d}t + \sup_{\tau>0} \tau^{-1/2} \int_0^1 \mathcal{D}^- \,\mathrm{d}t \\ \lesssim \Big((\ln \tfrac{1}{\varepsilon}) \int_0^1 \langle \big||\partial_x|^{-1/2}\sigma\big|^2\rangle \,\mathrm{d}t\Big)^{2/3} \\ + \Big(\int_0^1 \langle \big||\partial_x|^{-1/2}\sigma\big|^2\rangle \,\mathrm{d}t\Big)^{2/3} \Big(\varepsilon \int_0^1 \langle (\partial_x u)^2\rangle \,\mathrm{d}t\Big)^{1/3}. \end{aligned} \tag{3.25}$$

Not surprisingly, the control of the L^2-distance to the set of functions with a (one-sided) Lipschitz-bound gives control of some fractional derivative in some L^p-norm. More precisely, $\sup_{\tau>0} \tau^{-1/2} \int_0^1 \mathcal{D}^+ \,\mathrm{d}t + \sup_{\tau>0} \tau^{-1/2} \int_0^1 \mathcal{D}^- \,\mathrm{d}t$ has the same scaling as $\sup_{\Delta>0} \Delta^{-1/2} \int_0^1 \langle |u^\Delta - u|^{5/2}\rangle \,\mathrm{d}t$. Using ideas from [Otto9, Proposition 4] and interpolation with Corollary 3.13 we indeed obtain:

Lemma 3.15. *For any smooth L-periodic $u(x,t)$ with $u(\cdot,0) = u(\cdot,1) = 0$ and $0 < \varepsilon \leq 1$ it holds*

$$\begin{aligned}\sup_{\Delta>0} \Delta^{-(p-2)} \int_0^1 \langle |u^\Delta - u|^p\rangle \,\mathrm{d}t \lesssim \Big((\ln \tfrac{1}{\varepsilon}) \int_0^1 \langle \big||\partial_x|^{-1/2}\sigma\big|^2\rangle \,\mathrm{d}t\Big)^{2/3} \\ + \Big(\int_0^1 \langle \big||\partial_x|^{-1/2}\sigma\big|^2\rangle \,\mathrm{d}t\Big)^{2/3} \Big(\varepsilon \int_0^1 \langle (\partial_x u)^2\rangle \,\mathrm{d}t\Big)^{1/3} \end{aligned} \tag{3.26}$$

with $p \in [2, \frac{5}{2})$.

Remark 3.16. *In [CÁOSo7, Section 3.3], it was shown that admissible functions u as in (1.15) of finite energy can always be approximated by a sequence of smooth admissible functions $\{u_\alpha\}_{\alpha\downarrow 0}$ in the energy topology. Therefore Corollary 3.13 and Corollary 3.14 and Lemma 3.15, which were established for a smooth u, extend to our finite-energy u.*

We will apply Corollary 3.13 to derive the coercivity of the energy. To facilitate the notation we introduce the abbreviations

$$\begin{aligned} \Sigma &:= \langle\!\langle \big||\partial_x|^{-1/2}\sigma\big|^2\rangle\!\rangle, \\ DU &:= \langle\!\langle (\partial_x u)^2\rangle\!\rangle, \text{ and} \\ U &:= \langle\!\langle u^2\rangle\!\rangle. \end{aligned} \tag{3.27}$$

Lemma 3.17. *Let $0 < \varepsilon \ll 1$. Then for any L-periodic $u(x_1,x_2)$ with $u(\cdot,0) = u(\cdot,1)$ which is of finite energy, i.e.,*

$$L^{-1}E(u) = \varepsilon DU + (\ln \tfrac{1}{\varepsilon})\Sigma - U < +\infty,$$

we have

$$\varepsilon DU,\ (\ln \tfrac{1}{\varepsilon})\Sigma,\ U \lesssim \begin{cases} 1 & \text{for } L^{-1}E(u) \leq 1, \\ L^{-1}E(u) & \text{for } L^{-1}E(u) \geq 1. \end{cases} \tag{3.28}$$

Proof of Lemma 3.10. We fix t. The fractional Sobolev norm can be expressed as a suitable average of the L^2-modulus of continuity of ζ (this can easily be seen in Fourier space, cf. [LM68, p.59]):

$$\int_0^L \left||\partial_x|^{1/2}\zeta\right|^2 \,\mathrm{d}x \;\sim\; \int_0^\infty \tfrac{1}{\Delta} \int_0^L (\zeta(x+\Delta)-\zeta(x))^2 \,\mathrm{d}x\, \tfrac{1}{\Delta}\,\mathrm{d}\Delta. \tag{3.29}$$

We split the r.h.s. into a small scale part, an intermediate scale part, and a large scale part:

$$\begin{aligned}
&\int_0^\infty \tfrac{1}{\Delta} \int_0^L (\zeta(x+\Delta)-\zeta(x))^2 \,\mathrm{d}x\, \tfrac{1}{\Delta}\,\mathrm{d}\Delta \\
&\qquad = \int_0^r \tfrac{1}{\Delta} \int_0^L (\zeta(x+\Delta)-\zeta(x))^2 \,\mathrm{d}x\, \tfrac{1}{\Delta}\,\mathrm{d}\Delta \\
&\qquad\quad + \int_r^R \tfrac{1}{\Delta} \int_0^L (\zeta(x+\Delta)-\zeta(x))^2 \,\mathrm{d}x\, \tfrac{1}{\Delta}\,\mathrm{d}\Delta \\
&\qquad\quad + \int_R^\infty \tfrac{1}{\Delta} \int_0^L (\zeta(x+\Delta)-\zeta(x))^2 \,\mathrm{d}x\, \tfrac{1}{\Delta}\,\mathrm{d}\Delta,
\end{aligned} \tag{3.30}$$

where $0 < r \le R < +\infty$.

The most interesting term is the intermediate one, which we estimate as follows:

$$\int_r^R \tfrac{1}{\Delta} \int_0^L (\zeta(x+\Delta)-\zeta(x))^2 \,\mathrm{d}x\, \tfrac{1}{\Delta}\,\mathrm{d}\Delta \;\le\; (\ln \tfrac{R}{r}) \sup_{\Delta>0} \tfrac{1}{\Delta} \int_0^L (\zeta(x+\Delta)-\zeta(x))^2 \,\mathrm{d}x.$$

The application of Lemma 3.11, i.e.,

$$\sup_{\Delta>0} \tfrac{1}{\Delta} \int_0^L (\zeta^\Delta-\zeta)^2 \,\mathrm{d}x \;\lesssim\; \tau^{-1} \int_0^L |\zeta| \,\mathrm{d}x,$$

yields

$$\int_r^R \tfrac{1}{\Delta} \int_0^L (\zeta(x+\Delta)-\zeta(x))^2 \,\mathrm{d}x\, \tfrac{1}{\Delta}\,\mathrm{d}\Delta \;\lesssim\; (\ln \tfrac{R}{r})\, \tau^{-1} \int_0^L |\zeta| \,\mathrm{d}x. \tag{3.31}$$

We now turn to the large scale part in (3.30). Just using the triangle inequality in form of

$$\int_0^L (\zeta(x+\Delta)-\zeta(x))^2 \,\mathrm{d}x \;\le\; 4 \int_0^L \zeta^2 \,\mathrm{d}x$$

we obtain

$$\int_R^\infty \tfrac{1}{\Delta} \int_0^L (\zeta(x+\Delta)-\zeta(x))^2 \,\mathrm{d}x\, \tfrac{1}{\Delta}\,\mathrm{d}\Delta \;\lesssim\; R^{-1} \int_0^L \zeta^2 \,\mathrm{d}x. \tag{3.32}$$

Finally, we consider the small scale part in (3.30). We have by Jensen's inequality

$$\begin{aligned}
\int_0^L (\zeta(x+\Delta)-\zeta(x))^2 \,\mathrm{d}x &= \int_0^L \Big(\int_x^{x+\Delta} \partial_x\zeta(x') \,\mathrm{d}x' \Big)^2 \,\mathrm{d}x \\
&\le \int_0^L \Delta \int_x^{x+\Delta} (\partial_x\zeta(x'))^2 \,\mathrm{d}x' \,\mathrm{d}x \\
&= \Delta^2 \int_0^L (\partial_x\zeta)^2 \,\mathrm{d}x.
\end{aligned}$$

Hence we obtain

$$\int_0^r \tfrac{1}{\Delta} \int_0^L (\zeta(x+\Delta)-\zeta(x))^2 \,\mathrm{d}x \,\tfrac{1}{\Delta}\,\mathrm{d}\Delta \,\leq\, r \int_0^L (\partial_x \zeta)^2 \,\mathrm{d}x. \tag{3.33}$$

Collecting (3.31), (3.32) and (3.33) we obtain from (3.29) and (3.30)

$$\int_0^L \left||\partial_x|^{1/2}\zeta\right|^2 \mathrm{d}x \lesssim r\,\tfrac{1}{2}\int_0^L (\partial_x\zeta)^2\,\mathrm{d}x + (\ln\tfrac{R}{r})\,\tau^{-1}\int_0^L |\zeta|\,\mathrm{d}x + R^{-1}\,\tfrac{1}{2}\int_0^L \zeta^2\,\mathrm{d}x,$$

which entails

$$\langle \left||\partial_x|^{1/2}\zeta\right|^2\rangle \lesssim r\,\tfrac{1}{2}\langle(\partial_x\zeta)^2\rangle + (\ln\tfrac{R}{r})\,\tau^{-1}\,\langle|\zeta|\rangle + R^{-1}\,\tfrac{1}{2}\langle\zeta^2\rangle.$$

□

Proof of Lemma 3.11. We shall actually prove that for any L-periodic function $\zeta(x)$ with

$$\tau\partial\zeta(x) \,\leq\, 1 \quad \text{for all} \quad x,$$

we have

$$\int_0^L |\zeta(x+\Delta)-\zeta(x)|^2\,\mathrm{d}x \,\lesssim\, \Delta\,\tau^{-1}\int_0^L |\zeta(x)|\,\mathrm{d}x \quad \text{for all} \quad \Delta>0. \tag{3.34}$$

The statement of Lemma 3.11 follows by the application of (3.34) to $\zeta(x) = \tilde{\zeta}(-x,t)$.

Because of the rescaling

$$x \,=\, \Delta\,\widehat{x}, \quad L \,=\, \Delta\,\widehat{L}, \quad \zeta \,=\, \Delta\,\tau^{-1}\,\widehat{\zeta},$$

it is enough to show (3.34) for $\Delta = 1$ and $\tau^{-1} = 1$, that is under the assumption

$$\partial\zeta(x) \,\leq\, 1 \quad \text{for all} \quad x. \tag{3.35}$$

We split (3.34) into a statement for positive and for negative increments:

$$\int_0^L (\zeta(x+1)-\zeta(x))_+^2\,\mathrm{d}x \,\leq\, 2\int_0^L |\zeta(x)|\,\mathrm{d}x, \tag{3.36}$$

$$\int_0^L (\zeta(x+1)-\zeta(x))_-^2\,\mathrm{d}x \,\leq\, 4\int_0^L |\zeta(x)|\,\mathrm{d}x. \tag{3.37}$$

The statement (3.36) is easy to see. Indeed, because of (3.35), we have the pointwise bound $\zeta(x+1)-\zeta(x) \,\leq\, 1$, so that we obtain for the integrand

$$(\zeta(x+1)-\zeta(x))_+^2 \,\leq\, (\zeta(x+1)-\zeta(x))_+ \,\leq\, |\zeta(x+1)|+|\zeta(x)|.$$

This implies (3.36) after integration.

We now turn to (3.37). Because of L-periodicity we have

$$\int_0^L |\zeta(x)|(1-\partial\zeta(x))\,\mathrm{d}x \,=\, \int_0^L |\zeta(x)| - \partial(\tfrac{1}{2}\mathrm{sign}\zeta|\zeta|^2)(x)\,\mathrm{d}x \,=\, \int_0^L |\zeta(x)|\,\mathrm{d}x.$$

Hence inequality (3.37) will follow by integration from

$$(\zeta(x+1)-\zeta(x))_-^2 \;\le\; 4\int_x^{x+1} |\zeta(x')|(1-\partial\zeta(x'))\,\mathrm{d}x',$$

which by translation invariance can be reduced to

$$(\zeta(1)-\zeta(0))_-^2 \;\le\; 4\int_0^1 |\zeta(x)|(1-\partial\zeta(x))\,\mathrm{d}x. \tag{3.38}$$

Since by (3.35) the r.h.s. is positive, it is enough to consider the case $\zeta(1) \le \zeta(0)$. Now (3.38) follows from

$$\begin{aligned}(\zeta(1)-\zeta(0))_-^2 \;&\le\; -4\int_0^1 |\zeta(x)|\partial\zeta(x)\,\mathrm{d}x &(3.39)\\ &=\; -4\int_0^1 \tfrac{1}{2}\partial(\mathrm{sign}\zeta\,|\zeta|^2)(x)\,\mathrm{d}x &(3.40)\\ &=\; 2\,\mathrm{sign}\zeta(0)\,\zeta(0)^2 - 2\,\mathrm{sign}\zeta(1)\,\zeta(1)^2.\end{aligned}$$

In fact, to prove that (3.39) holds, we distinguish three cases:

Case $0 \le \zeta(1) \le \zeta(0)$: In this case

$$\begin{aligned}(\zeta(1)-\zeta(0))_-^2 \;&=\; (\zeta(0)-\zeta(1))^2\\ &\le\; \zeta(0)^2-\zeta(1)^2\\ &=\; \mathrm{sign}\zeta(0)\,\zeta(0)^2 - \mathrm{sign}\zeta(1)\,\zeta(1)^2.\end{aligned}$$

Case $\zeta(1) \le 0 \le \zeta(0)$: In this case

$$\begin{aligned}(\zeta(1)-\zeta(0))_-^2 \;&=\; (\zeta(0)-\zeta(1))^2\\ &\le\; 2\,(\zeta(0)^2+\zeta(1)^2)\\ &=\; 2\,(\mathrm{sign}\zeta(0)\,\zeta(0)^2 - \mathrm{sign}\zeta(1)\,\zeta(1)^2).\end{aligned}$$

Case $\zeta(1) \le \zeta(0) \le 0$: This follows from the first case. □

Before we start with the other proofs, let us note that $\mathcal{D} = \mathcal{D}^{\pm}$ is locally Lipschitz continuous in (t,τ). Indeed, by the triangle inequality we easily obtain for t_1, t_0 and for $\tau_1 \ge \tau_0$:

$$\begin{aligned}\mathcal{D}^{1/2}(t_1,\tau) - \mathcal{D}^{1/2}(t_0,\tau) \;&\le\; \langle |u(t_1,\cdot)-u(t_0,\cdot)|^2\rangle^{1/2},\\ \mathcal{D}^{1/2}(t,\tau_1) - \mathcal{D}^{1/2}(t,\tau_0) \;&\le\; (1-\frac{\tau_0}{\tau_1})\langle |u(t,\cdot)|^2\rangle^{1/2}.\end{aligned}$$

Clearly, $\mathcal{D}$ is monotonically increasing in τ. Indeed, let $\tau_2 > \tau_1 > 0$, and ζ be smooth and L-periodic with $\pm\,\tau_2\,\partial_x\zeta \le 1$, then also $\pm\,\tau_1\,\partial_x\zeta \le 1$ and hence

$$\begin{aligned}\mathcal{D}^{\pm}(u,\tau_1) \;&=\; \inf\{\,\langle(\zeta-u)^2\rangle \mid \zeta \text{ smooth and } L\text{-periodic}, \tau_1\partial_x\zeta \ge \pm 1\,\}\\ &\le\; \inf\{\,\langle(\zeta-u)^2\rangle \mid \zeta \text{ smooth and } L\text{-periodic}, \tau_2\partial_x\zeta \ge \pm 1\,\}\\ &=\; \mathcal{D}^{\pm}(u,\tau_2).\end{aligned} \tag{3.41}$$

Proof of Lemma 3.12. Let ζ_0 be admissible in the definition of $\mathcal{D}^-(0,\tau)$, i.e.,

$$\tau\partial_x\zeta_0 \geq -1. \tag{3.42}$$

For $\lambda > 0$ define ζ as the solution to the initial value problem

$$\begin{aligned} \partial_t\zeta - \partial_x(\tfrac{1}{2}\zeta^2) + \lambda\partial\mathcal{A}(\tau+t)\,\zeta &= \tfrac{1}{2}(\partial_x\zeta + (\tau+t)^{-1})\,(u-\zeta) \\ \zeta(\cdot,0) &= \zeta_0. \end{aligned} \tag{3.43}$$

Here, the functional $\mathcal{A}$ is defined by

$$\mathcal{A}(\tau,\zeta) = \tfrac{1}{2}\langle\, r(\partial_x\zeta)^2 + \eta + \tfrac{1}{\eta}(\ln^2\tfrac{R}{r})\,\tau^{-2}\,\zeta^2 + R^{-1}\,\zeta^2\rangle \tag{3.44}$$

for $\eta > 0$, $0 < r \leq R$, and $\tau > 0$, and the operator $\partial\mathcal{A}$ is (up to the factor L^{-1}) the functional derivative of (3.44) and thus given by

$$\partial\mathcal{A}(\tau)\,\zeta = -r\,\partial_x^2\zeta + \tfrac{1}{\eta}(\ln^2\tfrac{R}{r})\,\tau^{-2}\,\zeta + R^{-1}\,\zeta. \tag{3.45}$$

As we shall see, the reason for this choice of $\mathcal{A}$ is that

$$\min_\eta \mathcal{A}(\tau,\zeta) = \tfrac{1}{2}r\,\langle\,(\partial_x\zeta)^2\rangle + (\ln\tfrac{R}{r})\,\tau^{-1}\,\langle\zeta^2\rangle^{1/2} + \tfrac{1}{2}R^{-1}\,\langle\zeta^2\rangle$$

appears on the r.h.s. of the estimate of Lemma 3.10.

Because u is smooth and $r > 0$, a unique smooth solution to (3.43) always exists. Note that the solution ζ depends, next to the initial data and u, also on the parameters λ, η, τ, r, and R.

Step 1. Maximum principle. Here we argue that for ζ defined by (3.43) we have

$$(\tau+t)\partial_x\zeta(\cdot,t) \geq -1 \quad \text{for } t \geq 0. \tag{3.46}$$

To show (3.46) let us introduce

$$\varrho(x,t) := \partial_x\zeta + (\tau+t)^{-1}. \tag{3.47}$$

We shall argue that (3.43) can be rewritten as an advection-diffusion equation in terms of the "density" ϱ:

$$\begin{aligned} \partial_t\varrho - \partial_x(\tfrac{1}{2}\varrho\,(u+\zeta)) + (\tau+t)^{-1}\,\varrho + \lambda\,\partial\mathcal{A}(\tau+t)\,\varrho& \\ = \lambda\tfrac{1}{\eta}(\ln^2\tfrac{R}{r})\,(\tau+t)^{-3} + \lambda R^{-1}\,(\tau+t)^{-1}.& \end{aligned} \tag{3.48}$$

For a solution to (3.48) with non-negative initial data, non-negativity is preserved since the r.h.s. is positive. Due to (3.42) and (3.47) this is a reformulation of (3.46).

To see that (3.48) holds, we first rewrite the r.h.s. of (3.43):

$$\begin{aligned} \partial_t\zeta - \partial_x(\tfrac{1}{2}\zeta^2) + \lambda\partial\mathcal{A}(\tau+t)\,\zeta &= \tfrac{1}{2}(\partial_x\zeta + (\tau+t)^{-1})\,(u-\zeta) \\ &\overset{(3.47)}{=} \tfrac{1}{2}\varrho\,(u+\zeta) - (\partial_x\zeta + (t+\tau)^{-1})\zeta \\ &= \tfrac{1}{2}\varrho\,(u+\zeta) - \partial_x(\tfrac{1}{2}\zeta^2) - (\tau+t)^{-1}\zeta. \end{aligned}$$

Therefore we obtain

$$\partial_t \zeta + \lambda \partial \mathcal{A}(\tau + t)\, \zeta \;=\; \tfrac{1}{2} \varrho\, (u + \zeta) - (\tau + t)^{-1} \zeta.$$

Differentiating this equation w.r.t. x yields by linearity of $\partial \mathcal{A}$

$$\partial_t \partial_x \zeta + \lambda \partial \mathcal{A}(\tau + t)\, \partial_x \zeta \;=\; \partial_x (\tfrac{1}{2} \varrho (u + \zeta)) - (\tau + t)^{-1}\, \partial_x \zeta.$$

Hence, by definition (3.47) and linearity of $\partial \mathcal{A}$ we obtain

$$\begin{aligned} \partial_t \varrho + (\tau + t)^{-2} + \lambda \partial \mathcal{A}(\tau + t)\, \varrho - \lambda \partial \mathcal{A}(\tau + t)\, (\tau + t)^{-1} \\ = \; \partial_x (\tfrac{1}{2} \varrho\, (u + \zeta)) + (\tau + t)^{-2} - (\tau + t)^{-1}\, \varrho \end{aligned}$$

and therefore

$$\partial_t \varrho - \partial_x (\tfrac{1}{2} \varrho\, (u + \zeta)) + (\tau + t)^{-1}\, \varrho + \lambda \partial \mathcal{A}(\tau + t)\, \varrho \;=\; \lambda \partial \mathcal{A}(\tau + t)\, (\tau + t)^{-1}.$$

Appealing to the definition (3.45) of $\partial \mathcal{A}$ this yields (3.48).

Step 2. L^2-Contraction. In this step we show that there exists a constant $C > 0$ s.t.

$$\begin{aligned} \partial_t (\tfrac{1}{2} \langle (u - \zeta)^2 \rangle - \tfrac{1}{2} \langle u^2 \rangle) + (\tau + t)^{-1} \tfrac{1}{2} \langle (u - \zeta)^2 \rangle \\ \leq \; \lambda \mathcal{A}(\tau + t, u) \;\; + \tfrac{C}{4\lambda} \langle \big| |\partial_x|^{-1/2} \sigma \big|^2 \rangle. \end{aligned} \tag{3.49}$$

We first rewrite equation (3.43) as

$$-\partial_t \zeta + \tfrac{1}{2} (\tau + t)^{-1}\, (u - \zeta) + u\, \partial_x \zeta - \tfrac{1}{2} (\partial_x \zeta)\, (u - \zeta) \;=\; \lambda \partial \mathcal{A}(\tau + t)\, \zeta$$

and combine it with $\partial_t u - u\, \partial_x u \;=\; \sigma$ which gives

$$\begin{aligned} \partial_t (u - \zeta) + \tfrac{1}{2} (\tau + t)^{-1}\, (u - \zeta) - u\, \partial_x (u - \zeta) - \tfrac{1}{2} (\partial_x \zeta)\, (u - \zeta) \\ = \; \sigma + \lambda \partial \mathcal{A}(\tau + t)\, \zeta. \end{aligned}$$

We multiply this equation by $u - \zeta$ and apply Leibniz' rule to obtain

$$\begin{aligned} \partial_t \tfrac{1}{2} (u - \zeta)^2 + \tfrac{1}{2} (\tau + t)^{-1} (u - \zeta)^2 - u \tfrac{1}{2} \partial_x (u - \zeta)^2 - (\partial_x \zeta) \tfrac{1}{2} (u - \zeta)^2 \\ = \; \sigma (u - \zeta) + \lambda (\partial \mathcal{A}(\tau + t)\, \zeta)\, (u - \zeta). \end{aligned}$$

Taking averages w.r.t. x and integration by parts yields

$$\begin{aligned} \tfrac{1}{2} \partial_t \langle (u - \zeta)^2 \rangle + \tfrac{1}{2} (\tau + t)^{-1} \langle (u - \zeta)^2 \rangle + \langle (\partial_x u - \partial_x \zeta) \tfrac{1}{2} (u - \zeta)^2 \rangle \\ = \; \langle \sigma (u - \zeta) \rangle + \langle \lambda (\partial \mathcal{A}(\tau + t)\, \zeta)\, (u - \zeta) \rangle. \end{aligned} \tag{3.50}$$

On the other hand, multiplying $\partial_t u - u\, \partial_x u \;=\; \sigma$ with u and taking averages w.r.t. x we have

$$\partial_t \tfrac{1}{2} \langle u^2 \rangle \;=\; \langle \sigma\, u \rangle. \tag{3.51}$$

Because of $\langle(\partial_x u - \partial_x \zeta)\frac{1}{2}(u-\zeta)^2\rangle = 0$, the combination of (3.50) and (3.51) yields

$$\begin{aligned}
&\tfrac{1}{2}\partial_t\langle(u-\zeta)^2\rangle - \tfrac{1}{2}\partial_t\langle u^2\rangle + (\tau+t)^{-1}\tfrac{1}{2}\langle(u-\zeta)^2\rangle \\
&\quad = \langle\lambda(\partial\mathcal{A}(\tau+t)\,\zeta)\,(u-\zeta)\rangle - \langle\sigma\,\zeta\rangle, \\
&\overset{\text{Cauchy-Schwarz}}{\leq} \quad \langle\lambda(\partial\mathcal{A}(\tau+t)\,\zeta)\,(u-\zeta)\rangle + \langle\big||\partial_x|^{-1/2}\sigma\big|^2\rangle^{1/2}\langle(|\partial_x|^{1/2}\zeta)^2\rangle^{1/2}
\end{aligned}$$

Due to the convexity of $\mathcal{A}$ and by Young's inequality we thus obtain

$$\begin{aligned}
&\tfrac{1}{2}\partial_t\langle(u-\zeta)^2\rangle - \tfrac{1}{2}\partial_t\langle u^2\rangle + (\tau+t)^{-1}\tfrac{1}{2}\langle(u-\zeta)^2\rangle \\
&\quad \leq \lambda\mathcal{A}(\tau+t,u) - \lambda\mathcal{A}(\tau+t,\zeta) + \tfrac{C}{4\lambda}\langle\big||\partial_x|^{-1/2}\sigma\big|^2\rangle + \tfrac{\lambda}{C}\langle(|\partial_x|^{1/2}\zeta)^2\rangle, \quad (3.52)
\end{aligned}$$

where we choose $C > 0$ to be the constant in the estimate of Lemma 3.10. Since $\zeta(\cdot,t)$ fulfills the assumptions of Lemma 3.10 according to Step 1, more precisely $(\tau+t)\,\partial_x\zeta(x,t) \geq -1$ for $t \geq 1$, we have by Young's inequality (w.r.t. η)

$$\langle(|\partial_x|^{1/2}\zeta)^2\rangle^{1/2} \leq C\,\mathcal{A}(\tau+t,\zeta).$$

Hence (3.52) turns into

$$\begin{aligned}
&\tfrac{1}{2}\partial_t\langle(u-\zeta)^2\rangle - \tfrac{1}{2}\partial_t\langle u^2\rangle + (\tau+t)^{-1}\tfrac{1}{2}\langle(u-\zeta)^2\rangle \\
&\qquad\qquad \leq \lambda\mathcal{A}(\tau+t,u) + \tfrac{C}{4\lambda}\langle\big||\partial_x|^{-1/2}\sigma\big|^2\rangle. \quad (3.53)
\end{aligned}$$

Step 3. The integration of (3.53) in t gives

$$\begin{aligned}
&\tfrac{1}{2}\langle(u(\cdot,t)-\zeta(\cdot,t))^2\rangle - \tfrac{1}{2}\langle u^2(\cdot,t)\rangle + \int_0^t(\tau+t')^{-1}\tfrac{1}{2}\langle(u(\cdot,t')-\zeta(\cdot,t'))^2\rangle\,\mathrm{d}t' \\
&\leq \tfrac{1}{2}\langle(u(\cdot,0)-\zeta(\cdot,0))^2\rangle - \tfrac{1}{2}\langle u^2(\cdot,0)\rangle + \int_0^t \lambda\mathcal{A}(\tau+t',u(\cdot,t')) \\
&\qquad\qquad + \tfrac{C}{4\lambda}\langle\big||\partial_x|^{-1/2}\sigma(\cdot,t')\big|^2\rangle\,\mathrm{d}t'.
\end{aligned}$$

According to Step 1, $\zeta(x,t')$ is admissible in the definition of $\mathcal{D}^-(t',\tau+t')$, so that we obtain

$$\begin{aligned}
&\tfrac{1}{2}\mathcal{D}^-(t,\tau+t) - \tfrac{1}{2}\langle u^2(\cdot,t)\rangle + \int_0^t(\tau+t')^{-1}\tfrac{1}{2}\mathcal{D}^-(t',\tau+t')\,\mathrm{d}t' \\
&\leq \tfrac{1}{2}\langle(u(\cdot,0)-\zeta_0)^2\rangle - \tfrac{1}{2}\langle u^2(\cdot,0)\rangle \\
&\qquad\qquad + \int_0^t \lambda\mathcal{A}(\tau+t',u(\cdot,t')) + \tfrac{C}{4\lambda}\langle\big|\partial_x|^{-1/2}\sigma(\cdot,t')\big|^2\rangle\,\mathrm{d}t'.
\end{aligned}$$

Finally, since ζ_0 was an arbitrary admissible function in $\mathcal{D}^-(0,\tau)$, this turns into

$$\begin{aligned}
&\tfrac{1}{2}(\mathcal{D}^-(t,\tau+t) - \langle u^2(\cdot,t)\rangle) + \tfrac{1}{2}\int_0^t(\tau+t')^{-1}\mathcal{D}^-(t',\tau+t')\,\mathrm{d}t' \\
&\quad \leq \tfrac{1}{2}(\mathcal{D}^-(0,\tau) - \langle u^2(\cdot,0)\rangle) \\
&\qquad\qquad + \int_0^t \lambda\mathcal{A}(\tau+t',u(\cdot,t')) + \tfrac{C}{4\lambda}\langle\big||\partial_x|^{-1/2}\sigma(\cdot,t')\big|^2\rangle\,\mathrm{d}t' \quad (3.54)
\end{aligned}$$

for all $t \geq 0$ and $\tau > 0$. Since $\mathcal{D}^-$ is locally Lipschitz continuous in both variables and by translation invariance in t, (3.54) entails a differential version:

$$\partial_t \tfrac{1}{2}(\mathcal{D}^-(t,\tau) - \langle u^2 \rangle) + \partial_\tau \tfrac{1}{2}\mathcal{D}^-(t,\tau) + \tau^{-1}\tfrac{1}{2}\mathcal{D}^-(t,\tau) \\ \leq \lambda \mathcal{A}(\tau,u) + \tfrac{C}{4\lambda}\langle \big||\partial_x|^{-1/2}\sigma\big|^2 \rangle. \quad (3.55)$$

Indeed, a Lipschitz function is classically differentiable almost everywhere and its classical derivative agrees with its weak derivative.

Step 4. Optimization.

The l.h.s. of (3.55) does not depend on $\lambda > 0$ and holds for all $t \geq 0$ and $\tau > 0$. Therefore, we can now optimize on the r.h.s. of (3.55) in λ to derive:

$$\partial_t \tfrac{1}{2}(\mathcal{D}^-(t,\tau) - \langle u^2 \rangle) + \partial_\tau \tfrac{1}{2}\mathcal{D}^-(t,\tau) + \tau^{-1}\tfrac{1}{2}\mathcal{D}^-(t,\tau) \\ \lesssim \mathcal{A}(\tau,u)^{1/2} \langle \big||\partial_x|^{-1/2}\sigma\big|^2 \rangle^{1/2}. \quad (3.56)$$

Since (3.56) holds true for all $\eta > 0$ and $0 < r \leq R$, we optimize at fixed $\varepsilon = \frac{r}{R} \leq 1$ in η and R:

$$\begin{aligned} \min_{\eta,R} \mathcal{A}(\tau,u) &= \min_{\eta,R} \tfrac{1}{2}\langle r(\partial_x u)^2 + \eta + \tfrac{1}{\eta}(\ln^2 \tfrac{R}{r})\,\tau^{-2}\,u^2 + R^{-1}\,u^2 \rangle \\ &\sim \min_{R} R\,\varepsilon \langle (\partial_x u)^2 \rangle + (\ln \tfrac{1}{\varepsilon})\,\tau^{-1}\langle u^2 \rangle^{1/2} + R^{-1}\,\langle u^2 \rangle \\ &\sim \varepsilon^{1/2}\,\langle (\partial_x u)^2 \rangle^{1/2}\,\langle u^2 \rangle^{1/2} + (\ln \tfrac{1}{\varepsilon})\,\tau^{-1}\langle u^2 \rangle^{1/2}. \end{aligned}$$

□

Proof of Corollary 3.13. In the following proof, we repeatedly use that due to (1.15)

$$\begin{aligned} \langle\, u(t=0)^2 \,\rangle = \langle\, u(t=1)^2 \,\rangle = 0, \quad \text{and thus} \\ \mathcal{D}^-(u(t=0),\tau) = \mathcal{D}^-(u(t=1),\tau) = 0 \quad \text{for all } \tau > 0. \end{aligned} \quad (3.57)$$

Step 1. We drop the positive terms $\tau^{-1}\mathcal{D}^-$ and $\partial_\tau \mathcal{D}^-$, cf. (3.41), on the l.h.s. of (3.23) and integrate backwards in t and get due to (3.57)

$$\begin{aligned} &\langle u^2(\cdot,t)\rangle - \mathcal{D}^-(t,\tau) \\ &\quad \lesssim \int_t^1 \langle \big||\partial_x|^{-1/2}\sigma\big|^2 \rangle^{1/2}\,(\,\varepsilon^{1/2}\,\langle (\partial_x u)^2 \rangle^{1/2}\,\langle u^2 \rangle^{1/2} + (\ln \tfrac{1}{\varepsilon})\,\tau^{-1}\langle u^2 \rangle^{1/2}\,)^{1/2}\,\mathrm{d}t' \\ &\quad \leq \int_0^1 \langle \big||\partial_x|^{-1/2}\sigma\big|^2 \rangle^{1/2}\,(\,\varepsilon^{1/2}\,\langle (\partial_x u)^2 \rangle^{1/2}\,\langle u^2 \rangle^{1/2} + (\ln \tfrac{1}{\varepsilon})\,\tau^{-1}\langle u^2 \rangle^{1/2}\,)^{1/2}\,\mathrm{d}t'. \end{aligned}$$

Applying Jensen's and Cauchy-Schwarz' inequality in t gives

$$\langle u^2(\cdot,t)\rangle - \mathcal{D}^-(t,\tau) \lesssim \langle\!\langle \big||\partial_x|^{-1/2}\sigma\big|^2 \rangle\!\rangle^{1/2} \times \\ (\,\varepsilon^{1/2}\,\langle\!\langle (\partial_x u)^2 \rangle\!\rangle^{1/2}\,\langle\!\langle u^2 \rangle\!\rangle^{1/2} + (\ln \tfrac{1}{\varepsilon})\,\tau^{-1}\langle\!\langle u^2 \rangle\!\rangle^{1/2}\,)^{1/2}. \quad (3.58)$$

Averaging (3.58) w.r.t. t yields

$$\langle\!\langle u^2 \rangle\!\rangle \lesssim \langle \mathcal{D}^- \rangle(\tau) + \langle\!\langle \big| |\partial_x|^{-1/2} \sigma \big|^2 \rangle\!\rangle^{1/2} \times \\ (\varepsilon^{1/2} \langle\!\langle (\partial_x u)^2 \rangle\!\rangle^{1/2} \langle\!\langle u^2 \rangle\!\rangle^{1/2} + (\ln \tfrac{1}{\varepsilon})\, \tau^{-1} \langle\!\langle u^2 \rangle\!\rangle^{1/2})^{1/2}. \quad (3.59)$$

Step 2. Consider again (3.23). We drop the positive term $\partial_\tau \mathcal{D}^-$, cf. (3.41). We then average over $t \in [0,1]$. Because of (3.57), the $\partial_t \frac{1}{2}(\mathcal{D}^- - \langle u^2 \rangle)$-term vanishes. Using Cauchy-Schwarz' and Jensen's inequality as above we obtain

$$\tau^{-1} \langle \mathcal{D}^- \rangle(\tau) \lesssim \langle\!\langle \big| |\partial_x|^{-1/2} \sigma \big|^2 \rangle\!\rangle^{1/2} \times \\ (\varepsilon^{1/2} \langle\!\langle (\partial_x u)^2 \rangle\!\rangle^{1/2} \langle\!\langle u^2 \rangle\!\rangle^{1/2} + (\ln \tfrac{1}{\varepsilon})\, \tau^{-1} \langle\!\langle u^2 \rangle\!\rangle^{1/2})^{1/2}. \quad (3.60)$$

Combining inequalities (3.59) and (3.60) gives in our short hand notation, cf. (3.27),

$$U \lesssim (1+\tau)\, \Sigma^{1/2} \, (\varepsilon^{1/2} D U^{1/2} U^{1/2} + (\ln \tfrac{1}{\varepsilon}) \tau^{-1}\, U^{1/2})^{1/2}.$$

Choosing $\tau \sim 1$ yields

$$\begin{aligned} U &\lesssim \Sigma^{1/2} \, (\varepsilon^{1/2} D U^{1/2} U^{1/2} + (\ln \tfrac{1}{\varepsilon})\, U^{1/2})^{1/2} \\ &\lesssim \Sigma^{1/2} \, (\varepsilon D U)^{1/4} U^{1/4} + ((\ln \tfrac{1}{\varepsilon}) \Sigma)^{1/2}\, U^{1/4}, \end{aligned}$$

and by Young's inequality we absorb U into the l.h.s. to obtain (3.24):

$$U \lesssim \Sigma^{2/3} \; (\varepsilon\, D U)^{1/3} \; + \; ((\ln \tfrac{1}{\varepsilon}) \Sigma)^{2/3}.$$

□

Proof of Corollary 3.14. We start from (3.60) in the proof of Corollary 3.13, i.e.,

$$\tau^{-1} \langle \mathcal{D}^- \rangle(\tau) \\ \lesssim \langle\!\langle \big| |\partial_x|^{-1/2} \sigma \big|^2 \rangle\!\rangle^{1/2} \; (\varepsilon^{1/2} \langle\!\langle (\partial_x u)^2 \rangle\!\rangle^{1/2} \langle\!\langle u^2 \rangle\!\rangle^{1/2} + (\ln \tfrac{1}{\varepsilon})\, \tau^{-1} \langle\!\langle u^2 \rangle\!\rangle^{1/2})^{1/2},$$

which in our short hand notation turns into

$$\begin{aligned} &\tau^{-1} \langle \mathcal{D}^- \rangle(\tau) \\ &\quad \lesssim \Sigma^{1/2} \; (\, (\varepsilon D U)^{1/2}\, U^{1/2} + (\ln \tfrac{1}{\varepsilon}) \tau^{-1} U^{1/2} \,)^{1/2} \\ &\overset{\text{Triangle ineq.}}{\lesssim} \quad \tau^{1/8} \Sigma^{1/2} (\varepsilon D U)^{1/4} \, (\tau^{-1/2} U)^{1/4} + \tau^{-1/2} ((\ln \tfrac{1}{\varepsilon})\, \Sigma)^{1/2}\, U^{1/4} \\ &\overset{\text{Young}}{\lesssim} \quad \tau^{1/6} \Sigma^{2/3} (\varepsilon D U)^{1/3} \; + \; \tau^{-1/2} U \; + \; \tau^{-1/2} ((\ln \tfrac{1}{\varepsilon})\, \Sigma)^{1/2} U^{1/4} \\ &\overset{(3.24)}{\lesssim} \quad \tau^{1/6} \Sigma^{2/3} (\varepsilon D U)^{1/3} \; + \; \tau^{-1/2} \left(\Sigma^{2/3} \; (\varepsilon\, D U)^{1/3} \; + \; ((\ln \tfrac{1}{\varepsilon}) \Sigma)^{2/3} \right) \\ &\qquad + \tau^{-1/2} ((\ln \tfrac{1}{\varepsilon})\, \Sigma)^{1/2} \left(\Sigma^{2/3} \; (\varepsilon\, D U)^{1/3} \; + \; ((\ln \tfrac{1}{\varepsilon}) \Sigma)^{2/3} \right)^{1/4} \\ &\quad \lesssim \tau^{1/6} \Sigma^{2/3} (\varepsilon D U)^{1/3} \; + \; \tau^{-1/2} \left(\Sigma^{2/3} \; (\varepsilon\, D U)^{1/3} \; + \; ((\ln \tfrac{1}{\varepsilon}) \Sigma)^{2/3} \right) \\ &\qquad + \tau^{-3/8} ((\ln \tfrac{1}{\varepsilon})\, \Sigma)^{1/2} \left(\tau^{-1/2} \Sigma^{2/3} \; (\varepsilon\, D U)^{1/3} \right)^{1/4} \\ &\overset{\text{Young}}{\lesssim} \quad (\tau^{1/6} + \tau^{-1/2}) \Sigma^{2/3} (\varepsilon D U)^{1/3} \; + \; \tau^{-1/2} ((\ln \tfrac{1}{\varepsilon}) \Sigma)^{2/3}. \end{aligned}$$

Therefore we deduce for $\tau \leq 1$

$$\tau^{-1}\langle \mathcal{D}^- \rangle(\tau) \lesssim \tau^{-1/2} \Big(((\ln \tfrac{1}{\varepsilon})\Sigma)^{2/3} + \Sigma^{2/3}(\varepsilon DU)^{1/3} \Big). \tag{3.61}$$

On the other hand, for $\tau \geq 1$ we have

$$\begin{aligned} \langle \mathcal{D}^-(\tau) \rangle &\overset{\zeta=0}{\leq} U \\ &\lesssim \tau^{1/2} U \\ &\overset{(3.24)}{\lesssim} \tau^{1/2} \Big(((\ln \tfrac{1}{\varepsilon})\Sigma)^{2/3} + \Sigma^{2/3}(\varepsilon DU)^{1/3} \Big). \end{aligned} \tag{3.62}$$

Collecting estimates (3.61) and (3.62), we now obtain

$$\sup_{\tau>0} \tau^{-1/2}\langle \mathcal{D}^- \rangle(\tau) \lesssim ((\ln \tfrac{1}{\varepsilon})\Sigma)^{2/3} + \Sigma^{2/3}(\varepsilon DU)^{1/3}. \tag{3.63}$$

For $\mathcal{D}^+$ note that the change of variables $\widehat{t} = 1 - t$, $\widehat{u} = -u$ leaves the r.h.s. of (3.63) invariant whereas the l.h.s. turns into

$$\mathcal{D}^-(\widehat{u}(\cdot,\widehat{t}),\tau) = \mathcal{D}^-(-u(\cdot,1-t),\tau) = \mathcal{D}^+(u(\cdot,1-t),\tau),$$

which gives

$$\langle \mathcal{D}^-(\widehat{u},\tau) \rangle = \langle \mathcal{D}^+(u,\tau) \rangle.$$

Therefore we obtain (3.25) in our short hand notation, i.e.,

$$\sup_{\tau>0} \tau^{-1/2}\langle \mathcal{D}^+ \rangle(\tau) + \sup_{\tau>0} \tau^{-1/2}\langle \mathcal{D}^- \rangle(\tau) \lesssim ((\ln \tfrac{1}{\varepsilon})\Sigma)^{2/3} + \Sigma^{2/3}(\varepsilon DU)^{1/3}.$$

□

Proof of Lemma 3.15. The main ingredient is the following estimate of the modulus of continuity in the weak $L^{5/2}$-norm

$$\begin{aligned} \sup_{\Delta>0} \Delta^{-1/2} \sup_{M>0} M^{5/2} \langle\!\langle I(|u^\Delta - u| > M) \rangle\!\rangle& \\ \lesssim \sup_{\tau>0} \tau^{-1/2}\langle \mathcal{D}^+ \rangle + \sup_{\tau>0} \tau^{-1/2}\langle \mathcal{D}^- \rangle,& \end{aligned} \tag{3.64}$$

where I denotes the indicator function. To see that (3.64) holds, fix Δ, $M > 0$ and let $\zeta^+(x,t)$ and $\zeta^-(x,t)$ be L-periodic in x with $\pm\tau\partial_x\zeta^\pm \leq 1$ for some $\tau > \frac{\Delta}{M}$ given. Then we have

$$\begin{aligned} |\{|u^\Delta - u| > M\}| &= |\{u^\Delta - u > M\}| + |\{u^\Delta - u < -M\}| \\ &\leq |\{(u-\zeta^+)^\Delta - (u-\zeta^+) > (M - \tfrac{\Delta}{\tau})\}| \\ &\quad + |\{(u-\zeta^-)^\Delta - (u-\zeta^-) < -(M - \tfrac{\Delta}{\tau})\}| \\ &\leq (M - \tfrac{\Delta}{\tau})^{-2} \Big(\int_0^L ((u-\zeta^+)^\Delta - (u-\zeta^+))^2 \,\mathrm{d}x \\ &\quad + \int_0^L ((u-\zeta^-)^\Delta - (u-\zeta^-))^2 \,\mathrm{d}x \Big) \\ &\leq 4\,(M - \tfrac{\Delta}{\tau})^{-2} \Big(\int_0^L (u-\zeta^+)^2 \,\mathrm{d}x + \int_0^L (u-\zeta^-)^2 \,\mathrm{d}x \Big). \end{aligned}$$

Since $\zeta^{\pm}$ was arbitrary in the definition of $\mathcal{D}^{\pm}(\tau)$, we obtain

$$\langle I(|u^\Delta - u| > M)\rangle \leq 4\,(M - \tfrac{\Delta}{\tau})^{-2}(\mathcal{D}^+(\tau) + \mathcal{D}^-(\tau)).$$

Therefore we have

$$\langle I(|u^\Delta - u| > M)\rangle \leq \tau^{1/2} 4\,(M - \tfrac{\Delta}{\tau})^{-2}\,(\sup_{\tilde\tau>0} \tilde\tau^{-1/2}\mathcal{D}^+(\tilde\tau) + \sup_{\tilde\tau>0} \tilde\tau^{-1/2}\mathcal{D}^-(\tilde\tau)).$$

Now optimizing in $\tau > \frac{\Delta}{M}$ gives

$$\langle I(|u^\Delta - u| > M)\rangle \lesssim (\tfrac{\Delta}{M})^{1/2} M^{-2}\,(\sup_{\tilde\tau>0} \mathcal{D}^+(\tilde\tau) + \sup_{\tilde\tau>0} \mathcal{D}^-(\tilde\tau)),$$

which entails (3.64).

Plugging in Corollary 3.14 we obtain from (3.64) for all $\Delta > 0$

$$\Delta^{-1/2} \sup_{M>0} M^{5/2} \langle\!\langle I(|u^\Delta - u| > M)\rangle\!\rangle \lesssim ((\ln \tfrac{1}{\varepsilon})\Sigma)^{2/3} + \Sigma^{2/3}(\varepsilon DU)^{1/3}. \tag{3.65}$$

We can now interpolate the strong estimate on the modulus of continuity that we obtain from Corollary 3.13, i.e.,

$$\langle\!\langle |u^\Delta - u|^2\rangle\!\rangle \lesssim \langle\!\langle u^2\rangle\!\rangle \overset{(3.24)}{\lesssim} ((\ln \tfrac{1}{\varepsilon})\Sigma)^{2/3} + \Sigma^{2/3}(\varepsilon DU)^{1/3},$$

and the weak estimate (3.65). By Marcinkiewicz interpolation, cf. [BL76, Section 5.3], we obtain for $0 \leq \beta < 1$

$$\begin{aligned}\langle\!\langle |u^\Delta - u|^{2+\frac{1}{2}\beta}\rangle\!\rangle &\lesssim \langle\!\langle |u^\Delta - u|^2\rangle\!\rangle^{1-\beta}\,(\sup_{M>0} M^{5/2}\langle\!\langle I\,(|u^\Delta - u| > M)\rangle\!\rangle)^{\beta} \\ &\lesssim \Delta^{\frac{\beta}{2}}\,\left(((\ln \tfrac{1}{\varepsilon})\Sigma)^{2/3} + \Sigma^{2/3}(\varepsilon DU)^{1/3}\right).\end{aligned}$$

With the identification $p = 2 + \frac{\beta}{2}$ we obtain (3.26), i.e.,

$$\sup_{\Delta>0} \Delta^{-(p-2)} \langle\!\langle |u^\Delta - u|^p\rangle\!\rangle \lesssim ((\ln \tfrac{1}{\varepsilon})\Sigma)^{2/3} + \Sigma^{2/3}(\varepsilon DU)^{1/3}$$

for $p \in [2, \frac{5}{2})$, in our short hand notation. □

Proof of Lemma 3.17. Let $C > 0$ be a generic constant. Due to Remark 3.16 it follows that Corollary 3.13, which was established for smooth u, extends to our finite-energy u:

$$\begin{aligned}U &\lesssim ((\ln \tfrac{1}{\varepsilon})\Sigma)^{2/3}\,(1 + (\ln \tfrac{1}{\varepsilon})^{-2/3}\,(\varepsilon DU)^{1/3}) \\ &\overset{\varepsilon\ll 1}{\lesssim} ((\ln \tfrac{1}{\varepsilon})\Sigma)^{2/3}\,(1 + (\varepsilon DU)^{1/3}).\end{aligned} \tag{3.66}$$

Hence we obtain by Young's inequality

$$\begin{aligned} L^{-1}E(u) &= \varepsilon DU + (\ln \tfrac{1}{\varepsilon})\Sigma - U \\ &\overset{\varepsilon \ll 1}{\geq} \varepsilon DU + (\ln \tfrac{1}{\varepsilon})\Sigma - C\left((\ln \tfrac{1}{\varepsilon})\Sigma\right)^{2/3}\left(1 + (\varepsilon DU)^{1/3}\right) \\ &\overset{\text{Young}}{\gtrsim} \varepsilon DU + (\ln \tfrac{1}{\varepsilon})\Sigma - C, \end{aligned}$$

where C is the constant in estimate (3.66). This entails

$$\varepsilon DU + (\ln \tfrac{1}{\varepsilon})\Sigma \overset{\varepsilon \ll 1}{\lesssim} \begin{cases} 1 & \text{for } L^{-1}E(u) \leq 1, \\ L^{-1}E(u) & \text{for } L^{-1}E(u) \geq 1. \end{cases}$$

Therefore we obtain if we once again apply Young's inequality to (3.66):

$$U \overset{\varepsilon \ll 1}{\lesssim} \left((\ln \tfrac{1}{\varepsilon})\Sigma\right)^{2/3}\left(1 + (\varepsilon DU)^{1/3}\right) \overset{\varepsilon \ll 1}{\lesssim} \begin{cases} 1 & \text{for } L^{-1}E(u) \leq 1, \\ L^{-1}E(u) & \text{for } L^{-1}E(u) \geq 1. \end{cases}$$

□

Proof of Proposition 3.8. Due to Lemma 3.17, we have that for any u with $L^{-1}E(u) \leq 0$

$$\varepsilon DU,\ (\ln \tfrac{1}{\varepsilon})\Sigma,\ U \lesssim 1.$$

In particular

$$L^{-1}E(u) \geq -U \gtrsim -1.$$

□

Proof of Theorem 3.4. Let $0 < \varepsilon \ll 1$ and $L \geq 1$.

ad a) The upper bound on the minimal energy is the statement of Proposition 3.6, the lower bound is the statement of Proposition 3.8.

ad b) The upper bound

$$L^{-1}\int_0^L \int_0^1 u^2 \,\mathrm{d}t\,\mathrm{d}x \lesssim 1$$

was treated in Proposition 3.8. The lower bound

$$L^{-1}\int_0^L \int_0^1 u^2 \,\mathrm{d}t\,\mathrm{d}x \gtrsim 1$$

follows directly from the assumption $L^{-1}E(u) \sim -1$.

ad c1) Note that by Jensen's inequality

$$w^{-2(p-2)/p}\, L^{-1} \int_0^L \int_0^1 (u(x+w,t)-u(x,t))^2 \,\mathrm{d}t\,\mathrm{d}x \\ \lesssim \left(w^{-(p-2)}\, L^{-1} \int_0^L \int_0^1 (u(x+w,t)-u(x,t))^p \,\mathrm{d}t\,\mathrm{d}x \right)^{2/p} \tag{3.67}$$

for $p \in [2,\infty)$. Due to Lemma 3.17 we have for any u with $L^{-1}E(u) \sim -1$, that εDU, $(\ln \frac{1}{\varepsilon})\Sigma$, $U \lesssim 1$ (uniformly in ε). Hence the r.h.s. in (3.67) is bounded for $p \in [2, \frac{5}{2})$ (uniformly in ε) due to Lemma 3.15, which due to Remark 3.16 extends to our finite-energy u. Therefore with the identification $\alpha = 2(p-2)/p$ we have

$$L^{-1} \int_0^L \int_0^1 (u(x+w,t)-u(x,t))^2 \,\mathrm{d}t\,\mathrm{d}x \lesssim w^\alpha$$

for $\alpha \in [0, \frac{2}{5})$.

ad c2) We split the proof into an estimate for $w \leq 1$ and an estimate for $w \geq 1$. For $w \leq 1$ we have by Jensen's inequality

$$L^{-1} \int_0^L \int_0^L |u_w| \,\mathrm{d}t\,\mathrm{d}x \leq \left(L^{-1} \int_0^L \int_0^L u^2 \,\mathrm{d}t\,\mathrm{d}x \right)^{1/2} \\ \leq w^{-1/2} \left(L^{-1} \int_0^L \int_0^L u^2 \,\mathrm{d}t\,\mathrm{d}x \right)^{1/2}.$$

Due to Lemma 3.17, for u with $L^{-1}E(u) \sim -1$ the energy contributions are separately bounded. Hence we obtain

$$L^{-1} \int_0^L |u_w| \,\mathrm{d}x \lesssim w^{-1/2}.$$

We now turn to the case $w \geq 1$. By linearity we have that

$$\partial_t u_w - (\partial_x(\tfrac{1}{2}u^2))_w = \sigma_w.$$

Therefore by the triangle inequality we have

$$L^{-1} \int_0^L |\partial_t u_w| \,\mathrm{d}x \lesssim L^{-1} \int_0^L |(\partial_x(\tfrac{1}{2}u^2))_w| \,\mathrm{d}x + L^{-1} \int_0^L |\sigma_w| \,\mathrm{d}x. \tag{3.68}$$

We now appeal to the estimates

$$L^{-1} \int_0^L |(\partial_x(\tfrac{1}{2}u^2))_w| \,\mathrm{d}x \lesssim w^{-1} L^{-1} \int_0^L u^2 \,\mathrm{d}x \tag{3.69}$$

and

$$L^{-1} \int_0^L |\sigma_w| \,\mathrm{d}x \lesssim w^{-1/2} \left(L^{-1} \int_0^L \left| |\partial_x|^{-1/2} \sigma \right|^2 \mathrm{d}x \right)^{1/2}. \tag{3.70}$$

We first turn to (3.69). By definition,

$$\begin{aligned}\int_0^L |(\partial_x u^2)_w| \,\mathrm{d}x &= \int_0^L \Big| w^{-1} \int_{-\frac{w}{2}}^{\frac{w}{2}} \partial_x u^2(x+x') \,\mathrm{d}x' \Big| \,\mathrm{d}x \\ &= w^{-1} \int_0^L |u^2(x+\tfrac{w}{2}) - u^2(x-\tfrac{w}{2})| \,\mathrm{d}x \\ &\leq w^{-1} \int_0^L u^2 \,\mathrm{d}x.\end{aligned}$$

We now turn to (3.70), which is a standard convolution estimate. We start with Jensen's inequality in the form of

$$L^{-1} \int_0^L |\sigma_w| \,\mathrm{d}x \leq \left(L^{-1} \int_0^L |\sigma_w|^2 \,\mathrm{d}x \right)^{1/2}. \tag{3.71}$$

By definition,

$$\sigma_w(x,t) = \int_{\mathbb{R}} \eta^w(y) \, \sigma(x-y,t) \,\mathrm{d}y,$$

where $\eta^w(x) := w^{-1}\eta(\frac{x}{w})$ and $\eta(x) := I([-\frac{1}{2},\frac{1}{2}])(x)$. We appeal to the Fourier series $\mathcal{F}(\sigma)(\xi) = \frac{1}{\sqrt{L}} \int_0^L \sigma(x) \, \mathrm{e}^{-i\,x\xi} \,\mathrm{d}x$, $\xi \in 2\pi L^{-1}\mathbb{Z}$, of σ and to the Fourier transform $\mathcal{F}(\eta^w)(\xi) = \int_{\mathbb{R}} \eta^w(x) \, \mathrm{e}^{-i\,x\xi} \,\mathrm{d}x$, $\xi \in \mathbb{R}$, of η^w:

$$\begin{aligned}\int_0^L |\sigma_w|^2 \,\mathrm{d}x &= \sum_{\xi \in 2\pi L^{-1}\mathbb{Z}} |\mathcal{F}(\sigma_w)|^2(\xi) \\ &= \sum_{\xi \in 2\pi L^{-1}\mathbb{Z}} |\mathcal{F}(\eta^w)(\xi)|^2 |\mathcal{F}(\sigma)(\xi)|^2 \\ &= \sum_{\xi \in 2\pi L^{-1}\mathbb{Z}} |\mathcal{F}(\eta)(w\,\xi)|^2 |\mathcal{F}(\sigma)(\xi)|^2. \end{aligned} \tag{3.72}$$

We explicitly calculate the Fourier transform of η:

$$\mathcal{F}(\eta)(\xi) = \int_{\mathbb{R}} \eta(x) \, \mathrm{e}^{-i\,x\,\xi} \,\mathrm{d}x = \int_{-\frac{1}{2}}^{\frac{1}{2}} \mathrm{e}^{-i\,x\,\xi} \,\mathrm{d}x = 2\sin(\tfrac{\xi}{2}).$$

Hence we have

$$|\mathcal{F}(\eta)(\xi)| \lesssim \frac{1}{1+|\xi|} \lesssim \frac{1}{|\xi|^{1/2}}.$$

Thus (3.72) turns into

$$\int_0^L |\sigma_w|^2 \,\mathrm{d}x \lesssim \frac{1}{w} \sum_{\xi \in 2\pi L^{-1}\mathbb{Z}} \frac{1}{|\xi|} |\mathcal{F}(\sigma)(\xi)|^2 = \frac{1}{w} \int_0^L \big| |\partial_x|^{-1/2} \sigma \big|^2 \,\mathrm{d}x.$$

Now (3.70) follows from the last estimate together with (3.71).

In order to control the r.h.s. of (3.68), we collect estimates (3.69) and (3.70) and use again that for u with $L^{-1}E(u) \sim -1$ the energy contributions are separately bounded by Lemma 3.17 to obtain

$$L^{-1}\int_0^L |\partial_t u_w|\,\mathrm{d}x \lesssim w^{-1} + w^{-1/2} \overset{w\geq 1}{\lesssim} w^{-1/2}. \tag{3.73}$$

Hence we have for $w \geq 1$

$$\begin{aligned} L^{-1}\int_0^1\int_0^L |u_w(x,t)|\,\mathrm{d}x\,\mathrm{d}t &\overset{u(\cdot,0)=0}{=} L^{-1}\int_0^1\int_0^L |\int_0^t \partial_t u_w(x,t')\,\mathrm{d}t'|\,\mathrm{d}x\,\mathrm{d}t \\ &\leq L^{-1}\int_0^1\int_0^L\int_0^1 |\partial_t u_w(x,t')|\,\mathrm{d}t'\,\mathrm{d}x\,\mathrm{d}t \\ &= L^{-1}\int_0^1\int_0^L |\partial_t u_w|\,\mathrm{d}x\,\mathrm{d}t \\ &\overset{(3.73)}{\lesssim} w^{-1/2}. \end{aligned} \tag{3.74}$$

□

3.2.3. Compactness

Proposition 3.18. *Let $L \sim 1$ be fixed and $\{u^\varepsilon\}_{\varepsilon\downarrow 0}$ be a sequence such that $L^{-1}E_\varepsilon(u^\varepsilon) \sim -1$. Then $\{u^\varepsilon\}_{\varepsilon\downarrow 0}$ is compact in $L^2((0,L)\times(0,1))$.*

Proof of Proposition 3.18. The proof is a classical compensated compactness argument, in the sense that the strong equi-continuity properties in x compensate the weak equi-continuity in t. To start, let us first list some direct consequences of the results in the previous section.

Let $\{u^\varepsilon\}_{\varepsilon\downarrow 0}$ be a sequence such that

$$L^{-1}E_\varepsilon(u^\varepsilon) \sim -1. \tag{3.75}$$

We have due to Lemma 3.17 that the sequence $\{u^\varepsilon\}_{\varepsilon\downarrow 0}$ is bounded in $L^2((0,L)\times(0,1))$. Therefore, after extracting a subsequence we may assume that there exists $u^0 \in L^2((0,L)\times(0,1))$ such that :

$$u^\varepsilon \overset{\varepsilon\downarrow 0}{\longrightarrow} u^0 \text{ weakly in } L^2. \tag{3.76}$$

Hence our goal is to show that this weak convergence is in fact a strong convergence.

Let $\mathcal{F}$ denote the Fourier series w.r.t. x and the Fourier transform w.r.t. t. More precisely, for any L-periodic $g(x,t)$ we define

$$\mathcal{F}(g)(\xi,\theta) := \frac{1}{\sqrt{L}}\int_0^L\int_{\mathbb{R}} g(x,t)\,\mathrm{e}^{-it\theta}\mathrm{e}^{-ix\xi}\,\mathrm{d}t\,\mathrm{d}x,$$

where $\xi \in \frac{2\pi}{L}\mathbb{Z}$ and $\theta \in \mathbb{R}$ denote the dual variables to x and t, respectively. Since u^ε is L-periodic in x with $L \sim 1$ and supported in $t \in [0,1]$ we automatically have

$$|\mathcal{F}((u^\varepsilon)^2)(\xi,\theta)| \lesssim \int_0^1 \int_0^L (u^\varepsilon)^2 \,\mathrm{d}x\,\mathrm{d}t \lesssim 1. \tag{3.77}$$

By (3.76), we have

$$\mathcal{F}(u^\varepsilon) \xrightarrow{\varepsilon\downarrow 0} \mathcal{F}(u^0) \text{ pointwise.}$$

Therefore, we have for all $R > 0$

$$\int_{B_R(0)} |\mathcal{F}(u^\varepsilon) - \mathcal{F}(u^0)|^2 \,\mathrm{d}\xi\,\mathrm{d}\theta \xrightarrow{\varepsilon\downarrow 0} 0, \tag{3.78}$$

where $B_R(0) = \{(\xi,\theta) \in \frac{2\pi}{L}\mathbb{Z}\times\mathbb{R} \mid |\theta| < R \text{ and } |\xi| < R\}$ and $\int \cdot\,\mathrm{d}\xi\,\mathrm{d}\theta$ denotes the integration w.r.t. ξ and the discrete summation w.r.t. θ. Hence for strong convergence in L^2, it is enough to show that there is no concentration in the high frequencies, i.e.,

$$\int_{\left(\frac{2\pi}{L}\mathbb{Z}\times\mathbb{R}\right)-B_R(0)} |\mathcal{F}(u_\varepsilon)|^2 \,\mathrm{d}\xi\,\mathrm{d}\theta \xrightarrow{R\uparrow\infty} 0 \tag{3.79}$$

uniformly in ε, cf. [Peg85].

Before embarking on (3.79), we note that

$$\int_0^1 \int_0^L \left||\partial_x|^s u^\varepsilon\right|^2 \mathrm{d}x\,\mathrm{d}t \lesssim 1 \tag{3.80}$$

uniformly in ε for some $s > 0$. Indeed, since $L \sim 1$ we have by Theorem 3.4 c1) that

$$\Delta^{-\alpha} \int_0^1 \int_0^L |(u^\varepsilon)^\Delta - u^\varepsilon|^2 \,\mathrm{d}x\,\mathrm{d}t \lesssim 1$$

for $\alpha \in [0, \frac{2}{5})$ uniformly in ε. Therefore for $0 < r < 1$

$$\int_0^1 \int_0^1 \frac{1}{\Delta^{2/5+r}} \int_0^L |(u^\varepsilon)^\Delta - u^\varepsilon|^2 \,\mathrm{d}x\,\mathrm{d}\Delta\,\mathrm{d}t \lesssim 1$$

uniformly in ε, as well as for $1 < r < \infty$

$$\int_0^1 \int_1^\infty \frac{1}{\Delta^r} \int_0^L |(u^\varepsilon)^\Delta - u^\varepsilon|^2 \,\mathrm{d}x\,\mathrm{d}\Delta\,\mathrm{d}t \lesssim 1$$

uniformly in ε. This entails

$$\int_0^1 \int_0^\infty \Delta^{-2s} \int_0^L |(u^\varepsilon)^\Delta - u^\varepsilon|^2 \,\mathrm{d}x \frac{1}{\Delta}\,\mathrm{d}\Delta\,\mathrm{d}t \lesssim 1$$

for $s \in (0, \frac{1}{5})$ uniformly in ε. We once again refer to the characterization of fractional Sobolev spaces in [LM68, p.59] to deduce (3.80).

We now turn to the proof of (3.79). We will use the identity $\sigma^\varepsilon = -\partial_x(\frac{1}{2}(u^\varepsilon)^2) + \partial_t u^\varepsilon$ to provide for control of oscillations in t via its Fourier transformed version, namely

$$-i\,\theta\,\mathcal{F}(u^\varepsilon) \;=\; \mathcal{F}(\sigma^\varepsilon) - \tfrac{1}{2}\,i\,\xi\mathcal{F}((u^\varepsilon)^2). \tag{3.81}$$

Moreover, we have by assumption due to Lemma 3.17 that

$$\int_0^1\int_0^L \left||\partial_x|^{-1/2}\sigma^\varepsilon\right|^2 \mathrm{d}x\,\mathrm{d}t \xrightarrow{\varepsilon\downarrow 0} 0. \tag{3.82}$$

Therefore we have for $M_2 \gg M_1 \gg 1$

$$\begin{aligned}
&\int_{\{|\xi|>M_1\}\cup\{|\theta|>M_2\}} |\mathcal{F}(u^\varepsilon)|^2\,\mathrm{d}\xi\,\mathrm{d}\theta\\
&\le \int_{\{|\xi|>M_1\}} |\mathcal{F}(u^\varepsilon)|^2\,\mathrm{d}\xi\,\mathrm{d}\theta + \int_{\{|\xi|\le M_1\}\cap\{|\theta|>M_2\}} |\mathcal{F}(u^\varepsilon)|^2\,\mathrm{d}\xi\,\mathrm{d}\theta\\
&\overset{(3.81)}{\lesssim} \int_{\{|\xi|>M_1\}} |\mathcal{F}(u^\varepsilon)|^2\,\mathrm{d}\xi\,\mathrm{d}\theta + \int_{\{|\xi|\le M_1\}\cap\{|\theta|>M_2\}} \frac{|\mathcal{F}(\sigma^\varepsilon)|^2}{|\theta|^2}\,\mathrm{d}\xi\,\mathrm{d}\theta\\
&\quad + \int_{\{|\xi|\le M_1\}\cap\{|\theta|>M_2\}} \frac{1}{|\theta|^2}|\xi|^2|\mathcal{F}((u^\varepsilon)^2)|^2\,\mathrm{d}\xi\,\mathrm{d}\theta\\
&\le \frac{1}{M_1^{2s}}\int_{\{|\xi|>M_1\}} |\xi|^{2s}|\mathcal{F}(u^\varepsilon)|^2\,\mathrm{d}\xi\,\mathrm{d}\theta\,\mathrm{d}\xi\,\mathrm{d}\theta\\
&\quad + \frac{M_1}{M_2^2}\int_{\{|\xi|\le M_1\}\cap\{|\theta|>M_2\}} \frac{|\mathcal{F}(\sigma^\varepsilon)|^2}{|\xi|}\,\mathrm{d}\xi\,\mathrm{d}\theta\\
&\quad + \int_{\{|\xi|\le M_1\}\cap\{|\theta|>M_2\}} \frac{1}{|\theta|^2}|\xi|^2\,\mathrm{d}\xi\,\mathrm{d}\theta\;(\sup|\mathcal{F}((u^\varepsilon)^2)|)^2\\
&\lesssim \frac{1}{M_1^{2s}} + \frac{M_1}{M_2^2} + \frac{M_1^3}{M_2},
\end{aligned}$$

where the last inequality is a consequence of (3.80),(3.82), and (3.77). With the choice $M_1 = M^{1/4}$ and $M_2 = M$, this implies

$$\int_{\{|\xi|>M_1\}\cup\{|\theta|>M_2\}} |\mathcal{F}(u^\varepsilon)|^2\,\mathrm{d}\xi\,\mathrm{d}\theta \lesssim \frac{1}{M^{s/2}} + \frac{M^{1/4}}{M^2} + \frac{M^{3/4}}{M} \xrightarrow{M\uparrow\infty} 0$$

uniformly in ε, which yields (3.79). □

Proof of Theorem 3.5. We give a proof by contradiction. Let $0 < \varepsilon \ll 1$ and $L \sim 1$. Assume there exists u with $L^{-1}E(u) \sim -1$ such that for any u^* with

$$-\partial_x\tfrac{1}{2}(u^*)^2 + \partial_t u^* \;=\; 0$$

distributionally

$$L^{-1}\int_0^L\int_0^1 (u-u^*)^2\,\mathrm{d}t\,\mathrm{d}x \gtrsim 1. \tag{3.83}$$

Hence, there exist sequences $\{L_\varepsilon\}_{\varepsilon\downarrow 0}$, $\{u^\varepsilon\}_{\varepsilon\downarrow 0}$ with L_ε bounded and $L_\varepsilon^{-1}\, E(u^\varepsilon) \sim -1$ such that u^ε is not close to a weak solution to Burgers' equation. Rescaling according to $x = \frac{L_\varepsilon}{L}\,\widehat{x}$ and $u = \frac{L_\varepsilon}{L}\,\widehat{u}$, we may w.l.o.g. assume that $L_\varepsilon = L$. On the other hand, by Proposition 3.18, $\{u^\varepsilon\}_{\varepsilon\downarrow 0}$ is compact in L^2 and we claim that after extracting a subsequence, $\{u^\varepsilon\}_{\varepsilon\downarrow 0}$ converges in L^2 to a weak solution of Burgers' equation which is in contradiction to the assumption. Indeed, if we denote the L^2-limit of $\{u^\varepsilon\}_{\varepsilon\downarrow 0}$ by u^0 then $\{(u^\varepsilon)^2\}_{\varepsilon\downarrow 0}$ converges to $(u^0)^2$ in L^1. Therefore, like in (3.82) we have

$$\int_0^1 \int_0^L \left||\partial_x|^{-1/2}\sigma^\varepsilon\right|^2 \mathrm{d}x\,\mathrm{d}t \xrightarrow{\varepsilon\downarrow 0} 0,$$

and we obtain as desired

$$-\partial_x \tfrac{1}{2}(u^0)^2 + \partial_t u^0 = \lim_{\varepsilon\downarrow 0} \left(-\partial_x \tfrac{1}{2}(u^\varepsilon)^2 + \partial_t u^\varepsilon\right) = \lim_{\varepsilon\downarrow 0} \sigma^\varepsilon = 0 \text{ distributionally.}$$

□

4

Numerical simulation of the reduced energy functional

In this chapter, we address the numerical simulation of the reduced energy functional (1.14). The aim is to numerically explore the energy landscape with its local minima, in particular the deformation of the landscape under the variation of the external field. We start with a short introduction of the important features of the discretization; for a detailed presentation, see [Steo6] where the scheme was introduced. Afterwards, we explain the algorithms used to compute solution branches of stationary states, namely path-following techniques and branch switching. The simulations show:

- There exists a branch of stationary points connecting the $\widehat{w}^*$-periodic unstable mode to the concertina pattern. The bifurcation is subcritical. There exists a turning point after which the branch is stable (under perturbations of period $\widehat{w}^*$).
- The $\widehat{w}^*$-periodic concertina is unstable under perturbations of period $N\widehat{w}^*$. It turns out that the symmetries of the pattern lead to multiple bifurcations which can be systematically studied and computed with the help of representation theory.
- There is a cascade of secondary instabilities at which the pattern coarsens as the field increases.

At the end of this chapter, in Section 4.10, we provide a list of the parameters which are chosen in the numerical simulations. For notational convenience, we drop the $\widehat{\cdot}$ related to the rescaling of the reduced energy in this section, cf. (1.14).

4.1. Discretization of the reduced energy functional

The magnetization m_2 is approximated on a uniform Cartesian grid of step size $h_1 = \frac{L}{N_1}$ and $h_2 = \frac{1}{N_2}$ w.r.t. x_1 and x_2, respectively:

$$M_{j,k} \approx m_2\,(j\,h_1, k\,h_2)\,,\ j \in \{0\ldots, N_1 - 1\},\ k \in \{0, \ldots, N_2 - 1\}.$$

The discrete magnetization is N_1-periodic w.r.t. j, cf. Figure 4.1. The finite-difference discretization of the energy is straightforward in case of exchange, Zeeman, and the anisotropy energy. In case of the stray-field energy, one has to choose an appropriate approximation of the non-linearity and of the non-locality which can be computed at low cost avoiding the assembling and application of dense matrices.

One can think of several different discretizations of the non-linearity $\sigma = -\frac{1}{2}\partial_1 m_2^2 + \partial_2 m_2$, all of the same order. Our choice is motivated by the aim that the shear-invariance (3.8), i.e., the invariance of the energy under the transform

$$x_1 = s\,x_2 + \tilde{x}_1, \quad x_2 = \tilde{x}_2, \quad m_2 = \tilde{m}_2 - s, \tag{4.1}$$

is inherited by the discrete scheme. We therefore choose the following discretization of the non-linearity which is compatible with the shear-invariance

$$\Sigma_{j,k} = -\frac{1}{2h_1}\frac{1}{2}\left(\left(\frac{M_{j+1,k+1}+M_{j+1,k}}{2}\right)^2 - \left(\frac{M_{j-1,k+1}+M_{j-1,k}}{2}\right)^2\right) + \frac{1}{h_2}(M_{j,k+1} - M_{j,k}).$$

Figure 4.1 depicts the spatial extent of the difference stencil.

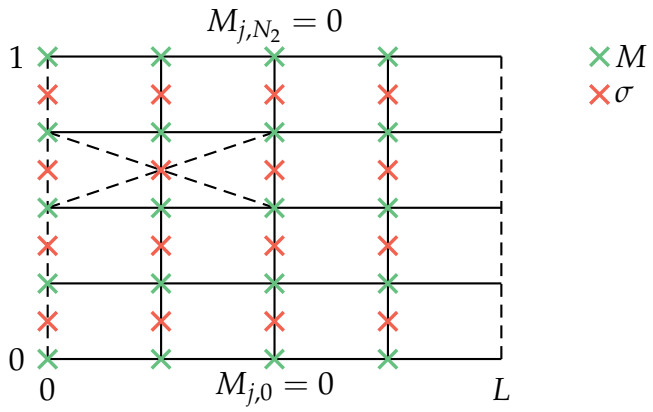

Figure 4.1.: Discrete approximation of the magnetization on the uniform grid.

In case of the non-locality, we use that the $H^{-1/2}$-norm can be represented as the Dirichlet energy of a potential u, which is the harmonic extension on $[0, L) \times (0, 1) \times \mathbb{R}$ with Neumann data σ at $[0, L) \times (0, 1)$, i.e.,

$$\frac{1}{2}\int_0^L \int_0^1 ||\partial_1|^{-1/2}\sigma|^2 \,\mathrm{d}x' = \int_0^L \int_0^1 \int_{\mathbb{R}} |\nabla u|^2 \,\mathrm{d}x = -\int_0^L \int_0^1 u(x_3 = 0)\,\sigma \,\mathrm{d}x',$$

where the potential $u : [0, L) \times (0, 1) \times \mathbb{R} \to \mathbb{R}$ satisfies

$$-(\partial_1^2 + \partial_3^2)u = 0 \quad x_3 \neq 0 \quad \text{and} \quad [\partial_3 u](x_3 = 0) = \sigma,$$

cf. (1.16). We discretize this equation w.r.t. x_1 and x_2:

$$\frac{-U_{j+1,k}(x_3) + 2U_{j,k}(x_3) - U_{j-1,k}(x_3)}{h_1^2} - \partial_3^2 U_{j,k}(x_3) = 0 \quad \text{for} \quad x_3 \neq 0$$
$$[\partial_3 U_{j,k}](x_3 = 0) = \sigma.$$

The application of the Discrete Fourier Transform (DFT) w.r.t. j turns the Neumann problem into an ordinary differential equation w.r.t. x_3 which can be explicitly solved. We obtain the discrete counterpart to the Fourier multiplier $|k_1|^{-1/2}$ in the continuous case:

$$|k_1|^{-1/2} \rightsquigarrow K(l)^{-1/2} = (\tfrac{2}{h_1}\sin(\tfrac{\pi l}{N_1}))^{-1/2}\ l \in \{0,\dots,N_1-1\}. \tag{4.2}$$

The DFT, denoted by $\mathcal{F}$, is normalized in the way that $\frac{1}{N_1}\bar{\mathcal{F}}\mathcal{F}$ is the identity, namely

$$\mathcal{F}(X)_k = \sum_{l=0}^{N_1-1} \mathrm{e}^{-i\frac{2\pi kl}{N_1}} X_l \quad \text{and} \quad \bar{\mathcal{F}}(Y)_l = \sum_{k=0}^{N_1-1} \mathrm{e}^{i\frac{2\pi lk}{N_1}} Y_k,$$

where X and Y denote some vectors of length N_1. The stray-field energy is thus approximated by

$$\tfrac{1}{2}\int_0^L \int_0^1 ||\partial_1|^{-1/2}\sigma|^2 \,\mathrm{d}x' \approx \tfrac{1}{2}h_1h_2\tfrac{1}{N_1}\sum_{l,k} K(l)^{-1}|\mathcal{F}(\Sigma)_{l,k}|^2.$$

We note that the application of the Fast Fourier Transform (FFT) allows a fast evaluation of the non-local term in the simulations.

The discrete energy functional is thus given by:

$$\begin{aligned} E_0^h(M) \;=\; & h_1\,h_2\; D_1M^TD_1M + \tfrac{1}{2}\,h_1\,h_2\;\tfrac{1}{N_1}(\bar{\mathcal{F}}(\Sigma))^TK^{-1}\mathcal{F}(\Sigma) \\ & - h_{\text{ext}}\;h_1\;h_2\;M^TM + Q\;h_1\;h_2\;(M.^2)^TM.^2, \end{aligned}$$

where the operator D_1 denotes the forward difference, i.e., $D_1\,M_{j,k} = \big(\frac{M_{j+1,k}-M_{j,k}}{h_1}\big)_{j,k}$, and where $M.^2$ denotes the componentwise square. The diagonal matrix K represents the discrete Fourier multiplier $K(l)$, cf. (4.2). The gradient of the energy is given by

$$\begin{aligned} D_ME_0^h(M) \;=\; & 2\,h_1\,h_2\;D_1^TD_1M + \;h_1\,h_2\;\tfrac{1}{N_1}D_M\Sigma^T\bar{\mathcal{F}}(K^{-1}\mathcal{F}(\Sigma)) \\ & - 2h_{\text{ext}}\;h_1\;h_2\;M + 4Q\,h_1h_2\;M.^3. \end{aligned}$$

The Hessian applied to some test vector V is given by

$$\begin{aligned} D_M^2E_0^h(M)(V) \;=\; & 2\,h_1\,h_2\;D_1^TD_1V \\ & + \;h_1\,h_2\;\tfrac{1}{N_1}D_M\Sigma^T\bar{\mathcal{F}}(K^{-1}\mathcal{F}(D_M\Sigma(V))) + \;h_1\,h_2\;\tfrac{1}{N_1}D_M^2\Sigma(V)^T\bar{\mathcal{F}}(K^{-1}\mathcal{F}(\Sigma)) + \\ & - 2h_{\text{ext}}\;h_1\;h_2\;V + 12Q\,h_1\;h_2\;V.M.^2. \end{aligned}$$

Hence, the matrix-vector product can be computed without assembling the Hessian, which is called matrix-free multiplication. In particular, the assembling of the dense matrix $\bar{\mathcal{F}}K^{-1}\mathcal{F}$ can be circumvented.

The discretization was validated in [Ste06], where the convergence of the scheme, as the grid size tends to zero, was numerically confirmed. Moreover, it was shown that the numerical solution coincides with the asymptotic solution close to the primary bifurcation, see Section 6.1.

4.2. Implementation and parallelization

The implementation is based on the C-library PETSc (Portable, Extensible Toolkit for Scientific Computation), [BBG+09]. It provides the necessary data structures for vectors and matrices, and Krylov subspace methods for the solution of linear equations. All modules are also available in a parallel implementation which is based on the MPI (Message Passing Interface) standard. For the evaluation of the DFT, we use the implementation of the FFT in the C-library FFTW, [FJ05]. The iterative linear solvers (Krylov subspace methods) in PETSc are compatible with matrix-free implementations.

The stray-field energy in the reduced energy functional is non-local w.r.t. only one space dimension. This can be used in a parallel implementation of the basic algebraic operations in the following way: The computational domain is subdivided in horizontal stripes which are distributed to the individual processors. We are aware of the fact that this parallelization scheme cannot lead to an optimal scaling in the limit: The length of the interfaces of n sub-domains, in case of an anisotropic, strip-like decomposition, scales like $\sim n$, while in case of an isotropic decomposition the total length of the interface scales like $\sim n^{1/2}$. Note that the idle time of the processors is negligible since the computational effort is uniformly distributed among the processors. For standard grid sizes (e.g., $N_1 = N_2 = 256$) a ring of 4 workstations leads for example to a speed-up of a factor of approximately 3.5.

4.3. Path following

Our aim is the computation of stationary points, in particular (local) minimizers, of the discrete energy functional for varying external field. For the computation of minimizers, iterative descent algorithms can be used. However, if the energy landscape is flat – in particular close to a bifurcation – these algorithms turn out to be slow. In such regions it is necessary to employ so-called path-following methods, cf. [DH08, Geo01]. Within that context we interpret the Euler-Lagrange-equation

$$D_M E_0^h(M, h_{\text{ext}}) = 0$$

for varying external field h_{ext} as a parameter-dependent equation

$$F(x, \lambda) = 0, \quad \text{i.e.,} \quad F = D_M E_0^h, \quad \text{and} \quad (x, \lambda) = (M, h_{\text{ext}}).$$

The aim is to iteratively approximate a branch of solutions $(x(s), \lambda(s))$, where s is a suitable parameterization of the branch, e.g. arc length.

Tangent path-following algorithm. Consider an approximate solution (x_0, λ_0) of the parameter-dependent equation and in addition an approximate tangent $t_0 = (t_0^x, t_0^\lambda)$ to the branch of solutions in that particular point. The path-following consists of the iteration of the following two steps for $n = 0, \ldots, N_{\max}$, cf. Figure 4.2:

1. Predictor. Choose a step size $\eta_n > 0$ and set

$$p_{n+1} = (x_n, \lambda_n) + \eta_n t_n.$$

2. Corrector. The next point on the branch (x_{n+1}, λ_{n+1}) is computed as a solution to the nonlinear equation

$$\begin{pmatrix} F(x_{n+1}, \lambda_{n+1}) \\ \Big(p_{n+1} - (x_{n+1}, \lambda_{n+1})\Big)^T t_n \end{pmatrix} = 0.$$

The next approximate tangent can be obtained as the normalized solution $t_{n+1} = \frac{t}{||t||}$ to the equation

$$\begin{pmatrix} DF(x_{n+1}, \lambda_{n+1}) \\ t_n^T \end{pmatrix} t = \begin{pmatrix} 0 \\ 1 \end{pmatrix}, \tag{4.3}$$

where we use that $0 = \frac{\mathrm{d}}{\mathrm{d}s} F(x(s), \lambda(s)) = DF(x(s), \lambda(s))t(s)$. The augmentation $t_n^T t = 1$ ensures that the orientation is preserved during the path-following procedure.

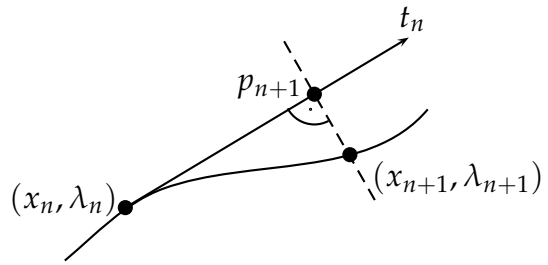

Figure 4.2.: Tangent predictor-corrector continuation method.

Inexact Newton method. We use the Newton method to solve the non-linear equation in the corrector step. To solve the linearized equation within the Newton method, we make use of the block structure of the Jacobian which contains a *symmetric* block of codimension 1 given by the Hessian of the energy:

$$DF = \begin{pmatrix} \mathrm{Hess} E_0^h(M, h_{\mathrm{ext}}) & -2M \\ -t^M & -t^{h_{\mathrm{ext}}} \end{pmatrix}.$$

Note that the solution of an equation of the form

$$\begin{pmatrix} A & b \\ c^T & d \end{pmatrix} \begin{pmatrix} y_1 \\ y_2 \end{pmatrix} = \begin{pmatrix} z_1 \\ z_2 \end{pmatrix}, \tag{4.4}$$

where A is a quadratic block of codimension 1, can be represented as

$$y_2 = \frac{z_2 - c^T A^{-1} z_1}{d - c^T A^{-1} b}, \quad y_1 = A^{-1} z_1 - y_2 A^{-1} b. \tag{4.5}$$

On the basis of the latter representation we can make use of the symmetry of the Hessian, i.e., the quadratic block A. Although it is necessary to solve two linear equations, related to $A^{-1}z_1$ and $A^{-1}b$, to obtain (y_1, y_2) , this approach is advantageous compared to an iterative scheme directly applied to the Jacobian DF. We make use of the symmetry and apply the conjugated-gradient (cg) method in order to invert the Hessian. Note that a matrix-free implementation of the Hessian is compatible with the application of the cg-method. Observe that the tangent in (4.3) can be computed on the basis of a similar decomposition, too. In the literature, the decomposition (4.4) is known as the Schur method.

The scheme described above falls into the class of inexact Newton methods since the linearized equation is only solved approximately via the cg-iteration. Provided that the residuum is sufficiently small, the quadratic convergence of the Newton iteration is not affected, see [GK99, Algorithm 10.1 and Proposition 10.2] and [Ste06].

4.4. Detection of bifurcation points and branch switching

In this section, we present a numerical method for the detection of bifurcations and branch-switching. A necessary criterion for a simple bifurcation in $s = s^*$ is that the determinant

$$\det \begin{pmatrix} DF(x(s), \lambda(s)) \\ (t^x(s), t^\lambda(s))^T \end{pmatrix}$$

changes its sign in $s = s^*$. For reasons of computational complexity it is of course not possible to use the determinant as an indicator function for a bifurcation. We pick up an approach which is presented in [Geo01]:

Theorem 4.1 ([Geo01]). *Let $(x(s^*), \lambda(s^*))$ be a simple bifurcation point, let the vector b be acute, i.e., not orthogonal, to the kernel of*

$$\begin{pmatrix} DF(x(s^*), \lambda(s^*)) \\ (t^x(s^*), t^\lambda(s^*))^T \end{pmatrix}^T$$

and the vector c be acute to the kernel of

$$\begin{pmatrix} DF(x(s^*), \lambda(s^*)) \\ (t^x(s^*), t^\lambda(s^*))^T \end{pmatrix}.$$

Then $\tau(x(s))$ defined via

$$\begin{pmatrix} \begin{pmatrix} DF(x, \lambda)) \\ (t^x, t^\lambda)^T \end{pmatrix} & b \\ c^T & 0 \end{pmatrix} \begin{pmatrix} \xi \\ \tau \end{pmatrix} = \begin{pmatrix} 0 \\ 1 \end{pmatrix} \tag{4.6}$$

changes sign at $s = s^*$.

The proof is a direct consequence of Cramer's rule.

Observe that

$$\tau = -\frac{1}{c^T \begin{pmatrix} DF(x,\lambda)) \\ (t^x, t^\lambda)^T \end{pmatrix}^{-1} b}, \quad \xi = -\tau \begin{pmatrix} DF(x,\lambda)) \\ (t^x, t^\lambda)^T \end{pmatrix}^{-1} b.$$

Hence the computation of τ and ξ can again be carried out with the help of the Schur method, cf. (4.4) and (4.5), applied to the matrix (DF, t^T). Note that ξ is orthogonal to the current tangent. Hence it can be used to obtain a predictor for the bifurcating branch and thus as the first step in the path following of the bifurcating branch.

Let us emphasize that the strategy above only works in case of simple bifurcation points. Symmetries of the energy and the primary solution branch can lead to multiple bifurcations as we are going to discuss in the following section. Luckily, the multiple bifurcations which occur in case of the concertina pattern can be reduced to the computation of simple bifurcations. This allows us to develop and apply modifications of the methods discussed above.

4.5. Bifurcations with symmetries

In this section, we want to discuss the symmetries of the concertina pattern which play an important role for the understanding of the secondary bifurcations. We refer the reader to the two text books [GS02] and [Hoy06] for a brief introduction into bifurcation problems with symmetries. In the presence of symmetries, one cannot expect to observe the generic case of a one-dimensional bifurcation since the symmetries can lead to higher degeneracies. On the other hand, a precise knowledge of the symmetries in general allows to characterize the bifurcations which can occur and hence to identify the generic bifurcations in the presence of symmetries. In case of the concertina pattern, it is possible to reduce the multiple bifurcations to simple bifurcations within a certain symmetry class. We start with the identification of the symmetries of the energy functional. We note that most of the statements are discussed on the basis of the reduced rescaled energy but can be correspondingly adapted to the discrete energy.

Lemma 4.2. *The reduced energy functional* (1.14) *is invariant under the following types of symmetries, namely*

$$\begin{aligned} \textit{translation} \quad & E_0(m_2(x_1, x_2)) = E_0(m_2(r + x_1, x_2)), \quad r \in [0, L), \\ \textit{rotation} \quad & E_0(m_2(s + x_1, x_2)) = E_0(m_2(s - x_1, 1 - x_2)), \quad s \in [0, L), \\ \textit{reflection} \quad & E_0(m_2(t + x_1, x_2)) = E_0(-m_2(t - x_1, x_2)), \quad t \in [0, L). \end{aligned}$$

They form a group (by composition), whose generator is given by translations with $r \in [0, L)$, rotation w.r.t. $(0, \frac{1}{2})$, i.e., $s = 0$, and reflection at the x_2-axis, i.e., $t = 0$.

Remark 4.3. *It is easily seen that the energy is invariant under the transforms in Lemma 4.2. Another symmetry is given by* $E_0(m_2(x_1, x_2)) = E_0(-m_2(x_1, 1 - x_2))$.

In case of the discrete energy similar relations hold. Of course, one has to require that the parameters are chosen from the discrete set, more precisely $r, s, t \in \mathbb{N}h_1$. *The discrete magnetization can be translated, rotated and reflected on the Cartesian grid.*

Although the Euler-Lagrange equation inherits the invariance of the energy under the symmetries, solutions clearly need not to be invariant under these symmetries. The concertina pattern inherits a discrete subgroup of symmetries generated by translation by an integer multiple of its period, rotation around the center of a quadrangular domain and reflection w.r.t. a vertical walls under a change of sign of m_2, cf. Figure 4.3.

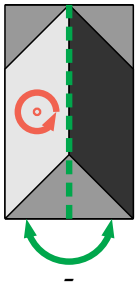

Figure 4.3.: Reflectional and rotational symmetry of one fold of the concertina pattern.

Generic bifurcations in the presence of symmetries. To apply the abstract framework for the identification of the generic bifurcations in the presence of symmetries as described in [GS02], it is necessary to identify the symmetries as linear representations on the vector space of admissible magnetizations. It turns out that generically the induced representation of the symmetries of the primary solution branch on the kernel of the Hessian in the bifurcation is irreducible. The central theorem, the so called Equivariant-Branching Lemma, entails the existence of bifurcating branches using a symmetry-preserving Liapunov-Schmidt reduction. An additional genericity result finally allows the reduction of the multiple bifurcation to simple bifurcations (on fixed-point subspaces of the isotropy subgroups), see below. We need the following definitions:

Definition 4.4. *Let* Γ *be a finite group and* V *be a vector space. A* **linear representation** *of* Γ *is a homomorphism* $\varrho : \Gamma \to \mathrm{O}(V)$.

With an abuse of notation we write $\gamma v = \varrho(\gamma)(v)$ for all $\gamma \in \Gamma$ and $v \in V$. We have to generalize the notion of invariance:

Definition 4.5. *Let* Γ *be a linear representation over the vector space* V *and* $F : V \times \mathbb{R} \to V$ *a parameter-dependent map. Then* F *is* **Γ-equivariant** *provided* $F(\gamma v, \lambda) = \gamma F(v, \lambda)$ *for all* $\gamma \in \Gamma$ *and* $v \in V$. *Similarly,* $A \in \mathrm{GL}(V)$ *is equivariant provided* $\gamma A = A\gamma$ *for all* $\gamma \in \Gamma$.

Since E_0 is Γ-invariant, we have that the gradient DE_0 is Γ-equivariant. Moreover, if m_2 is Γ invariant, then the Hessian in m_2, i.e., $D^2E_0(m_2)$, is equivariant, too. Both statements are a direct consequence of the application of the chain rule.

Consider now a stationary concertina pattern of some period w, which we think of as a solution to the Euler-Lagrange equation on the Nw-periodic domain for $N \in \mathbb{N}$. Due to translation invariance, we can assume that the center of a vertical wall is located at $x_1 = 0$. We are interested in bifurcations where we allow for Nw-periodic perturbations. The group action generated by rotation in $(\frac{w}{4}, 0)$, reflection at $x_1 = 0$, and translation by w, cf. Figure 4.4, on the space of Nw-periodic perturbations is a linear representation of the group D_{2N}. Here D_{2N} denotes the dihedral group, i.e., the symmetry group of the regular polygon with N edges. To see this, we refer to Figure 4.4 which depicts the action of D_{2N} for $N = 2$.

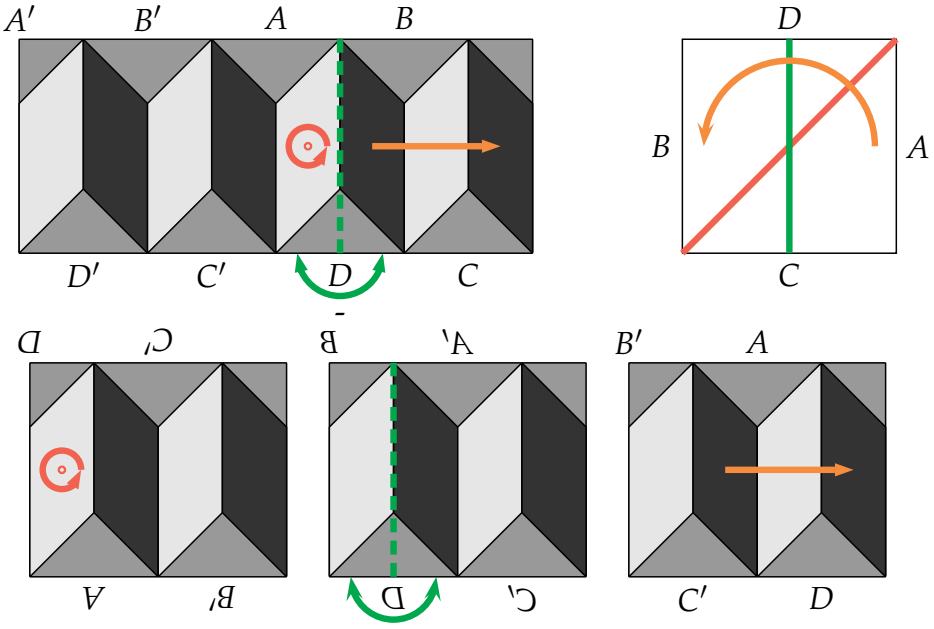

Figure 4.4.: Symmetry transforms on the $2w$-periodic domain which leave the w-periodic pattern invariant: The left image in the top row shows two copies of the $2w$-periodic domain. Rotation (red), reflection under change of sign $m_2 \rightsquigarrow -m_2$ (green), and translation by w (orange) of the $2w$-periodic concertina are representations of the symmetry group of the square and correspond to reflections at the symmetry axes of the square and rotation by 180°, respectively. The images in the bottom row show the result of the symmetry transforms restricted to the $2w$-periodic domain on the level of the location of the edges. Note that due to periodicity, the rotations w.r.t. the center of the bright or the dark facets are equivalent. Similarly, reflections w.r.t. the first and third or second and fourth vertical wall are equivalent.

Due to the invariance of the magnetization m_2, the kernel of the Hessian is a D_{2N}-invariant subspace. Therefore we obtain an induced representation of D_{2N} on the

kernel of the Hessian. Of course, the elements in the kernel need not to be pointwise invariant. We need the following definition:

Definition 4.6. *Let Γ be a linear representation on V. The representation is* **irreducible** *if the only invariant subspaces are $\{0\}$ and V. Let $C \subset \mathrm{GL}(V)$ be the set of commuting linear invertible maps, i.e., if $A \in C$ then $\gamma A = A\gamma$ for all $\gamma \in \Gamma$. The representation is* **absolutely irreducible** *if C contains only scalar multiples of the identity.*

Note that for a complex representation both properties are equivalent.

In [GSS88, Proposition 3.2] it is stated that the induced representation on the kernel is generically absolutely irreducible. This is not true for a bifurcation in the variational setting. In fact, the perturbation which is constructed in [GSS88] for a general parameter-dependent equation with symmetries – in order to prove the property of being absolute irreducible – is not compatible with the variational structure. It cannot be integrated in order to obtain a perturbation of the energy. Nevertheless, one can construct an integrable perturbation of the bifurcation equation which entails that the representation on the kernel is generically irreducible.

Representations of D_{2N}. In order to classify the possible bifurcations, we have to identify the irreducible representations of D_{2N}. The absolute irreducible representations are well known. In fact, there are four one-dimensional representations and $N-1$ two-dimensional representations of D_{2N}, cf. [Ser77, Section 5.3] . Both the one- and the two-dimensional representations can be realized as real representations over $\mathbb{R}$ and $\mathbb{R}^2$, respectively. Hence, in case of the dihedral group the irreducible representations coincide with the absolutely irreducible representations. Let us come back to the example of the w-periodic concertina as a solution on the $2w$-periodic domain, i.e., $N = 2$. Denote by τ and ϱ the generators of D_4 where we think of τ as a reflection and of ϱ as a rotation by $\frac{\pi}{2}$, respectively. In case of D_4 the irreducible representations are up to equivalence (i.e., conjugation or change of basis) given by:

- Four one-dimensional representations: Trivial representation, i.e., $\gamma(\tau) = 1$, $\gamma(\varrho) = 1$; $\gamma(\tau) = 1$, $\gamma(\varrho) = -1$; $\gamma(\tau) = -1$, $\gamma(\varrho) = 1$; $\gamma(\tau) = -1$, $\gamma(\varrho) = -1$.
- One two-dimensional representation: Natural representation, i.e., $\gamma(\tau) = \begin{pmatrix} 1 & 0 \\ 0 & -1 \end{pmatrix}$ and $\gamma(\varrho) = \begin{pmatrix} 0 & -1 \\ 1 & 0 \end{pmatrix}$.

Generalized Liapunov-Schmidt reduction. The Liapunov-Schmidt reduction always allows to reduce the analysis of a bifurcation of a parameter-dependent equation (infinite dimensional) to an analysis of the bifurcation of a finite dimensional parameter-dependent equation defined on the kernel of the Hessian:

$$f : \ker \mathrm{Hess} E_0(m_2, h_{\mathrm{ext}}) \times \mathbb{R} \to \ker \mathrm{Hess} E_0(m_2, h_{\mathrm{ext}}).$$

In particular, the critical point can be assumed to be $(0,0)$. As shown in Section 1.3 in [GS02], the reduction can be performed in such a way that the symmetries of the

system are preserved. Using the generalized Liapunov-Schmidt reduction, we are now ready to state and to apply the basic general existence theorem for symmetry breaking branches, the so called Equivariant-Branching Lemma.

Theorem 4.7. *[GSo2, Lemma 1.31] Let $\Gamma \subset \mathrm{O}(n)$ be a finite group.*

1. *Assume Γ acts absolutely irreducible on $V = \mathbb{R}^n$.*
2. *Let $f : \mathbb{R}^n \times \mathbb{R} \to \mathbb{R}^n$ be Γ-equivariant, i.e., $f(\gamma v, \lambda) = \gamma f(v, \lambda)$, which implies*

$$\begin{aligned} f(0, \lambda) &= 0, \\ Df(0, \lambda) &= c(\lambda)\,\mathrm{id}\,. \end{aligned}$$

3. *Assume $c(0) = 0$ (bifurcation occurs) and $c'(0) \neq 0$ (eigenvalue crossing condition).*
4. *Assume $\Sigma \subset \Gamma$ is an axial subgroup, i.e., a subgroup s.t. $\dim\{v \in V \mid \gamma v = v \text{ for all } \gamma \in \Sigma\} = 1$.*

Then there exists a unique branch of solutions to $f(v, \lambda)$ emanating from $(0, 0)$ where the symmetry of the solutions is Σ.

Theorem 4.7 is of importance because the axial subgroups of D_{2N} are easy to identify. In case of the two-dimensional representations (which numerically turn out to be the relevant ones), there are two conjugacy classes of axial subgroups, cf. Figure 4.5. They correspond to configurations which are either invariant under rotation w.r.t. the center of a facet of the fold or to configurations which are invariant under reflection at a vertical wall with change of sign $m_2 \rightsquigarrow -m_2$. As shown in [GSo2], the application of the following theorem entails that the solutions which are guaranteed by the Equivariant-Branching Lemma are generically the only solutions of the bifurcation equation:

Theorem 4.8. *[GSo2, Theorem 2.24] Let $f : \mathbb{C} \to \mathbb{C}$ be D_n-equivariant. Then there exist $p, q : \mathbb{R}^2 \to \mathbb{R}$ such that*

$$f(z) = p(u, v)z + q(u, v)\bar{z}^{n-1}, \tag{4.7}$$

where $u = z\bar{z}$ and $v = z^n + \bar{z}^n$. Moreover, any f of the form (4.7) is D_n-equivariant.

Theorem 4.8 characterizes D_n-equivariant functions. In order to apply Theorem 4.8 we have to identify the action of D_n on $\mathbb{C}$ with the standard action on $\mathbb{R}^2$. For our case of a variational bifurcation equation we note that

$$\nabla \times f = 0 \quad \text{is equivalent to} \quad np_v - q_u = 0. \tag{4.8}$$

Clearly, the necessary condition for the bifurcation is that $p(0) = 0$.

We want to show that any solution of the equation $f = 0$ generically corresponds to a solution given by Theorem 4.7. To see this, we distinguish three types of solutions:

- The first type is the trivial equilibrium solution $z = 0$.
- The second type of solutions corresponds to z parallel to $\bar{z}^{n-1}$ which entails that $\operatorname{Im} z^n = 0$. Notice that $\operatorname{Im} z^n = 0$ implies that z is in the fixed-point subspace of some axial subgroup. The solutions in the second case thus correspond to the solutions given by the Equivariant-Branching Lemma.
- Finally, let us assume that z is not parallel to $\bar{z}^{n-1}$ in which case $p = q = 0$. However, generically $q(0) \neq 0$, even in the variational setting. In fact, one can perturb q by $q + \varepsilon$ which preserves
  - the D_n-equivariance,
  - the variational structure, i.e., relation (4.8),
  - and, obviously, the necessary condition for a bifurcation, i.e., $p(0) = 0$.

  Hence, by continuity, there are generically no solutions such that $p = q = 0$.

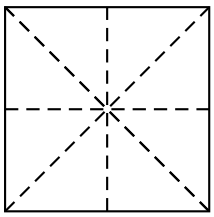

Figure 4.5.: Reflections of the square, each corresponding to an axial subgroup of D_4.

4.6. Adaption of numerical algorithms

In the last section it was shown that multiple bifurcations related to symmetries can be reduced to simple bifurcations on the fixed-point subspace of an axial subgroup. We now show how this can be used for an adaption of the numerical algorithms for the bifurcation detection and branch switching discussed in Section 4.4. The detection of a bifurcation can be realized by choosing the augmentation (4.6) in Theorem 4.1 from the fixed-point subspace of the axial subgroup. Although the resulting matrix is rank-deficient, the linear equation restricted to the fixed-point subspace has a unique solution due to Theorem 4.7 and Theorem 4.8. Note that iterative methods like the cg-method are oblivious to the degeneracy of the matrix and produce a solution in the fixed-point subspace if the iteration is started in that subspace – in particular at 0. Hence, the augmentation by a vector from the fixed-point subspace together with an iterative solver that leaves the fixed-point subspace invariant can be used for the detection of the simple bifurcation in the fixed-point subspace.

Let us now specify how this general approach can be used in the computation of the multiple secondary bifurcations of the concertina pattern by a specific choice of

the augmentation. As an example we come back to the secondary bifurcations of the w-periodic concertina in the class of $2w$-periodic configurations. In that case we choose the augmentation in Theorem 4.1 (up to translation by $\frac{w}{2}$ which yields an augmentation in an equivalent fixed-point subspace) as $b = c = (v, 0)$, where v is the discrete approximation of

$$v_1 = \sin\left(\tfrac{2\pi x_1}{2w}\right)\sin(\pi x_2) \quad \text{or}$$
$$v_2 = \cos\left(\tfrac{2\pi(x_1+\frac{w}{4})}{2w}\right)\sin(\pi x_2).$$

Note that v_1 is invariant under the axial subgroup related to a reflection with change of sign at the vertical wall located at $x_1 = 0$ whereas v_2 is invariant under the axial subgroup related to a rotation by 180° w.r.t. to the quadrangular domain with center in $(\frac{w}{4}, \frac{1}{2})$. Figure 6.5 (top left) shows the computed secondary branches in case of $2w^*$-periodic perturbations. There are two reflectional and two rotational symmetric branches (conjugated by a translation by $\frac{w}{2}$) emanating at the secondary bifurcation at an external field $h_{\text{ext}} \approx 9$. Bifurcation branches in case of $4w^*$-periodic perturbations are shown in the introduction, cf. Figure 1.23. Figure 1.24 and Figure 1.25 display the corresponding configurations along the branches.

4.7. Energy minimization

The simulation of the hysteresis loop relies on the iterative minimization of the energy, see e.g. Figure 1.29. For the minimization of the energy we use a Newton method which is globalized using a steepest descent method: The Newton direction is an energy decreasing direction in the neighborhood of the minimum. Depending on the starting point of the iteration we therefore us the negative gradient as a descent direction at the beginning and later on switch to the Newton method to speed up convergence close to the stationary point. Since the energy is to highest order quartic in M, the line minimization along the gradient can be explicitly computed. The linearized equation in the Newton algorithm is solved by a conjugate-gradient iteration, see [GK99, Algorithm 10.1 and Proposition 10.2] and [Ste06].

4.8. Numerical computation of the period of global minimizers

In this section we explain how the global minimizer of the energy density $\frac{E_0}{L}$ as a function of the external field h_{ext} is computed. We look for an appropriate scheme in order to solve the following minimization problem: For given external field h_{ext}, minimize

$$\frac{E_0(m_2, h_{\text{ext}})}{w} \quad \text{among all } w\text{-periodic } m_2 \text{ for } 0 < w < \infty. \tag{4.9}$$

On the discrete level we want to minimize

$$\frac{E_0^h(M, h_{\text{ext}})}{w} \quad \text{among all } N_1\text{-periodic } M \in \mathbb{R}^{N_1 \times N_2} \text{ and } 0 < w < \infty, \tag{4.10}$$

where the period of the computational domain is $L = w$. Note that the discrete magnetization M does not depend explicitly on the period. Instead, the grid size $h_1 = \frac{w}{N_1}$ depends on w if we fix the number of grid points w.r.t. x_1, i.e., N_1. This entails that total derivatives w.r.t. the period – which are required for a numerical minimization of (4.10) – do not contain partial derivatives of M w.r.t. the period. More precisely, the first derivative is for example given by

$$D_w\big(\tfrac{E_0^h(M,h_{\text{ext}})}{w}\big) = -\frac{E_0^h(M,h_{\text{ext}})}{w^2} + \frac{D_{h_1}E_0^h(M,h_{\text{ext}})}{w}\frac{1}{N_1}. \tag{4.11}$$

Computation of the branch. For the computation of the approximation to the branch of solutions $(M(h_{\text{ext}}), w(h_{\text{ext}}), h_{\text{ext}})$ of (4.10), we apply a tangent predictor-corrector path-following method. In order to apply this iterative method, we need a good starting point $(M_0, w_0, h_{\text{ext}_0})$, i.e., a stationary point which (indeed) belongs to the minimal branch. For h_{ext} close to the critical field h_{ext}^*, we choose the period of the unstable mode $w = w^*$ and minimize $\frac{E_0^h(M,h_{\text{ext}})}{w}$ w.r.t. (M, w). The result is used as a starting point for the tangent predictor-corrector algorithm applied to the equation

$$D_{M,w}\left(\tfrac{E_0^h(M,h_{\text{ext}})}{w}\right) = 0,$$

(for a fixed number of grid points). The result of a simulation is shown in Figure 1.16 in the introduction.

4.9. Computation of derivatives of the energy

In order to compute the marginal stable branch, see Section 1.8.2, we need to compute derivatives of the minimal energy w.r.t. the period w – the outcome of a simulation is amongst others shown in Figure 1.18. A naive approach for the computation of the second derivative of the minimal energy per period $\frac{d^2}{dw^2}E_0(w)$, where

$$E_0(w) = \min_{m_2\ w\text{-periodic}} E_0(m_2, w),$$

is given by the post-processing via finite differences of the minimal energy per period $E_0^h(w_i)$ for a set of periods w_i. Let us introduce the family of minimizers

$$m_2^w = \operatorname*{argmin}_{m_2\ w\text{-periodic}} E_0(m_2, w),$$

which we assume are differentiable w.r.t. w. A more robust approach makes use of the following observation:

$$\begin{aligned}\frac{\mathrm{d}^2}{\mathrm{d}w^2}E_0(w) &= \frac{\mathrm{d}^2}{\mathrm{d}w^2}E_0(m_2^w) = \frac{\mathrm{d}}{\mathrm{d}w}(D_{m_2}E_0\partial_w m_2^w + \partial_w E_0)\\ &= D_{m_2}\partial_w E_0\partial_w m_2^w + \partial_w^2 E_0,\end{aligned}$$

where we used that $D_{m_2} E_0(m_2^w) = 0$, since by assumption m_2^w minimizes the energy. In order to numerically compute the second derivatives of the minimal energy per period given by

$$\frac{\mathrm{d}^2}{\mathrm{d}w^2} E_0^h(M^w) = D_{m_2} \partial_w E_0^h \partial_w M^w + \partial_w^2 E_0^h,$$

we need the quantity $\partial_w M^w$. (Notice that in contrast to the computation of the period of the global minimizers, M^w depends on the period w due to the implicit function theorem.) For that purpose we differentiate the Euler-Lagrange equation:

$$0 = \frac{\mathrm{d}}{\mathrm{d}w}(D_M E_0^h(M^w)) = \mathrm{Hess} E_0^h(M^w) \partial_w M^w + (\partial_w D_M E_0^h)(M^w).$$

Hence $\partial_w M$ is obtained by solving the latter linear equation. Similar as in (4.11) the derivative of the energy w.r.t. w amounts to $\partial_w D_M E_0^h = \partial_{h_1} D_M E_0^h \frac{1}{N_1}$.

4.10. Practical issues of the simulations

4.10.1. General remarks

The Newton iteration in the simulation is stopped if the norm of the residuum drops below a certain threshold $\sim 10^{-6}$ to 10^{-8}. We usually observe 3 to 4 steps of the Newton iteration within the region of quadratic convergence. The necessary resolution of the walls was investigated in [Steo6]. As soon as the interfaces are not properly resolved, the iterations usually do not converge which is related to the fact that the discrete energy is in that case not coercive. Instead of a plot of the discrete values (e.g. h_{ext}-$\langle m_2^2 \rangle^{1/2}$-plot) we usually show the linear interpolant for reasons of a clear presentation. Below, we list the parameters which are chosen in the numerical simulations. If not stated differently, we neglect uniaxial anisotropy and polycrystalline anisotropy. The choice of the constant c_0, which appears in the wall energy, is described below in the context of Figure 1.15.

4.10.2. Choice of parameters

Figure 1.11 shows the result of a path-following of the w^*-periodic branch where we chose $N_1 = 512$ and $N_2 = 256$. We used a uniform step-size $\eta = 0.1$. The path-following procedure was started at the bifurcation point, i.e., $(x_0, \lambda_0) = (M_0, h_{\mathrm{ext}0}) = (0, h_{\mathrm{ext}}^*)$, where the M-component of the tangent was chosen as the discretization of the unstable mode while the field component is zero.

Figure 1.12 shows configurations computed in a path-following of the w^*-periodic branch where we chose $N_1 = 512$ and $N_2 = 256$. We used a uniform step-size $\eta = 1$. The path-following procedure was started at the bifurcation point.

Figure 1.15 shows the value of the maximum of m_2 – computed in the same path-following process shown in figure 1.12 – compared to the optimal period which was

obtained from a Matlab minimization of the domain theoretic energy. The constant $c_0 = 3.26$ in the line-energy density was obtained by a fit of the simulation results of the one-dimensional energy (2.2) using 4096 grid points on a domain of size $\frac{w^*}{2}$ where m_2^0 varies between 20 and 100, cf. Chapter 2, in particular (2.3).

Figure 1.16 shows the result of the path-following for the computation of the optimal period as described in Section 4.8 where we chose $N_1 = 512$ and $N_2 = 256$. We used a uniform step-size $\eta = 0.03$.

Figure 1.18 shows a plot of the contour lines of the second derivative of the energy per period and the first derivative of the energy density. The data results from a path-following using $N_1 = N_2 = 256$ and $\eta = 0.1$ of w-periodic branches for $w = (1 + 0.025\,n)w^*$, $n = 0, 1, 2, \ldots$. The derivatives of the energy and the energy density are computed as described in the previous section.

Figure 1.19 shows a plot of the contour lines of the second derivative of the energy per period and the first derivative of the energy density. The data results from a path-following of w-periodic branches for $w = (1 + 0.5\,n)w^*$, $n = 0, 1, 2, \ldots$ using $N_1 = 4096$, $N_2 = 256$ and $\eta = 0.5$. The derivatives of the energy and the energy density are computed as described in the previous section. The contour lines are obtained on the basis of an interpolation of the data on an equidistant grid w.r.t. w and h_{ext}.

Figure 1.20 shows a plot of the contour lines of the second derivative of the energy per period and the first derivative of the energy density. This plot was generated with the help of a Matlab routine which minimizes the amplitude functional on an equidistant grid w.r.t. δk_1 and δh_{ext}. We plot the results using the identification $\delta w = -\frac{2\pi}{(w^*)^2}\delta k_1$.
Figure 1.21 shows a plot of the contour lines of the second derivative of the energy per period and the first derivative of the energy density. Although the magnetization is smooth close to the bifurcation, we have to choose a relatively fine grid since the discrete critical field and the discrete critical anisotropy depend on the number of grid-points. The data for the reduced energy results from a path-following of w-periodic branches for $w = (1 + 0.005\,n)w^*$, $n = 0, 1, 2, \ldots$, using $N_1 = N_2 = 512$ and $\eta = 0.002$. The derivatives of the energy and the energy density are computed as described in the previous section. The result for the amplitude functional was generated with the help of a Matlab routine which minimizes the amplitude functional on an equidistant grid w.r.t. δk_1 and δh_{ext}. The contour lines are plotted using the identification $\delta w = -\frac{2\pi}{(w^*)^2}\delta k_1$.

Figure 1.22 shows the result of the bifurcation detection which was computed on the Nw^*-periodic domain using $N_1 = 128$ and $N_2 = 128$ grid-points. Here $\eta = 0.1$ which is the error the secondary critical fields.

Figure 1.23 shows the result of the bifurcation detection where $N_1 = 256$, $N_2 = 128$ and $\eta = 0.1$.

Figure 1.24 and Figure 1.25 show the configurations along the secondary branches as indicated in Figure 1.23.

Figure 1.26 shows the result of a steepest descent simulation for the $5w^*$-periodic pattern where $N_1 = 1024$ and $N_2 = 128$. The energy is subsequently minimized for different values of the external field using the previous result as a starting point for the minimization. The increment in the external field is $\Delta h_{\text{ext}} = 0.2$.

Figure 1.27 shows a plot of the contour lines of the second derivative of the energy per period and the first derivative of the energy density. The data results from a path-following of w-periodic branches for $w = (1 + 0.25\,n)w^*$, $n = 0, 1, 2, \ldots$, using $N_1 = 1024$, $N_2 = 128$ and $\eta = 0.25$. The derivatives of the energy and the energy density are computed as described in the previous section.

Figure 1.28 shows the result of a path-following of the Nw^*-periodic branch, $N = 1, 2, 3, 4$, where we chose $N_1 = 512$ and $N_2 = 64$. We used a uniform step-size $\eta = 0.1$. The path-following procedure was started at $h_{\text{ext}} = 12$, where the first stationary point was obtained by an energy minimization.

Figure 1.30 shows the result of an iterative energy minimization including uniaxial and polycrystalline anisotropy. In that case $N_1 = 1024$, $N_2 = 128$, $L = 6w^*$, $\delta h_{\text{ext}} = 0.1$. Moreover, we chose $Q = 2 \times 10^{-4}$, $\delta = 0.02$, and $\varepsilon = 0.0005$. Let us note that $\varepsilon(d = 5\text{ nm}, \ell = 70\,\mu\text{m}, t = 20\text{ nm}) = 5.2 \times 10^{-4}$, $\delta(d = 5\text{nm}, \ell = 70\,\mu\text{m}, t = 20nm) = 1.9 \times 10^{-2}$. The variance of the random external field was chosen as $(\sigma^*)^2 = 110.83$ – for a motivation of that value see Subsection 7.1.2.

Figure 1.32 shows the result of the path following started at the bifurcation for $N_1 = N_2 = 256$ and $\eta = 0.1$.

Figure 1.33 shows the result of the path following started at the bifurcation for $N_1 = N_2 = 128$ and $\eta = 0.2$.

Figure 6.5 shows the result of different path-following and branch switching procedures. We always chose $N_1 = N_2 = 256$. The step size η was chosen between 0.1 for the primary branches and 0.02 for the secondary branches.

Figure 6.6: See Figure 6.5 for the description of the simulation of the reduced energy. The Euler-Lagrange equation of the amplitude functional was explicitly solved in Mathematica. The obtained data was exported for a discrete set of values of the external field and plotted in Matlab.

Figure 6.7, see Figure 6.6.

Figure 7.3 shows the result of an iterative energy minimization. In that case $N_1 = 1024$, $N_2 = 128$, $L = 6w^*$, $\delta h_{\text{ext}} = 0.1$. The variance of the random external field was chosen as $(\sigma^*)^2 = 1.73$. The dominant wave number is independent of the specific choice of σ^* provided it is sufficiently small so that the linear ripple theory is valid.

5

Bloch wave analysis

This chapter addresses the relation between the instability of periodic patterns under long wave-length modulations (Eckhaus instability) and the concavity of the minimal energy per period. This relation is established on the basis of an asymptotic Bloch wave analysis in Theorem 5.1. The use of Theorem 5.1 is threefold: Together with the extended bifurcation analysis in Chapter 6 it implies the instability of the $\widehat{w}^*$-periodic concertina and explains the deviation of the initially observed experimental period from the period of the unstable mode $\widehat{w}^*$, cf. Figure 1.20. In conjunction with the numerical computation of the second derivative of the minimal energy per period, we can derive the marginal Eckhaus stable state for moderate external field $\widehat{h}_{\text{ext}}$ also away from the bifurcation, see Section 4.9 and Figure 1.18. Finally, in combination with the asymptotic analysis on the basis of domain theory we obtain the scaling of the period of the marginal Eckhaus stable state for large external field $\widehat{h}_{\text{ext}} \gg 1$ in Chapter 2, cf. Figure 1.19.

In Section 5.2 we sketch a generalization of Theorem 5.1 to functionals with an additional non-linear constraint.

5.1. Main result and proof

Theorem 5.1. *Let $\{\widehat{m}_2^{\widehat{w}}\}_{\widehat{w}}$ be a family of $\widehat{w}$-periodic stationary points of the reduced energy functional* (1.14) *which is differentiable w.r.t. $\widehat{w}$. Consider infinitesimal perturbations $\widehat{\delta m_2}$ of Bloch form, i.e.,*

$$\widehat{\delta m_2} \;=\; \mathrm{e}^{i\xi\widehat{x}_1} v(\widehat{x}_1, \widehat{x}_2), \tag{5.1}$$

where $v : [0,\widehat{w}) \times (0,1) \to \mathbb{C}$ is $\widehat{w}$-periodic in $\widehat{x}_1$. Then for small wave numbers, i.e., $\xi = \frac{2\pi}{N}$ where the integer $N \gg 1$, we have that the smallest eigenvalue of the Hessian is bounded by the second derivative of the minimal energy per period, more precisely

$$\inf_{\widehat{\delta m_2} \text{ in } (5.1)} \frac{\text{Hess } \widehat{E}_0(\widehat{m}_2^{\widehat{w}})(\widehat{\delta m_2}, \widehat{\delta m_2})}{\int_{(0,N\widehat{w})\times(0,1)} |\widehat{\delta m_2}|^2 \,\mathrm{d}\widehat{x}_1 \,\mathrm{d}\widehat{x}_2} \;\lessapprox\; \widehat{\xi}^2 \frac{\frac{\mathrm{d}^2}{\mathrm{d}\widehat{w}^2}(\widehat{E}_0(\widehat{m}_2^{\widehat{w}}))}{\int_{(0,\widehat{w})\times(0,1)} (\widehat{\partial}_1 \widehat{m}_2^{\widehat{w}})^2 \,\mathrm{d}\widehat{x}_1 \,\mathrm{d}\widehat{x}_2}.$$

Here we denote by $f(\xi) \lessapprox \xi^2 g$ that for $\xi \to 0$ it holds that that $f(\xi) \leq \xi^2 g$ up to higher order terms.

Before we step into the proof, let us comment on the result of Theorem 5.1. Consider a smooth branch of $\widehat{w}$-periodic stationary points $\widehat{m}_2^{\widehat{w}}$ and let $\widehat{E}_0(\widehat{w}) = \widehat{E}_0(\widehat{m}_2^{\widehat{w}})$ be the corresponding energy. For local energy functionals the geometric interpretation of concavity immediately leads to a building plan for a suitable destabilizing (finite) perturbation: By cutting, gluing, and if necessary additional smoothing, one can construct an inner variation which mimics a wave length modulation, see Figure 5.1.

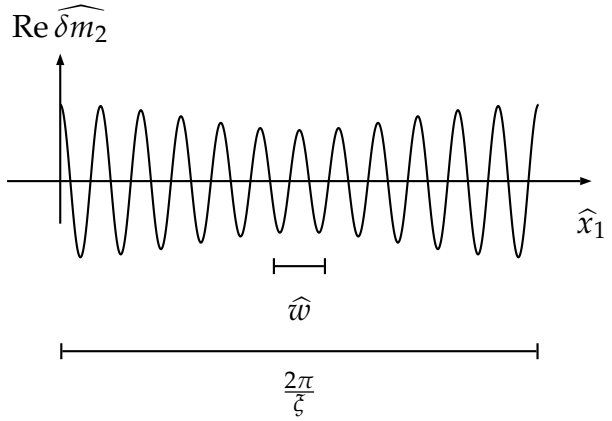

Figure 5.1.: Sinusoidal modulation of a $\widehat{w}$ periodic function.

Not surprisingly, one obtains in case of a local energy functional that the energy of the modulation is equal to the modulation of the energy (up to higher order terms). Theorem 5.1 shows that this can be generalized to non-local energies, at least in the case of sinusoidal modulation functions.

We subdivide the proof of Theorem 5.1 into several steps. In a first step we determine how Hess $\widehat{E}_0(\widehat{m}_2)(\widehat{\delta m_2}, \widehat{\delta m_2})$ acts as an operator applied to the modulated v. In particular we have to determine how the non-locality commutes with the modulation. In the case of the reduced stray-field energy, i.e., the non-local operator $|\partial_1|^{-1/2}$, the modulation amounts to a shift of the Fourier symbol $|k_1|^{-1/2} \rightsquigarrow |k_1 + \xi|^{-1/2}$. Afterwards we choose a suitable Ansatz for v and use an asymptotic expansion of the operator to derive that the leading order term in the expansion is related to the second derivative of the energy $\widehat{E}_0(\widehat{w}) := \widehat{E}_0(\widehat{m}_2^{\widehat{w}})$. The perturbation corresponds to the infinitesimal variation of an inner variation; for details on the Ansatz we refer to the paragraph which follows right after the end of the proof of Theorem 5.1.

An analog of Theorem 5.1 can, for example, be proofed for constrained minimization problems with local energy contributions. Note that the reduced energy functional can be rewritten to fit into that framework by introducing a second variable. This approach is sketched in Section 5.2.

Proof of Theorem 5.1. For notational convenience we drop the $\widehat{\cdot}$.

Step 1. Consider a modulation perturbation $\delta m_2 = \mathrm{e}^{i\xi x_1} v(x_1, x_2)$, where $\xi = \frac{2\pi}{Nw}$, $N \in \mathbb{N}$, and where v is w-periodic w.r.t. x_1. In this step we will see how the Hessian $\mathrm{Hess} E_0(m_2)(\delta m_2, \delta m_2)$ acts as an operator applied to v. More precisely, we derive the following formula:

$$\begin{aligned}
&\frac{1}{N}\mathrm{Hess} E_0(m_2)(\delta m_2, \delta m_2) \\
&\qquad = 2\int_{(0,w)\times(0,1)} |(\partial_1 + i\xi)v|^2 \,\mathrm{d}x_1\,\mathrm{d}x_2 \\
&\qquad\quad + \int_{(0,w)\times(0,1)} \left| |\partial_1 + i\xi|^{-1/2}(-(\partial_1 + i\xi)(m_2 v) + \partial_2 v) \right|^2 \mathrm{d}x_1\,\mathrm{d}x_2 \\
&\qquad\quad + \int_{(0,w)\times(0,1)} \left(|\partial_1|^{-1}(-\partial_1 \tfrac{m_2^2}{2} + \partial_2 m_2) \right) (-\partial_1 |v|^2)\,\mathrm{d}x_1\,\mathrm{d}x_2 \\
&\qquad\quad - 2\,h_{\mathrm{ext}} \int_{(0,w)\times(0,1)} |v|^2 \,\mathrm{d}x_1\,\mathrm{d}x_2.
\end{aligned} \tag{5.2}$$

Before we come to the proof of (5.2), let us recall that the Hessian (evaluated on Nw-periodic perturbations such as $\delta m_2 = \mathrm{e}^{i\xi x_1} v(x_1, x_2)$ as above) is given by:

$$\begin{aligned}
&\mathrm{Hess} E_0(m_2)(\delta m_2, \delta m_2) \\
&\qquad = 2\int_{(0,Nw)\times(0,1)} |\partial_1 \delta m_2|^2 \,\mathrm{d}x_1\,\mathrm{d}x_2 \\
&\qquad\quad + \int_{(0,Nw)\times(0,1)} \left| |\partial_1|^{-1/2}(-\partial_1(m_2 \delta m_2) + \partial_2 \delta m_2) \right|^2 \mathrm{d}x_1\,\mathrm{d}x_2 \\
&\qquad\quad + \int_{(0,Nw)\times(0,1)} \left(|\partial_1|^{-1}(-\partial_1 \tfrac{m_2^2}{2} + \partial_2 m_2) \right) (-\partial_1 |\delta m_2|^2)\,\mathrm{d}x_1\,\mathrm{d}x_2 \\
&\qquad\quad - 2\,h_{\mathrm{ext}} \int_{(0,Nw)\times(0,1)} |\delta m_2|^2 \,\mathrm{d}x_1\,\mathrm{d}x_2.
\end{aligned} \tag{5.3}$$

Notice that we allow for complex perturbations in order to simplify the notations in the proof, so that we think of the Hessian as a sesquilinear form – we always assume that the second argument is the one that is complex conjugated. This also necessitates the absolute values in (5.2) and (5.3).

In order to obtain (5.2), we have to derive how the modulation commutes with the local and non-local differential operators w.r.t. the x_1-variable; the Zeeman contribution and ∂_2 are obviously oblivious to the modulation. Let us start with the local operator for which we observe that

$$\begin{aligned}
\partial_1(\mathrm{e}^{i\xi x_1} v(x_1, x_2)) &= \mathrm{e}^{i\xi x_1}(\partial_1 + i\xi) v(x_1, x_2), \\
\partial_1(\mathrm{e}^{-i\xi x_1} \bar{v}(x_1, x_2)) &= \mathrm{e}^{-i\xi x_1}(\partial_1 - i\xi) \bar{v}(x_1, x_2).
\end{aligned} \tag{5.4}$$

Using the representation of the non-local operator in Fourier space, we similarly obtain that

$$\begin{aligned}
|\partial_1|^{-1/2}(\mathrm{e}^{i\xi x_1} v(x_1, x_2)) &= \mathrm{e}^{i\xi x_1} |\partial_1 + i\xi|^{-1/2} v(x_1, x_2), \\
|\partial_1|^{-1/2}(\mathrm{e}^{-i\xi x_1} \bar{v}(x_1, x_2)) &= \mathrm{e}^{-i\xi x_1} |\partial_1 - i\xi|^{-1/2} \bar{v}(x_1, x_2),
\end{aligned} \tag{5.5}$$

where $|\partial_1 \pm i\xi|^{-1/2}$ denotes the operator with Fourier symbol $|ik_1 \pm i\xi|^{-1/2}$. The modulation thus leads to a shift of the Fourier multiplier. Hence, we obtain formula (5.2) by replacing δm_2 and $\overline{\delta m_2}$ by v and $\bar{v}$, respectively, and the local and non-local operators acting on δm_2 and $\overline{\delta m_2}$ by (5.4) and (5.5), respectively. We emphasize, and later on use, that the non-local contribution can be written as

$$\begin{aligned}\int_{(0,w)\times(0,1)} \big||\partial_1 + i\xi|^{-1/2} v\big|^2 \,\mathrm{d}x_1\,\mathrm{d}x_2 \\ &= \int_{(0,w)\times(0,1)} (|\partial_1 + i\xi|^{-1/2} v)(|\partial_1 - i\xi|^{-1/2}\bar{v})\,\mathrm{d}x_1\,\mathrm{d}x_2 \\ &= \int_{(0,w)\times(0,1)} v(|\partial_1 - i\xi|^{-1}\bar{v})\,\mathrm{d}x_1\,\mathrm{d}x_2. \end{aligned} \tag{5.6}$$

Let us finally define

$$\mathrm{Hess}^{\xi} E_0(m_2)(v,v) \;:=\; \frac{1}{N}\mathrm{Hess} E_0(m_2)(\delta m_2, \delta m_2). \tag{5.7}$$

Notice that $\mathrm{Hess}^{\xi} E_0(m_2)$ is defined on w-periodic functions and that we can allow for arbitrary values of ξ on the level of (5.7).

Step 2. Consider $v^{\xi} := v_0 + \xi v_1$ where v_0 and v_1 are w-periodic functions. (Later on we chose specific v_0 and v_1 in Step 3.) Then

$$\begin{aligned}\mathrm{Hess}^{\xi}(m_2)(v^{\xi}, v^{\xi}) \;=\; &\mathcal{L}^0(v_0,v_0) + \xi\big(\mathcal{L}^1(v_0,v_0) + \mathcal{L}^0(v_1,v_0) + \mathcal{L}^0(v_0,v_1)\big) \\ &+ \xi^2\big(\tfrac{1}{2}\mathcal{L}^2(v_0,v_0) + \mathcal{L}^1(v_1,v_0) + \mathcal{L}^1(v_0,v_1) + \mathcal{L}^0(v_1,v_1)\big) + \mathcal{O}(\xi^3), \end{aligned} \tag{5.8}$$

where the sesquilinear forms $\mathcal{L}^0$, $\mathcal{L}^1$, and $\mathcal{L}^2$ are given by

$$\begin{aligned}\mathcal{L}^0(v,r) = {} & 2\int_{(0,w)\times(0,1)} \partial_1 v\, \partial_1 \bar{r}\,\mathrm{d}x_1\,\mathrm{d}x_2 \\ &+ \int_{(0,w)\times(0,1)} \Big(|\partial_1|^{-1/2}(-\partial_1(m_2\, v) + \partial_2 v)\Big) \\ &\qquad\qquad \Big(|\partial_1|^{-1/2}(-\partial_1(m_2\,\bar{r}) + \partial_2\bar{r})\Big)\,\mathrm{d}x_1\,\mathrm{d}x_2 \\ &+ \int_{(0,w)\times(0,1)} \Big(|\partial_1|^{-1}(-\partial_1 \tfrac{m_2^2}{2} + \partial_2 m_2)\Big)(-\partial_1(v\,\bar{r}))\,\mathrm{d}x_1\,\mathrm{d}x_2 \\ &- 2h_{\mathrm{ext}}\int_{(0,w)\times(0,1)} v\,\bar{r}\,\mathrm{d}x_1\,\mathrm{d}x_2, \end{aligned} \tag{5.9}$$

and

$$\begin{aligned}&\mathcal{L}^1(v,r) \\ &\quad= \; 2\int_{(0,w)\times(0,1)} (-i\,\partial_1 v\,\bar{r} + v\, i\,\partial_1\bar{r})\,\mathrm{d}x_1\,\mathrm{d}x_2 \\ &\qquad + \int_{(0,w)\times(0,1)} (-i\, m_2\, v)|\partial_1|^{-1}(-\partial_1(m_2\,\bar{r}) + \partial_2\bar{r})\,\mathrm{d}x_1\,\mathrm{d}x_2\end{aligned}$$

$$+\int_{(0,w)\times(0,1)}(-\partial_1(m_2\,v)+\partial_2 v)|\partial_1|^{-1}(i\,m_2\,\bar{r})\,\mathrm{d}x_1\,\mathrm{d}x_2$$
$$+\int_{(0,w)\times(0,1)}(-\partial_1(m_2\,v)+\partial_2 v)\;(|\partial_1|^{-3}\,i\partial_1)\;(-\partial_1(m_2\,\bar{r})+\partial_2\bar{r})\,\mathrm{d}x_1\,\mathrm{d}x_2, \tag{5.10}$$

and

$$\begin{aligned}\mathcal{L}^2(v,r) \;=\; & 4\int_{(0,w)\times(0,1)} v\,\bar{r}\,\mathrm{d}x_1\,\mathrm{d}x_2\\ &+2\int_{(0,w)\times(0,1)} i\,m_2\,v|\partial_1|^{-3}\,i\partial_1(-\partial_1(m_2\bar{r})+\partial_2\bar{r})\,\mathrm{d}x_1\,\mathrm{d}x_2\\ &+2\int_{(0,w)\times(0,1)}(-\partial_1(m_2 v)+\partial_2 v)|\partial_1|^{-3}\,i\partial_1(-i\,m_2\,\bar{r})\,\mathrm{d}x_1\,\mathrm{d}x_2\\ &+2\int_{(0,w)\times(0,1)}(m_2 v)|\partial_1|^{-1}(m_2\,\bar{r})\,\mathrm{d}x_1\,\mathrm{d}x_2\\ &+2\int_{(0,w)\times(0,1)}(-\partial_1(m_2 v)+\partial_2 v)\;|\partial_1|^{-3}\;(-\partial_1(m_2\bar{r})+\partial_2\bar{r})\,\mathrm{d}x_1\,\mathrm{d}x_2.\end{aligned} \tag{5.11}$$

Notice that (5.9) is just the Hessian, see (5.3), evaluated on perturbations defined on the domain $(0,w)\times(0,1)$. In order to show (5.8), notice that the local contributions in (5.7) and (5.2), respectively, can be easily expanded w.r.t. ξ. For the non-local operator, see (5.6), we calculate the asymptotic expansion of the Fourier symbol w.r.t. ξ:

$$|ik_1-i\xi|^{-1} \;=\; |k_1-\xi|^{-1} \;=\; |k_1|^{-1}+\xi\tfrac{k_1}{|k_1|}|k_1|^{-2}+2\xi^2|k_1|^{-3}+\xi^3\,\mathcal{R}(k_1,\xi). \tag{5.12}$$

The error in the Taylor expansion $\mathcal{R}(k_1,\xi)$ is of the order $\mathcal{O}(1)$ uniformly in k_1 provided $\xi \ll \frac{2\pi}{w}$. In fact, by homogeneity only ξk_1^{-1} matters since (5.12) is in principle an expansion in ξk_1^{-1} due to

$$|ik_1-i\xi|^{-1}=|k_1|^{-1}|1-\tfrac{\xi}{k_1}|^{-1}.$$

Since $|k_1|\geq\frac{2\pi}{w}$, the ratio ξk_1^{-1} is small independent of k_1 for $\xi\ll\frac{2\pi}{w}$ which entails that $\mathcal{R}(k_1,\xi)=\mathcal{O}(1)$. Observe that $\frac{k_1}{|k_1|}|k_1|^{-2}\mathcal{F}(v)=\mathcal{F}(-i|\partial_1|^{-3}\partial_1 v)$, so that $\frac{k_1}{|k_1|}|k_1|^{-2}\bar{\mathcal{F}}(\bar{v})=\bar{\mathcal{F}}(i|\partial_1|^{-3}\partial_1\bar{v})$. Hence we derive from (5.12) that

$$\begin{aligned}&\int_{(0,w)\times(0,1)}\big(|\partial_1+i\xi|^{-1/2}u\big)\big(|\partial_1-i\xi|^{-1/2}\bar{v}\big)\,\mathrm{d}x_1\,\mathrm{d}x_2\\ &\qquad=\int_{(0,w)\times(0,1)} u\,\big(|\partial_1-i\xi|^{-1}\bar{v}\big)\,\mathrm{d}x_1\,\mathrm{d}x_2\\ &\qquad=\int_{(0,w)\times(0,1)} u\,\big(|\partial_1|^{-1}\bar{v}\big)\,\mathrm{d}x_1\,\mathrm{d}x_2\\ &\qquad\quad+\xi\int_{(0,w)\times(0,1)} u\,\big(i|\partial_1|^{-3}\partial_1\bar{v}\big)\,\mathrm{d}x_1\,\mathrm{d}x_2\\ &\qquad\quad+2\,\xi^2\int_{(0,w)\times(0,1)} u\,|\partial_1|^{-3}\bar{v}\,\mathrm{d}x_1\,\mathrm{d}x_2+\mathcal{O}(\xi^3).\end{aligned} \tag{5.13}$$

Using (5.13), it is now a straightforward calculation to obtain the expansion (5.8) from the representation (5.2).

Step 3. The formulas derived in Step 1 and Step 2 hold for any stationary point m_2 whereas in this step it becomes important to take m_2 from the family of stationary points $\{m_2^w\}_w$ differentiable w.r.t. w: Consider the following Ansatz for the perturbation v^ξ:

$$v^\xi = v_0 + \xi v_1 \quad \text{where} \quad v_0 = -\partial_1 m_2^w \quad \text{and} \quad v_1 = i\, L m_2^w, \tag{5.14}$$

and $L = x_1\partial_1 + w\partial_w$. Based on a differentiation w.r.t. w of the rescaled Euler-Lagrange equation, we will show in this step that

$$\mathcal{L}^0(v_1,\cdot) + \mathcal{L}^1(v_0,\cdot) \;=\; \mathcal{L}^0(iLm_2^w,\cdot) + \mathcal{L}^1(-\partial_1 m_2^w,\cdot) \;=\; 0. \tag{5.15}$$

As we will see, the constant and linear term in the expansion (5.8) vanish, so that (5.15) will entail that

$$\mathrm{Hess}^\xi(m_2^w)(v^\xi,v^\xi) \;=\; \xi^2(\tfrac{1}{2}\mathcal{L}^2(v_0,v_0) - \mathcal{L}^0(v_1,v_1)) + \mathcal{O}(\xi^3). \tag{5.16}$$

For a motivation of Ansatz (5.14) we refer to the paragraph which follows right after the end of the proof.

First we have to show that v^ξ is well defined, i.e., that Lm_2^w is w-periodic. In fact, we have due to the periodicity of m_2^w that

$$\begin{aligned} Lm_2^w(x_1+w) &= (x_1+w)\partial_1 m_2^w(x_1+w) + w\partial_w m_2^w(x_1+w) \\ &= (x_1+w)\partial_1 m_2^w(x_1) + w\tfrac{\mathrm{d}}{\mathrm{d}w}(m_2^w(x_1+w)) - w\partial_1 m_2^w(x_1) \\ &= (x_1+w)\partial_1 m_2^w(x_1) + w\partial_w m_2^w(x_1) - w\partial_1 m_2^w(x_1) \\ &= x_1\partial_1 m_2^w(x_1) + w\partial_w m_2^w(x_1) \\ &= Lm_2^w(x_1). \end{aligned}$$

To see (5.16), we use the expansion (5.8) which was derived in Step 2. Due to periodicity of m_2^w and translational invariance of E_0, $\partial_1 m_2^w$ is in the null space of the Hessian $\mathrm{Hess}E_0(m_2^w)$, so that

$$\mathcal{L}^0(\cdot,\partial_1 u) \;=\; \mathcal{L}^0(\partial_1 u,\cdot) \;=\; 0. \tag{5.17}$$

This entails that the constant (in ξ) term in (5.8) vanishes. The l.h.s. of (5.8) is purely real. On the other hand, $\mathcal{L}^1(v_0,v_0)$ is purely imaginary, see (5.10) and (5.14). Moreover $\mathcal{L}^0(v_0,v_1) = \overline{\mathcal{L}^0(v_1,v_0)}$ is purely imaginary, see (5.9) and (5.14). Hence, the linear term in (5.8) vanishes. So far we have shown that the leading order contribution in (5.8), where v_0 and v_1 are as in (5.14), is (at least) quadratic in ξ. Using (5.15) then (5.16) follows. In fact, by testing (5.15) with v_1 we derive that

$$\begin{aligned} &\mathrm{Hess}^\xi(v^\xi,v^\xi) \\ &\quad= \xi^2(\tfrac{1}{2}\mathcal{L}^2(v_0,v_0) + \mathcal{L}^1(v_1,v_0) + \mathcal{L}^1(v_0,v_1) + \mathcal{L}^0(v_1,v_1)) + \mathcal{O}(\xi^3) \\ &\quad= \xi^2(\tfrac{1}{2}\mathcal{L}^2(v_0,v_0) - \mathcal{L}^0(v_1,v_1)) + \mathcal{O}(\xi^3). \end{aligned} \tag{5.18}$$

We now address (5.15). Let us note that by abuse of notation we do not distinguish the linear forms $\mathcal{L}_i(v,\cdot)$ and their Riesz representations w.r.t L^2 in the following. We have by definition (5.10) that

$$\begin{aligned}\mathcal{L}^1(-\partial_1 m_2^w,\cdot) = -i\Big(&-4\,\partial_1^2 m_2^w - (m_2^w\partial_1 - \partial_2)|\partial_1|^{-1}(m_2^w\partial_1 m_2^w)\\ &- m_2^w|\partial_1|^{-1}(\partial_1(m_2^w\partial_1 m_2^w) - \partial_2\partial_1 m_2^w)\\ &+ (m_2^w\partial_1 - \partial_2)(|\partial_1|^{-3}\partial_1)(-\partial_1(m_2^w\partial_1 m_2^w) + \partial_2\partial_1 m_2^w)\Big)\\ = -i\Big(&-4\,\partial_1^2 m_2^w - m_2^w\partial_1|\partial_1|^{-1}\partial_1\tfrac{(m_2^w)^2}{2} + \underline{\partial_2|\partial_1|^{-1}\partial_1\tfrac{(m_2^w)^2}{2}}\\ &\underline{-m_2^w|\partial_1|^{-1}\partial_1^2\tfrac{(m_2)^2}{2} + m_2^w|\partial_1|^{-1}\partial_2\partial_1 m_2^w}\\ &\underline{-m_2^w\partial_1|\partial_1|^{-3}\partial_1^3\tfrac{(m_2^w)^2}{2} + m_2^w\partial_1|\partial_1|^{-3}\partial_1\partial_2\partial_1 m_2^w}\\ &\underline{+\partial_2|\partial_1|^{-3}\partial_1\partial_1^2\tfrac{(m_2^w)^2}{2}} - \partial_2|\partial_1|^{-3}\partial_1\partial_2\partial_1 m_2^w\Big).\end{aligned}$$

Observe that $|\partial_1|^{-3}\partial_1^2 = -|\partial_1|^{-1}$ which yields that the underlined terms cancel. Therefore we obtain

$$\mathcal{L}^1(-\partial_1 m_2^w,\cdot) = i\left(4\,\partial_1^2 m_2^w + m_2^w|\partial_1|^{-1}\partial_1^2\tfrac{(m_2^w)^2}{2} - |\partial_1|^{-1}\partial_2^2 m_2^w\right). \tag{5.19}$$

Consider the rescaling

$$x_1 = w\tilde{x}_1 \quad\text{and}\quad \tilde{m}_2^w(\tilde{x}_1) = m_2^w(w\tilde{x}_1). \tag{5.20}$$

Under this rescaling the Euler-Lagrange equation, i.e.,

$$0 = -2\,\partial_1^2 m_2^w + (m_2^w\partial_1 - \partial_2)|\partial_1|^{-1}(-\partial_1\tfrac{(m_2^w)^2}{2} + \partial_2 m_2^w) - 2\,h_{\text{ext}}\,m_2^w,$$

turns into

$$0 = -\tfrac{2}{w^2}\,\tilde{\partial}_1^2\tilde{m}_2^w + (\tfrac{1}{w}\,\tilde{m}_2^w\tilde{\partial}_1 - \partial_2)w\,|\tilde{\partial}_1|^{-1}(-\tfrac{1}{w}\,\tilde{\partial}_1\tfrac{(\tilde{m}_2^w)^2}{2} + \partial_2\tilde{m}_2^w) - 2\,h_{\text{ext}}\,\tilde{m}_2^w. \tag{5.21}$$

The latter expression (5.21) has the right form in order to differentiate w.r.t. w. We apply chain rule and use that the Hessian is related to the differentiated r.h.s. of the Euler-Lagrange equation (w.r.t. m_2^w). After rescaling into the original variables we therefore obtain

$$0 = \tfrac{1}{w}(4\,\partial_1^2 m_2^w + m_2^w\partial_1|\partial_1|^{-1}\partial_1\tfrac{(m_2^w)^2}{2} - |\partial_1|^{-1}\partial_2^2 m_2^w) + \mathcal{L}^0\big((\partial_w\widetilde{m}_2^w)(w^{-1}\cdot),\cdot\big). \tag{5.22}$$

To obtain (5.15), we compare (5.19) and (5.22) multiplied by iw, using the relation

$$(w\partial_w\widetilde{m}_2^w)(w^{-1}x_1) = (x_1\partial_1 m_2^w + w\partial_w m_2^w)(x_1) = Lm_2^w(x_1). \tag{5.23}$$

Step 4. In this step we show that

$$w^2 \tfrac{\mathrm{d}^2}{\mathrm{d}w^2} E_0(m_2^w) = \tfrac{1}{2}\mathcal{L}^2(v_0, v_0) - \mathcal{L}^0(v_1, v_1). \tag{5.24}$$

Let us rewrite the the minimal energy with the help of the rescaled quantities (5.20), i.e.,

$$\begin{aligned} &E_0(m_2^w) \\ &= \int_{(0,w)} \int_{(0,1)} \Big((\partial_1 m_2)^2 + \tfrac{1}{2}\big(|\partial_1|^{-1/2}(-\partial_1 \tfrac{m_2^2}{2} + \partial_2 m_2)\big)^2 - h_{\mathrm{ext}} m_2^2 \Big) \,\mathrm{d}x_2 \,\mathrm{d}x_1 \\ &= \int_{(0,1)} \Bigg(w \int_{(0,1)} \Big(w^{-2}(\tilde{\partial}_1 \tilde{m}_2^w)^2 + \tfrac{1}{2}\big(w^{1/2}|\tilde{\partial}_1|^{-1/2}(-w^{-1}\tilde{\partial}_1 \tfrac{(\tilde{m}_2^w)^2}{2} + \partial_2 \tilde{m}_2^w)\big)^2 \\ &\qquad - h_{\mathrm{ext}}(\tilde{m}_2^w)^2 \Big) \,\mathrm{d}x_2 \Bigg) \,\mathrm{d}\tilde{x}_1 =: \widetilde{E}_0^w(\widetilde{m}_2^w). \end{aligned} \tag{5.25}$$

The r.h.s of (5.25) has the right form in order to differentiate w.r.t. w. It holds that

$$\begin{aligned} \tfrac{\mathrm{d}^2}{\mathrm{d}w^2} \widetilde{E}_0^w(\widetilde{m}_2^w) = \partial_w^2 \widetilde{E}_0^w(\widetilde{m}_2^w) + 2\partial_w D_{\tilde{m}_2} \widetilde{E}_0^w(\widetilde{m}_2^w)\partial_w \tilde{m}_2^w \\ + D_{\tilde{m}_2}^2 \widetilde{E}_0^w(\widetilde{m}_2^w)(\partial_w \tilde{m}_2^w, \partial_w \tilde{m}_2^w) + D_{\tilde{m}_2} \widetilde{E}_0^w(\widetilde{m}_2^w)\partial_w^2 \tilde{m}_2^w, \end{aligned}$$

where $D_{\tilde{m}_2}$ denotes the functional derivative. The last contribution vanishes; it is equal to the rescaled Euler-Lagrange equation tested with $\partial_w^2 \tilde{m}_2^w$. By differentiating the rescaled Euler-Lagrange equation w.r.t. w, and testing with $\tilde{m}_2^w$, we obtain

$$\partial_w D_{\tilde{m}_2} \tilde{E}_0^w(\tilde{m}_2^w)\partial_w \tilde{m}_2^w + D_{\tilde{m}_2}^2 \tilde{E}_0^w(\tilde{m}_2^w)(\partial_w \tilde{m}_2^w, \partial_w \tilde{m}_2^w) = 0.$$

Using the latter identity, we have so far shown that

$$\tfrac{\mathrm{d}^2}{\mathrm{d}w^2} E_0(m_2^w) = \tfrac{\mathrm{d}^2}{\mathrm{d}w^2} \widetilde{E}_0^w(\widetilde{m}_2^w) = \partial_w^2 \tilde{E}_0^w(\tilde{m}_2^w) - D_{\tilde{m}_2}^2 \tilde{E}_0^w(\tilde{m}_2^w)(\partial_w \tilde{m}_2^w, \partial_w \tilde{m}_2^w). \tag{5.26}$$

We are now ready to identify the r.h.s. of (5.26) with the r.h.s. of (5.24) and start with the easy part, namely the second contribution in (5.26). By scaling into the original variables and using the relation (5.23), namely $(w\partial_w \tilde{m}_2^w)(w^{-1}x_1) = Lm_2^w(x_1)$, we obtain

$$\begin{aligned} w^2 D_{\tilde{m}_2}^2 \tilde{E}_0^w(\tilde{m}_2^w)(\partial_w \tilde{m}_2^w, \partial_w \tilde{m}_2^w) &= \mathrm{Hess} E_0^w(m)(Lm, Lm) \\ &\overset{(5.9)}{=} \mathcal{L}_0(Lm, Lm) \\ &= \mathcal{L}_0(v_1, v_1). \end{aligned} \tag{5.27}$$

We finally address the first contribution in (5.26). From definition (5.11) it follows

that

$$\begin{aligned}
&\tfrac{1}{2}\mathcal{L}^2(v_0,v_0)\\
&=\int_{(0,w)\times(0,1)}\Big(2(\partial_1 m_2^w)^2\\
&\quad-\, m_2^w\,\partial_1 m_2^w|\partial_1|^{-3}\,\partial_1(-\partial_1(m_2^w\partial_1 m_2^w)+\partial_2\partial_1 m_2^w)\\
&\quad+(-\partial_1(m_2^w\partial_1 m_2^w)+\partial_2\partial_1 m_2^w)|\partial_1|^{-3}\,\partial_1(\,m_2^w\,\partial_1 m_2^w)\\
&\quad+(m_2^w\partial_1 m_2^w)|\partial_1|^{-1}(m_2^w\partial_1 m_2^w)\\
&\quad+(-\partial_1(m_2^w\partial_1 m_2^w)+\partial_2\partial_1 m_2^w)|\partial_1|^{-3}(-\partial_1(m_2^w\partial_1 m_2^w)+\partial_2\partial_1 m_2^w)\Big)\,\mathrm{d}x_1\,\mathrm{d}x_2
\end{aligned}$$

By expanding the latter expression and using again the relation that $|\partial_1|^{-3}\partial_1^2 = -|\partial_1|^{-1}$ we find that

$$\tfrac{1}{2}\mathcal{L}^2(v_0,v_0)=\int_{(0,w)\times(0,1)}\Big(2(\partial_1 m_2^w)^2+(|\partial_1|^{-1/2}\partial_2 m_2^w)^2\Big)\,\mathrm{d}x_1\,\mathrm{d}x_2.$$

On the other hand, due to (5.25), we have

$$\begin{aligned}
w^2\partial_w^2\tilde{E}_0^w(\tilde{m}_2^w)&=w^2\int_0^1\int_0^1\Big(2w^{-3}(\tilde{\partial}_1\tilde{m}_2^w)^2+\big(|\tilde{\partial}_1|^{-1/2}(\partial_2\tilde{m}_2^w)^2\Big)\,\mathrm{d}\tilde{x}_1\,\mathrm{d}x_2\\
&=\int_{(0,w)\times(0,1)}\Big(2(\partial_1 m_2^w)^2+\big(|\partial_1|^{-1/2}(\partial_2 m_2^w)^2\Big)\,\mathrm{d}x_1\,\mathrm{d}x_2.
\end{aligned}$$

This establishes

$$w^2\partial_w^2\tilde{E}_0^w(\tilde{m}_2^w)=\tfrac{1}{2}\mathcal{L}^2(v_0,v_0). \tag{5.28}$$

Collecting (5.27) and (5.28) yields together with (5.26) that

$$w^2\tfrac{\mathrm{d}^2}{\mathrm{d}w^2}E_0(m_2^w)=\tfrac{1}{2}\mathcal{L}^2(v_0,v_0)-\mathcal{L}^0(v_1,v_1).$$

Step 5. In this step we conclude as follows:

$$\begin{aligned}
\xi^2 w^2\tfrac{\mathrm{d}^2}{\mathrm{d}w^2}E_0(m_2^w)&\overset{(5.24)}{=}\xi^2(\tfrac{1}{2}\mathcal{L}^2(v_0,v_0)-\mathcal{L}^0(v_1,v_1))\\
&\overset{(5.16)}{=}\mathrm{Hess}^\xi(v^\xi,v^\xi)+\mathcal{O}(\xi^3)\\
&\overset{(5.7)}{=}\frac{1}{N}\mathrm{Hess}E_0(m_2^w)(\delta m_2^\xi,\delta m_2^\xi)+\mathcal{O}(\xi^3)\\
&=\frac{\mathrm{Hess}E_0(m_2^w)(\delta m_2^\xi,\delta m_2^\xi)}{\int_{(0,Nw)\times(0,1)}|\delta m_2^w|^2\,\mathrm{d}x_1\,\mathrm{d}x_2}\int_{(0,w)\times(0,1)}|v^\xi|^2\,\mathrm{d}x_1\,\mathrm{d}x_2+\mathcal{O}(\xi^3),
\end{aligned}$$

where $\delta m_2^\xi=\mathrm{e}^{i\xi x_1}v^\xi$ and $v^\xi = -\partial_1 m_2^w+\xi i\, Lm_2^w$. Observe that

$$\int_{(0,w)\times(0,1)}|v^\xi|^2\,\mathrm{d}x_1\,\mathrm{d}x_2=\int_{(0,w)\times(0,1)}|\partial_1 m_2^w|^2\,\mathrm{d}x_1\,\mathrm{d}x_2+\mathcal{O}(\xi).$$

This establishes the statement in Theorem 5.1. □

Although Theorem 5.1 is formulated in the context of the reduced energy (1.14), it can be shown to hold for a broader class of energies, for example of the form

$$E(m) = \int_{(0,w)\times Y} \sum_l a_l(\partial_x^l m)^2 + b_l(|\partial_x|^l B_l(m, \partial_x m))^2 \,\mathrm{d}x\,\mathrm{d}y, \tag{5.29}$$

where Y is some subset of $\mathbb{R}^n$, $m : (0,w)\times Y \to \mathbb{R}$ is w-periodic, and B_l denote differential operators w.r.t. the second variable y. The reduced energy functional is contained in that formulation in the form of

$$\begin{aligned} &a_0 = -h_{\text{ext}}, \\ &a_1 = 1, \\ &B_{-1/2}(m, \partial_x m) = \sigma(m) = -\partial_x \tfrac{m^2}{2} + \partial_y m = -m\partial_x m + \partial_y m, \quad b_{-1/2} = 1/2. \end{aligned}$$

By subdividing our proof into several steps we tried to highlight the crucial ingredients necessary for a generalization: The first step is the derivation of the expansion (5.8). Establishing (5.15), on the basis of the differentiation of the Euler-Lagrange equation w.r.t. the period, then yields in combination with the introduction of the rescaled energy density (5.24). Notice that the identities in Step 4 are a consequence of the homogeneity of the local and non-local differential operators.

Relation between the infinitesimal perturbation and the modulation by an inner variation. Not surprisingly, the infinitesimal variation (5.14) can be related to an inner variation in the form of a sinusoidal wave-length modulation. To see this, consider an inner variation due the modulation via a function ζ: Let Φ_ε be the flux defined via

$$\begin{aligned} \partial_\varepsilon \Phi_\varepsilon(x_1) &= \zeta(\Phi_\varepsilon(x_1)), \\ \Phi_0(x_1) &= x_1. \end{aligned}$$

Let u^w be a family of w-periodic stationary points, then we define the inner variation

$$u_\varepsilon^w(\Phi_\varepsilon(x_1)) = u^{\Phi_\varepsilon'(x_1)w}(\Phi_\varepsilon'(x_1)x_1).$$

Therefore it holds that

$$\tfrac{\mathrm{d}}{\mathrm{d}\varepsilon}|_{\varepsilon=0}\, u_\varepsilon^w(x_1) \approx \zeta(-\partial_1 u^w) + \zeta'(x_1\partial_1 + w\partial_w)u^w,$$

so that in case of $\zeta = \mathrm{e}^{i\xi x_1}$ we obtain (5.14).

5.2. Bloch wave analysis for general energy functionals

In this section we address the generalization of the Bloch wave analysis: We consider functionals defined on functions with values in a general linear space Y including a general non-holonomic *non-linear* constraint.

Let $e : Y \times Y \to \mathbb{R}$ and $g : Y \times Y \to Z$, where Y and Z are some linear (Banach) spaces. For $u : [0, w) \to Y$ which is w-periodic consider (as a model problem) the minimization of the energy

$$E(u) = \int_0^w e(u, \partial_x u)\,\mathrm{d}x \quad \text{subject to} \quad g(u, \partial_x u) = 0, \tag{5.30}$$

in the sense that $g(u(x), \partial_x u(x)) = 0$ holds pointwise in x as a Z-valued equation. Notice that the reduced energy functional can be rewritten to fit into this framework. In fact, the stray-field contribution can be localized introducing a second variable $b = (b_1, b_3)$:

$$\int_0^w (|\partial_1|^{-1/2}\sigma)^2\,\mathrm{d}x_1 = \inf\Big\{ \int_0^w \int_0^\infty b_1^2 + b_3^2\,\mathrm{d}x_3\,\mathrm{d}x_1 \Big|\ b : [0,w) \times [0,\infty) \to \mathbb{R}^2 \\ \partial_1 b_1 + \partial_3 b_3 = 0 \text{ for } x_3 \neq 0 \text{ and } b_3 = \sigma \text{ at } x_3 = 0 \Big\}. \tag{5.31}$$

Using the equivalence (5.31), the minimization of the reduced energy w.r.t m_2 can be replaced by a minimization both w.r.t m_2 and b; this means that we identify u in (5.30) with (m_2, b); the space Y in this case is a space of the form $\mathbb{R} \times \{b : [0,\infty) \to \mathbb{R}^2\}$. Obviously, m_2 is coupled to b via a non-linear constraint involving the non-linear charge density $\sigma = -\partial_1 \frac{m_2^2}{2} + \partial_2 m_2$.

In the following we sketch the proof of the generalization of Theorem 5.1 to functionals including a non-linear constraint of the form (5.30). In contrast to the proof of Theorem 5.1, we use a (slightly) different method which can be applied in case of local energy contributions. In that case, one does not need to rescale since the calculation of the commutator relations for $L = x\partial_x + w\partial_w$ and the differential operators is straight-forward. On the other hand, the non-linear constraint necessitates additional assumptions for the existence of the Ansatz of the Bloch eigenfunction.

We start with some preliminary observations. Let $u(s)$ be a finite variation that is admissible in (5.30) with $u(0) = u_0$, $\frac{\mathrm{d}}{\mathrm{d}s} u(s)_{s=0} = \delta u$, and $\frac{\mathrm{d}^2}{\mathrm{d}s^2} u(s)_{s=0} = \delta^2 u$, where u_0 is some stationary point of the energy. Then for $s = 0$

$$g_u\,\delta u + g_p\,\partial_x \delta u = 0, \tag{5.32}$$

$$\delta u \cdot g_{uu}\,\delta u + 2\delta u \cdot g_{up}\,\partial_x \delta u + \partial_x \delta u \cdot g_{pp}\,\partial_x \delta u + g_u\,\delta^2 u + g_p\,\partial_x \delta^2 u = 0, \tag{5.33}$$

which hold as Z-valued equations pointwise in x with the abbreviation $g_u(x) = g_u(u(x), \partial_x u(x))$, etc. Notice that p denotes the derivative w.r.t. the second variable. The relations (5.32) and (5.33) can be seen to hold by differentiating the constraint $g(u(s), \partial_x u(s)) = 0$ w.r.t. to s, evaluated at $s = 0$.

Let us assume that there exists a Lagrange multiplier $\varphi : [0, w) \to Z^*$, where Z^* denotes the dual space of Z, s.t. the Euler-Lagrange equation takes the form

$$e_u(u_0, \partial_x u_0) - \partial_x e_p(u_0, \partial_x u_0) + \varphi g_u(u_0, \partial_x u_0) - \partial_x(\varphi g_p(u_0, \partial_x u_0)) = 0, \tag{5.34}$$

as a Y-valued equation valid for all $x \in [0, w)$. (This is related to the fact that g_p is invertible. We address the meaning in case of our energy functional,i.e., (5.31), after the end of the proof.) The Hessian in the w-periodic stationary point u_0 is given by

$$\begin{aligned}\mathrm{Hess}E(u_0)\,(\delta u, \delta u) = \int_0^w \Bigg(\begin{pmatrix} \delta u \\ \partial_x \delta u \end{pmatrix} \cdot \begin{pmatrix} e_{uu} & e_{up} \\ e_{up} & e_{pp} \end{pmatrix} \begin{pmatrix} \delta u \\ \partial_x \delta u \end{pmatrix} \\ + \varphi \begin{pmatrix} \delta u \\ \partial_x \delta u \end{pmatrix} \cdot \begin{pmatrix} g_{uu} & g_{up} \\ g_{up} & g_{pp} \end{pmatrix} \begin{pmatrix} \delta u \\ \partial_x \delta u \end{pmatrix} \Bigg) \mathrm{d}x \end{aligned} \tag{5.35}$$

for δu subject to (5.32). This can be seen by differentiating $E(u(s))$ twice w.r.t. s, inserting (5.34) tested with $\delta^2 u$, and finally appealing to (5.33).

Consider the family of minimizers

$$u_0^w = \mathrm{argmin}\{E(u) |\, u \text{ is } w\text{-periodic and suffices the constraint (5.30)}\}.$$

Let us assume that this family is differentiable w.r.t. w. However, for notational convenience we most of the time drop the w in the following and write u_0 instead and similarly e instead of $e^w = e(u^w, \partial_x u^w)$. Consider a Bloch wave Ansatz for the infinitesimal variation of the form $\delta u = \mathrm{e}^{i\xi x} v^\xi$, i.e., a sinusoidal modulation of a w-periodic function v^ξ, for $0 < \xi = \frac{2\pi}{Nw} \ll 1$ where $N \in \mathbb{N}$. Notice that the perturbation δu is in general complex. For any sesquilinear form we assume that the second argument is the one that is complex conjugated. Let us plug in our Ansatz into the Hessian:

$$\begin{aligned}&\frac{1}{N}\mathrm{Hess}E(u_0)\,(\delta u, \delta u) \\ &\quad = \int_0^w \Bigg(\begin{pmatrix} v^\xi \\ \partial_x v^\xi \end{pmatrix} \cdot \begin{pmatrix} e_{uu} & e_{up} \\ e_{up} & e_{pp} \end{pmatrix} \begin{pmatrix} \bar{v}^\xi \\ \partial_x \bar{v}^\xi \end{pmatrix} \\ &\qquad\qquad + \varphi \begin{pmatrix} v^\xi \\ \partial_x v^\xi \end{pmatrix} \cdot \begin{pmatrix} g_{uu} & g_{up} \\ g_{up} & g_{pp} \end{pmatrix} \begin{pmatrix} \bar{v}^\xi \\ \partial_x \bar{v}^\xi \end{pmatrix} \Bigg) \mathrm{d}x \\ &\quad + \xi \int_0^w (i v^\xi \cdot e_{pp}\, \partial_x \bar{v}^\xi - i \partial_x v^\xi \cdot e_{pp}\, \bar{v}^\xi + \varphi(i v^\xi \cdot g_{pp}\, \partial_x \bar{v}^\xi - i \partial_x v^\xi \cdot g_{pp}\, \bar{v}^\xi))\, \mathrm{d}x \\ &\quad + \xi^2 \int_0^w (v^\xi \cdot e_{pp}\, \bar{v}^\xi + \varphi v^\xi \cdot g_{pp}\, \bar{v}^\xi)\, \mathrm{d}x \\ &\quad =: \mathcal{L}^0(v^\xi, v^\xi) + \xi \mathcal{L}^1(v^\xi, v^\xi) + \xi^2 \mathcal{L}^2(v^\xi, v^\xi). \end{aligned} \tag{5.36}$$

On the level of the constraint (5.32) we find

$$g_u v^\xi + g_p\, (\partial_x v^\xi + i \xi v^\xi) = 0. \tag{5.37}$$

Assume that v^ξ is of the form $v^\xi = v_0 + \xi v_1 + \xi^2 v_2$ – in contrast to (5.14), the quadratic term is necessary due to the constraint, see below. We plug this Ansatz

into (5.36) and obtain the following expansion:

$$\begin{aligned}\mathrm{Hess}E(u_0)\,((v^\xi,\partial_x v^\xi),(v^\xi,\partial_x v^\xi))&\\ &= \mathcal{L}^0(v_0,v_0)\\ &\quad+\xi(\mathcal{L}^1(v_0,v_0)+\mathcal{L}^0(v_1,v_0)+\mathcal{L}^0(v_0,v_1))\\ &\quad+\xi^2(\mathcal{L}^2(v_0,v_0)+\mathcal{L}^1(v_0,v_1)+\mathcal{L}^1(v_1,v_0)+\mathcal{L}^0(v_1,v_1)\\ &\qquad+\mathcal{L}^0(v_0,v_2)+\mathcal{L}^0(v_2,v_0))+\mathcal{O}(\xi^3).\end{aligned}\tag{5.38}$$

Similarly we expand the constraint (5.37) for which we obtain

$$\begin{aligned}0 =& g_u v_0 + g_p\partial_x v_0\\ &+\xi(g_u v_1 + g_p(\partial_x v_1 + iv_0))\\ &+\xi^2(g_u v_2 + g_p(\partial_x v_2 + iv_1))+\mathcal{O}(\xi^3).\end{aligned}\tag{5.39}$$

As in the proof of Theorem 5.1 we choose $v_0 = \partial_x u$ and $v_1 = -iLu$, where $L = x\partial_x + w\partial_w$. However, due to the non-linear constraint it is now necessary to assume that there exists v_2 such that (5.37) holds up to order ξ^2, i.e.,

$$g_u v_2 + g_p(\partial_x v_2 + iv_1) = 0.\tag{5.40}$$

This is again related to the fact that g_p is invertible. Note that for a general perturbation r, that is not necessarily admissible in (5.32), we have that

$$\mathcal{L}^0(v_0,r) = -\int \partial_x\varphi(g_u r + g_p\partial_x r)\,\mathrm{d}x,\tag{5.41}$$

which can be seen by differentiating (5.34) w.r.t. x, testing with r. Let us come back to (5.38). Due to (5.32) and (5.41) with the choice of $\delta u = \partial_x u$ we obtain that $\mathcal{L}^0(v_0,v_0) = 0$. Observe that $\mathcal{L}^1(r,r) = 0$ for any real function r. Moreover, we have that $\mathcal{L}^0(v_0,v_1)$ and $\mathcal{L}^0(v_1,v_0)$ are purely imaginary since v_0 is purely real and v_1 is purely imaginary. Since the l.h.s. of (5.38) is purely real we thus obtain

$$\begin{aligned}\mathrm{Hess}E(u_0)(v^\xi,v^\xi) = \xi^2(&\mathcal{L}^2(v_0,v_0)+\mathcal{L}^1(v_0,v_1)+\mathcal{L}^1(v_1,v_0)\\ &+\mathcal{L}^0(v_1,v_1)+\mathcal{L}^0(v_2,v_0)+\mathcal{L}^0(v_0,v_2))+\mathcal{O}(\xi^3).\end{aligned}\tag{5.42}$$

Our goal is to identify the latter expression (5.42) with the second derivative of the minimal energy $E(w) = E(u_0^w)$ where $u_0^w = \mathrm{argmin}\{E(u)\,|\,u\ w\text{-periodic}\}$. Appealing to (5.41), we deduce from (5.40) that $\mathcal{L}^0(v_0,v_2)+\mathcal{L}^0(v_2,v_0) = 2\int\partial_x\varphi g_p Lu\,\mathrm{d}x$. Therefore, we find that (5.42) does not depend on v_2 up to order ξ^2 – as expected due to our assumption that u_0^w is a family of stationary points. More precisely, since

v_0 is real and $v_1 = -iLu$ we find that

$$\begin{aligned}
&\mathcal{L}^2(v_0, v_0) + \mathcal{L}^1(v_1, v_0) + \mathcal{L}^1(v_0, v_1) + \mathcal{L}^0(v_1, v_1) + \mathcal{L}^0(v_2, v_0) + \mathcal{L}^0(v_0, v_2) \\
&= \int_0^w (v_0 \cdot e_{pp}\bar{v}_0 + \varphi v_0 \cdot g_{pp}\bar{v}_0)\,\mathrm{d}x \\
&\quad + i\int_0^w (v_1 \cdot e_{pp}\partial_x\bar{v}_0 - \partial_x v_1 \cdot e_{pp}\bar{v}_0)\,\mathrm{d}x + i\int_0^w (v_0 \cdot e_{pp}\partial_x\bar{v}_1 - \partial_x v_0 \cdot e_{pp}\bar{v}_1)\,\mathrm{d}x \\
&\quad + i\int_0^w \varphi(v_1 \cdot g_{pp}\partial_x\bar{v}_0 - \partial_x v_1 \cdot g_{pp}\bar{v}_0)\,\mathrm{d}x \\
&\quad + i\int_0^w \varphi(v_0 \cdot g_{pp}\partial_x\bar{v}_1 - \partial_x v_0 \cdot g_{pp}\bar{v}_1)\,\mathrm{d}x \\
&\quad + \mathcal{L}^0(v_1, v_1) + 2\int_0^w \partial_x\varphi g_p Lu\,\mathrm{d}x \\
&= \int_0^w (v_0 \cdot e_{pp}v_0 + \varphi v_0 \cdot g_{pp}v_0)\,\mathrm{d}x \\
&\quad - 2\int_0^w (\partial_x Lu \cdot e_{pp}\partial_x u - Lu \cdot e_{pp}\partial_x^2 u)\,\mathrm{d}x \\
&\quad - 2\int_0^w \varphi(\partial_x Lu \cdot g_{pp}\partial_x u - Lu \cdot g_{pp}\partial_x^2 u)\,\mathrm{d}x \\
&\quad + \mathcal{L}^0(v_1, v_1) - 2\int_0^w \varphi(\partial_x u \cdot g_{up}Lu + \partial_x^2 u \cdot g_{pp}Lu + g_p\partial_x Lu)\,\mathrm{d}x,
\end{aligned}$$

where we just replaced v_0 and v_1 by our specific Ansatz and integrated by parts in the last contribution. Collecting all terms containing the Lagrange multiplier φ, we find

$$\begin{aligned}
&\mathcal{L}^2(v_0, v_0) + \mathcal{L}^1(v_1, v_0) + \mathcal{L}^1(v_0, v_1) + \mathcal{L}^0(v_1, v_1) + \mathcal{L}^0(v_2, v_1) + \mathcal{L}^0(v_0, v_2) \\
&= \int_0^w (v_0 \cdot e_{pp}v_0 + \varphi v_0 \cdot g_{pp}v_0)\,\mathrm{d}x \\
&\quad - 2\int_0^w (\partial_x Lu \cdot e_{pp}\partial_x u - Lu \cdot e_{pp}\partial_x^2 u)\,\mathrm{d}x \\
&\quad - 2\int_0^w \varphi(\partial_x Lu \cdot g_{pp}\partial_x u + \partial_x u \cdot g_{up}Lu + g_p\partial_x Lu)\,\mathrm{d}x \\
&\quad + \mathcal{L}^0(v_1, v_1).
\end{aligned} \tag{5.43}$$

We now turn to the second derivative of the minimal energy $\frac{\mathrm{d}^2}{\mathrm{d}w^2}E(w)$. Let us recall that by assumption the energy density is given by $e = e(u_0^w, \partial_x u_0^w)$. Therefore it holds that

$$\begin{aligned}
\tfrac{\mathrm{d}}{\mathrm{d}w}E(w) &= \tfrac{\mathrm{d}}{\mathrm{d}w}\int_0^w e\,\mathrm{d}x \\
&= e + \int_0^w \partial_w e\,\mathrm{d}x \\
&= \tfrac{1}{w}\int_0^w \Big(\partial_x(xe) + w\partial_w e\Big)\,\mathrm{d}x \\
&= \tfrac{1}{w}\int_0^w \Big(e + Le\Big)\,\mathrm{d}x,
\end{aligned}$$

where $L = x\partial_x + w\partial_w$. The second derivative is given by

$$\begin{aligned}
\tfrac{\mathrm{d}^2}{\mathrm{d}w^2}E(w) &= -\tfrac{1}{w^2}\int_0^w \Big(e + Le\Big)\,\mathrm{d}x + \tfrac{1}{w}(e+Le) + \tfrac{1}{w}\int_0^w \Big(\partial_w e + \partial_w Le\Big)\,\mathrm{d}x \\
&= \tfrac{1}{w^2}\int_0^w -\Big(e + Le\Big) + \partial_x(x(e+Le)\,\mathrm{d}x + \tfrac{1}{w}\int_0^w \Big(\partial_w e + \partial_w Le\Big)\,\mathrm{d}x \\
&= \tfrac{1}{w^2}\int_0^w \Big(x\partial_x(e+Le) + w\partial_w e + w\partial_w Le\Big)\,\mathrm{d}x_1 \\
&= \tfrac{1}{w^2}\int_0^w \Big(L^2 e + Le\Big)\,\mathrm{d}x. \qquad (5.44)
\end{aligned}$$

In order to identify (5.44) with (5.43), we use the Euler-Lagrange equation – once tested with Lu, see (5.51), once tested with L^2u, see (5.52) – which introduces the Lagrange multiplier into (5.44). In order to rewrite the outcome, we moreover apply the differentiated constraint $g = 0$ – once applying L, see (5.54), once applying L^2, see (5.53). Let us start by expanding:

$$\begin{aligned}
&w^2\tfrac{\mathrm{d}^2}{\mathrm{d}w^2}E(w) \\
&= \int_0^w (L^2 + L)e\,\mathrm{d}x \\
&= \int_0^w \Bigg(\begin{pmatrix} Lu \\ L\partial_x u \end{pmatrix} \cdot \begin{pmatrix} e_{uu} & e_{up} \\ e_{up} & e_{pp} \end{pmatrix} \begin{pmatrix} Lu \\ L\partial_x u \end{pmatrix} \\
&\qquad + e_u L^2 u + e_p L^2 \partial_x u + e_u Lu + e_p L\partial_x u \Bigg)\,\mathrm{d}x. \qquad (5.45)
\end{aligned}$$

In order to apply our strategy, it is necessary to rewrite the latter expression using the relations

$$L\partial_x = \partial_x L - \partial_x, \qquad (5.46)$$
$$\partial_x L = L\partial_x + \partial_x, \qquad (5.47)$$

and

$$L^2\partial_x = \partial_x L^2 - 2\partial_x L + \partial_x, \qquad (5.48)$$
$$\partial_x L^2 = L^2\partial_x + 2L\partial_x + \partial_x. \qquad (5.49)$$

Integration by parts in the second line in (5.45) will then turn the terms containing first derivatives of e into second derivatives of e. In fact, due to (5.46), the identity (5.45) turns into

$$\begin{aligned}
&w^2\tfrac{\mathrm{d}^2}{\mathrm{d}w^2}E(w) \\
&= \int_0^w \begin{pmatrix} Lu \\ \partial_x Lu \end{pmatrix} \cdot \begin{pmatrix} e_{uu} & e_{up} \\ e_{up} & e_{pp} \end{pmatrix} \begin{pmatrix} Lu \\ \partial_x Lu \end{pmatrix} \mathrm{d}x \\
&\quad + \int_0^w (-2(Lu \cdot e_{up}\partial_x u + \partial_x Lu \cdot e_{pp}\partial_x u) + \partial_x u \cdot e_{pp}\partial_x u)\,\mathrm{d}x \\
&\quad + \int_0^w (e_u L^2 u + e_p L^2\partial_x u + e_u Lu + e_p L\partial_x u)\,\mathrm{d}x.
\end{aligned}$$

Due to (5.46) and (5.48) we find that

$$\begin{aligned}
&\int_0^w (e_u L^2 u + e_p L^2 \partial_x u + e_u L u + e_p L \partial_x u)\,\mathrm{d}x \\
&= \int_0^w (e_u L^2 u + e_p(\partial_x L^2 u - 2\partial_x L u + \partial_x u) + e_u L u + e_p(\partial_x L u - \partial_x u))\,\mathrm{d}x \\
&= \int_0^w (e_u L^2 u + e_p(\partial_x L^2 u - 2\partial_x L u) + e_u L u + e_p \partial_x L u)\,\mathrm{d}x.
\end{aligned}$$

Integration by parts yields that

$$-2\int_0^w e_p \partial_x L u\,\mathrm{d}x = 2\int_0^w (L u \cdot e_{up}\partial_x u + L u \cdot e_{pp}\partial_x^2 u)\,\mathrm{d}x. \tag{5.50}$$

Using the Euler-Lagrange equation (5.34) tested with Lu we find that

$$\begin{aligned}
\int_0^w (e_u L u + e_p \partial_x L u)\,\mathrm{d}x &= -\int_0^w (\varphi g_u L u - \partial_x(\varphi g_p) L u)\,\mathrm{d}x \\
&= -\int_0^w (\varphi g_u L u + \varphi g_p \partial_x L u)\,\mathrm{d}x.
\end{aligned} \tag{5.51}$$

Plugging in (5.35), (5.50) and (5.51) we hence obtain

$$\begin{aligned}
&w^2 \tfrac{\mathrm{d}^2}{\mathrm{d}w^2} E(w) \\
&= \mathcal{L}^0(v_1, v_1) - \int_0^w \varphi \begin{pmatrix} Lu \\ \partial_x L u \end{pmatrix} \cdot \begin{pmatrix} g_{uu} & g_{up} \\ g_{up} & g_{pp} \end{pmatrix} \begin{pmatrix} Lu \\ \partial_x L u \end{pmatrix} \mathrm{d}x + \int_0^w \partial_x u \cdot e_{pp} \partial_x u\,\mathrm{d}x \\
&\quad + 2\int_0^w (L u \cdot e_{pp}\partial_x^2 u - \partial_x L u \cdot e_{pp}\partial_x u)\,\mathrm{d}x + \int_0^w (e_u L^2 u + e_p \partial_x L^2 u)\,\mathrm{d}x \\
&\quad - \int_0^w (\varphi g_u L u + \varphi g_p \partial_x L u)\,\mathrm{d}x.
\end{aligned}$$

Using once again (5.46), we rewrite the second term in the latter expression:

$$\begin{aligned}
&w^2 \tfrac{\mathrm{d}^2}{\mathrm{d}w^2} E(w) \\
&\quad = \mathcal{L}^0(v_1, v_1) - \int_0^w \varphi \begin{pmatrix} Lu \\ L\partial_x u \end{pmatrix} \cdot \begin{pmatrix} g_{uu} & g_{up} \\ g_{up} & {}_{pp} \end{pmatrix} \begin{pmatrix} Lu \\ L\partial_x u \end{pmatrix} \mathrm{d}x \\
&\qquad - \int_0^w \varphi(2Lu \cdot g_{up}\partial_x u + 2L\partial_x u \cdot g_{pp}\partial_x u + \partial_x u \cdot g_{pp}\partial_x u)\,\mathrm{d}x \\
&\qquad + \int_0^w \partial_x u \cdot e_{pp}\partial_x u\,\mathrm{d}x + 2\int_0^w (Lu \cdot e_{pp}\partial_x^2 u - \partial_x L u \cdot e_{pp}\partial_x u)\,\mathrm{d}x \\
&\qquad + \int_0^w (e_u L^2 u + e_p \partial_x L^2 u)\,\mathrm{d}x \\
&\qquad - \int_0^w (\varphi g_u L u + \varphi g_p \partial_x L u)\,\mathrm{d}x.
\end{aligned}$$

Notice that due to (5.46)

$$2L\partial_x u \cdot g_{pp}\partial_x u + \partial_x u \cdot g_{pp}\partial_x u = 2\partial_x L u \cdot g_{pp}\partial_x u - \partial_x u \cdot g_{pp}\partial_x u.$$

If we once again use the Euler-Lagrange equation (5.34) tested with $L^2 u$ we find that

$$\int_0^w (e_u L^2 u + e_p \partial_x L^2 u)\,\mathrm{d}x = -\int_0^w (\varphi g_u L^2 u + \varphi g_p \partial_x L^2 u)\,\mathrm{d}x. \tag{5.52}$$

Due to (5.49) we therefore obtain

$$\int_0^w (e_u L^2 u + e_p \partial_x L^2 u)\,\mathrm{d}x = -\int_0^w \varphi(g_u L^2 u + g_p L^2 \partial_x u + 2 g_p L \partial_x u + g_p \partial_x u.)\,\mathrm{d}x,$$

The application of L^2 to the constraint $g = 0$ yields

$$\begin{pmatrix} Lu \\ L\partial_x u \end{pmatrix} \cdot \begin{pmatrix} g_{uu} & g_{up} \\ g_{up} & g_{pp} \end{pmatrix} \begin{pmatrix} Lu \\ L\partial_x u \end{pmatrix} = -(g_u L^2 u + g_p L^2 \partial_x u). \tag{5.53}$$

Therefore we derive that

$$\begin{aligned} w^2 \tfrac{\mathrm{d}^2}{\mathrm{d}w^2} E(w) = \mathcal{L}^0(v_1, v_1) &+ \int_0^w v_0 \cdot e_{pp} v_0\,\mathrm{d}x + \int_0^w \underline{\varphi(g_u L^2 u + g_p L^2 \partial_x u)\,\mathrm{d}x} \\ &- 2\int_0^w \varphi(Lu \cdot g_{up} \partial_x u + \partial_x Lu \cdot g_{pp} \partial_x u)\,\mathrm{d}x + \int_0^w \varphi v_0 \cdot g_{pp} v_0\,\mathrm{d}x \\ &+ 2\int_0^w (Lu \cdot e_{pp} \partial_x^2 u - \partial_x Lu \cdot e_{pp} \partial_x u)\,\mathrm{d}x \\ &- \int_0^w (\underline{\varphi g_u L^2 u + \varphi g_p L^2 \partial_x u} + 2\varphi g_p L \partial_x u + \varphi g_p \partial_x u)\,\mathrm{d}x \\ &- \int_0^w (\varphi g_u Lu + \varphi g_p \partial_x Lu)\,\mathrm{d}x. \end{aligned}$$

The underlined terms cancel so that we obtain

$$\begin{aligned} w^2 \tfrac{\mathrm{d}^2}{\mathrm{d}w^2} E(w) = \mathcal{L}^0(v_1, v_1) &+ \int_0^w v_0 \cdot e_{pp} v_0\,\mathrm{d}x + \int_0^w \varphi v_0 \cdot g_{pp} v_0\,\mathrm{d}x \\ &+ 2\int_0^w (Lu \cdot e_{pp} \partial_x^2 u - \partial_x Lu \cdot e_{pp} \partial_x u)\,\mathrm{d}x \\ &- 2\int_0^w \varphi(Lu \cdot g_{up} \partial_x u + \partial_x Lu \cdot g_{pp} \partial_x u)\,\mathrm{d}x \\ &- \int_0^w \varphi(2 g_p L \partial_x u + g_p \partial_x u + g_u Lu + g_p \partial_x Lu)\,\mathrm{d}x. \end{aligned}$$

Let us once more use the relations (5.46) and (5.47) to rewrite the last line:

$$\begin{aligned} &- \int_0^w \varphi(2 g_p L \partial_x u + g_p \partial_x u + g_u Lu + g_p \partial_x Lu)\,\mathrm{d}x \\ &= -\int_0^w \varphi(2 g_p (\partial_x Lu - \partial_x u) + g_p \partial_x u + g_u Lu + g_p (L\partial_x u + \partial_x u))\,\mathrm{d}x \\ &= -\int_0^w \varphi(2 g_p \partial_x Lu + g_u Lu + g_p L \partial_x u)\,\mathrm{d}x. \end{aligned}$$

Due to

$$0 = Lg = g_u Lu + g_p L \partial_x u, \tag{5.54}$$

we hence obtain

$$-\int_0^w \varphi(2g_pL\partial_x u + g_p\partial_x u + g_u Lu + g_p\partial_x Lu)\,\mathrm{d}x = -\int_0^w \varphi\, 2g_p\partial_x Lu\,\mathrm{d}x.$$

Therefore

$$\begin{aligned} w^2\tfrac{\mathrm{d}^2}{\mathrm{d}w^2}E(w) = \mathcal{L}^0(v_1,v_1) &+ \int_0^w v_0\cdot e_{pp}v_0\,\mathrm{d}x + \int_0^w \varphi v_0\cdot g_{pp}v_0\,\mathrm{d}x \\ &+ 2\int_0^w (Lu\cdot e_{pp}\partial_x^2 u - \partial_x Lu\cdot e_{pp}\partial_x u)\,\mathrm{d}x \\ &- 2\int_0^w \varphi(Lu\cdot g_{up}\partial_x u + \partial_x Lu\cdot g_{pp}\partial_x u + g_p\partial_x Lu)\,\mathrm{d}x. \end{aligned}$$

A comparison to (5.43) shows that

$$\xi^2 w^2\tfrac{\mathrm{d}^2}{\mathrm{d}w^2}E(w) \approx N^{-1}\mathrm{Hess}E(u^w)(\delta u^\xi,\delta u^\xi),$$

where $\delta u^\xi = \partial_x u^w - \xi i L u^w + \xi^2 v_2$ and $\xi = \frac{2\pi}{N}$, $0 \ll N \in \mathbb{N}$. This completes the sketch of the proof.

Remark 5.2. *Let us shortly address the existence of the Lagrange multiplier in case of our energy* (5.31)*. In our case, g_p is given as m_2 in the sense of a multiplication operator. Is is useful to state this more precisely, see below.*

On can show that the b-component of the minimizer satisfies $\nabla\times b = 0$. Hence, there exists a potential V, s.t. $b = -(\partial_1,\partial_3)^T V$. The Euler-Lagrange equation turns into

$$-2\partial_1^2 m_2 - 2h_{\mathrm{ext}} + m_2\partial_1 V - \partial_2 V = 0.$$

In particular, the Lagrange multiplier φ can be identified with V. This can be used to show that the term, which is related to the multiplier φ in the Hessian, is of the form

$$\int_0^w V\partial_1(\delta m_2)^2\,\mathrm{d}x_1.$$

In case of our energy (5.31)*, equation* (5.40) *turns into*

$$-\partial_1(m_2 v_2) + \partial_2 v_2 - i m_2 v_1 = -\partial_3 V_2 \quad on \quad x_3 = 0,$$

where $v^1 = -iLm_2$.

6

Bifurcation analysis

In this chapter we investigate the bifurcation of the reduced rescaled energy functional (1.14). We recall the outcome of the classical bifurcation analysis which was performed in [CÁOS07], see Section 6.1. This analysis is afterwards extended to take into account small variations of the wave number, see Section 6.2. On the basis of the amplitude functional – which we obtain from the extended bifurcation analysis – we study the stability of minimizers close to the bifurcation, see Section 6.3. In particular we will see that $\widehat{w}^*$-periodic states are Eckhaus unstable close to the bifurcation. This instability is related to a degeneracy of the amplitude functional. At the end of that section we provide a comparison to the classical, non-degenerate Eckhaus instability. In Section 6.4 we further generalize the extended bifurcation analysis to spatially varying amplitudes. We formally derive a non-local Ginzburg-Landau functional representing an approximation of the energy close to the bifurcation on $\widehat{w}$-periodic functions with period $\widehat{w}$ close to $\widehat{w}^*$. This provides the most general tool to investigate the Eckhaus instability. Finally, in Section 6.5, we will see that the secondary bifurcations originate from multiple primary bifurcations and can hence be asymptotically investigated near the degenerate primary bifurcation.

We drop the $\widehat{\cdot}$ in this chapter to simplify the notation.

6.1. Classical bifurcation analysis.

In [CÁOS07], a bifurcation analysis was carried out for the reduced energy functional by deriving the asymptotic energy close to the bifurcation. Let us shortly review the set-up and the outcome of that analysis: Consider small perturbations of the critical field

$$h_{\text{ext}} = h_{\text{ext}}^* + \delta h_{\text{ext}}$$

and a perturbation of the uniform magnetization $m_2 = 0$ of the form

$$m_2 = A m_2^* + A^2 m_2^{**} + \mathcal{O}(A^3), \tag{6.1}$$

where $m_2^* = \cos(k_1^* x_1)\sin(\pi x_2)$ is the unstable mode with wavenumber $k_1^* = \frac{2\pi}{w^*}$. Since the cubic non-linearity of the energy degenerates on the kernel of the Hessian,

it is necessary to take into account the second order term in the expansion (6.1). (The degeneracy is caused by the invariance of the energy under the transform $m_2 \rightsquigarrow -m_2$ and $x_2 \rightsquigarrow -x_2$.) Evaluating E_0 on the Ansatz (6.1) and neglecting all terms of higher order $\mathcal{O}(A^5)$ in the expansion of the energy w.r.t. the amplitude A at the field $h_{\text{ext}} = h^*_{\text{ext}}$, an optimization in m_2^{**} of the A^4-term in the expansion yields that

$$m_2^{**} = \tfrac{1}{10}(\tfrac{2}{\pi})^{1/3} \sin(2k_1^* x_1) \sin(2\pi x_2).$$

One obtains that the asymptotic energy close to the bifurcation is described by the amplitude functional

$$E_0(Am_2^* + A^2 m_2^{**}) \approx -\tfrac{(32\pi)^{1/3}}{4}\, \delta h_{\text{ext}}\, A^2 - \tfrac{\pi}{640} A^4. \tag{6.2}$$

Since the quartic coefficient is negative, the bifurcation is subcritical and hence the w^*-periodic branch emanating at the critical field is unstable. From an optimization of the asymptotic energy (6.2) w.r.t. the amplitude A one can derive an asymptotic expansion of the bifurcation branch as a function of δh_{ext}. Obviously the optimal amplitude A will scale as $\delta h_{\text{ext}}^{1/2}$. We note that the fourth order coefficient $\frac{\pi}{640}$ is small compared to the second order coefficient and the scale h^*_{ext} of δh_{ext}. (This is related to the numerical observation that the bifurcation is just slightly subcritical, see Figure 1.11). Hence the bifurcation is near-degenerate and it is necessary to take into account higher order terms. For an unfolding we have to consider an extended Ansatz of (6.1) for the magnetization of the form

$$m_2 = Am_2^* + A^2 m_2^{**} + A^3 m_2^{***} + \mathcal{O}(A^4), \tag{6.3}$$

where $m_2^*(k_1) = \cos(k_1 x_1) \sin(\pi x_2)$. Since we are interested in the behavior of the energy for varying wave number we take into account small perturbations of the wave number $k_1 = k_1^* + \delta k_1$. As we will see, after optimization of the A^4-term w.r.t. m_2^{**} and of the A^6-term w.r.t. m_2^{***} this leads to and expansion of the energy of the form

$$\tfrac{k_1^*}{2\pi} E_0 \approx (-c_2 \delta h_{\text{ext}} + \tilde{c}_2 \delta k_1^2) A^2 + (-c_4 + \tilde{c}_4 \delta k_1) A^4 + c_6 A^6, \tag{6.4}$$

see (6.18) in the following Section 6.2. Note that in case of the near-degenerate bifurcation, i.e., $|c_4| \ll 1$, we expect a different scaling behavior of minimizers then in case of the classical bifurcation analysis, namely

$$A \sim \delta h_{\text{ext}}^{1/4} \sim \delta k_1^{1/2}. \tag{6.5}$$

Let us now start with the unfolding of the near-degenerate bifurcation and the derivation of the amplitude functional. For that purpose we take into account an additional term in the energy of the form

$$+Q \int_{(0,w)\times(0,1)} m_2^4 \, \mathrm{d}x_1 \, \mathrm{d}x_2$$

so that the energy degenerates for some value $Q = Q^*(k_1^*)$ of the quality factor.

Recall that in case of high anisotropy we can interpret the parameter Q close to the critical field as a reduced value for the quality factor, cf. Section 1.10.

6.2. Unfolding of the near-degenerate bifurcation: Extended Ansatz.

The goal is to obtain an asymptotic expansion of the energy in the neighborhood of the (quadratic near-degenerate) bifurcation. For that purpose we have to determine the branch along which the energy decreases the most to higher order: Consider a cubic perturbation of the uniform magnetization $m_2 = 0$ as in (6.3), i.e.,

$$m_2 = Am_2^* + A^2 m_2^{**} + A^3 m_2^{***} + \mathcal{O}(A^4), \tag{6.6}$$

where $m_2^*(k_1) = \cos(k_1 x_1)\sin(\pi x_2)$ and where the wave number is close to the critical one, i.e., $k_1 = k_1^* + \delta k_1$. Observe that the uniform magnetization $m_2 = 0$ becomes unstable under perturbation by $m_2^*(k_1)$ at a field

$$h_{\text{ext}}^*(k_1) = k_1^2 + \tfrac{\pi^2}{2|k_1|}.$$

It is useful to rewrite the energy in terms of a quadratic, cubic and quartic form:

$$\begin{aligned} E_0(m_2) =& \tfrac{1}{2}\langle m_2, \mathcal{L}m_2\rangle + \tfrac{1}{3}\mathcal{N}_3(m_2, m_2, m_2) + \tfrac{1}{4}\mathcal{N}_4(m_2, m_2, m_2, m_2) \\ &- (h_{\text{ext}} - h_{\text{ext}}^*(k_1)) \int_{(0,w)\times(0,1)} m_2^2 \,\mathrm{d}x_1\,\mathrm{d}x_2 \\ &+ (Q - Q^*(k_1)) \int_{(0,w)\times(0,1)} m_2^4 \,\mathrm{d}x_1\,\mathrm{d}x_2, \end{aligned}$$

where

$$\begin{aligned} \tfrac{1}{2}\langle u, \mathcal{L}v\rangle =& \int_{(0,w)\times(0,1)} \partial_1 u \partial_1 v + \tfrac{1}{2}(|\partial_1|^{-1/2}\partial_2 u)(|\partial_1|^{-1/2}\partial_2 v)\,\mathrm{d}x_1\,\mathrm{d}x_2 \\ &- \int_{(0,w)\times(0,1)} h_{\text{ext}}^*(k_1) u\, v \,\mathrm{d}x_1\,\mathrm{d}x_2, \\ \tfrac{1}{3}\mathcal{N}_3(u, v, r) =& \int_{(0,w)\times(0,1)} (|\partial_1|^{-1/2}(-\partial_1 \tfrac{u\,v}{2}))\ (|\partial_1|^{-1/2}\partial_2 r)\,\mathrm{d}x_1\,\mathrm{d}x_2, \\ \tfrac{1}{4}\mathcal{N}_4(u, v, r, s) =& \tfrac{1}{2}\int_{(0,w)\times(0,1)} (|\partial_1|^{-1/2}(-\partial_1 \tfrac{u\,v}{2}))(|\partial_1|^{-1/2}(-\partial_1 \tfrac{r\,s}{2}))\,\mathrm{d}x_1\,\mathrm{d}x_2 \\ &+ \int_{(0,w)\times(0,1)} Q^*(k_1)\, u\, v\, r\, s \,\mathrm{d}x_1\,\mathrm{d}x_2. \end{aligned} \tag{6.7}$$

We plug Ansatz (6.3) into the energy and expand the resulting expression w.r.t. the amplitude A. Then as in [CÁOS07, Subsection 2.2.1] m_2^{**} is given as the solution to the minimization of the contribution of order A^4, i.e.,

$$\mathcal{L}m_2^{**} + \tfrac{1}{3}\big(\mathcal{N}_3(m_2^*, m_2^*, \cdot) + \mathcal{N}_3(m_2^*, \cdot, m_2^*) + \mathcal{N}_3(\cdot, m_2^*, m_2^*)\big) = 0. \tag{6.8}$$

(We note that by abuse of notation we identify linear forms with their L^2-Riesz representation.) Fredholm's alternative states that this equation is uniquely solvable since the cubic non-linearity vanishes on the kernel of the Hessian:

$$\mathcal{N}_3(m_2^*, m_2^*, m_2^*) = 0.$$

Using the definition of $\mathcal{L}$ and $\mathcal{N}_3$ equation (6.8) turns into

$$-2\partial_1^2 m_2^{**} - |\partial_1|^{-1}\partial_2^2 m_2^{**} - 2\,h_{\text{ext}}^*(k_1) m_2^{**} - \tfrac{\pi}{2}\sin(2k_1x_1)\sin(2\pi x_2) = 0. \tag{6.9}$$

Notice that $|\partial_1|^{-1}$ acts on a pure mode as

$$|\partial_1|^{-1}\sin(k_1x_1) = |k_1|^{-1}\sin(k_1x_1) \quad \text{and} \quad |\partial_1|^{-1}\cos(k_1x_1) = |k_1|^{-1}\cos(k_1x_1). \tag{6.10}$$

Equation (6.9) can be explicitly solved and we obtain

$$m_2^{**} = \tfrac{\pi}{2}\tfrac{|k_1|}{6|k_1|^3+\pi^2}\,\sin(2k_1x_1)\sin(2\pi x_2).$$

The form of m_2^{**} is a consequence of the r.h.s. in (6.8) which is quadratic in m_2^*. (For example in case of $\mathcal{N}_3(m_{2*}, m_2^*, 0)$, which contains the expression $(m_2^*)^2 = \frac{1}{4}(1+\cos(2k_1x_1))(1-\cos(2\pi x_2))$, the differentiation w.r.t. x_2 and x_1 cancels the constant terms and turns the the cos into sin.) Due to (6.9) we see that the k_1-dependent factor in the amplitude of m_2^{**} is inversely proportional to the eigenvalue λ of m_2, i.e., $\lambda m_2 = \mathcal{L}_2 m_2$. The coefficient in the energy expansion of quartic order A^4 is given by

$$-\tfrac{1}{2}\langle m_2^{**}, \mathcal{L}m_2^{**}\rangle + \mathcal{N}_4(m_2^*, m_2^*, m_2^*, m_2^*). \tag{6.11}$$

A straightforward calculation shows that this term vanishes and hence the bifurcation is degenerate provided

$$Q = Q^*(k_1) = \frac{(5\pi^2 - 18|k_1|^3)|k_1|}{36(6|k_1|^3+\pi^2)}. \tag{6.12}$$

Let us motivate the k_1-dependence of (6.12): Since the amplitude $A_2(k)$ of m_2^{**} is inversely proportional to the eigenvalue λ of m_2, $\lambda m_2 = \mathcal{L}_2 m_2$ see above, the k_1-dependent factor in the first contribution in (6.11) is proportional to the amplitude of m_2^{**} multiplied by the size of the domain, i.e., $\frac{2\pi}{k_1^*}$. Due to homogeneity, the integrals in the second term are linear in k_1. Hence, the condition that (6.11) vanishes amounts to an equation of the form $aA_2(k_1) + b + cQ^*(k_1) = 0$. This explains the form of the numerator in (6.12).

Note that $Q^*(k_1^*)\frac{9}{64} = \frac{k_1^*}{1280}$ so that

$$\tfrac{2\pi}{k_1^*}Q^*(k_1^*) = \tfrac{\pi}{640}, \tag{6.13}$$

which is the fourth order coefficient of the energy in the bifurcation, see (1.19) in Section 1.6. We now optimize the coefficient in the expansion of the energy of order A^6 in m_2^{***}. This leads to the equation

$$\mathcal{L}m_2^{***} + \tfrac{1}{3}\sum_{\tau\in S^3}\mathcal{N}_3(\tau(m_2^*, m_2^{**}, \cdot)) + \mathcal{N}_4(m_2^*, m_2^*, m_2^*, \cdot) = 0, \tag{6.14}$$

where $\tau \in S^3$ denote permutations. Since m_2^{**} is a second order harmonic of m_2^*, the r.h.s. of the latter equation contains third order harmonics of m_2^*, which

are given by $m_2^{***1} = \cos(k_1 x_1)\sin(\pi x_2)$, $m_2^{***2} = \cos(3k_1 x_1)\sin(3\pi x_2)$, $m_2^{***3} = \cos(3k_1 x_1)\sin(3\pi x_2)$, and $m_2^{***4} = \cos(k_1 x_1)\sin(\pi x_2)$. Fredholm's alternative provides a unique solution to that equation if $Q^*(k_1)$ as in (6.12), cf. (6.7). By general considerations this entails that only the first three harmonics can appear on the r.h.s. of the equation. A straightforward but lengthy calculation shows that the cubic perturbation is given by

$$m_2^{***} = \tfrac{k_1^2}{6|k_1|^3+\pi^2}\Big(-\tfrac{k_1}{24k_1}\cos(k_1x_1)\sin(3\pi x_2) - \tfrac{(18|k_1|^3+\pi^2)}{8(48|k_1|^3-2\pi^2)}\cos(3k_1x_1)\sin(\pi x_2) - \tfrac{(-18|k_1|^3+47\pi^2)}{144(8|k_1|^3+\pi^2)}\cos(3k_1x_1)\sin(3\pi x_2)\Big).$$

Let us again give a motivation for the k_1-dependence of the amplitudes, in particular the divergence of the second amplitude for $k_1 = \left(\frac{\pi^2}{24}\right)^{1/3}$: By testing (6.14) with each of the third order harmonics we read off that the corresponding amplitude A_3^i of m_2^{***i} satisfies an equation of the form $A_3^i \mathrm{EV}(m_2^{***i}) + a_i A_2(k_1) + c_i + Q^*(k_1)d_i = 0$, where EV denotes the eigenvalue of m_2^{***i} as an eigenfunction of $\mathcal{L}_2$. The amplitudes are therefore inversely proportional to $A_2(k_1)$ and $\mathrm{EV}(m_2^{***1}) = \frac{8\pi^2}{|k_1|}$, $\mathrm{EV}(m_2^{***2}) = \frac{48|k_1|^3-2\pi^2}{3|k_1|}$, and $\mathrm{EV}(m_2^{***3}) = 2\frac{8|k_1|^3+\pi^2}{|k_1|}$, respectively. The simple structure of the first numerator is due to the fact that m_2^{***1} has the same wave number as m_2^*, namely the wave number k_1.

The divergence of A_3^2 in k_1 is related to the fact that for the value of $k_1 = (\frac{\pi^2}{24})^{1/3}$ not only m_2^* but also m_2^{***2} is in the null space of the Hessian at the field $h_{\mathrm{ext}}^*(k_1)$.

The coefficient to order A^6 is then given by

$$-\tfrac{1}{2}\langle m_2^{***}, \mathcal{L}m_2^{***}\rangle + 2\mathcal{N}_4(m_2^{**}, m_2^{**}, m_2^*, m_2^*) + 4\mathcal{N}_4(m_2^{**}, m_2^*, m_2^{**}, m_2^*). \tag{6.15}$$

Altogether we obtain the following expansion of the energy per length close to $m_2 = 0$, $h_{\mathrm{ext}} = h_{\mathrm{ext}}^*(k_1^*)$ and $Q = Q^*(k_1^*)$:

$$\begin{aligned}\tfrac{|k_1|}{2\pi}E_0(A, k_1, h_{\mathrm{ext}}) \\ \approx -(h_{\mathrm{ext}} - h_{\mathrm{ext}}^*(k_1))\tfrac{1}{4}A^2 + (Q - Q^*(k_1))\tfrac{9}{64}A^4 + e(k_1)\tfrac{1}{64}A^6,\end{aligned} \tag{6.16}$$

where

$$\begin{aligned} h_{\mathrm{ext}}^*(k_1) &= k_1^2 + \tfrac{\pi^2}{2|k_1|}, \\ Q^*(k_1) &= \tfrac{|k_1|(5\pi^2-18|k_1|^3)}{36(6|k_1|^3+\pi^2)}, \\ e(k_1) &= \tfrac{|k_1|^3}{(6|k_1|^3+\pi^2)^2}\Big(-\tfrac{\pi^2}{9} - \tfrac{(18|k_1|^3+\pi^2)^2}{24(48|k_1|^3-2\pi^2)} - \tfrac{(-18|k_1|^3+47\pi^2)^2}{9\times 144(8|k_1|^3+\pi^2)} \\ &\qquad + \pi^2 + \tfrac{\pi^2(5\pi^2-18|k_1|^3)}{6(6|k_1|^3+\pi^2)}\Big). \end{aligned} \tag{6.17}$$

Notice that the first three terms in e stem from the quadratic contribution in (6.15) and are hence quadratic in the amplitudes A_3^i multiplied by the eigenvalue of

m_2^{***i}. Due to homogeneity, the quartic contribution consists of two terms which are quadratic in A_2, the latter one is multiplied by $Q^*(k_1)$.

For k_1 close to the critical wave number k_1^*, i.e., $k_1 = k_1^* + \delta k_1$, $Q = Q^*(k_1^*) + \delta Q$, and $h_{\text{ext}} = h_{\text{ext}}^*(k_1^*) + \delta h_{\text{ext}}$, we expand the energy w.r.t. δk_1 and obtain that

$$\begin{aligned}\tfrac{k_1^*}{2\pi} E_0(A, \delta k_1, \delta h_{\text{ext}}) \approx \Big(-\delta h_{\text{ext}} + \tfrac{\mathrm{d}^2}{\mathrm{d}k_1^2}|_{k_1=k_1^*} h_{\text{ext}}^*(k_1)\, \tfrac{\delta k_1^2}{2} \Big)\, \tfrac{1}{4} A^2 \\ + \big(\delta Q - \tfrac{\mathrm{d}}{\mathrm{d}k_1}|_{k_1=k_1^*} Q^*(k_1)\, \delta k_1\big)\, \tfrac{9}{64} A^4 + e(k_1^*) \tfrac{1}{64} A^6. \quad (6.18)\end{aligned}$$

Note that $\frac{\mathrm{d}}{\mathrm{d}k_1}|_{k_1=k_1^*} h_{\text{ext}}^*(k_1) = 0$ since k_1^* is the minimizer of the dispersion relation $h_{\text{ext}}^*(k_1)$ so that the first non-constant contribution is quadratic in δk_1. We expect that the choice of $\delta Q = -Q^*(k_1^*)$ in (6.18) provides an approximation of our reduced model. For $\delta Q = 0$ we are in the degenerate case.

In the next section the analysis of the amplitude functional (6.18) is presented. Before we step into it let us remark that the numerical value of $e(k_1^*)$ is positive. This implies the existence of a turning point of the primary bifurcation branch emanating at the critical field, cf. Figure 1.11.

6.3. Analysis of the amplitude functional

We now present the analysis of the amplitude functional. On the one hand, we are interested in absolute minimizers, i.e.,

$$\arg\min_{A, \delta k_1} \tfrac{k_1^*}{2\pi} E_0(A, \delta k_1, \delta h),$$

and on the other hand in the stability of local minimizers, i.e., minimizers for prescribed wave-number δk_1. The outcome of the analysis is summarized by the plot in Figure 6.2.

The Bloch wave analysis in Theorem 5.1 showed that concavity of the minimal energy as a function of the *period* translates into an instability under long wave-length modulation. The following observation shows that concavity of the energy per period $E_0(w)$ w.r.t. the period is equivalent to concavity of the energy *density* w.r.t the wave number:

$$\tfrac{\mathrm{d}^2}{\mathrm{d}k_1^2}\big(\tfrac{k_1}{2\pi} E_0\big(\tfrac{2\pi}{k_1}\big)\big) = \tfrac{\mathrm{d}}{\mathrm{d}k_1}\Big(\tfrac{1}{2\pi} E_0\big(\tfrac{2\pi}{k_1}\big) - \tfrac{1}{k_1} E_0'\big(\tfrac{2\pi}{k_1}\big)\Big) = \tfrac{2\pi}{k_1^3} E_0''\big(\tfrac{2\pi}{k_1}\big). \quad (6.19)$$

To simplify the analysis, we introduce the following rescaling of the energy:

Rescaling of the amplitude functional. For an energy density e of the form

$$e = (-c_2\, \delta h_{\text{ext}} + \tilde{c}_2\, \delta k_1^2)\, A^2 + (-c_4 + \tilde{c}_4\, \delta k_1)\, A^4 + c_6 A^6,$$

let

$$\begin{aligned} A^2 &= (2\,\tilde{c}_2)^{1/2}(3\,c_6)^{-1/2}\varrho, \\ -c_4 &= (6\tilde{c}_2 c_6)^{1/2}2^{-1}\delta q, \\ c_2\,\delta h_{\text{ext}} &= 2\,\tilde{c}_2\,\delta h, \\ \tilde{c}_4 &= (6\tilde{c}_2 c_6)^{1/2}\,\varepsilon, \\ e &= (2\,\tilde{c}_2)^{3/2}\,(3\,c_6)^{-1/2}\widehat{e}. \end{aligned}$$

Then the rescaled energy density takes the form

$$\widehat{e} = (-\delta h\, + \tfrac{1}{2}\delta k_1^2\,)\varrho + (\tfrac{1}{2}\delta q + \varepsilon\delta k_1)\,\varrho^2 + \tfrac{1}{3}\varrho^3.$$

Due to the rescaling above the minimization of $\widehat{e}$ is restricted to $\varrho \geq 0$. In case of the amplitude functional (6.18) we have

$$\begin{aligned} c_6 &= e(k_1^*), \\ \tilde{c}_4 &= -\tfrac{9}{64}\tfrac{\mathrm{d}}{\mathrm{d}k_1}|_{k_1=k_1^*}Q(k_1^*), \\ \tilde{c}_2 &= \tfrac{1}{8}\tfrac{\mathrm{d}^2}{\mathrm{d}k_1^2}|_{k_1=k_1^*}h_{\text{ext}}(k_1^*), \\ c_4 &= -\tfrac{9}{64}\delta Q, \\ c_2 &= \tfrac{1}{4}. \end{aligned} \tag{6.20}$$

Coercivity of the amplitude functional. The amplitude functional $\widehat{e}$ is coercive for $\varepsilon \leq 2^{1/2}3^{-1/2}$. In fact, we have by the Cauchy-Schwarz inequality that

$$\varepsilon\delta k_1\varrho^2 \geq -\tfrac{1}{2}(\varepsilon^2\varrho^3 + \delta k_1^2\varrho).$$

Hence the energy is bounded from below if and only if $\varepsilon \leq 2^{1/2}3^{-1/2}$. Using the formulas (6.20) above we find that

$$0.711 \approx \varepsilon \leq 2^{1/2}3^{-1/2} \approx 0.816.$$

Hence the amplitude functional for the reduced energy is coercive.

General characterization of optimal and marginally Eckhaus stable states. Let us list the criteria for minimality and stability for energies of the form $\widehat{e} = \widehat{e}(\varrho, \delta k_1)$. The optimal amplitude ϱ^a as a function of the wave number δk_1 is characterized via

$$0 = \frac{\partial\widehat{e}}{\partial\varrho}(\varrho^a(\delta k_1), \delta k_1) \quad \text{and} \quad 0 < \frac{\partial^2\widehat{e}}{\partial\varrho^2}(\varrho^a(\delta k_1), \delta k_1).$$

The absolute minimizer (among all δk_1) satisfies the additional relations

$$0 = \frac{\partial\widehat{e}}{\partial\delta k_1}(\varrho^a(\delta k_1^a), \delta k_1^a) \quad \text{and} \quad 0 < \det \mathrm{Hess}\,\widehat{e}\,(\varrho^a(\delta k_1^a), \delta k_1^a).$$

Eckhaus unstable states, i.e., those states $\varrho^a(\delta k_1)$ for which the energy $\widehat{e}(\varrho^a(\delta k_1), \delta k_1)$ is concave, can be characterized via the relation

$$0 > \det \operatorname{Hess} \widehat{e}\,(\varrho^a(\delta k_1), \delta k_1),$$

see below. The marginally Eckhaus-stable state $(\varrho^a(\delta k_1^s), \delta k_1^s)$ is described by

$$0 = \det \operatorname{Hess} \widehat{e}\,(\varrho^a(\delta k_1^s), \delta k_1^s).$$

In fact, a straightforward calculation shows that

$$\frac{\mathrm{d}^2 \widehat{e}(\varrho^a(\delta k_1), \delta k_1)}{\mathrm{d}\delta k_1^2} = \frac{1}{\frac{\partial^2 \widehat{e}}{\partial \varrho^2}(\varrho^a(\delta k_1), \delta k_1)} \det \operatorname{Hess} \widehat{e}\,(\varrho^a(\delta k_1), \delta k_1).$$

Absolute minimizer and marginally Eckhaus-stable state of the amplitude functional of the reduced energy. In the following we apply the general criteria from the previous paragraph to obtain the branch of absolute minimizers $(\varrho^a(\delta k_1^a), \delta k_1^a)$ and the marginal stability curve $(\varrho^a(\delta k_1^s), \delta k_1^s)$ for our amplitude functional as a function of the external field. The result is plotted in Figure 6.2 and Figure 6.3.

We have that

$$\frac{\partial \widehat{e}}{\partial \varrho} = -\delta h + \tfrac{1}{2}\delta k_1^2 + 2\varepsilon \delta k_1 \varrho + \delta q \varrho + \varrho^2. \tag{6.21}$$

This is a quadratic form in ϱ and δk_1. In order to determine the set of stationary points we rewrite the equation in the form of $\frac{1}{2} x \cdot Ax + bx + c$ where $x = \begin{pmatrix} \varrho \\ \delta k_1 \end{pmatrix}$:

$$\frac{\partial \widehat{e}}{\partial \varrho} = \begin{pmatrix} \varrho \\ \delta k_1 \end{pmatrix} \cdot \begin{pmatrix} 1 & \varepsilon \\ \varepsilon & \frac{1}{2} \end{pmatrix} \begin{pmatrix} \varrho \\ \delta k_1 \end{pmatrix} + \delta q \varrho - \delta h. \tag{6.22}$$

Since $\frac{1}{2} x \cdot Ax + bx + c = \frac{1}{2}(x - A^{-1}b) \cdot A(x - A^{-1}b) - \frac{1}{2} b \cdot A^{-1} b + c$ and due to $0.711 \approx \varepsilon > \sqrt{\frac{1}{2}} \approx 0.707$ we have that $\det A < 0$, so that the stationary points lie on a hyperbola of center

$$\begin{aligned} A^{-1}b &= -\frac{2}{2 - 4\varepsilon^2} \begin{pmatrix} \frac{1}{2} & -\varepsilon \\ -\varepsilon & 1 \end{pmatrix} \begin{pmatrix} \delta q \\ 0 \end{pmatrix} \\ &= \frac{\delta q}{4\varepsilon^2 - 2} \begin{pmatrix} 1 \\ -2\varepsilon \end{pmatrix}, \end{aligned}$$

with direction of the principal axes $\left(-\frac{-1 \pm \sqrt{1 + 16\varepsilon^2}}{4\varepsilon}, 1 \right)$ and level sets $\frac{\delta q^2}{8\varepsilon^2 - 4} - \delta h$.

The sufficient condition amounts to

$$0 < \frac{\partial^2 \widehat{e}}{\partial \varrho^2}(\varrho^a(\delta k_1), \delta k_1) = 2(\varrho^a(\delta k_1) + \varepsilon \delta k_1 + \tfrac{1}{2}\delta q). \tag{6.23}$$

This cuts the $(\varrho, \delta k_1)$-plane into a stable and an unstable (w.r.t perturbations of ϱ) half-plane. Stationarity w.r.t. δk_1 amounts to

$$0 = \frac{\partial \widehat{e}}{\partial \delta k_1} = \varrho(\varepsilon\varrho + \delta k_1). \tag{6.24}$$

The absolute minimizer is located in the intersection of the hyperbola defined via (6.22) with the line (6.24).

Let us turn to the question of Eckhaus (in)stability. We have that

$$\det \begin{pmatrix} \frac{\partial^2 \widehat{e}}{\partial \varrho^2} & \frac{\partial^2 \widehat{e}}{\partial \varrho \partial \delta k_1} \\ \frac{\partial^2 \widehat{e}}{\partial \varrho \partial \delta k_1} & \frac{\partial^2 \widehat{e}}{\partial \delta k_1^2} \end{pmatrix} = (2 - 4\varepsilon^2)\,\varrho^2 - 2\varepsilon\delta k_1 \varrho - \delta k_1^2 + \delta q \varrho \tag{6.25}$$

$$= \begin{pmatrix} \varrho \\ \delta k_1 \end{pmatrix} \cdot \begin{pmatrix} 2 - 4\varepsilon^2 & -3\varepsilon \\ -3\varepsilon & -1 \end{pmatrix} \begin{pmatrix} \varrho \\ \delta k_1 \end{pmatrix} + \delta q \varrho. \tag{6.26}$$

Since $0.711 \approx \varepsilon < \sqrt{\frac{3}{2}} \approx 1.225$ the stability is thus related to a hyperbola of center

$$-\frac{\delta q}{10\varepsilon^2 + 4} \begin{pmatrix} -1 \\ 3\varepsilon \end{pmatrix},$$

with direction of the principal axes

$$\begin{pmatrix} -\frac{1}{\varepsilon} \\ 1 \end{pmatrix} \quad \text{and} \quad \begin{pmatrix} \frac{4}{3}\varepsilon \\ 1 \end{pmatrix},$$

and level sets $\frac{\delta q^2}{5\varepsilon^2 + 2}$.

Thus the marginally Eckhaus-stable state is located in the intersection of the two hyperbolas defined via (6.22) and (6.26). We note that the stability criterion only depends on the value of δq but is independent of the value of the perturbation of the field δh.

The marginal stable wave-number. There is a largest infinitesimal wave-number $\delta k^*(\delta q)$ s.t. for all $\delta k_1 > \delta k_1^*$ we have that $\varrho^a(\delta k_1)$ is unstable (independent of the external field δh); the infinitesimal period of that state is given by $\delta w^* = -\frac{2\pi}{(k^*)^2}\delta k_1^*$. On the level of the experiment we hence expect that no pattern of period smaller than $w^* + \delta w^*$ can be observed. The explicit formula for δk_1^* can be obtained from the characterization (6.25). This infinitesimal wave-number corresponds to the turning point of the hyperbola defined by $\det \mathrm{Hess} = 0$. It is the root of the discriminant which we obtain by solving $\det \mathrm{Hess} = 0$ for ϱ, namely

$$\delta k^* = \frac{4\varepsilon\delta q + \mathrm{sign}(\delta q)\sqrt{(4\varepsilon\delta q)^2 - 4\delta q^2(-12\varepsilon^2 + 8)}}{2(-12\varepsilon^2 + 8)}.$$

For the degenerate bifurcation we have $\delta w^* = 0$, cf. Figure 6.3, where as for the near-degenerate bifurcation for the reduced energy functional, i.e., $\delta Q = -Q^*(k_1^*)$ we find $\delta w^* = 0.212$, cf. Figure 6.2.

6.3.1. Comparison to the classical Eckhaus instability

In the classical, non-degenerate case the (appropriately rescaled) amplitude functional is given by

$$\widehat{e} = (-\delta h + \tfrac{1}{2}\delta k_1^2)\varrho + \tfrac{1}{2}\varrho^2.$$

In that case the optimal state for prescribed wave-number is given by

$$\varrho^a(\delta k_1) = \delta h - \tfrac{1}{2}\delta k_1^2 \quad \text{provided} \quad |\delta k_1| \leq (2\delta h)^{1/2}.$$

The absolute minimizer is given by

$$(\varrho^a, \delta k_1^a) = (\delta h, 0).$$

The marginal Eckhaus stable state is characterized via

$$0 = \det \operatorname{Hess} E = \varrho^a - \delta k_1^2 = \delta h - \tfrac{3}{2}\delta k_1^2.$$

Hence, for $|\delta k_1| > (\frac{2}{3}\delta h)^{1/2}$ the minimizer $\varrho^a(\delta k_1)$ is Eckhaus unstable. The region of instability is centered at $\delta k_1 = 0$.

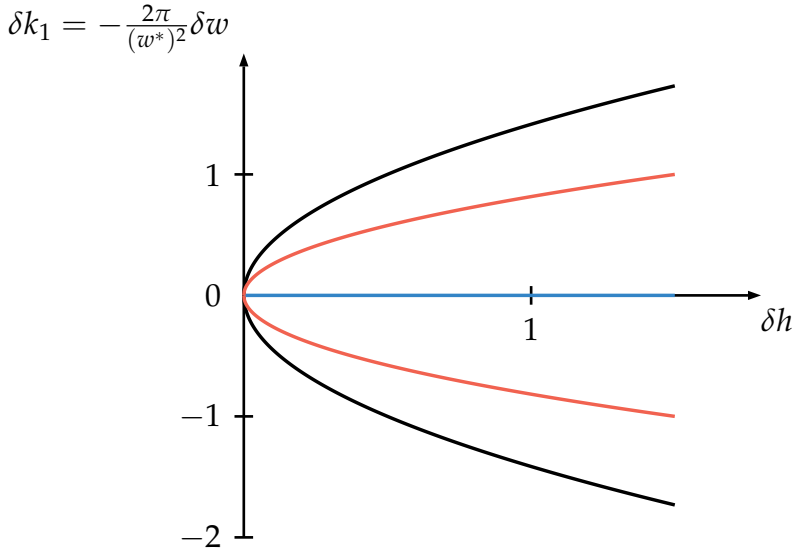

Figure 6.1.: The optimal (blue) state and the marginal Eckhaus stable (red) state for the non-degenerate energy. The black parabola bounds the region of existence of stable – under perturbation of amplitude – states.

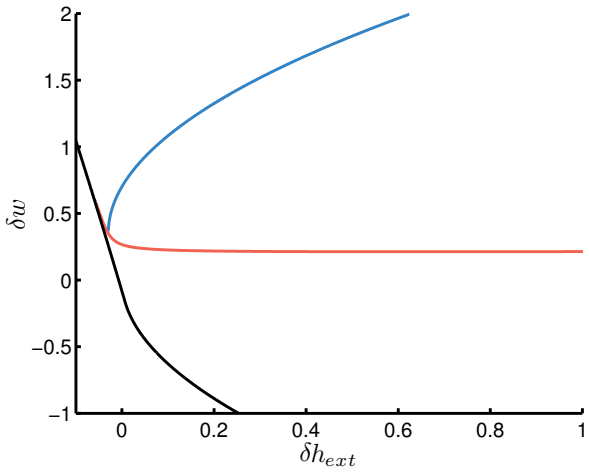

Figure 6.2.: The optimal (blue) and marginal Eckhaus stable (red) state as predicted by the analysis of the amplitude functional for $\delta Q = -Q^*(k_1^*)$. The black curve bounds the region of existence of stable states.

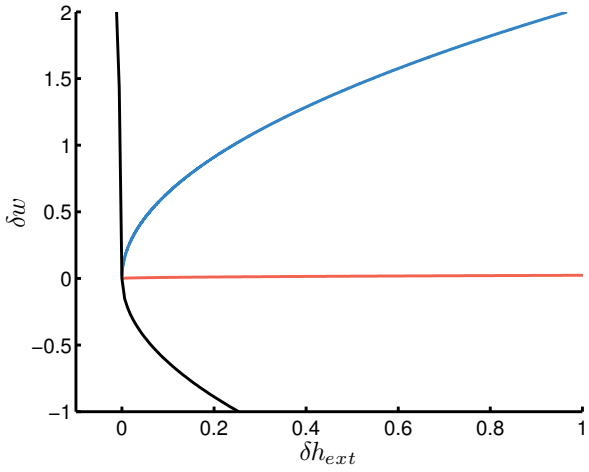

Figure 6.3.: The optimal (blue) and marginal Eckhaus stable (red) state as predicted by the analysis of the amplitude functional for $\delta Q = 0$. The black curve bounds the region of existence of stable states.

6.4. Derivation of the general amplitude functional

The bifurcation analysis based on the extended Ansatz can be generalized by considering spatially varying amplitudes within a two-scale approach. This approach builds on the central observation that a function of wave number *close* to k_1^* can be written as the slow modulation of a function of wave number k_1^*.

Two scale expansion and scaling of parameters. Motivated by the extended bifurcation analysis we make the following Ansatz

$$\begin{aligned} m_2(x_1,x_2) =& \varepsilon^{1/2}\,\tfrac{1}{2}\Big(\mathrm{e}^{ik_1^* x_1}\sin(\pi x_2)\,A(X_1)+c.c.\Big)\\ &+\varepsilon^{1}\,\tfrac{1}{2}\Big(\mathrm{e}^{i2k_1^* x_1}\sin(2\pi x_2)\,B(X_1)+c.c.\Big)\\ &+\varepsilon^{3/2}\,\tfrac{1}{2}\Big(\mathrm{e}^{ik_1^* x_1}\sin(3\pi x_2)\,C_1(X_1)+c.c.\\ &\qquad+\mathrm{e}^{i3k_1^* x_1}\sin(\pi x_2)\,C_2(X_1)+c.c.\\ &\qquad+\mathrm{e}^{i3k_1^* x_1}\sin(3\pi x_2)\,C_3(X_1)+c.c.\Big)\\ &+\mathcal{O}(\varepsilon^2), \end{aligned} \tag{6.27}$$

where the slow variable X_1 is given by

$$X_1 = \varepsilon x_1.$$

In this Ansatz, the amplitudes A, B and C_i, $i=1,2,3$ are assumed to be periodic with period $\frac{2\pi}{k_1^*}$. At the end of the derivation on p. 142, we come back to the point that higher order terms in (6.27) do not appear in the leading order term of the energy expansion.

The scaling behavior of amplitude and wave number as discussed in the previous section motivates the scaling behavior in ε of the amplitude and the slow variable, cf. (6.5). For the same reason we rescale the external field in the form of

$$h_{\mathrm{ext}} = h_{\mathrm{ext}}^*(k_1^*) + \varepsilon^2\,\delta h_{\mathrm{ext}}.$$

Moreover we rescale the anisotropy parameter Q as

$$Q = Q^*(k_1^*) + \varepsilon\delta Q.$$

Our program is as follows: We plug in the Ansatz as above into the rescaled reduced energy (1.14) augmented by anisotropy and determine the expansion w.r.t. ε. By a successive minimization of the coefficients with increasing order of ε the amplitudes B and C_i, $i=1,2,3$ are slaved to A using Fredholm type conditions. In the end, we obtain an amplitude functional which coincides with the amplitude functional derived in the extended bifurcation analysis in the previous chapter in case of constant amplitude, i.e., $A = \tilde{A}\mathrm{e}^{i\delta K_1 X_1}$. We note that the derivation is only on a formal level. A rigorous derivation could be based on the notion of Γ-convergence.

In order to derive the amplitude functional, we have to determine how the differential operators effectively act on the slow variable X_1 and therefore on the amplitudes A, B and C_i, $i = 1, 2, 3$. We have that

$$\partial_{X_1} = \varepsilon^{-1}\partial_{x_1}. \tag{6.28}$$

This entails that

$$\partial_{x_1}(\mathrm{e}^{ik_1^* x_1}F(\varepsilon x_1)) = \mathrm{e}^{ik_1^* x_1}(ik_1^* F(\varepsilon x_1) + \varepsilon\partial_{X_1}F(\varepsilon x_1)). \tag{6.29}$$

We use the Fourier representation in order to derive the commutator relation for the modulation and the non-local operator $|\partial_{x_1}|^{-1}$. As for the differentiation, the modulation just leads to a shift of the Fourier multiplier:

$$|\partial_{x_1}|^{-1}(\mathrm{e}^{ik_1^* x_1}\mathrm{e}^{i\varepsilon K_1 x_1}) = |\partial_{x_1}|^{-1}(\mathrm{e}^{(ik_1^* + i\varepsilon K_1)x_1}) = |k_1^* + \varepsilon K_1|^{-1}\mathrm{e}^{ik_1^* x_1}\mathrm{e}^{i\varepsilon K_1 x_1}. \tag{6.30}$$

In short hand notation we write

$$|\partial_{x_1}|^{-1}(\mathrm{e}^{ik_1^* x_1}F(X_1)) = \mathrm{e}^{ik_1^* x_1}|ik_1^* + \varepsilon\partial_{X_1}|^{-1}F(X_1). \tag{6.31}$$

From the Fourier representation (6.30) we obtain that

$$|ik_1^* + \varepsilon\partial_{X_1}|^{-1} = \frac{1}{k_1^*} + \varepsilon\frac{i}{(k_1^*)^2}\partial_{X_1} - \varepsilon^2\frac{1}{(k_1^*)^3}\partial_{X_1}^2 - \varepsilon^3\frac{i}{(k_1^*)^4}\partial_{X_1}^3 + \varepsilon^4\frac{1}{(k_1^*)^5}\partial_{X_1}^4 + \mathcal{O}(\varepsilon^5),$$

i.e., the expansion of (6.31), cf. Step 2 in the proof of Theorem 5.1 in Chapter 5. Let us point out that in contrast to the Bloch wave analysis for the eigenvalue in Chapter 5 – where we prescribed the modulation function – we here prescribe the function to be modulated.

In a first step the two-scale Ansatz for m_2 together with the expansion of the parameters is plugged into the energy. Using the commutator relations for the differential operators, which were derived above, and neglecting the oscillatory integrands – these contribution vanish as ε tends to zero to any order, see (6.32) – one obtains the following expansion after an integration w.r.t. x_2:

$$E_0(m_2) = \varepsilon E^1(A) + \varepsilon^2 E^2(A, B) + \varepsilon^3 E^3(A, B, C) + \mathcal{O}(\varepsilon^4).$$

As we will see, the scaling is chosen in such a way that the energy, after appropriate choice of B and C_i in terms of A, is of the order $\sim \varepsilon^3$. Let us start with the simplest

contribution, namely the Zeeman energy:

$$
\begin{aligned}
m_2^2 =& \varepsilon \tfrac{1}{4} \sin^2(\pi x_2) \Big(\mathrm{e}^{i2k_1^* x_1} A^2 + c.c. + 2|A|^2 \Big) \\
&+ \varepsilon^{3/2} \tfrac{1}{4} \sin(\pi x_2) \sin(2\pi x_2) 2 \Big(\mathrm{e}^{i3k_1^* x_1} AB + c.c. + \mathrm{e}^{-ik_1^* x_1} A\bar{B} + c.c. \Big) \\
&+ \varepsilon^2 \tfrac{1}{4} \Big(\sin(2\pi x_2)^2 (\mathrm{e}^{i4k_1^* x_1} B^2 + c.c. + 2|B|^2) \\
&\quad + \sin(\pi x_2) \sin(3\pi x_2) 2 (\mathrm{e}^{i2k_1^* x_1} AC_1 + c.c. + A\bar{C}_1 + c.c.) \\
&\quad + \sin(\pi x_2) \sin(\pi x_2) 2 (\mathrm{e}^{i4k_1^* x_1} AC_2 + c.c. + \mathrm{e}^{-i2k_1^* x_1} A\bar{C}_2 + c.c.) \\
&\quad + \sin(\pi x_2) \sin(3\pi x_2) 2 (\mathrm{e}^{i4k_1^* x_1} AC_3 + c.c. + \mathrm{e}^{-i2k_1^* x_1} A\bar{C}_3 + c.c.) \Big) \\
&+ \varepsilon^{5/2} \tfrac{1}{4} \Big(\sin(2\pi x_2) \sin(3\pi x_2) 2 (\mathrm{e}^{i3k_1^* x_1} BC_1 + c.c. + \mathrm{e}^{ik_1^* x_1} B\bar{C}_1 + c.c.) \\
&\quad + \sin(2\pi x_2) \sin(\pi x_2) 2 (\mathrm{e}^{i5k_1^* x_1} BC_2 + c.c. + \mathrm{e}^{-ik_1^* x_1} B\bar{C}_2 + c.c.) \\
&\quad + \sin(2\pi x_2) \sin(3\pi x_2) 2 (\mathrm{e}^{i4k_1^* x_1} BC_3 + c.c. + \mathrm{e}^{-ik_1^* x_1} B\bar{C}_3 + c.c.) \Big) \\
&+ \varepsilon^3 \tfrac{1}{4} \Big(\sin(3\pi x_2)^2 (\mathrm{e}^{i2k_1^* x_1} C_1^2 + c.c. + 2|C_1|^2) \\
&\quad + \sin(\pi x_2)^2 (\mathrm{e}^{i5k_1^* x_1} C_2^2 + c.c. + 2|C_2|^2) \\
&\quad + \sin(3\pi x_2)^2 (\mathrm{e}^{i5k_1^* x_1} C_3^2 + c.c. + 2|C_3|^2) \\
&\quad + \sin(3\pi x_2) \sin(\pi x_2) 2 (\mathrm{e}^{i4k_1^* x_1} C_1 C_2 + c.c. + \mathrm{e}^{-i2k_1^* x_1} C_1 \bar{C}_1 + c.c.) \\
&\quad + \sin(3\pi x_2)^2 2 (\mathrm{e}^{i4k_1^* x_1} C_1 C_3 + c.c. + \mathrm{e}^{-i2k_1^* x_1} C_1 \bar{C}_3 + c.c.) \\
&\quad + \sin(\pi x_2) \sin(3\pi x_2) 2 (\mathrm{e}^{i6k_1^* x_1} C_2 C_3 + c.c. + C_2 \bar{C}_3 + c.c.) \Big) \\
&+ \mathcal{O}(\varepsilon^4).
\end{aligned}
$$

We see that most of the contributions are oscillating on a length-scale one (in particular all contributions of fractional order in ε). Since the variation of A, B, and C_i is on a scale of order ε^{-1}, these expressions become small if we integrate w.r.t. x_1 over a periodic domain of size $\sim \varepsilon^{-1}$. In fact, for a function D which is $\frac{2\pi}{k_1^*}$-periodic we have that

$$
\begin{aligned}
\int_0^{\frac{2\pi}{\varepsilon k_1^*}} \mathrm{e}^{-ik_1 * x_1} D(\varepsilon x_1) \, \mathrm{d}x_1 &= \int_0^{\frac{2\pi}{\varepsilon k_1^*}} \frac{1}{ik_1^*} (\partial_{x_1} \mathrm{e}^{-ik_1 * x_1}) D(\varepsilon x_1) \, \mathrm{d}x_1 \\
&= -\frac{\varepsilon}{ik_1^*} \int_0^{\frac{2\pi}{\varepsilon k_1^*}} \mathrm{e}^{-ik_1 * x_1} \partial_{X_1} D(\varepsilon x_1) \, \mathrm{d}x_1. \qquad (6.32)
\end{aligned}
$$

Integration by parts therefore entails by iteration that the oscillatory integral on the l.h.s. of (6.32) can be bounded to any order in ε if we assume that D is sufficiently smooth. Hence we obtain for small $\varepsilon \ll 1$

$$
\varepsilon \int_0^{\frac{2\pi}{\varepsilon k_1^*}} \int_0^1 m_2^2 \, \mathrm{d}x_2 \, \mathrm{d}x_1 \approx \frac{1}{4} \int_0^{\frac{2\pi}{k_1^*}} \Big(\varepsilon |A|^2 + \varepsilon^2 |B|^2 + \varepsilon^3 (|C_1|^2 + |C_2|^2 + |C_3|^2) \Big) \, \mathrm{d}X_1,
$$

which follows from the rescaling $\varepsilon x_1 = X_1$ and the evaluation of the integral w.r.t x_2. Similarly we obtain

$$\varepsilon \int_0^{\frac{2\pi}{\varepsilon k_1^*}} \int_0^1 m_2^4 \,\mathrm{d}x_2 \,\mathrm{d}x_1 \approx \frac{1}{16} \int_0^{\frac{2\pi}{k_1^*}} \Big(\varepsilon^2 \tfrac{9}{4} |A|^4 + \varepsilon^3 \big(6|A|^2|B|^2 - \tfrac{3}{2}|A|^2 (A\bar{C}_1 + c.c.) + \tfrac{3}{2}(A^3\bar{C}_2 + c.c.) - \tfrac{1}{2}(A^3\bar{C}_3 + c.c.) \big) \Big) \,\mathrm{d}X_1.$$

In the same way, using (6.28) and neglecting the oscillatory integrals, the exchange energy turns into

$$\begin{aligned}
&\varepsilon \int_0^{\frac{2\pi}{\varepsilon k_1^*}} \int_0^1 (\partial_{x_1} m_2)^2 \,\mathrm{d}x_2 \,\mathrm{d}x_1 \\
&\approx \tfrac{1}{4} \int_0^{\frac{2\pi}{k_1^*}} \Big(\varepsilon (k_1^*)^2 |A|^2 + \varepsilon^2 (i k_1^* A \partial_{X_1} \bar{A} + c.c. + (2k_1^*)^2 |B|^2) \\
&\qquad + \varepsilon^3 (|\partial_{X_1} A|^2 + 2i k_1^* B \partial_{X_1} \bar{B} + c.c. + (k_1^*)^2 |C_1|^2 \\
&\qquad\quad + (3k_1^*)^2 |C_2|^2 + (3k_1^*)^2 |C_3|^2) \Big) \,\mathrm{d}X_1.
\end{aligned}$$

The stray-field energy is more complicated. This is rather due to the fact that it is non-linear and involves differentiation in two variables than due to the fact that it involves a non-local operator which can be expanded. Due to the non-linearity in the charge density several resonances can appear. A straightforward calculation shows that the expansion of the charge density is given by the following expression (resonating contributions in the energy, as σ is squared, are highlighted):

$$\begin{aligned}
&\sigma(m_2) \\
&= -\partial_{x_1} \tfrac{m_2^2}{2} + \partial_{x_2} m_2 \\
&= \varepsilon^{1/2} \tfrac{\pi}{2} \cos(\pi x_2) \Big(\underbrace{\mathrm{e}^{i k_1^* x_1} A + c.c.}_{\cdots\cdots} \Big) \\
&+ \varepsilon \Big(\pi \cos(2\pi x_2) \underbrace{(\mathrm{e}^{i 2 k_1^* x_1} B + c.c.)}_{\sim\sim\sim\sim\sim\sim\sim\sim\sim\sim} - \tfrac{1}{8} \sin^2(\pi x_2) \underbrace{(2 i k_1^* \mathrm{e}^{i 2 k_1^* x_1} A^2 + c.c.)}_{\sim\sim\sim\sim\sim\sim\sim\sim\sim\sim} \Big) \\
&+ \varepsilon^{3/2} \Big(\tfrac{3\pi}{2} \cos(3\pi x_2) (\mathrm{e}^{i k_1^* x_1} C_1 + c.c.) \\
&\qquad + \tfrac{\pi}{2} \cos(\pi x_2) (\mathrm{e}^{i 3 k_1^* x_1} C_2 + c.c.) + \tfrac{3\pi}{2} \cos(3\pi x_2) (\mathrm{e}^{i 3 k_1^* x_1} C_3 + c.c.) \\
&\qquad - \tfrac{1}{4} \sin(\pi x_2) \sin(2\pi x_2) (3 i k_1^* \mathrm{e}^{i 3 k_1^* x_1} AB + c.c. + (-i k_1^*) \underbrace{\mathrm{e}^{-i k_1^* x_1} A \bar{B} + c.c.}_{\cdots\cdots\cdots\cdots}) \Big)
\end{aligned}$$

$$
\begin{aligned}
&+\varepsilon^2\Big(-\tfrac{1}{8}\sin^2(2\pi x_2)(4ik_1^* \mathrm{e}^{i4k_1^* x_1} B^2 + c.c.) \\
&\quad -\tfrac{1}{8}\sin^2(\pi x_2)(\mathrm{e}^{i2k_1^* x_1}\partial_{X_1} A^2 + c.c. + 2\partial_{X_1}|A|^2) \\
&\quad -\tfrac{1}{2}\sin(\pi x_2)\sin(3\pi x_2)(2ik_1^* \mathrm{e}^{i2k_1^* x_1} AC_1 + c.c.) \\
&\quad -\tfrac{1}{2}\sin^2(\pi x_2)(4ik_1^* \mathrm{e}^{i4k_1^* x_1} AC_2 + c.c. + (-2ik_1^*)\mathrm{e}^{-i2k_1^* x_1} A\bar{C}_2 + c.c.) \\
&\quad -\tfrac{1}{2}\sin(\pi x_2)\sin(3\pi x_2)(4ik_1^* \mathrm{e}^{i2k_1^* x_1} AC_1 + c.c. \\
&\qquad\qquad + (-2ik_1^*)\mathrm{e}^{-i2k_1^* x_1} A\bar{C}_3 + c.c.)\Big) \\
&+\varepsilon^{5/2}\Big(-\tfrac{1}{4}\sin(\pi x_2)\sin(2\pi x_2)(\mathrm{e}^{i3k_1^* x_1}\partial_{X_1}(AB) + c.c. + \mathrm{e}^{-ik_1^* x_1}\partial_{X_1}(A\bar{B}) + c.c.) \\
&\quad -\tfrac{1}{4}\sin(2\pi x_2)\sin(3\pi x_2)(3ik_1^* \mathrm{e}^{i3k_1^* x_1} BC_1 + c.c. + ik_1^* \mathrm{e}^{ik_1^* x_1} B\bar{C}_1 + c.c.) \\
&\quad -\tfrac{1}{4}\sin(2\pi x_2)\sin(\pi x_2)(5ik_1^* \mathrm{e}^{i5k_1^* x_1} BC_2 + c.c. + (-ik_1^*)\mathrm{e}^{-ik_1^* x_1} B\bar{C}_2 + c.c.) \\
&\quad -\tfrac{1}{4}\sin(\pi x_2)\sin(3\pi x_2)(5ik_1^* \mathrm{e}^{i5k_1^* x_1} BC_3 + c.c. + (-ik_1^*)\mathrm{e}^{-ik_1^* x_1} B\bar{C}_3 + c.c.)\Big). \\
&+\mathcal{O}(\varepsilon^3).
\end{aligned}
$$

Using the expansion of the non-locality, one can derive the expansion of the stray-field contribution.

From the calculation above we can now derive the expansion of the energy. We note that there are no contributions of fractional order in ε – the corresponding integrals are all of oscillatory type, see (6.32). The first coefficient, i.e.,

$$
E^1(A) = \int_0^{\frac{2\pi}{k_1^*}} \Big((k_1^*)^2 + \tfrac{\pi^2}{2k_1^*} - h_{\mathrm{ext}}^*\Big)\frac{|A|^2}{4}\,\mathrm{d}X_1,
$$

obviously vanishes by definition of k_1^* and h_{ext}^*.

Neglecting the oscillatory integrands, the coefficient to order ε^2 is given by

$$
\begin{aligned}
&E^2(A,B) \\
&= \int_0^{\frac{2\pi}{k_1^*}} \Big(\big(k_1^* - \tfrac{\pi^2}{4(k_1^*)^2}\big)\frac{iA\partial_{X_1}\bar{A} + c.c.}{4} + \tfrac{3k_1^*}{16}\frac{|A|^4}{16} + \tfrac{9}{4}Q^*(k_1^*)\frac{|A|^4}{16} \\
&\qquad + \tfrac{\pi}{2}\frac{iA^2\bar{B} + c.c.}{8} + \big((2k_1^*)^2 + \tfrac{\pi^2}{k_1^*} - h_{\mathrm{ext}}^*\big)\frac{|B|^2}{4}\Big)\,\mathrm{d}X_1. \qquad (6.33)
\end{aligned}
$$

The first term vanishes since k_1^* is the minimizer of the dispersion relation. Given A, we can minimize E^2 in B and obtain

$$
B = \frac{-\pi i k_1 A^2}{2(6(k_1^*)^3 + \pi^2)}. \qquad (6.34)
$$

We find that the remaining term in (6.33) vanishes if $Q = Q^*(k_1^*) = \frac{5\pi^2 - 18(k_1^*)^3}{36(6(k_1^*)^3 + \pi^2)}k_1^*$, which is just the critical value identified in the extended bifurcation analysis in (6.12).

We now come to the cubic contribution for which we obtain

$$
\begin{aligned}
&E^3(A,B,C_1,C_2,C_3)\\
&=\int_0^{\frac{2\pi}{k_1^*}}\Big(\tfrac{1}{4}(|\partial_{X_1}A|^2-\delta h_{\text{ext}}|A|^2+\tfrac{\pi^2}{2(k_1^*)^3}\partial_{X_1}|A|^2)+\tfrac{3}{64}\frac{iA^2\partial_{X_1}\bar{A}^2+c.c.}{16}\\
&\quad+\tfrac{3}{16}\frac{(\partial_{X_1}|A|^2)(|\partial_{X_1}|^{-1}\partial_{X_1}|A|^2)}{16}+\delta Q\frac{9|A|^4}{64}\\
&\quad+Q^*(k_1^*)\frac{6|A|^2|B|^2}{16}+\Big(2k_1^*-\tfrac{\pi^2}{4(k_1^*)^2}\Big)\frac{iB\partial_{X_1}\bar{B}+c.c.}{4}\\
&\quad+\tfrac{1}{4}((k_1^*)^2+\tfrac{3\pi^2}{2k_1^*}-h_{\text{ext}}^*)|C_1|^2-Q^*(k_1^*)\frac{3|A|^2(A\bar{C}_1+c.c.)}{32}\\
&\quad+\frac{-(i\pi A\bar{B}C_1+c.c.)}{8}+\frac{-k_1^*|A|^2(\bar{A}C_1+c.c.)}{128}\\
&\quad+\tfrac{1}{4}((3k_1^*)^2+\tfrac{\pi^2}{6k_1^*}-h_{\text{ext}}^*)|C_2|^2+Q^*(k_1^*)\frac{3(A^3\bar{C}_2+c.c.)}{32}\\
&\quad+\frac{-(i\pi AB\bar{C}_2+c.c.)}{16}+\frac{3k_1^*(A^3\bar{C}_2+c.c.)}{128}\\
&\quad+\tfrac{1}{4}((3k_1^*)^2+\tfrac{3\pi^2}{2k_1^*}-h_{\text{ext}}^*)|C_3|^2-Q^*(k_1*)\frac{A^3\bar{C}_3+c.c.}{32}\\
&\quad+\frac{3i\pi AB\bar{C}_3+c.c.}{16}+\frac{-k_1^*(A^3\bar{C}_3+c.c.)}{128}\Big)\,\mathrm{d}X_1.
\end{aligned}
$$

We note that there is no contribution of the form $B\partial_{X_1}\bar{A}^2+c.c.$. Such a term would be potentially contained in the expansion of the cubic stray-field contribution, i.e., $2\partial_{x_2}m_2|\partial_{x_1}|^{-1}(-\partial_{x_1}\frac{m_2^2}{2})$. However, the differential operator w.r.t. x_1 is of order zero so that on the level of the Fourier multiplier $(|\partial_{x_1}|^{-1}\partial_{x_1})\mathrm{e}^{\pm ik_1^*x_1}$ turns into

$$
\frac{\pm ik_1^*+i\varepsilon K_1}{|\pm ik_1^*+i\varepsilon K_1|}\overset{\varepsilon K_1\ll ik_1^*}{=}\pm i.
$$

This shows that there are no contributions of the form $B\partial_{X_1}\bar{A}^2+c.c.$. Plugging in the optimal B as given by (6.34), we obtain by minimizing w.r.t. C_1, C_2, and C_3 that

$$
\begin{aligned}
C_1&=-\frac{(k_1^*)^2|A|^2A}{24(6(k_1^*)^3+\pi^2)},\\
C_2&=-\frac{(18(k_1^*)^3+\pi^2)(k_1^*)^2A^3}{8(6(k_1^*)^3+\pi^2)(48(k_1^*)^3-2\pi^2)},\\
C_3&=-\frac{(-18(k_1^*)^3+47\pi^2)(k_1^*)^2A^3}{144(6(k_1^*)^3+\pi^2)(8k_1^3+\pi^2)}.
\end{aligned}
$$

Therefore, the first non-trivial coefficient of the amplitude functional – namely that

of cubic order in ε – is given by:

$$
\begin{aligned}
E^3(A) = \int_0^{\frac{2\pi}{k_1^*}} \Big(& \tfrac{(k_1^*)^3}{(6(k_1^*)^3+\pi^2)^2} \Big(-\tfrac{\pi^2}{9} - \tfrac{(18(k_1^*)^3+\pi^2)^2}{24(48(k_1^*)^3-2\pi^2)} \\
& \qquad - \tfrac{(18(k_1^*)^3-47\pi^2)^2}{9\times 144(8(k_1^*)^3+\pi^2)} + \tfrac{\pi^2(5\pi^2-18(k_1^*)^3)}{6(6(k_1^*)^3+\pi^2)} + \pi^2 \Big) \tfrac{|A|^6}{64} \\
& + \Big(\tfrac{\pi^2(k_1^*)^2}{(6(k_1^*)^3+\pi^2)^2} (2k_1^* - \tfrac{\pi^2}{4(k_1^*)^2}) + \tfrac{3}{64} \Big) \frac{iA^2\partial_{X_1}\bar{A}^2 + c.c.}{16} \\
& + \delta Q\ \tfrac{9}{4}\frac{|A|^4}{16} + \tfrac{3}{16}\frac{\big||\partial_{X_1}|^{-1/2}\partial_{X_1}|A|^2\big|^2}{16} \\
& + \Big(1 + \tfrac{\pi^2}{2(k_1^*)^3} \Big) \frac{|\partial_{X_1}A|^2}{4} - \delta h_{\text{ext}}\ \frac{|A|^2}{4} \Big)\, \mathrm{d}X_1.
\end{aligned}
$$

The amplitude functional thus has the form of a non-local Ginzburg-Landau functional.

Let us come back to our Ansatz (6.27). One might suspect that next order terms ($\sim \varepsilon^2$) in (6.27) could lead to an additional contribution in the E^3 coefficient of the energy, e.g., via a mode interaction in the stray-field energy with the ε^1-coefficient in (6.27). Based on the level of the extended bifurcation analysis, let us argue that there is no need to worry. In fact, the algebraic rules yield that an additional fourth order coefficient in (6.6) satisfies an equation of the form

$$\mathcal{L}m_2^{****} = g,$$

where g is some linear combination of terms of the form

$$\mathcal{N}_3(\tau_1(m_2^{**}, m_2^{**}, \cdot)) \quad \text{and} \quad \mathcal{N}_4(\tau_2(m_2^{**}, m_2^{*}, , m_2^{*}, \cdot)),$$

where $\tau_1 \in S^3$ and $\tau_2 \in S^4$. A straightforward calculation shows that the r.h.s. is proportional to $\sin(4k_1^* x_1)\sin(4\pi x_2)$. Therefore the next-order term in (6.27) should be of the form

$$\mathrm{e}^{i4k_1^* x_1}\sin(4\pi x_2)\, D(X_1) + c.c.,$$

for some $\frac{2\pi}{k_1^*}$-periodic D. Obviously, there are no resonances with the other coefficients.

Spatially-constant amplitude. Let us first show how the case of a constant amplitude is related to the extended bifurcation analysis: For $A = \tilde{A}\ \mathrm{e}^{i\theta(X_1)} = \tilde{A}\ \mathrm{e}^{i\delta K_1 X_1}$ the energy to leading order becomes a function of the amplitude $\tilde{A}$ and the infinitesimal perturbation of the wave number perturbation δK_1. In fact, we have

$$
\begin{aligned}
|\partial_{X_1}A|^2 &= \delta K_1^2 |\tilde{A}|^2, \\
iA^2\partial_{X_1}\bar{A}^2 + c.c. &= 2\delta K_1 \tilde{A}^4.
\end{aligned}
$$

Hence

$$E^3(\tilde{A}\,\mathrm{e}^{i\delta K_1 X_1}) = \tfrac{2\pi}{k_1^*}\Big(\tfrac{(k_1^*)^3}{(6(k_1^*)^3+\pi^2)^2}\Big(-\tfrac{\pi^2}{9} - \tfrac{(18(k_1^*)^3+\pi^2)^2}{24(48(k_1^*)^3-2\pi^2)} - \tfrac{(-18(k_1^*)^3+47\pi^2)^2}{9\times144(8(k_1^*)^3+\pi^2)} + \tfrac{\pi^2(5\pi^2-18(k_1^*)^3)}{6(6(k_1^*)^3+\pi^2)} + \pi^2\Big)\frac{\tilde{A}^6}{64} + \Big(\tfrac{\pi^2(k_1^*)^2}{(6(k_1^*)^3+\pi^2)^2}\Big(2k_1^* - \tfrac{\pi^2}{4(k_1^*)^2}\Big) + \tfrac{3}{64}\Big)\frac{\delta K_1\tilde{A}^4}{8} + \Big(1+\tfrac{\pi^2}{2(k_1^*)^3}\Big)\frac{\delta K_1\tilde{A}^2}{4} - \delta h_{\mathrm{ext}}\frac{\tilde{A}^2}{4}\Big).$$

A comparison with (6.16) and (6.17) indeed confirms the equivalence of the spatially-constant amplitude for the two-scale approach and the extended bifurcation analysis. To see this, notice that

$$1+\tfrac{\pi^2}{2(k_1^*)^3} = \tfrac{1}{2}\tfrac{\mathrm{d}^2}{\mathrm{d}k_1^2}_{|k_1=k_1^*} h_{\mathrm{ext}}^*(k_1),$$
$$\tfrac{1}{8}\Big(\tfrac{\pi^2(k_1^*)^2}{(6(k_1^*)^3+\pi^2)^2}\Big(2k_1^* - \tfrac{\pi^2}{4(k_1^*)^2}\Big) + \tfrac{3}{64}\Big) = -\tfrac{9}{64}\tfrac{\mathrm{d}}{\mathrm{d}k_1}_{|k_1=k_1^*} Q^*(k_1).$$

As outlined in [Eck92], it is tempting to use the result of an extended bifurcation analysis for an *algorithmic derivation* of the generalized amplitude functional: However, this algorithmic derivation – the replacement of δK_1 by ∂_{X_1} and $\tilde{A}$ by a spatially varying amplitude A, as explained in that reference – would miss the term $\int \partial_{X_1}|A|^2|\partial_{X_1}|^{-1}\partial_{X_1}|A|^2\,\mathrm{d}X_1$, which obviously vanishes for constant amplitude.

Quasi-periodic solutions. It is known that – besides the stationary constant amplitude solutions – there are stationary states of the classical Ginzburg-Landau functional

$$E(A) = \int_0^{\frac{2\pi}{k_1^*}} -\delta h|A|^2 + \tfrac{1}{2}|\partial_{X_1}A|^2 + \tfrac{1}{4}|A|^4\,\mathrm{d}X_1$$

with spatially varying amplitude and phase, i.e., $A = \tilde{A}(X_1)\mathrm{e}^{i\theta(X_1)}$. In order to investigate these states it is useful to introduce the "angular momentum"

$$H = \tilde{A}^2\frac{\mathrm{d}\theta}{\mathrm{d}X_1}.$$

A straightforward calculation shows that stationary solutions exhibit conservation of the angular momentum, i.e.,

$$\frac{\mathrm{d}}{\mathrm{d}X_1}H = 0.$$

Moreover the "energy"

$$\tfrac{1}{2}\Big(\frac{\mathrm{d}\tilde{A}}{\mathrm{d}X_1}\Big)^2 + V(\tilde{A})$$

is conserved, where

$$V(\tilde{A}) = \frac{1}{2}\delta h\tilde{A}^2 - \frac{1}{4}\tilde{A}^4 + \frac{H^2}{2\tilde{A}^2}.$$

Then stationarity amounts to

$$\frac{\mathrm{d}^2\tilde{A}}{\mathrm{d}X_1^2} = -\frac{\mathrm{d}V}{\mathrm{d}\tilde{A}}.$$

In the special case where $H = 0$ one can construct solutions of constant phase whose amplitude suffices

$$\delta h\tilde{A} - \tilde{A}^3 + \frac{\mathrm{d}^2\tilde{A}}{\mathrm{d}X_1^2} = 0.$$

There is the trivial constant solution $\tilde{A} = \pm(\delta h)^{1/2}$ and the hyperbolic tangent. The so called defect solutions correspond to a hetero-clinic orbit connecting the constant amplitude via the hyperbolic tangent profile. In case of $H > 0$, there are solutions corresponding to compression-dilatation waves, i.e., solutions of non-constant phase, cf. [Hoyo6]. As shown in [DE91], the quartic degenerate bifurcation (without non-locality) can be treated similarly by identifying analog integrals. Depending on their value, there exist periodic and quasi-periodic solutions. Nevertheless, the non-local term cannot be treated with that method. On the other hand the bifurcation analysis in Section 6.5 suggests that quasi-periodic stationary points exist – though all unstable.

6.5. Secondary bifurcations as splitting from multiple primary bifurcations

It is known that secondary bifurcations are often intimately related to multiple primary bifurcations. This was first suggested in a work by Bauer, Keller, and Reiss in [BKR75]. A model example can be found in [IJ90, V.6]. We will see in this section that the secondary instabilities of the concertina pattern are also related to degenerate primary bifurcations. The secondary parameter, besides the external field, that leads to a splitting of the double eigenvalue is given by the period of the system. As the secondary parameter varies, the secondary bifurcation branches move along the primary branches, see Figure 6.5. For a critical value of this parameter, the secondary branches coalesce into a multiple primary bifurcation point. Usually, secondary bifurcations occur if there exist symmetries of the system. We now start with a bifurcation analysis that we subsequently compare to our numerical simulations. As mentioned in Subsection 1.8.5, the physical relevance of a finite artificial period of the domain is related to defects and inhomogeneities in the sample. They effectively reduce the characteristic wave length of interactions to a small multiple of the period of the concertina.

Consider the reduced sample of size $(\widehat{L},0)\times(0,1)$ where $\widehat{L}$ is arbitrary but fixed. As depicted in Figure 6.4, the Hessian of the reduced energy (1.14) in $\widehat{m}_2 = 0$ degenerates for the following values of the external field:

$$\widehat{h}^*_{\text{ext}}(\widehat{k}_1) \;=\; \widehat{k}_1^2 + \tfrac{\pi^2}{2\widehat{k}_1}, \text{ where } \quad \widehat{k}_1 = \tfrac{2\pi l}{\widehat{L}}, \quad l \in \mathbb{N}.$$

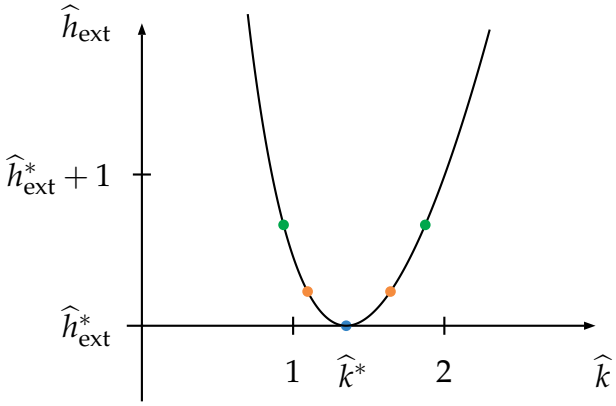

Figure 6.4.: Dispersion relation $\widehat{h}_{\text{ext}}(k)$. The marked points correspond to wave numbers $\widehat{k}_l$ and $\widehat{k}_m$ s.t. (6.35) is fulfilled. Dark green corresponds to $l = 2$ and $m = 1$ while orange corresponds to $l = 3$ and $m = 2$.

Depending on the specific value of $\widehat{L}$, there may exist two distinct integers l and m s.t. the l-mode ($m_2^l = \cos(\frac{2\pi l\widehat{x}_1}{\widehat{L}})\sin(\pi\widehat{x}_2)$) and the m-mode ($m_2^m = \cos(\frac{2\pi m\widehat{x}_1}{\widehat{L}})\sin(\pi\widehat{x}_2)$) become unstable for the same value of $\widehat{h}_{\text{ext}}$. This is the case if the corresponding values of the critical field coincide, i.e.,

$$(\widehat{k}_1^l)^2 + \tfrac{\pi^2}{2\widehat{k}_1^l} = (\widehat{k}_1^m)^2 + \tfrac{\pi^2}{2\widehat{k}_1^m},$$

where

$$\widehat{k}_1^r = \tfrac{2\pi r}{\widehat{L}}, \quad r = l, m.$$

From this expression we can derive that a multiple primary bifurcation occurs provided

$$\widehat{L}^*(l,m) = 2(2\pi lm(l+m))^{1/3} \tag{6.35}$$

at a field

$$\widehat{h}_{\text{ext}} = \tfrac{\pi^{4/3}(l^2+ml+m^2)}{(2lm(l+m))^{2/3}}.$$

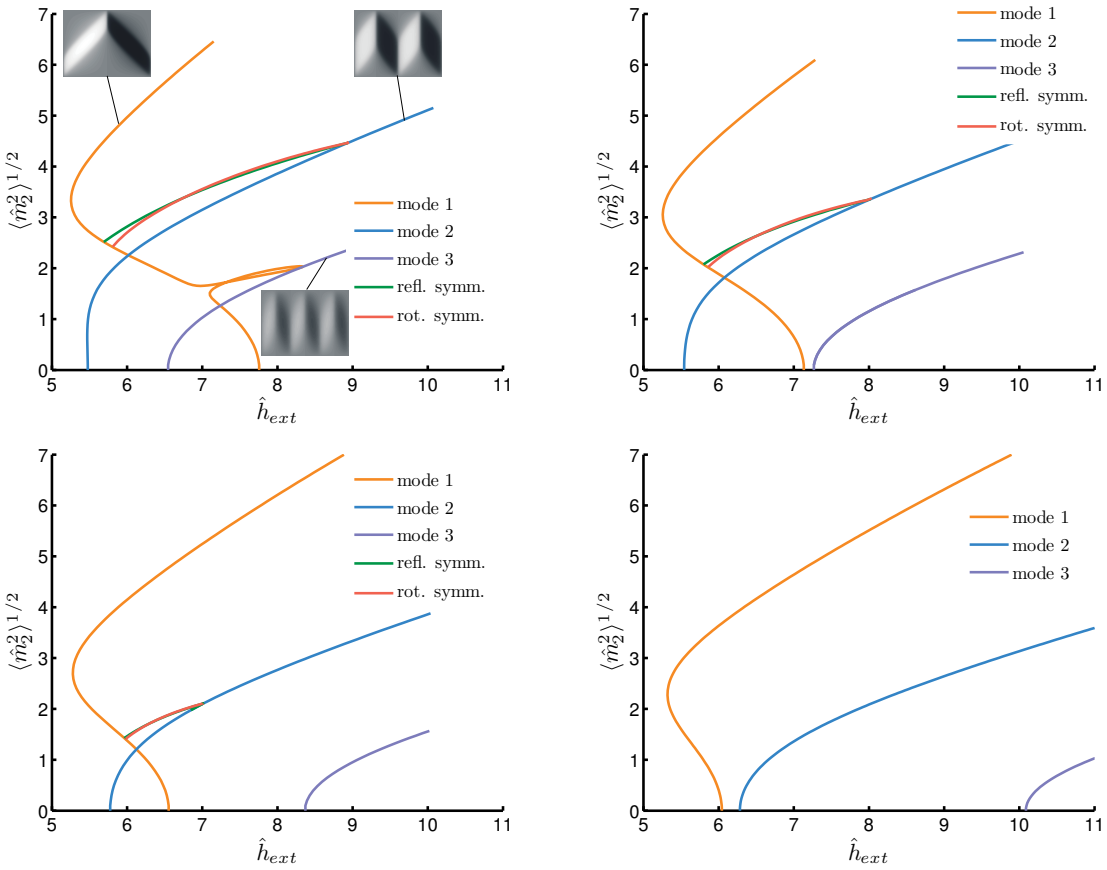

Figure 6.5.: Numerical simulations: The bifurcation diagram for $\widehat{L} = 2\widehat{w}^*$ (top left), $\widehat{L} = 1.8\widehat{w}^*$ (top right), $\widehat{L} = 1.6\widehat{w}^*$ (bottom left), $\widehat{L} = 1.4\widehat{w}^*$ (bottom right) showing the first three primary branches and secondary bifurcations. The primary branches correspond to the unstable modes $\sin(\frac{2\pi r \hat{x}_1}{\widehat{L}})\cos(\pi \hat{x}_2)$, $r = 1, 2, 3$. Note that $r = 2$ for $\widehat{L} = 2\widehat{w}^*$ corresponds to the $\widehat{w}^*$-periodic concertina branch. The secondary branches correspond to reflectional or rotational symmetric solutions, see Section 4.5. The simulations confirm that the secondary bifurcations originate in degenerate primary bifurcations.

In the following, we show that as $\widehat{L}$ varies in the neighborhood of $\widehat{L}^*(l, m)$, cf. (6.35), the multiple bifurcation splits up into two simple bifurcations and secondary bifurcations in the neighborhood of the primary bifurcation, cf. Figure 6.5. In order to simplify the calculations, let us rescale in the following way:

$$\begin{aligned} (\widehat{L}\,\widetilde{x}_1, \widetilde{x}_2) &= (\widehat{x}_1, \widehat{x}_2), \\ \widehat{L}\,\widetilde{u}(\tfrac{\widetilde{x}_1}{\widehat{L}}, \widetilde{x}_2) &= \widehat{m}_2(\widehat{x}_1, \widehat{x}_2), \\ \widehat{L}\,\widetilde{h}_{\text{ext}} &= \widehat{h}_{\text{ext}}, \\ \widehat{L}^4\,\widetilde{E}_0 &= \widehat{E}_0. \end{aligned}$$

We thus obtain

$$\widetilde{E}_0(\widetilde{u},\widetilde{h}_{\text{ext}},\widehat{L}) \;=\; \tfrac{1}{\widehat{L}^3}\int_Q(\widetilde{\partial}_1\widetilde{u})^2\,\mathrm{d}\widetilde{x} \;+\; \tfrac{1}{2}\int_Q\Big(|\widetilde{\partial}_1|^{-1/2}\widetilde{\sigma}\Big)^2\,\mathrm{d}\widetilde{x} \;-\; \widetilde{h}_{\text{ext}}\int_Q\widetilde{u}^2\,\mathrm{d}\widetilde{x},$$

where $Q=(0,1)\times(0,1)$ is periodic in the first coordinate and $\widetilde{\sigma}=-\widetilde{\partial}_1\frac{\widetilde{m}_2^2}{2}+\widetilde{\partial}_2\widetilde{m}_2$. For notational convenience, set $\lambda \;=\; \frac{1}{\widehat{L}^3}$ and $\mu=\widetilde{h}_{\text{ext}}$. We also drop the tilde so that:

$$E_0(u,\mu,\lambda) \;=\; \lambda\int_Q(\partial_1 u)^2\,\mathrm{d}x' \;+\; \tfrac{1}{2}\int_Q\Big(|\partial_1|^{-1/2}\sigma\Big)^2\,\mathrm{d}x' \;-\; \mu\int_Q u^2\,\mathrm{d}x'.$$

We rewrite the energy in terms of a quadratic, cubic and quartic term:

$$\begin{aligned}E_0(u,\lambda,\mu) \;&=\tfrac{1}{2}\langle u,\mathcal{L}u\rangle \;+\; \tfrac{1}{3}\mathcal{N}_3(u,u,u)+\tfrac{1}{4}\mathcal{N}_4(u,u,u,u)\\ &\quad+(\lambda-\lambda^*)\int_Q(\partial_1 u)^2\,\mathrm{d}x'\\ &\quad-(\mu-\mu^*)\int_Q u^2\,\mathrm{d}x',\end{aligned}\tag{6.36}$$

where

$$\begin{aligned}\tfrac{1}{2}\langle u,\mathcal{L}v\rangle \;&=\;\lambda^*\int_Q\partial_1 u\,\partial_1 v\,\mathrm{d}x'\\ &\quad+\;\tfrac{1}{2}\int_Q(|\partial_1|^{-1/2}\partial_2 u)(|\partial_1|^{-1/2}\partial_2 v)\,\mathrm{d}x' \;-\; \mu^*\int_Q u\,v\,\mathrm{d}x',\\ \tfrac{1}{3}\mathcal{N}_3(u,v,r) \;&=\;-\int_Q\Big(|\partial_1|^{-1/2}\partial_1\big(\tfrac{1}{2}u\,v\big)\Big)\Big(|\partial_1|^{-1/2}\partial_2 r\Big)\,\mathrm{d}x',\\ \tfrac{1}{4}\mathcal{N}_4(u,v,r,s) \;&=\;\tfrac{1}{2}\int_Q\Big(|\partial_1|^{-1/2}\partial_1\big(\tfrac{1}{2}u\,v\big)\Big)\Big(\,|\partial_1|^{-1/2}\partial_1\big(\tfrac{1}{2}r\,s\big)\Big)\,\mathrm{d}x'.\end{aligned}$$

By definition we have that $\mathcal{L}$ is symmetric.

For all values of $\lambda\in\mathbb{R}$ and $\mu\in\mathbb{R}$, we have that $u=0$ is a solution to the Euler-Lagrange equation. With our rescaling as above, the Hessian in $u=0$ degenerates provided

$$\mu \;=\; \lambda\,(k_1^l)^2+\tfrac{\pi^2}{2k_1^l},\quad \text{where}\quad k_1^l=2\pi l,\quad l\in\mathbb{N}.$$

As discussed above, the kernel generically is one-dimensional (up to translation). However, for

$$\lambda^*=\tfrac{1}{16\pi lm(l+m)},\quad \text{at}\quad \mu^*=\tfrac{\pi(l^2+ml+m^2)}{4lm(l+m)}$$

the kernel of the Hessian is spanned (up to translation) by the two modes

$$\cos(2\pi\,r\,x_1)\sin(\pi x_2),\quad r=l,m.\tag{6.37}$$

Our plan is to calculate a general stationary point as a bifurcation from criticality on the basis of the asymptotic energy. We use an Ansatz of the following form

$$u=Au_l+A^2u_{ll}+Bu_m+B^2u_{mm}+ABu_{lm},\tag{6.38}$$

where u_l and u_m either share

- a rotational symmetry with center in $(0, \frac{1}{2})$, i.e., $u_r = \cos(2\pi r\, x_1)\sin(\pi x_2)$, $r = l, m$, or
- a reflectional symmetry with change of sign at the axis $x_1 = 0$, i.e., $u_r = \sin(2\pi r\, x_1)\sin(\pi x_2)$, $r = l, m$.

We note that in the particular case of $l = 3m$ both symmetries occur, see below. We recall that both transforms are symmetries of the energy, see Section 4.5 Moreover, these two cases are (up to translation) the only cases where mode-interactions between u_l and u_m can occur which are – as we will see – the origin of the secondary bifurcation. In the following, we only consider the rotational symmetric case $u_r = \cos(2\pi r\, x_1)\sin(\pi x_2)$ for $r = l, m$. We note that it turns out that the reflectional symmetric case leads to the same asymptotic energy. We will obtain u_{ll}, u_{mm}, and u_{lm} by minimizing the coefficients in the expansion of the energy – restricted to the two-dimensional manifold parameterized by (6.38).

Let us plug in our Ansatz (6.38) and expand the energy. Using that $\mathcal{L}u_r = 0$ and that $\mathcal{N}_3(u_r, u_r, u_r) = \mathcal{N}_3(\tau(u_l, u_m, u_m)) = \mathcal{N}_3(\tau(u_m, u_l, u_l)) = 0$, where τ denotes a standard permutation in S^3 (which is a result of the invariance of the energy under the transform $u \to -u$, $x_2 \to 1 - x_2$), the first term in the expansion in $\delta\lambda = \delta\mu = 0$ is of quartic order. More precisely, we obtain up to higher order terms that:

$$
\begin{aligned}
E_0 \;\approx\; & A^4\Big(\tfrac{1}{2}\langle u_{ll}, \mathcal{L}u_{ll}\rangle + \tfrac{1}{6}\sum_{\tau\in S^3}\mathcal{N}_3(\tau(u_l, u_l, u_{ll})) + \tfrac{1}{4}\mathcal{N}_4(u_l, u_l, u_l, u_l)\Big) \\
& + B^4\Big(\tfrac{1}{2}\langle u_{mm}, \mathcal{L}u_{mm}\rangle + \tfrac{1}{6}\sum_{\tau\in S^3}\mathcal{N}_3(\tau(u_m, u_m, u_{mm})) + \tfrac{1}{4}\mathcal{N}_4(u_m, u_m, u_m, u_m)\Big) \\
& + A^2B^2\Big(\tfrac{1}{2}\langle u_{lm}, \mathcal{L}u_{lm}\rangle + \langle u_{ll}, \mathcal{L}u_{mm}\rangle + \tfrac{1}{3}\sum_{\tau\in S^3}\mathcal{N}_3(\tau(u_l, u_m, u_{lm})) \\
& \qquad + \tfrac{1}{6}\sum_{\tau\in S^3}\mathcal{N}_3(\tau(u_{ll}, u_m, u_m)) + \tfrac{1}{6}\sum_{\tau\in S^3}\mathcal{N}_3(\tau(u_{mm}, u_l, u_l)) \\
& \qquad + \tfrac{1}{16}\sum_{\tau\in S^4}\mathcal{N}_4(\tau(u_l, u_l, u_m, u_m))\Big) \\
& + A^3B\Big(\langle u_{ll}, \mathcal{L}u_{lm}\rangle + \tfrac{1}{6}\sum_{\tau\in S^3}\mathcal{N}_3(\tau(u_l, u_l, u_{lm})) \\
& \qquad + \tfrac{1}{3}\sum_{\tau\in S^3}\mathcal{N}_3(\tau(u_m, u_l, u_{ll})) + \tfrac{1}{24}\sum_{\tau\in S^4}\mathcal{N}_4(\tau(u_l, u_l, u_l, u_m))\Big) \\
& + AB^3\Big(\langle u_{mm}, \mathcal{L}u_{lm}\rangle + \tfrac{1}{6}\sum_{\tau\in S^3}\mathcal{N}_3(\tau(u_m, u_m, u_{lm})) \\
& \qquad + \tfrac{1}{3}\sum_{\tau\in S^3}\mathcal{N}_3(\tau(u_l, u_m, u_{mm})) + \tfrac{1}{24}\sum_{\tau\in S^4}\mathcal{N}_4(\tau(u_m, u_m, u_m, u_l))\Big) \\
& + \delta\lambda\tfrac{1}{4}(A^2(2\pi l)^2) + B^2(2\pi m)^2) \\
& - \delta\mu\tfrac{1}{4}(A^2 + B^2),
\end{aligned}
\tag{6.39}
$$

where S^d, $d = 3, 4$, denote the standard permutations. We simultaneously minimize w.r.t. u_{ll}, u_{mm}, and u_{lm} and obtain the following equations: Minimization w.r.t. u_{ll} entails

$$A^4\big(\mathcal{L}u_{ll} + \tfrac{1}{6}\sum_{\tau\in S^3}\mathcal{N}_3(\tau(u_l,u_l,\cdot))\big) + A^2B^2\big(\mathcal{L}u_{mm} + \tfrac{1}{6}\sum_{\tau\in S^3}\mathcal{N}_3(\tau(\cdot,u_m,u_m))\big) + A^3B\big(\mathcal{L}u_{lm} + \tfrac{1}{3}\sum_{\tau\in S^3}\mathcal{N}_3(\tau(\cdot,u_l,u_m))\big) = 0,$$

minimization w.r.t. u_{mm} entails

$$B^4\big(\mathcal{L}u_{mm} + \tfrac{1}{6}\sum_{\tau\in S^3}\mathcal{N}_3(\tau(u_m,u_m,\cdot))\big) + A^2B^2\big(\mathcal{L}u_{ll} + \tfrac{1}{6}\sum_{\tau\in S^3}\mathcal{N}_3(\tau(\cdot,u_l,u_l))\big) + AB^3\big(\mathcal{L}u_{lm} + \tfrac{1}{3}\sum_{\tau\in S^3}\mathcal{N}_3(\tau(\cdot,u_l,u_m))\big) = 0,$$

and minimization w.r.t. u_{lm} entails

$$A^2B^2\big(\mathcal{L}u_{lm} + \tfrac{1}{3}\sum_{\tau\in S^3}\mathcal{N}_3(\tau(u_l,u_m,\cdot))\big) + A^3B\big(\mathcal{L}u_{ll} + \tfrac{1}{6}\sum_{\tau\in S^3}\mathcal{N}_3(\tau(\cdot,u_l,u_l))\big) + AB^3\big(\mathcal{L}u_{mm} + \tfrac{1}{6}\sum_{\tau\in S^3}\mathcal{N}_3(\tau(\cdot,u_m,u_m))\big) = 0.$$

Multiplication by B^2, A^2 and AB shows that these equations reduce to one equation, namely

$$A^3B^3\big(\mathcal{L}u_{lm} + \tfrac{1}{3}\sum_{\tau\in S^3}\mathcal{N}_3(\tau(u_l,u_m,\cdot))\big) + A^4B^2\big(\mathcal{L}u_{ll} + \tfrac{1}{6}\sum_{\tau\in S^3}\mathcal{N}_3(\tau(\cdot,u_l,u_l))\big) + A^2B^4\big(\mathcal{L}u_{mm} + \tfrac{1}{6}\sum_{\tau\in S^3}\mathcal{N}_3(\tau(\cdot,u_m,u_m))\big) = 0.$$

The latter equation holds (independently of A and B) provided

$$\mathcal{L}u_{ll} + \tfrac{1}{6}\sum_{\tau\in S^3}\mathcal{N}_3(\tau(u_l,u_l,\cdot)) = 0, \tag{6.40}$$

and

$$\mathcal{L}u_{mm} + \tfrac{1}{6}\sum_{\tau\in S^3}\mathcal{N}_3(\tau(u_m,u_m,\cdot)) = 0, \tag{6.41}$$

and

$$\mathcal{L}u_{lm} + \tfrac{1}{3}\sum_{\tau\in S^3}\mathcal{N}_3(\tau(u_l,u_m,\cdot)) = 0. \tag{6.42}$$

Let us turn to the question of solvability. As mentioned above, the invariance of the energy under the transform $u \to -u$, $x_2 \to 1 - x_2$ entails that

$$\mathcal{N}_3(\tau(u_l,u_l,u_l)) = \mathcal{N}_3(\tau(u_m,u_m,u_m)) = 0, \tag{6.43}$$

and

$$\mathcal{N}_3(\tau(u_l, u_m, u_l)) = \mathcal{N}_3(\tau(u_l, u_m, u_m)) = 0. \tag{6.44}$$

Due to (6.43) and (6.44) and the fact that u_l and u_m span the kernel of $\mathcal{L}$, a unique solution to each of the equations (6.40), (6.41), and (6.42) exists due to Fredholm's alternative. It holds that

$$\begin{aligned}\tfrac{1}{3}\sum_{\tau\in S^3}\mathcal{N}_3(\tau(u_l, u_m, \cdot))&\\ = -4\pi\left(\sin(2\pi(l+m)x_1) + \tfrac{1}{2}\sin(2\pi(l-m)x_1)\right)\sin(2\pi x_2).&\end{aligned} \tag{6.45}$$

Notice that we do not distinguish the linear form, cf. (6.44), and its Riesz representation, cf. (6.45), w.r.t. notation. Moreover, we note that the different amplitudes of $\sin(2\pi(l-m)x_1)$ and $\sin(2\pi(l+m)x_1)$ on the r.h.s. of (6.45) are due to the fact that the trigonometric identities lead to cancellations in the sum of $u_l\partial_1 u_m$ and $u_m\partial_1 u_l$. Without loss of generality we may assume $l > m$. A straightforward calculation shows that

$$u_{ll} = a_{ll}\sin(4\pi l x_1)\sin(2\pi x_2), \quad \text{where} \quad a_{ll} = \tfrac{4lm(l+m)}{3l^2+ml+m^2},$$

$$u_{mm} = a_{mm}\sin(4\pi m x_1)\sin(2\pi x_2), \quad \text{where} \quad a_m = \tfrac{4lm(l+m)}{3m^2+ml+l^2},$$

$$\begin{aligned}u_{lm} = a_{l+m}\sin(2\pi(l+m)x_1)\sin(2\pi x_2) + a_{l-m}\sin(2\pi(l-m)x_1)\sin(2\pi x_2),&\\ \text{where} \quad a_{l+m} = \tfrac{8(l+m)}{5}, \quad a_{l-m} = \tfrac{4(l^2-m^2)}{7m+l}.&\end{aligned}$$

The pairs (u_{ll}, u_{mm}) and (u_{ll}, u_{lm}) are L^2-orthogonal for all values $l > m$. This is not true for (u_{mm}, u_{lm}) in the particular case of $l = 3m$. Let us note that the formulas for the amplitudes are consistent in the sense that a_{l-m} vanishes for $l = m$ in which case $\frac{1}{2}u_{lm} = u_{ll} = u_{mm}$.

With this at hand, we are ready to calculate the coefficients in the amplitude functional. Without loss of generality we assume $l > m$. We use the Euler-Lagrange equations (6.40), (6.41), and (6.42), and the symmetry properties of the operators to simplify the coefficients, namely

$$\mathcal{N}_4(v, u, u, v) = \mathcal{N}_4(\tau_3(\tau_1(u, v), \tau_2(u, v)))$$

for arbitrary $\tau_1, \tau_2, \tau_3 \in S^2$ and

$$\mathcal{N}_4(u, u, v, v) = \mathcal{N}_4(v, v, u, u).$$

Moreover, due to L^2-orthogonality of (u_{ll}, u_{mm}), we finally obtain from (6.39)

$$\begin{aligned}
E_0 \;&= A^4\Big(-\tfrac{1}{2}\langle u_{ll}, \mathcal{L}u_{ll}\rangle + \tfrac{1}{4}\mathcal{N}_4(u_l,u_l,u_l,u_l)\Big)\\
&\quad + B^4\Big(-\tfrac{1}{2}\langle u_{mm}, \mathcal{L}u_{mm}\rangle + \tfrac{1}{4}\mathcal{N}_4(u_m,u_m,u_m,u_m)\Big)\\
&\quad + A^2B^2\Big(-\tfrac{1}{2}\langle u_{lm}, \mathcal{L}u_{lm}\rangle + \tfrac{1}{2}\mathcal{N}_4(u_l,u_l,u_m,u_m) + \mathcal{N}_4(u_m,u_l,u_m,u_l)\Big)\\
&\quad + A^3B\,\Big(-\langle u_{lm}, \mathcal{L}u_{ll}\rangle + \mathcal{N}_4(u_l,u_l,u_l,u_m)\Big)\\
&\quad + AB^3\,\Big(-\langle u_{lm}, \mathcal{L}u_{mm}\rangle + \mathcal{N}_4(u_m,u_m,u_m,u_l)\Big)\\
&\quad + \delta\lambda\tfrac{1}{4}(A^2(2\pi l)^2) + B^2(2\pi m)^2)\\
&\quad - \delta\mu\tfrac{1}{4}(A^2+B^2).
\end{aligned} \tag{6.46}$$

We emphasize that for $l > m$ – due to the form of u_l and u_m and since u_{ll} and u_{lm} are L^2-orthogonal – the A^3B-contribution vanishes. Moreover, a lengthy but straightforward calculation yields the following values for the coefficients in the expansion:

$$\begin{aligned}
-\tfrac{1}{2}\langle u_{ll}, \mathcal{L}u_{ll}\rangle + \tfrac{1}{4}\mathcal{N}_4(u_l,u_l,u_l,u_l) &= -\tfrac{\pi lm(l+m)}{3l^2+ml+m^2} + \tfrac{3\pi l}{8}\\
&= \pi l\tfrac{9l^2-5ml-5m^2}{8(3l^2+ml+m^2)},
\end{aligned}$$

$$\begin{aligned}
-\tfrac{1}{2}\langle u_{mm}, \mathcal{L}u_{mm}\rangle + \tfrac{1}{4}\mathcal{N}_4(u_m,u_m,u_m,u_m) &= -\tfrac{\pi lm(l+m)}{3m^2+ml+l^2} + \tfrac{3\pi m}{8}\\
&= \pi m\tfrac{9m^2-5ml-5l^2}{8(3m^2+ml+l^2)},
\end{aligned}$$

$$\begin{aligned}
-\tfrac{1}{2}\langle u_{lm}, \mathcal{L}u_{lm}\rangle + \tfrac{1}{2}\mathcal{N}_4(u_m,u_m,u_l,u_l) + \mathcal{N}_4(u_m,u_l,u_m,u_l)&\\
= -\pi\tfrac{(l+m)(23m+9l)}{5(7m+l)} + 0 + \tfrac{3\pi l}{2} &= \pi\tfrac{-3l^2+41ml-46m^2}{10(7m+l)},
\end{aligned}$$

$$\begin{aligned}
-\langle u_{mm}\mathcal{L}u_{lm}\rangle + \mathcal{N}_4(u_m,u_m,u_m,u_l) &= \delta_{2m,l-m}(2\pi\tfrac{l^2-m^2}{7m+l} + \tfrac{3\pi m}{2})\\
&= \delta_{2m,l-m}\pi(\tfrac{-4l^2+25m^2+3lm}{2(7m+l)}).
\end{aligned}$$

6.5.1. Stationary points of the amplitude functional.

Based on the asymptotic expansion of the energy (6.46), we want to characterize all stationary points close to the bifurcation. We distinguish two cases:

Case $l \neq 3m$. In this case an explicit characterization of the stationary points is possible. To simplify the notation let us rewrite the energy (6.46) in the form

$$E_0 = e_{AA}A^4 + e_{BB}B^4 + e_{AB}A^2B^2 + \delta\lambda\tfrac{1}{4}(b_A A^2 + b_B B^2) - \delta\mu\tfrac{1}{4}(A^2 + B^2).$$

We use the amplitude functional in order to calculate the stationary points close to $u = 0$, i.e., $(A, B)(\delta\lambda, \delta\mu)$, s.t.

$$\frac{\partial E_0}{\partial A} = 0 \quad \text{and} \quad \frac{\partial E_0}{\partial B} = 0.$$

This is equivalent to

$$\begin{aligned} 2e_{AA}A^3 + e_{AB}AB^2 + \delta\lambda\tfrac{1}{4}b_A A - \delta\mu\tfrac{1}{4}A = 0, \\ 2e_{BB}B^3 + e_{AB}A^2B + \delta\lambda\tfrac{1}{4}b_B B - \delta\mu\tfrac{1}{4}B = 0. \end{aligned}$$

By factorizing the equation we can distinguish four cases, namely

a) $A = 0$ and $B = 0$,

b) $A = 0$ and $B \neq 0$,

c) $A \neq 0$ and $B = 0$,

d) $A \neq 0$ and $B \neq 0$.

Let us characterize the (real) solutions:

ad a) This corresponds to the trivial solution which exists for all $\delta\lambda$ and all $\delta\mu$.

ad b) This corresponds to the primary bifurcation branch as obtained from the classical bifurcation analysis. A solution $A^2 \geq 0$ exists, provided $(-e_{AA})^{-1}(\delta\lambda b_A - \delta\mu \geq 0$.

ad c) This corresponds to the primary bifurcation branch as obtained from the classical bifurcation analysis. A solution $B^2 \geq 0$ exists, provided $(-e_{BB})^{-1}(\delta\lambda b_B - \delta\mu \geq 0$.

ad d) This corresponds to secondary bifurcation branches. A solution (A, B) s.t. $A^2 \geq 0$ and $B^2 \geq 0$ exists, provided both

$$\begin{aligned} \tfrac{(2b_A e_{BB} - b_B e_{AB})\delta\lambda + (2e_{BB}e_{AB})(-\delta\mu)}{e_{AB}^2 - 4e_{AA}e_{BB}} \geq 0, \\ \tfrac{(2b_B e_{AA} - b_A e_{AB})\delta\lambda + (2e_{AA} - e_{AB})(-\delta\mu)}{e_{AB}^2 - 4e_{AA}e_{BB}} \geq 0. \end{aligned}$$

As an example, we consider the case $m = 2$ and $l = 1$. Then

$$e_{AA} = \tfrac{7\pi}{20}, \quad e_{BB} = -\tfrac{7\pi}{24}, \quad e_{AB} = \tfrac{4\pi}{15}, \quad b_A = 4(2\pi)^2 \quad \text{and} \quad b_B = (2\pi)^2.$$

Therefore, solutions of type b) exist provided

$$\delta\mu \geq 4(2\pi)^2\delta\lambda$$

and of type c) provided

$$\delta\mu \leq (2\pi)^2\delta\lambda.$$

Moreover, solutions of type d) only exist if

$$\delta\mu \geq \tfrac{208\pi^2\delta\lambda}{17} \quad \text{and} \quad \delta\mu \leq \tfrac{44\pi^2\delta\lambda}{13}.$$

In particular, existence is related to $\delta\lambda < 0$, i.e., $L > L^*(l, m)$. It is useful to think of $\delta\lambda$ as fixed, since it is related to the infinitesimal period of the domain, see the paragraph before (6.36).

Our calculations show that the existence of secondary branches is related to the crossing of primary branches as the period L passes some critical value, cf. (6.35). For $L > L^*(l, m)$ we find a secondary bifurcation branch connecting the primary mode-l-branch with the primary mode-m-branch. Notice that the mode-l-branch bifurcates for a smaller value of μ, i.e., smaller external field h_{ext}, than the mode-m-branch.

Figure 6.6 shows a comparison of the result of the bifurcation detection algorithm on the basis of the reduced model and the result of the asymptotic analysis. The asymptotic analysis shows no difference in energy of the rotational symmetric bifurcation and the reflectional symmetric bifurcation, see Chapter 4 and Figure 6.7.

Case $l = 3m$. The explicit characterization of the set of solutions is difficult for $B = 0$, so that we solely refer to numerical computations: The Euler-Lagrange equation of the amplitude functional was solved in Mathematica and plotted in matlab, see Figure 6.7. The plot shows that the asymmetry of the equation leads to a loop of the bifurcation branch which can be interpreted as a perturbation of the secondary bifurcation for $l \neq 3m$.

Let us finally remark that that the form of the diagrams depends only on the quantities $l/(\gcd(l, m))$ and $m/(\gcd(l, m))$.

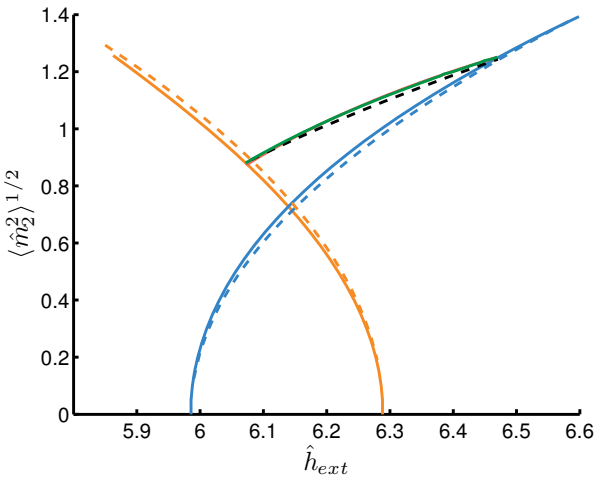

Figure 6.6.: Numerical simulations (solid) and asymptotics (dashed): The figure shows a comparison of the bifurcation diagram for the $\widehat{L} = 1.5\widehat{w}^*$-periodic domain ($\lambda^* \approx 0.003316$, $\delta\lambda \approx -0.000368$) including the branch corresponding to the mode $m = 1$ (orange) and the branch corresponding to the mode $l = 2$ (blue). The reflectional (green) and rotational (red) symmetric branches coincide to leading order with the secondary branch based on the asymptotics (black).

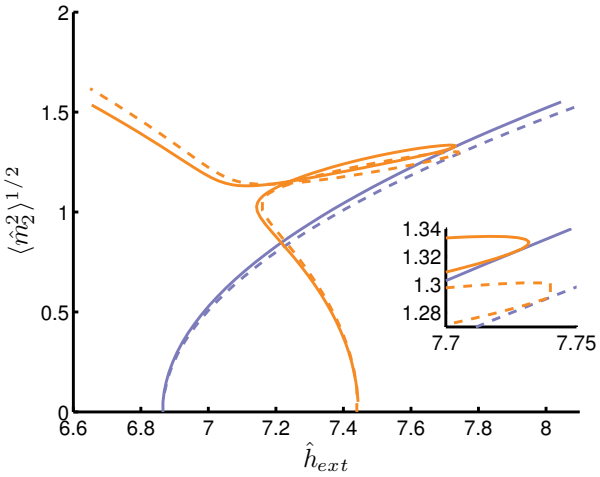

Figure 6.7.: Numerical simulations (solid) and asymptotics (dashed): The figure shows a comparison of part of the bifurcation diagram for the $\widehat{L} = 1.9\widehat{w}^*$-periodic domain ($\lambda^* \approx 0.001658$, $\delta\lambda \approx -0.000208$) including the branch corresponding to the mode $m = 1$ (orange) and the branch corresponding to the mode $l = 3$ (violet). The zoom-in shows that the turning point does not coincide with the osculation point. This is the generic case.

7

The effect of polycrystalline anisotropy

In this chapter, the effect of a polycrystalline anisotropy is investigated on the basis of the reduced energy functional (1.10). This form of anisotropy leads to an additional contribution which has the form of a random transversal external field. In particular, we will address the relation of the oscillatory ripple structure, which is observed in polycrystalline Permalloy material, and the concertina, see Section 7.1. Subsection 7.1.2 addresses the discretization and numerical simulation of the random field.

It is well known that an additional spatial-temporal random torque in the Landau-Lifshitz-Gilbert equation, modeling thermal fluctuations, leads to a divergence in the large wave-numbers, cf. [BG05, Abe10]. In Section 7.2 we therefore address the different effects of a spatial randomness, i.e., quenched disorder, and a spatial-temporal randomness.

7.1. The ripple

The ripple denotes the typical in-plane oscillation of a magnetization in a thin film that is small in amplitude (and scale with respect to typical domain patterns), see Figure 1.30; the wave vector is always in direction of the (locally averaged) magnetization, see Figure 7.1.

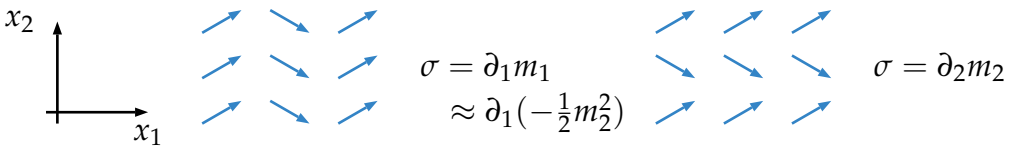

Figure 7.1.: An oscillation in the direction of average magnetization leads to a smaller, quadratic scaling in the charge density.

The ripple is triggered by an effective field of random direction on a small scale. Several origins for this effective field are proposed in the literature, see for instance [Har68, Section C]; in polycrystalline thin films, the random orientation of the grains,

more precisely their crystalline anisotropy, and local stresses via magnetostriction are seen as the main causes. In our discussion, we shall focus on the first one.

Hoffmann [Hof68] and Harte [Har68], based on the torque equilibrium linearized around a spatially constant magnetization (solely determined by the external field and anisotropy). Hereby they identified the linear response to such a small-scale, small-amplitude random effective field. The main finding is that the stray field – which penalizes transversal more than longitudinal perturbations of the magnetization because the former lead to a stronger charge oscillation – results in a strong anisotropic response. The anisotropic rescaling (1.11) leading to our reduced model and the anisotropic response of the ripple obviously have the same origin.

We will see that both the ripple and the transition between ripple and concertina can be explained within the framework of an extension of our reduced model. Our analysis of the ripple is mainly a reformulation of the classical results by Hoffmann. However, the new insight is that the finite width of the sample leads to a (continuous) transition from the ripple to the concertina.

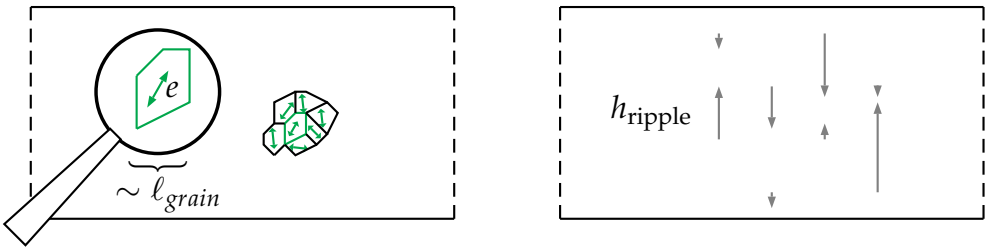

Figure 7.2.: A polycrystalline anisotropy acts like a transversal (to the direction of the mean magnetization) random field on length scales large compared to the grain size.

7.1.1. Extension of the reduced model to polycrystalline anisotropy

We now heuristically explain how to extend our reduced model. We start from the three-dimensional model (1.1) with a uniaxial anisotropy of strength Q and position-dependent easy axis $e(x)$, i.e., with the augmentation $-Q\int_\Omega (m\cdot e)^2\,\mathrm{d}x$ of the micromagnetic energy (1.1), cf. Figure 7.2 (left). Under the assumptions of our reduced model, i.e., $m_3 \equiv 0$, $m = m(x_1, x_2)$, $m_2^2 \ll 1$, this term is, up to additive constants, to leading order approximated by

$$-Q\int_\Omega (m\cdot e)^2\,\mathrm{d}x \approx -2Qt\int_{\Omega'} m_2\overline{e_1e_2}\,\mathrm{d}x_1\,\mathrm{d}x_2, \tag{7.1}$$

where

$$\overline{e_1e_2}(x_1,x_2) = t^{-1}\int_0^t e_1e_2(x_1,x_2,x_3)\,\mathrm{d}x_3$$

denotes the vertical average of the product of the first two components of the easy axis. A random anisotropy therefore acts to leading order as a transversal external

stochastic field

$$h_{\text{ripple}} = Q\overline{e_1 e_2}. \tag{7.2}$$

As mentioned, the position dependence of e arises from the random orientation of the grains of size ℓ_{grain}. Provided $t \ll \ell_{\text{grain}} \ll w^*$ (where we take w^* as a typical length scale of the magnetization pattern), the stationary statistics of $\overline{e_1 e_2}$ are characterized by

$$\langle \overline{e_1 e_2}(0,0)\overline{e_1 e_2}(x_1,x_2)\rangle = \ell_{\text{grain}}^2 \delta(x_1)\delta(x_2)\langle \overline{e_1 e_2}(0,0)^2\rangle, \tag{7.3}$$

where $\langle\cdot\rangle$ denotes the ensemble average and δ the Dirac function. For example in case of a uniform distribution of the easy axis e in $\mathbb{S}^1$ and column-like grains, i.e., the distribution $(\cos\phi \sin\phi, 0)$, $\phi \in [0, 2\pi)$, we obtain

$$\langle \overline{e_1 e_2}^2\rangle = \tfrac{1}{2\pi}\int_0^{2\pi} (e_1 e_2)^2(\phi)\,\mathrm{d}\phi = \tfrac{1}{8}.$$

Let us note that different axial anisotropies can be similarly treated, leading to a different factor in the latter identity.

The dominant wave number of the magnetization. For subcritical fields $h_{\text{ext}} < h_{\text{ext}}^*$, we neglect the nonlinear term in the charge density in (1.10). The resulting energy functional is quadratic and linear in m_2. Hence, it is conveniently expressed in terms of $\mathcal{F}m_2(k_1,k_2)$, which denotes the Fourier transform of m_2 w.r.t. x_1 (we assume an infinite stripe at that point, periodic stripes of large period L lead to similar results) and the Fourier sine series in x_2 (related to the edge pinning $m_2 = 0$ at $x_2 = 0, \ell$):

$$\begin{aligned} &E(m_2)\\ &\quad\approx \int_{-\infty}^{\infty} \sum_{k_2 \in \frac{\pi\mathbb{Z}}{\ell}} (d^2k_1^2 + \tfrac{1}{2}tk_2^2k_1^{-1} - h_{\text{ext}})|\mathcal{F}(m_2)|^2 - 2Q\mathcal{F}(\overline{e_1 e_2})\mathcal{F}^{-1}(m_2)\,\mathrm{d}k_1. \end{aligned} \tag{7.4}$$

A uniaxial anisotropy, constant throughout the sample, is neglected at that point but can be easily included afterwards since it only leads to a shift of the external field. The explicit minimization yields

$$\mathcal{F}(m_2)(k_1,k_2) = \frac{1}{(d^2k_1^2 + \frac{1}{2}tk_2^2k_1^{-1} - h_{\text{ext}})}\mathcal{F}(h_{\text{ripple}})(k_1,k_2). \tag{7.5}$$

We interpret this m_2 as the ripple. Since (7.3) on the level of $\mathcal{F}(\overline{e_1 e_2})$ reads

$$\langle |\mathcal{F}(\overline{e_1 e_2})(k_1,k_2)|^2\rangle = \ell_{\text{grain}}^2 \langle \overline{e_1 e_2}(0,0)^2\rangle,$$

(7.5) is best expressed in terms of the energy spectrum:

$$\langle |\mathcal{F}m_2(k_1,k_2)|^2\rangle = Q^2 \frac{\ell_{\text{grain}}^2}{(d^2k_1^2 + \frac{1}{2}tk_2^2k_1^{-1} - h_{\text{ext}})^2}\langle \overline{e_1 e_2}(0,0)^2\rangle. \tag{7.6}$$

The numerator clearly displays the afore mentioned anisotropic response of m_2 to the isotropic field $\overline{e_1 e_2}$.

As we will see below, from formula (7.6), one can infer the predominant wave number of the ripple given by

$$\langle k_1 \rangle = \frac{\langle \sum_{k_2} \int_{-\infty}^{\infty} |k_1| |\mathcal{F}(m_2)|^2 \, \mathrm{d}k_1 \rangle}{\langle \sum_{k_2} \int_{-\infty}^{\infty} |\mathcal{F}(m_2)|^2 \, \mathrm{d}k_1 \rangle} = \frac{\langle ||\nabla|^{1/2} m_2|^2 \rangle}{\langle |m_2|^2 \rangle}. \tag{7.7}$$

There are three different scaling regimes for the wave number.

- For moderate stabilizing fields, i.e., $t^2 d^{-2} \gg -h_{\mathrm{ext}} \gg d^{2/3} \ell^{-4/3} t^{2/3}$, one can show that

  $$\langle |k_1| \rangle \sim (-h_{\mathrm{ext}})^{1/2} d^{-1}. \tag{7.8}$$

  This is the characteristic wave number which was derived by Hoffmann and Harte , cf. [Hof68, p.34, (7) and (9)] and [Har68, p.1515, (97b)]. However, Hoffman includes an additional uniaxial anisotropy with easy axis e_1 of strength Q_u, i.e., $+Q_u \int_\Omega m_2^2 \, \mathrm{d}x$, so that the external field is shifted in the sense that the dominant wave number turns into $\langle |k_1| \rangle \sim (Q_u - h_{\mathrm{ext}})^{1/2} d^{-1}$.

- We note that for large stabilizing fields, i.e., in the limit $-h_{\mathrm{ext}} \gg t^2 d^{-2}$, the amplitude of the ripple tends to zero.

- For small stabilizing fields and destabilizing fields up to the critical field, more precisely $-d^{2/3} \ell^{-4/3} t^{2/3} \ll h_{\mathrm{ext}} \leq h_{\mathrm{ext}}^* = 3(\frac{\pi}{2})^{4/3} d^{2/3} \ell^{-4/3} t^{2/3}$, one can show that the dominant wave number scales as

  $$\langle |k_1| \rangle \sim d^{-2/3} \ell^{-2/3} t^{1/3}. \tag{7.9}$$

  More precisely, as h_{ext} approaches the critical field h_{ext}^*, the dominant wave number $\langle |k_1| \rangle$ approaches the critical wave number k_1^*, i.e., the wave number of the unstable mode, see below.

We thus learn from the analysis that, as the strength h_{ext} of the external field increases from moderate negative values towards its critical value, the average wave length of the ripple continuously increases

- from the values characteristic to a film which is infinite in both x_1- and x_2-directions, cf. Section 7.2 and (7.28) therein,

- to the wave length of the unstable mode that is at the origin of the concertina pattern, see Figure 7.3.

It is thus not surprising that ripple and small-amplitude concertina are difficult to distinguish.

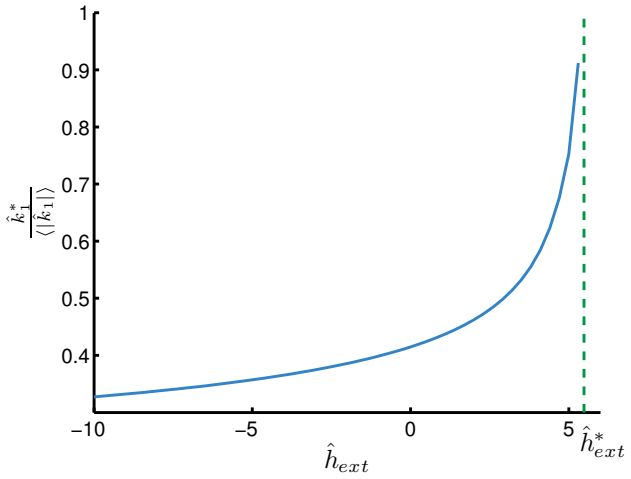

Figure 7.3.: Numerical simulations: The dominant wave number of the transversal component of the magnetization computed on the basis of the reduced model augmented by a transversal random field. As the external field approaches the critical field the dominant wave number increases towards the critical wave number.

Arguments for scaling behavior of the dominant wave number. Let us first give an argument for (7.8) and afterwards turn to (7.9). For moderate stabilizing external field, i.e.,

$$t^2 d^{-2} \gg -\widehat{h}_{\text{ext}} = d^{-2/3}\ell^{4/3}t^{-2/3}(-h_{\text{ext}}) \gg 1, \tag{7.10}$$

consider the rescaling

$$k_1 = d^{-1}(-h_{\text{ext}})^{1/2}\,\widehat{k}_1 \quad \text{and} \quad k_2 = d^{-1/2}t^{-1/2}(-h_{\text{ext}})^{3/4}\,\widehat{k}_2$$

and set

$$\alpha = d^{1/2}\ell^{-1}t^{1/2}(-h_{\text{ext}})^{-3/4}. \tag{7.11}$$

Then

$$\begin{aligned}\frac{\pi}{\ell}\sum_{k_2\in\frac{\pi}{\ell}\mathbb{Z}}\int_{-\infty}^{\infty}\frac{1}{(d^2k_1^2+\frac{1}{2}t\frac{k_2^2}{|k_1|}-h_{\text{ext}})^2}\,\mathrm{d}k_1 \\ = \frac{\pi}{\ell}d^{-1}(-h_{\text{ext}})^{1/2}\,(-h_{\text{ext}})^{-2}\sum_{k_2\in\pi\alpha\mathbb{Z}}\int_{-\infty}^{\infty}\frac{1}{(\widehat{k}_1^2+\frac{1}{2}\frac{\widehat{k}_2^2}{|\widehat{k}_1|}+1)^2}\,\mathrm{d}\widehat{k}_1.\end{aligned}$$

Since $\alpha \ll 1$ in the Regime (7.10), we can approximate the sum over $\widehat{k}_2$ by an integral, more precisely

$$\pi\alpha\sum_{k_2\in\pi\alpha\mathbb{Z}}\int_{-\infty}^{\infty}\frac{1}{(\widehat{k}_1^2+\frac{1}{2}\frac{\widehat{k}_2^2}{|\widehat{k}_1|}+1)^2}\,\mathrm{d}\widehat{k}_1 \overset{\alpha\ll1}{\approx} \int_{-\infty}^{\infty}\int_{-\infty}^{\infty}\frac{1}{(\widehat{k}_1^2+\frac{1}{2}\frac{\widehat{k}_2^2}{|\widehat{k}_1|}+1)^2}\,\mathrm{d}\widehat{k}_2\,\mathrm{d}\widehat{k}_1.$$

To see that the latter integral is finite, we refer to Figure 7.4 which depicts the scaling regimes of the integrand. From Figure 7.4 we read off that

$$\begin{aligned}
&\int_{-\infty}^{\infty}\int_{-\infty}^{\infty} \frac{1}{(\widehat{k}_1^2+\frac{1}{2}\frac{\widehat{k}_2^2}{|\widehat{k}_1|}+1)^2}\,\mathrm{d}\widehat{k}_1\,\mathrm{d}\widehat{k}_2 \\
&\qquad\sim \int_0^1\int_0^{\widehat{k}_1^{1/2}} 1\;\mathrm{d}\widehat{k}_2\,\mathrm{d}\widehat{k}_1 + \int_0^1\int_{\widehat{k}_1^{1/2}}^1 |\widehat{k}_1|^2\widehat{k}_2^{-4}\;\mathrm{d}\widehat{k}_2\,\mathrm{d}\widehat{k}_1 \\
&\qquad\qquad + \int_1^\infty\int_0^{\widehat{k}_2^{2/3}} |\widehat{k}_1|^2\widehat{k}_2^{-4}\;\mathrm{d}\widehat{k}_1\,\mathrm{d}\widehat{k}_2 + \int_1^\infty\int_0^{\widehat{k}_1^{3/2}} \widehat{k}_1^{-4}\;\mathrm{d}\widehat{k}_2\,\mathrm{d}\widehat{k}_1 \\
&\qquad< +\infty. \qquad (7.12)
\end{aligned}$$

Altogether we obtain that

$$\begin{aligned}
&\tfrac{\pi}{\ell}\sum_{k_2\in\frac{\pi}{\ell}\mathbb{Z}}\int_{-\infty}^{\infty} \frac{1}{(d^2k_1^2+\frac{1}{2}t\frac{k_2^2}{|k_1|}-h_{\mathrm{ext}})^2}\,\mathrm{d}k_1 \\
&\qquad= d^{-3/2}t^{-1/2}(-h_{\mathrm{ext}})^{-3/4}\pi\alpha\sum_{\widehat{k}_2\in\pi\alpha\mathbb{Z}}\int_{-\infty}^{\infty}\frac{1}{(\widehat{k}_1^2+\frac{1}{2}\frac{\widehat{k}_2^2}{|\widehat{k}_1|}+1)^2}\,\mathrm{d}\widehat{k}_1 \\
&\qquad\overset{\alpha\ll 1}{\lesssim} d^{-3/2}t^{-1/2}(-h_{\mathrm{ext}})^{-3/4}.
\end{aligned}$$

Notice that this is the average squared ripple amplitude $\sum_{k_2}\int|\mathcal{F}(m_2)|^2\,\mathrm{d}k_1$which was derived by Hoffmann in [Hof68, p.34, (10)], see (7.6). Similarly we have that

$$\begin{aligned}
&\tfrac{\pi}{\ell}\sum_{k_2\in\frac{\pi}{\ell}\mathbb{Z}}\int_{-\infty}^{\infty} \frac{|k_1|}{(d^2k_1^2+\frac{1}{2}t\frac{k_2^2}{|k_1|}-h_{\mathrm{ext}})^2}\,\mathrm{d}k_1 \\
&\qquad\approx d^{-3/2}t^{-1/2}(-h_{\mathrm{ext}})^{-3/4}\,d^{-1}(-h_{\mathrm{ext}})^{1/2}\int_{-\infty}^{\infty}\int_{-\infty}^{\infty}\frac{|\widehat{k}_1|}{(\widehat{k}_1^2+\frac{1}{2}\frac{\widehat{k}_2^2}{|\widehat{k}_1|}+1)^2}\,\mathrm{d}\widehat{k}_1\,\mathrm{d}\widehat{k}_2.
\end{aligned}$$

Since the latter integral is finite – which can be seen in a similar way using the decomposition as in (7.12) – we obtain for $\alpha\ll 1$ that the dominant wave number is given by

$$\langle|k_1|\rangle\sim d^{-1}(-h_{\mathrm{ext}})^{1/2}.$$

(We note that higher order moments do not exist, more precisely $\langle|k_1|^r\rangle$ is infinite for $r>\frac{3}{2}$). In the same manner one can show that

$$\langle|k_2|\rangle\sim(dt)^{-1/2}(-h_{\mathrm{ext}})^{3/4}.$$

Note that the anisotropic response of the magnetization, i.e., $\langle|k_2|\rangle\ll\langle|k_1|\rangle$, only is equivalent to the lower bound in the regime (7.10).

Let us briefly address the case of large stabilizing field $-h_{\mathrm{ext}}\gg t^2d^{-2}$. In that case the scale separation is not valid anymore so that the anisotropic approximation

$d^2k_1^2 + \frac{t^2}{2}\frac{k_2^2}{|k_1|} - h_{\text{ext}}$ of $d^2|k'|^2 + \frac{t^2}{2}\frac{k_2^2}{|k'|} - h_{\text{ext}}$ fails. However, on the basis of the latter expression one can show that the amplitude of the magnetization $\langle \delta m_2^2 \rangle^{1/2}$ in the limit $-h_{\text{ext}} \gg t^2 d^{-2}$ converges to zero, see Section 7.2.

We now turn to small stabilizing external fields $\alpha \gg 1$, cf. (7.11). Using the rescaling

$$k_1 = d^{-2/3}\ell^{-2/3}t^{1/3}\widehat{k}_1 \quad \text{and} \quad k_2 = \ell^{-1}\widehat{k}_2$$

we obtain that

$$\begin{aligned}
&\tfrac{\pi}{\ell}\sum_{k_2\in\frac{\pi}{\ell}\mathbb{Z}}\int_{-\infty}^{\infty}\frac{1}{(d^2k_1^2+\frac{1}{2}t\frac{k_2^2}{|k_1|}-h_{\text{ext}})^2}\,\mathrm{d}k_1\\
&\quad=\tfrac{\pi}{\ell}\,d^{-2/3}\ell^{-2/3}t^{1/3}\,d^{-4/3}\ell^{8/3}t^{-4/3}\sum_{\widehat{k}_2\in\pi\mathbb{Z}}\int_{-\infty}^{\infty}\frac{1}{(\widehat{k}_1^2+\frac{1}{2}\frac{\widehat{k}_2^2}{|\widehat{k}_1|}+\frac{1}{\alpha^{4/3}})^2}\,\mathrm{d}\widehat{k}_1\,\mathrm{d}\widehat{k}_2\\
&\quad\overset{\alpha\gg1}{\sim} d^{-2}\ell t^{-1}.
\end{aligned}$$

The latter sum/integral is finite since $(\widehat{k}_1^2 + \frac{1}{2}\widehat{k}_2^2|\widehat{k}_1|^{-1})^{-2}$ is integrable on $(0,\infty)\times(\pi,\infty)$:

$$\begin{aligned}
&\int_{\pi}^{\infty}\int_{-\infty}^{\infty}(\widehat{k}_1^2+\frac{1}{2}\widehat{k}_2^2|\widehat{k}_1|^{-1})^{-2}\,\mathrm{d}\widehat{k}_1\,\mathrm{d}\widehat{k}_2\\
&\qquad\sim\int_{\pi}^{\infty}\int_{0}^{|\widehat{k}_2|^{2/3}}\widehat{k}_1^2\widehat{k}_2^{-4}\,\mathrm{d}\widehat{k}_1\,\mathrm{d}\widehat{k}_2+\int_{\pi}^{\infty}\int_{|\widehat{k}_2|^{2/3}}^{0}\widehat{k}_1^{-4}\,\mathrm{d}\widehat{k}_1\,\mathrm{d}\widehat{k}_2\sim 1. \quad (7.13)
\end{aligned}$$

Moreover

$$\begin{aligned}
&\tfrac{\pi}{\ell}\sum_{k_2\in\frac{\pi}{\ell}\mathbb{Z}}\int_{-\infty}^{\infty}\frac{|k_1|}{(d^2k_1^2+\frac{1}{2}t\frac{k_2^2}{|k_1|}-h_{\text{ext}})^2}\,\mathrm{d}k_1\\
&\qquad=\pi d^{-2}\ell t^{-1}d^{-2/3}\ell^{-2/3}t^{1/3}\sum_{\widehat{k}_2\in\pi\mathbb{Z}}\int_{-\infty}^{\infty}\frac{\widehat{k}_1}{(\widehat{k}_1^2+\frac{1}{2}\frac{\widehat{k}_2^2}{|\widehat{k}_1|}+\frac{1}{\alpha^{4/3}})^2}\,\mathrm{d}\widehat{k}_1\,\mathrm{d}\widehat{k}_2\\
&\qquad\overset{\alpha\gg1}{\sim} d^{-2}\ell t^{-1}d^{-2/3}\ell^{-2/3}t^{1/3}.
\end{aligned}$$

In fact, the integral is finite which can be seen similar to (7.13) so that we obtain

$$\langle |k_1| \rangle \sim d^{-2/3}\ell^{-2/3}t^{1/3}.$$

In the same way one obtains that

$$\langle |k_2| \rangle \sim \ell^{-1}.$$

Observe that that $\langle |k_2| \rangle \ll \langle |k_1| \rangle$ is equivalent to the lower bound characterizing Regime III, (1.17).

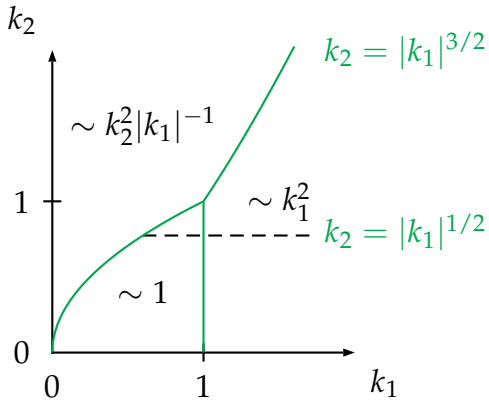

Figure 7.4.: The scaling regimes of $k_1^2 + k_2^2|k_1|^{-1} + 1$.

Finally we turn to the case of small external destabilizing field. Provided that $0 \leq h_{\text{ext}} < h_{\text{ext}}^* = 3(\frac{\pi}{2})^{4/3} d^{2/3} \ell^{-4/3} t^{2/3}$ the density $|\mathcal{F}(m_2)|^2$ is integrable. Observe that, as h_{ext} approaches the critical field h_{ext}^*, the density $|\mathcal{F}(m_2)|^2$ concentrates at $k_1^* = 2\pi d^{-2/3} \ell^{-2/3} t^{1/3}$ and $k_2^* = \pi \ell^{-1}$ respectively. In fact, the minimum of $d^2 k_1^2 + \frac{t}{2} k_2^2 |k_1|^{-1}$ among $k_1 \in \mathbb{R}$ and $k_2 \in \frac{\pi}{\ell}\mathbb{Z}$ is attained at k_1^* and k_2^*, respectively, and it holds that

$$d^2 (k_1^*)^2 + \tfrac{t}{2} (k_2^*)^2 |k_1^*|^{-1} = h_{\text{ext}}^*.$$

Due to the uniform integrability away from the singularity as $h_{\text{ext}} \to h_{\text{ext}}^*$ one can show that

$$\langle |k_1| \rangle \to k_1^* \quad \text{in the limit} \quad h_{\text{ext}} \to h_{\text{ext}}^*.$$

A refinement of the analysis even shows that $\langle |k_1| \rangle$ monotonically decreases as h_{ext} increases, see Figure 7.3.

Summing up the above analysis shows that the dominant wave-length grows from values $\sim (-h_{\text{ext}})^{-1/2} d$ to $w^* = (32\pi)^{1/3} d^{2/3} \ell^{2/3} t^{-1/3}$ as the external field h_{ext} increases from moderate negative values $h_{\text{ext}} \sim -t^2 d^{-2}$ to h_{ext}^*.

7.1.2. Discretization and numerical simulation of the random field

We now address the numerical simulation of our augmented model (7.14). Let us therefore first rewrite the additional term (7.1) in the rescaled variables (1.11). We obtain

$$\widehat{E} = \text{old} - 2 \int \widehat{h}_{\text{ripple}} \widehat{m}_2 \, \mathrm{d}\widehat{x}_1 \, \mathrm{d}\widehat{x}_2, \tag{7.14}$$

where $\widehat{h}_{\text{ripple}}$ is a stationary Gaussian field of vanishing mean and of variance

$$\langle \widehat{h}_{\text{ripple}}(0,0) \widehat{h}_{\text{ripple}}(\widehat{x}_1, \widehat{x}_2) \rangle = (\sigma^*)^2 \delta(\widehat{x}_1) \delta(\widehat{x}_2), \tag{7.15}$$

where $\sigma^* = d^{-10/6}\ell^{5/6}t^{-1/6}Q\ell_{\text{grain}}\langle\overline{e_1e_2}(0,0)^2\rangle^{1/2}$. For a typical film of 30 nm thickness and 70 µm width the grain size is of the order $\ell_{\text{grain}} = 15\text{nm}$, see Section 1.12. For a local strength of anisotropy $Q = 5 \times 10^{-3}$ we obtain that $(\sigma^*)^2 = 125.87$. On the level of the discretization, $\widehat{h}_{\text{ripple}}$ in (7.2) is modeled as a Gaussian random variable of mean zero, which is identically and independently distributed from grid point to grid point and has variance $(\sigma^*)^2\Delta\widehat{x}_1{}^{-1}\Delta\widehat{x}_2{}^{-1}$, where $\Delta\widehat{x}_i$ denotes the grid size. For the value of $(\sigma^*)^2 = 110.83$, our numerical simulation indeed shows a continuous transition from the ripple to the concertina pattern instead of a first-order phase transition due to a subcritical bifurcation, see Figure 1.30.

7.2. Thermal fluctuations vs. quenched disorder

In the following, we want to contrast the effect of thermal fluctuations to the effect of quenched disorder. Thermal fluctuations can be modeled by a random external field term in the Landau-Lifshitz-Gilbert equation (LLGe) that is white noise in *space and time*. On the other hand, as we have seen, quenched disorder related to the polycrystallinity of the material can be modeled by a random field term that is white noise in *space*.

It is known that the space-time white noise in the LLGe leads to a divergence in small wave-lengths, cf. [BG05, Section 2.4, Figure 1 and 2]. In fact, the exchange energy is not strong enough to suppress these excitations. Within the numerical simulations, one observes a mesh-size dependence of the solution, cf. [Abe10], which can be remediated by a suitable renormalization. These effects are related to the presence of phase transitions in the Heisenberg spin model. Hence it is not surprising that the critical dimension for that effect is two, cf. Table 7.18. Both effects are investigated below on the basis of the linearization of the energy for bulk material and thin films. The analysis shows that the expected average infinitesimal amplitude is given by

$$\langle|\delta m|^2\rangle = \int \lambda(k)^{-j}\,\mathrm{d}k \tag{7.16}$$

and that the dominant wave number of the magnetization is given by

$$\langle|k|\rangle = \frac{\int \lambda(k)^{-j}|k|\,\mathrm{d}k}{\int \lambda(k)^{-j}\,\mathrm{d}k}, \tag{7.17}$$

where $\lambda(k)$ denotes the eigenvalues of the linearization of the energy parameterized by the wave number in Fourier space. We will see that $j = 1$ in case of thermal fluctuations and $j = 2$ in case of quenched disorder. Note that (7.17) is just a reformulation of the expectation for the ripple wave number in (7.7). We will see that (7.16) and (7.17) diverge in case of thermal fluctuations, i.e., $j = 1$, though only logarithmically in a thin film. In case of quenched disorder, i.e., $j = 2$, (7.16) and (7.17) are finite. But only in a thin film the dominant wave length is determined by both exchange and stray-field energy and turns out to be much larger than the atomistic length scale, i.e., the exchange length d, and the typical grain size ℓ_{grain}.

7.2.1. Thermal fluctuations.

We consider the Langevin dynamics of the LLGe and take into account a white-noise torque. The stationary measure which is associated to the dynamics is given by the Gibbs distribution

$$\frac{1}{Z}\exp(-E(m))\,\mathrm{d}m, \tag{7.18}$$

where E denotes the micromagnetic energy (1.1). We start with the effect of thermal fluctuations in a bulk sample where we think of the energy E as the full micromagnetic energy (1.1). Afterwards we consider a two-dimensional thin film. In that case the magnetization is assumed to be in-plane, i.e., $m_3 = 0$, so that the stray-field energy can be approximated by

$$\tfrac{t}{2}\int_{\Omega'} ||\nabla'|^{-1/2}\nabla'\cdot m'|^2\,\mathrm{d}x_1\,\mathrm{d}x_2,$$

cf. (1.9). In order to derive expectations for the spatially averaged magnetization and the dominant wave number, we need the following identities. Let $A \in \mathbb{R}^{n\times n}$ be a symmetric positive definite matrix. Then

$$\int_{\mathbb{R}^n} |x|^2 \mathrm{e}^{\frac{-x\cdot Ax}{2}}\,\mathrm{d}x = (2\pi)^{n/2}\Big(\prod_{i=1}^n \lambda_i^{-1/2}\Big)\Big(\sum_{i=1}^n \lambda_i^{-1}\Big)$$

and

$$\int_{\mathbb{R}^n} \mathrm{e}^{\frac{-x\cdot Ax}{2}}\,\mathrm{d}x = (2\pi)^{n/2}\Big(\prod_{i=1}^n \lambda_i^{-1/2}\Big),$$

where λ_i, $i = 1,\dots,n$ denote the eigenvalues of the matrix A. In fact, using substitution of coordinates $x = Q^T\widehat{x}$ where $Q \in \mathrm{O}(N)$ is s.t. $QAQ^T = \mathrm{diag}(\lambda)$, this is a consequence of the one-dimensional identities

$$\int_{\mathbb{R}} |x|^2 \mathrm{e}^{\frac{-\lambda x^2}{2}}\,\mathrm{d}x = \Big(\tfrac{2\pi}{\lambda^3}\Big)^{1/2} \quad \text{and} \quad \int_{\mathbb{R}} \mathrm{e}^{\frac{-\lambda x^2}{2}}\,\mathrm{d}x = \Big(\tfrac{2\pi}{\lambda}\Big)^{1/2}. \tag{7.19}$$

Bulk sample $d = 3$**.** To simplify the discussions we assume that the bulk sample is given by a periodic cube $(0,L)^3$ of period L so large that is does not affect the characteristic length scale of the minimizer. Moreover, we consider a uniform external magnetic field $H_{\mathrm{ext}} = (-h_{\mathrm{ext}},0,0)$ so that $m^* = (1,0,0)$ is the global minimizer of the energy for $h_{\mathrm{ext}} < 0$. If we approximate the energy $E(m)$ for m close to m^* with the help of its Hessian, more precisely

$$\begin{aligned} E(m) &\approx \tfrac{1}{2}\mathrm{Hess}E(m^*)(m_\sharp, m_\sharp) \\ &= d^2\int_{(0,L)^3} |\nabla m_\sharp|^2\,\mathrm{d}x + \int_{(0,L)^3} \big||\nabla|^{-1}\nabla\cdot m_\sharp\big|^2\,\mathrm{d}x - h_{\mathrm{ext}}\int_{(0,L)^3} |m_\sharp|^2\,\mathrm{d}x, \end{aligned}$$

where $m_\sharp = (m_2, m_3)$, then the measure (7.18) can be explicitly analyzed. To circumvent the subtleties related to the measure $\mathrm{d}m$, it is helpful to think of $m_\sharp$ as a high-dimensional finite difference approximation ${m_\sharp}^{\Delta x}$ on a uniform Cartesian grid of grid size $\Delta x = L/N$ for some large $N \in \mathbb{N}$. Under these assumptions the expectation of the average stationary magnetization is approximated by

$$\frac{\int ||m_\sharp||_{L^2}^2 \mathrm{e}^{-E(m)}\,\mathrm{d}m}{\int \mathrm{e}^{-E(m)}\,\mathrm{d}m} \approx \frac{\int_{\mathbb{R}^{N^3}\times\mathbb{R}^{N^3}} \Delta x^3 ||{m_\sharp}^{\Delta x}||_{l^2}^2 \mathrm{e}^{-\frac{{m_\sharp}^{\Delta x}\cdot \mathrm{Hess}E^{\Delta x}(m^*){m_\sharp}^{\Delta x}}{2}}\,\mathrm{d}m_2^{\Delta x}\,\mathrm{d}m_3^{\Delta x}}{\int_{\mathbb{R}^{N^3}\times\mathbb{R}^{N^3}} \mathrm{e}^{-\frac{{m_\sharp}^{\Delta x}\cdot \mathrm{Hess}E^{\Delta x}(m^*){m_\sharp}^{\Delta x}}{2}}\,\mathrm{d}m_2^{\Delta x}\,\mathrm{d}m_3^{\Delta x}}. \quad (7.20)$$

Using (7.19) we find that (7.20) turns into

$$\frac{\int ||m_\sharp||_{L^2}^2 \mathrm{e}^{\frac{-\mathrm{Hess}E(m^*)(m_\sharp,m_\sharp)}{2}}\,\mathrm{d}\delta m}{\int \mathrm{e}^{\frac{-\mathrm{Hess}E(m^*)(m_\sharp,m_\sharp)}{2}}\,\mathrm{d}m_\sharp} \approx \sum_{l\in\{0,\dots,N-1\}^3} \big((\lambda_{\mathrm{div}}^{\Delta x}(l))^{-1} + (\lambda_{\mathrm{curl}}^{\Delta x}(l))^{-1}\big), \quad (7.21)$$

where $\lambda_{\mathrm{div}}^{\Delta x}$ and $\lambda_{\mathrm{curl}}^{\Delta x}$ denote the eigenvalues of $\Delta x^{-3}\mathrm{Hess}E^{\Delta x}(m^*)$. In fact, the application of the discrete Fourier transform $\mathcal{F}$ to the vector field ${m_\sharp}^{\Delta x} = (0, m_2^{\Delta x}, m_3^{\Delta x})$ shows that

$$\mathrm{Hess}E^{\Delta x}(m^*)(m_\sharp^{\Delta x}, m_\sharp^{\Delta x}) = 2\Delta x^3 \sum_{l=(l_1,l_2,l_3)\in\{0,\dots,N-1\}^3} \begin{pmatrix} \mathcal{F}(m_2^{\Delta x})_l \\ \mathcal{F}(m_3^{\Delta x})_l \end{pmatrix} \cdot \begin{pmatrix} d^2|K(l)|^2 + \frac{K(l_2)^2}{|K(l)|^2} - h_{\mathrm{ext}} & \frac{K(l_2)K(l_3)}{|K(l)|^2} \\ \frac{K(l_2)K(l_3)}{|K(l)|^2} & d^2|K(l)|^2 + \frac{K(l_3)^2}{|K(l)|^2} - h_{\mathrm{ext}} \end{pmatrix} \begin{pmatrix} \mathcal{F}(m_2^{\Delta x})_l \\ \mathcal{F}(m_3^{\Delta x})_l \end{pmatrix},$$

where

$$K(l) = \tfrac{2}{\Delta x}\sin(\tfrac{\pi l}{N}) = \tfrac{2}{\Delta x}\big(\sin(\tfrac{\pi l_1}{N}), \sin(\tfrac{\pi l_2}{N}), \sin(\tfrac{\pi l_3}{N})\big)$$

is the discrete Fourier multiplier, see (4.2) in Chapter 4. To each 2×2-dimensional block of the Hessian in Fourier space, there is one eigenvalue associated to a divergence-free eigenvector, given by

$$\lambda_{\mathrm{div}}^{\Delta x}(l) = 2(d^2|K(l)|^2 - h_{\mathrm{ext}}),$$

and one eigenvalue associated to a curl-free eigenvector, given by

$$\lambda_{\mathrm{curl}}^{\Delta x}(l) = 2(d^2|K(l)|^2 + \frac{|K((0,l_2,l_3)|^2}{|K(l)|^2} - h_{\mathrm{ext}}),$$

respectively, where $l = (l_1, l_2, l_3) \in \{0, \dots, N-1\}^3$. In the limit Δx to zero, $K(l)$ converges to $k_l = \frac{2\pi}{L} l \in \frac{2\pi}{L}\mathbb{Z}^3$. Hence, the r.h.s. in (7.21) is not bounded due to

a divergence in the large wave numbers, i.e., $|k_l| \gg (|h_{\text{ext}}|)^{1/2} d^{-1}$, even in case of stabilizing external field $h_{\text{ext}} < 0$. This entails that the dominant wave number diverges as the inverse grid size, i.e.,

$$\langle |k_i| \rangle \sim \frac{\sum_{l \in \{0,\dots,N-1\}^3} |K(l_i)| \left((\lambda^{\Delta x}_{\text{div}}(l))^{-1} + (\lambda^{\Delta x}_{\text{curl}}(l))^{-1} \right)}{\sum_{l \in \{0,\dots,N-1\}^3} \left((\lambda^{\Delta x}_{\text{div}}(l))^{-1} + (\lambda^{\Delta x}_{\text{curl}}(l))^{-1} \right)} \sim \Delta x^{-1} \tag{7.22}$$

for $i = 1, 2, 3$. The dominant wave number is defined in analogy to the dominant wave number in case of quenched disorder, see (7.23), and can be identified with

$$\langle |k_i| \rangle = \frac{\int \| |\nabla|^{1/2} m_\sharp \|_{L^2}^2 \mathrm{e}^{-E(m)} \, \mathrm{d}m_\sharp}{\int \| m_\sharp \|^2 \mathrm{e}^{-E(m)} \, \mathrm{d}m_\sharp}.$$

Thin film $d = 2$. We now discuss the effect of thermal fluctuations in a periodic thin film $(0, L)^2$. We assume that the magnetization is in-plane, i.e., $m_3 = 0$. Then the Hessian is given by:

$$\mathrm{Hess} E^{2-d}(m^*)(m_2, m_2) = 2 \int |\nabla' m_2^2| \, \mathrm{d}x' + t \int ||\nabla'|^{-1/2} \partial_2 m_2|^2 \, \mathrm{d}x' - 2 h_{\text{ext}} \int m_2^2 \, \mathrm{d}x'.$$

The eigenvalues of the (discrete) Hessian are given by

$$\lambda^{\Delta x}(l) = 2(d^2 |K(l)|^2 + \tfrac{t}{2} \frac{|K(l_2)|^2}{|K((l_1, l_2)|} - h_{\text{ext}}),$$

where $l = (l_1, l_2) \in \{0, \dots, N-1\}^2$. In the limit Δx to zero, $K(l)$ converges as before to $k_l \in \frac{2\pi}{L}\mathbb{Z}$. Note that the contribution coming from the stray-field only has a significant damping effect on the small wave numbers. For large wave numbers we find a logarithmic divergence of the sum $\sum (\lambda^{\Delta x})^{-1}$ – which is the expectation of the average amplitude of the magnetization – as Δx tends to zero. Similar as before the dominant wave number diverges as

$$\langle |k_i| \rangle \sim \frac{\sum_{l \in \{0,\dots,N-1\}^3} |K(l_i)| (\lambda^{\Delta x}(l))^{-1}}{\sum_{l \in \{0,\dots,N-1\}^3} (\lambda^{\Delta x})^{-1}} \sim {\Delta x_i}^{-1}, \ i = 1, 2. \tag{7.23}$$

Both can be seen using the approximation

$$\lambda^{\Delta x} \overset{\Delta x \downarrow 0}{\to} \sim \begin{cases} d^2 k_1^2 + \frac{t^2}{2} \frac{k_2^2}{|k_1|} - h_{\text{ext}} & \text{for} \quad \langle |k_2| \rangle \ll \langle |k_1| \rangle \\ d^2 k_2^2 + \frac{t^2}{2} |k_2| - h_{\text{ext}} & \text{for} \quad \langle |k_2| \rangle \gg \langle |k_1| \rangle. \end{cases}$$

We skip the detailed argument at that point. It uses the same rescaling as in the case of a thin film for quenched disorder, see below.

7.2.2. Quenched disorder.

Bulk sample $d = 3$. Again we start with the discussion of the bulk sample where we take into account a position-dependent easy axis $e(x) \in \mathbb{S}^2$ in order to model a local anisotropy. For an external field $H_{\text{ext}} = (-h_{\text{ext}}, 0, 0)$ we consider the linearization of the energy close to m^*, i.e.,

$$d^2 \int_{(0,L)^3} |\nabla m_\sharp|^2 \,\mathrm{d}x + \int_{(0,L)^3} \big||\nabla|^{-1} \nabla \cdot m_\sharp\big|^2 \,\mathrm{d}x \\ - h_{\text{ext}} \int_{(0,L)^3} |m_\sharp|^2 \,\mathrm{d}x - 2 \int_{(0,L)^3} \left(h^2_{\text{ripple}} m_2 + h^3_{\text{ripple}} m_3\right) \mathrm{d}x,$$

where h^2_{ripple} and h^3_{ripple} are stationary Gaussian fields of vanishing mean and covariance

$$\langle h^2_{\text{ripple}}(0) h^2_{\text{ripple}}(x)\rangle = \langle h^3_{\text{ripple}}(0) h^3_{\text{ripple}}(x)\rangle = \sigma^2 \delta(x_1)\delta(x_2)\delta(x_3). \tag{7.24}$$

Moreover

$$\langle h^2_{\text{ripple}}(0) h^3_{\text{ripple}}(x)\rangle = 0. \tag{7.25}$$

Again, $\langle\cdot\rangle$ denotes the ensemble average and δ the Dirac distribution. The explicit minimization of the linearization of the energy in Fourier space yields that

$$\begin{pmatrix} \mathcal{F}(h^2_{\text{ripple}})(k) \\ \mathcal{F}(h^3_{\text{ripple}})(k) \end{pmatrix} = \tfrac{1}{2} A(k) \begin{pmatrix} \mathcal{F}(m_2)(k) \\ \mathcal{F}(m_3)(k) \end{pmatrix},$$

where $\mathcal{F}$ now denotes the Fourier series w.r.t. x_1, x_2 and x_3 and

$$A(k) = \begin{pmatrix} d^2|k|^2 + \frac{k_2^2}{|k|^2} - h_{\text{ext}} & \frac{k_2 k_3}{|k|^2} \\ \frac{k_2 k_3}{|k|^2} & d^2|k|^2 + \frac{k_3^2}{|k|^2} - h_{\text{ext}} \end{pmatrix}, \quad k \in \tfrac{2\pi}{L}\mathbb{Z}.$$

Let $v_1(k) = \frac{1}{(k_2^2+k_3^2)^{1/2}}(-k_3, k_2)$ and $v_2(k) = \frac{1}{(k_2^2+k_3^2)^{1/2}}(k_2, k_3)$ be the eigenvectors of the matrix $A(k)$. Then

$$\begin{aligned} \begin{pmatrix} \mathcal{F}(m_2)(k) \\ \mathcal{F}(m_3)(k) \end{pmatrix} &= A(k)^{-1} \begin{pmatrix} \mathcal{F}(h^2_{\text{ripple}})(k) \\ \mathcal{F}(h^3_{\text{ripple}})(k) \end{pmatrix} \\ &= (\lambda_{\text{div}}(k)^{-1} a(k) v_1(k) + \lambda_{\text{curl}}(k)^{-1} a(k) v_2(k)), \end{aligned}$$

where

$$a(k) = v_1(k) \cdot \mathcal{F}(h_{\text{ripple}}) = \frac{1}{(k_2^2+k_3^2)^{1/2}}(-k_3 \mathcal{F}(h^2_{\text{ripple}})(k) + k_2 \mathcal{F}(h^3_{\text{ripple}})(k)),$$

$$b(k) = v_2(k) \cdot \mathcal{F}(h_{\text{ripple}}) = \frac{1}{(k_2^2+k_3^2)^{1/2}}(k_2 \mathcal{F}(h^2_{\text{ripple}})(k) + k_3 \mathcal{F}(h^3_{\text{ripple}})(k)).$$

The eigenvalues are given by

$$\lambda_{\mathrm{div}}(k) = (d^2|k|^2 - h_{\mathrm{ext}}) \quad \text{and} \quad \lambda_{\mathrm{curl}}(k) = (d^2|k|^2 + \tfrac{k_2^2+k_3^2}{|k|^2} - h_{\mathrm{ext}}),$$

as before, see p. 165. Since $v_1(k)$ and $v_2(k)$ are orthonormal and due to (7.24) and (7.25), we obtain

$$\langle \sum_k |\mathcal{F}(m_\sharp)|^2 \rangle \sim \sigma^2 \sum_k (\lambda_{\mathrm{div}}(k)^{-2} + \lambda_{\mathrm{curl}}(k)^{-2}) \sim \sigma^2 \sum_k \lambda_{\mathrm{div}}(k)^{-2}.$$

The r.h.s. is finite since $(1+|\widehat{k}|^2)^{-2}$ is integrable in dimensions less or equal to four. Using the rescaling $k = d^{-1}(-h_{\mathrm{ext}})^{1/2}\widehat{k}$ we find that the dominant wave number scales as

$$\frac{\langle \sum_k |k_i||\mathcal{F}(m_\sharp)|^2 \rangle}{\langle \sum_k |\mathcal{F}(m_\sharp)|^2 \rangle} \sim d^{-1} h_{\mathrm{ext}}^{1/2}, \tag{7.26}$$

$i = 1, 2, 3$.

Thin film $d = 2$**.** In case of a thin film we consider the energy

$$d^2 \int_{(0,L)^2} |\nabla' m_2|^2 \,\mathrm{d}x_1\,\mathrm{d}x_2 + \tfrac{t}{2} \int_{(0,L)^2} \left| |\nabla'|^{-1//2} \partial_2 m_2 \right|^2 \mathrm{d}x_1\,\mathrm{d}x_2 \\ - h_{\mathrm{ext}} \int_{(0,L)^2} |m_2^2|^2 \,\mathrm{d}x_1\,\mathrm{d}x_2 - 2\int_{(0,L)^2} h_{\mathrm{ripple}} m_2 \,\mathrm{d}x_1\,\mathrm{d}x_2,$$

where h_{ripple} is a stationary Gaussian field of vanishing mean and covariance $\langle h_{\mathrm{ripple}}(0) h_{\mathrm{ripple}}(x)\rangle = \sigma^2 \delta(x_1)\delta(x_2)$. The explicit minimization in Fourier space yields that

$$\langle \sum_{k'} |\mathcal{F}(m_\sharp)|^2 \rangle = \sigma^2 \sum_k \lambda(k')^{-2}, \tag{7.27}$$

where

$$\lambda(k) = d^2|k'|^2 + \tfrac{t}{2}\tfrac{k_2^2}{|k'|^2} - h_{\mathrm{ext}}.$$

Clearly, for $h_{\mathrm{ext}} < 0$ the right hand side in (7.27) is finite since $(|k'|^2+1)^{-2}$ is integrable in dimension two. We use the rescaling

$$k_1 = d^{-1} h_{\mathrm{ext}}^{1/2} \widehat{k}_1,$$
$$k_2 = (dt)^{-1/2}(-h_{\mathrm{ext}})^{3/4}\widehat{k}_2.$$

Let $\alpha = dt^{-1}(-h_{\mathrm{ext}})^{1/2}$. Then

$$d^2|k'|^2 + \tfrac{t^2}{2}\tfrac{k_2^2}{|k'|} - h_{\mathrm{ext}} = h_{\mathrm{ext}} \left(\widehat{k}_1^2 + \alpha \widehat{k}_2^2 + \tfrac{\widehat{k}_2^2}{|\widehat{k}_1| + \alpha^{1/2}|\widehat{k}_2|} + 1 \right) \\ \sim \begin{cases} \widehat{k}_1^2 + \tfrac{\widehat{k}_2^2}{|k_1|} + 1 & \text{for} \quad |\widehat{k}_2| \ll \alpha^{-1/2}|\widehat{k}_1| \\ \alpha k_2^2 + \alpha^{-1/2}|k_2| + 1 & \text{for} \quad |k_2| \gg \alpha^{-1/2}|k_1|. \end{cases}$$

For large sample size L we can approximate the sum by the integral

$$(\tfrac{\pi}{L})^2 \sum_{k' \in (\frac{\pi}{L}\mathbb{Z})^2} \frac{1}{(d^2|k'|^2 + \frac{1}{2}t\frac{k_2^2}{|k'|} - h_{\text{ext}})^2} \sim h_{\text{ext}}^{-2} \Big(\int_{-\infty}^{\infty} \int_0^{\alpha^{-1/2}|\widehat{k}_1|} (\widehat{k}_1^2 + \tfrac{\widehat{k}_2^2}{|k_1|} + 1)^{-2} \, \mathrm{d}\widehat{k}_2 \, \mathrm{d}\widehat{k}_1 + \int_{-\infty}^{\infty} \int_{\alpha^{1/2}|\widehat{k}_2|}^{\infty} (\alpha k_2^2 + \alpha^{-1/2}|k_2| + 1)^{-2} \, \mathrm{d}\widehat{k}_1 \, \mathrm{d}\widehat{k}_2 \Big).$$

For $\alpha \ll 1$ the second integral tends to zero while the first integral is of order one. Hence, the expectation for the dominant wave number is

$$\langle |k_1| \rangle \sim d^{-1}(-h_{\text{ext}})^{1/2} \quad \text{and} \quad k_2 \sim (dt)^{-1/2}(-h_{\text{ext}})^{3/4}. \tag{7.28}$$

This is the dominant wave-length of the ripple in an extended thin film, cf. (7.8). Let us collect the main results (7.22), (7.23) and (7.26), (7.28) in Table 7.18.

	$d = 2$	$d = 3$
quenched disorder	$\langle \lvert k_1 \rvert \rangle \sim d^{-1} \lvert h_{\text{ext}} \rvert^{1/2}$ $\langle \lvert k_2 \rvert \rangle \sim d^{-1/2} t^{-1/2} \lvert h_{\text{ext}} \rvert^{3/4}$ for $0 < \lvert h_{\text{ext}} \rvert \ll t^2 d^{-2}$	$\langle \lvert k_i \rvert \rangle \sim d^{-1} \lvert h_{\text{ext}} \rvert^{1/2}$, $i = 1,2,3$
thermal fluctuations	$\langle \lvert k_i \rvert \rangle \sim \Delta x^{-1}$, $i = 1,2$	$\langle \lvert k_i \rvert \rangle \sim \Delta x^{-1}$, $i = 1,2$

Table 7.1.: Thermal fluctuations vs. quenched disorder in bulk samples ($d = 3$) and thin films ($d = 2$). The dominant wave-numbers in case of thermal fluctuations scale like the grid-size of the discretization.

At the beginning of this chapter the relation between the ripple and the concertina in polycrystalline material was investigated. Afterwards, we addressed the investigation of the different effects of thermal fluctuations and quenched disorder. The outcome of this analysis is in correspondence with numerical simulations. Thermal fluctuations, i.e., a spatial-temporal white-noise torque in the LLGe, lead to a divergence in the small wave-lengths. Quenched disorder in dimension three leads to an excitation of small wave-numbers of order $d^{-1}|h_{\text{ext}}|^{1/2}$. Only in dimension two it leads to an anisotropic response of the magnetization, i.e., the ripple.

8

General remarks

8.1. Some notes on hardware and software

Our simulations were run on Intel® Core™ 2 Duo 1.86GHz or Pentium ™ 4 3.00GHz CPUs with 2GB RAM. The operating system was Debian GNU/Linux 3.1 and the program was compiled with gcc version 3.3.5. As external packages PETSc 2.3.2 [BBG+09] together with MPICH2 1.0.4p1 and the libraries FFTW3-3.1.2 [FJ05] and SLEPc 2.3.2 [HRV05] were used. PETSc uses the Intel® MKL™ library in version 8.0.1.

Wolfram Mathematica® was used for the investigation of the amplitude functional. The visualization of our numerical results was done in MATLAB® by The MathWorks in version R2007a. The same version was also used for the minimizations related to domain theory. Schematic figures were drawn using PSTricks.

Our code was developed with the help of Eclipse with the CDT plug-in. Typesetting was done in LaTeX.

I am grateful for the countless contributors to the Open Source programming community for providing the numerous tools I have used.

A

List of notations and symbols

d	Exchange length. p. 2
E	Micromagnetic energy. p. 2
E_0	Reduced energy. p. 12
H_{ext}	External field $H_{\text{ext}} = (-h_{\text{ext}}, 0, 0)$. p. 3
H_{stray}	Stray field H_{stray} generated by magnetization m. p. 2
ℓ	Sample's width. p. 3
m	Magnetization $m = (m_1, m_2, m_3) : \Omega \to \mathbb{S}^2$. p. 1
ν	(Outward pointing) normal. p. 2
Ω	Domain occupied by sample. p. 1
Q	Quality factor (strength of anisotropy). p. 3
t	Sample's thickness. p. 3
w_a	Optimal period, i.e., absolute minimizer of the energy density. p. 18
w_m	Maximal period. p. 27
w_s	Marginally stable period, o.e. $\frac{\mathrm{d}^2}{\mathrm{d}w^2} E(\widehat{w}_s) = 0$. p. 22
w^*	Period of the unstable mode. p. 7
$\widehat{\ }$	Non-dimensionalized lengths and reduced units. p. 12
$[\ \ ]$	Jump of some quantity across an interface. p. 2
$\lvert\nabla\rvert^{-s}$	Operator associated to Fourier multiplier $\lvert\nabla\rvert^{-s}$. p. 3
$'$	In-plane components of some quantity, e.g. $x' = (x_1, x_2)$, $\nabla' = (\partial_1 \partial_2)^T$. p. 11
$\approx$	Asymptotically equal in a certain regime. p. 8
$\gtrsim$	$f \gtrsim g$ means $fC \geq g$ for a generic constant $C > 0$. p. 5
$\lesssim$	$f \lesssim g$ means $f \leq Cg$ for a generic constant $C > 0$. p. 5
$\sim$	$\sim$ stands for both $\lesssim$ and $\gtrsim$. p. 5
$\ll$	$f \ll g$: there exists $C > 1$ such that $Cf < g$ independent of the parameters involved. p. 5

Bibliography

[Abe10] C. Abert. Cell-size independent micromagnetic simulations including temperature. *Diploma thesis, University of Hamburg*, 2010.

[BBG+09] S. Balay, K. Buschelman, W.D. Gropp, D. Kaushik, M.G. Knepley, L. C. McInnes, B. F. Smith, and H. Zhang. PETSc Web page, 2009. http://www.mcs.anl.gov/petsc.

[BG05] D. V. Berkov and N. L. Gorn. Stochastic dynamic simulations of fast remagnetization processes: recent advances and applications. *Journal of Magnetism and Magnetic Materials"*, 290-291(Part 1):442 – 448, 2005. Proceedings of the Joint European Magnetic Symposia (JEMS' 04).

[BKR75] L. Bauer, H. B. Keller, and E. L. Reiss. Multiple eigenvalues lead to secondary bifurcation. *SIAM Rev.*, 17:101–122, 1975.

[BL76] J. Bergh and J. Löfström. *Interpolation spaces. An introduction*. Springer-Verlag, Berlin, 1976. Grundlehren der Mathematischen Wissenschaften, No. 223.

[BM96] T. Bridges and A. Mielke. Instability of spatially-periodic states for a family of semilinear pde's on an infinite strip. *Mathematische Nachrichten*, 197(22):2 – 25, 1996.

[BS89] P. Bryant and H. Suhl. Thin-film magnetic patterns in an external field. *Applied Physics Letters*, 54(22):2224–2226, 1989.

[CÁO06a] R. Cantero-Álvarez and F. Otto. Critical fields in ferromagnetic thin films: identification of four regimes. *J. Nonlinear Sci.*, 16(4):351–383, 2006.

[CÁO06b] R. Cantero-Álvarez and F. Otto. Oscillatory buckling mode in thin-film nucleation. *J. Nonlinear Sci.*, 16(4):385–413, 2006.

[CÁOS07] R. Cantero-Álvarez, F. Otto, and J. Steiner. The concertina pattern: a bifurcation in ferromagnetic thin films. *J. Nonlinear Sci.*, 17(3):221–281, 2007.

[CG08] B. D. Cullity and C. D. Graham. *Introduction to Magnetic Materials*. Wiley-IEEE Press, 2008.

[DE91] A. Doelman and W. Eckhaus. Periodic and quasi-periodic solutions of degenerate modulation equations. *Phys. D*, 53(2-4):249–266, 1991.

[DH08] P. Deuflhard and A. Hohmann. *Numerische Mathematik. 1*. Walter de Gruyter & Co., Berlin, fourth edition, 2008. Eine algorithmisch orientierte Einführung.

[DKM+01] A. DeSimone, R. V. Kohn, S. Müller, F. Otto, and R. Schäfer. Two-dimensional modelling of soft ferromagnetic films. *R. Soc. Lond. Proc. Ser. A Math. Phys. Eng. Sci.*, 457(2016):2983–2991, 2001.

[DKMO05] A. DeSimone, R. V. Kohn, S. Müller, and F. Otto. Recent analytical developments in micromagnetics. In Giorgio Bertotti and Isaak Mayergoyz, editors, *The Science of Hysteresis*, volume 2, chapter 4, pages 269–381. Elsevier Academic Press, 2005.

[Eck92] W. Eckhaus. On modulation equations of the Ginzburg-Landau type. In *ICIAM 91 (Washington, DC, 1991)*, pages 83–98. SIAM, Philadelphia, PA, 1992.

[Fel61] Ernst Feldtkeller. Blockierte Drehprozesse in dünnen magnetischen Schichten. *Elektronische Rechenanlagen*, 3(4):167–175, 1961.

[FJ05] M. Frigo and S. G. Johnson. The design and implementation of fftw3. In *Proceedings of the IEEE*, pages 216–231, 2005.

[Geo01] K. Georg. Matrix-free numerical continuation and bifurcation. *Numer. Funct. Anal. Optim.*, 22 (3-4):303–320, 2001.

[GK99] C. Geiger and C. Kanzow. *Numerische Verfahren zur Lösung unrestringierter Optimierungsaufgaben*. Springer, Berlin, Heidelberg, New York, 1999.

[GS02] M. Golubitsky and I. Stewart. *The symmetry perspective*, volume 200 of *Progress in Mathematics*. Birkhäuser Verlag, Basel, 2002. From equilibrium to chaos in phase space and physical space.

[GSS88] M. Golubitsky, I. Stewart, and D. G. Schaeffer. *Singularities and groups in bifurcation theory. Vol. II*, volume 69 of *Applied Mathematical Sciences*. Springer-Verlag, New York, 1988.

[Har68] K. J. Harte. Theory of magnetization ripple in ferromagnetic films. *Journal of Applied Physics*, 39(3):1503 –1524, 1968.

[Hof68] H. Hoffmann. Theory of magnetization ripple. *IEEE Trans. Magnetics*, 4 (1):32–38, 1968.

[Hoy06] R. B. Hoyle. *Pattern formation*. Cambridge University Press, Cambridge, 2006. An introduction to methods.

[HRV05] V. Hernandez, J.E. Roman, and V. Vidal. SLEPc: A scalable and flexible toolkit for the solution of eigenvalue problems. *ACM Transactions on Mathematical Software*, 31(3):351–362, September 2005.

[HS98] A. Hubert and R. Schäfer. *Magnetic Domains: The Analysis of Magnetic Microstructures*. Springer-Verlag, 1998.

[IJ90] G. Iooss and D. D. Joseph. *Elementary stability and bifurcation theory*. Undergraduate Texts in Mathematics. Springer-Verlag, New York, second edition, 1990.

[LL35] L. Landau and E. Lifshitz. On the theory of the dispersion of magnetic permeability in ferromagnetic bodies. *Physikalische Zeitschrift der Sowjetunion*, 8:153–169, 1935.

[LM68] J.-L. Lions and E. Magenes. *Problèmes aux limites non homogènes et applications. Vol. 1*. Travaux et Recherches Mathématiques, No. 17. Dunod, Paris, 1968.

[Mar00] M. P. Marder. *Condensed Matter Physics*. John Wiley & Sons, 2000.

[Mel03] C. Melcher. The logarithmic tail of Néel walls. *Arch. Ration. Mech. Anal.*, 168(2):83–113, 2003.

[Mie07] A. Mielke. Instabilities of families of periodic solutions. Private communication, 2007.

[Ole63] O. Oleinik. Discontinuous solutions of non-linear differential equations. *Amer. Math. Soc. Transl. (2)*, 26:95–172, 1963.

[OS10] F. Otto and J. Steiner. The concertina pattern. *Calculus of Variations and Partial Differential Equations*, 39:139–181, 2010.

[Ott09] F. Otto. Optimal bounds on the Kuramoto-Sivashinsky equation. *Journal of Functional Analysis*, 257(7):2188 – 2245, 2009.

[Peg85] R. L. Pego. Compactness in L^2 and the Fourier transform. *Proc. Amer. Math. Soc.*, 95(2):252–254, 1985.

[RS78] M. Reed and B. Simon. *Methods of modern mathematical physics. IV. Analysis of operators*. Academic Press, New York, 1978.

[Sei08] C. Seis. Instability of blocked states in ferromagnetic thin films. *Diploma thesis, University of Bonn*, 2008.

[Ser77] J.-P. Serre. *Linear representations of finite groups*. Springer-Verlag, New York, 1977. Translated from the second French edition by Leonard L. Scott, Graduate Texts in Mathematics, Vol. 42.

[Ste06] J. Steiner. Reduzierte Modelle für dünne ferromagnetische Filme: Analysis und Numerik. *Diploma thesis, University of Bonn*, 2006.

[vdBV82] H. van den Berg and D. Vatvani. Wall clusters and domain structure conversions. *Magnetics, IEEE Transactions on*, 18(3):880 – 887, 1982.

Lebenslauf Jutta Steiner

Aus Gründen des Datenschutzes enthält die elektronische Version dieser Dissertation keinen Lebenslauf.